Mediating the Exchange Coupling and Anisotropy in Nanoscale Magnets via Interfacial Interactions

by

Ryan Daniel Desautels

A thesis submitted to
The Faculty of Graduate Studies of
The University of Manitoba
in partial fulfillment of the requirements
of the degree of

Doctor of Philosophy

Department of Physics and Astronomy
The University of Manitoba
Winnipeg, Manitoba, Canada
December 2015

Thesis advisor Author

Johan van Lierop **Ryan Daniel Desautels**

Mediating the Exchange Coupling and Anisotropy in Nanoscale Magnets via Interfacial Interactions

Abstract

Nanoscale materials behave differently than their bulk counterparts due, in part, to the reduced length scales and the increased surface to core atom ratio. As the length scales decrease, the surface atoms become increasingly important as they make up a larger percentage of the total number of atoms. These surface atoms have magnetic properties that differ from the core atoms due to a surface anisotropy that alters the interparticle, intraparticle, and exchange interactions. In this work, we have synthesized three different nanoscale systems that will allow us to explore the physics of the different interactions. Cu/γ-Fe_2O_3 core/shell nanoparticles were chosen because the γ-Fe_2O_3 cores have vacancies in their B-sites, broken coordination at the surface, and experience superexchange interactions. As a comparison, multiphase undoped and V-doped SiO_2/FeCo nanoparticles were chosen as these nanoparticles do not suffer from vacancies or surface disorder and experience both direct exchange interactions from the nanoparticle core and superexchange interactions between the FeCo core and the metal silicate interfacial phase. Finally, Fe nanocrystallites were grown in a Cu matrix as they present no vacancies or surface disorder, and they are single phase. We observed that the interfacial phases that form in these core/shell and nanocrystallite/matrix nanoscale systems alters significantly the physics of the magnetism. The overall magnetic properties, the elemental magnetism, and the atomic magnetism were all observed to be altered by this interfacial phase, along with the interparticle and intraparticle interactions. In addition, the thickness of this interfacial phase, and thus the strength of its affect, was controlled by controlling the thickness of the shells or the amount of intermixing in the case of the nanostructured thin film.

Contents

List of Figures

List of Tables

Acknowledgments

I have several people whom deserve significant thanks for providing me with an environment necessary to allow me to succeed as a scientist. First and foremost, Dr. Johan van Lierop, my advisor, who provided support and encouraged me to pursue the topics that I found interesting. I would also like to thank Dr. van Lierop for providing me with several significant opportunities to expand my knowledge and experimental horizons through his numerous collaborations. I was provided with the opportunity to travel to Taiwan for three months to work with Dr. Ko-Wei Lin. This resulted in a significant portion of my thesis (Chapter 5). In addition, through collaborations with Dr. John Freeland at the Advanced Photon Source (Argonne National Laboratory) I was given the opportunity to work at a foremost beamline facility. Dr. van Lierop also provided me with an opportunity to do two 5-month internships with Dr. Michael Rowe at the Toyota Research Institute of North America which also has resulted in a significant portion of this work (Chapter 4).

I would also like to thank Dr. Freeland further for helping my understanding of XAS, XMCD, and XMRS experiments performed at the APS (supported by U.S. DOE under Contract No. DE-AC02-06CH11357) and for answering all of my questions regarding the experiments and the data analysis. My work has benifited greatly from these experiments and his help.

I am also grateful for the help and assistance of all the members of Dr. van Lierop's research group (the Nanomagnetism Research Group). Thanks are also extended to Gillis Roy and Peiqing Wang for their help with obtaining any kind of experimental equipment needed.

My sincerest thanks to my family, whose support and encouragement has allowed

me to pursue my goals. Finally, I would like to thank Elizabeth Skoropata. Her constant, unwavering support, encouragement, and friendship has made all of this possible.

To my wife Elizabeth, your support, encouragement and friendship has made all of this possible.

Chapter 1

Introduction

Magnetism is a class of physical phenomena that are mediated by applied magnetic fields, and every material is influenced in some way by this field. More specifically, magnetic materials, of which there are several basic types (paramagnetic, diamagnetic, ferromagnetic, ferrimagnetic and antiferromagnetic, see Fig. 1.1) are abundant and everywhere. Every element known falls into one of these categories (Fig. 1.2). However, of interest in this thesis are the transition metals of Fe, Co, Cu, and V and how they interact amongst themselves, and through orbital and spin exchange via oxygen in nanostructures. In the bulk, Fe and Co are ferromagnetic with a permanent magnetic moment, V is antiferromagnetic, and Cu is diamagnetic. Magnetic nanoparticles or nanocrystallites (matrix embedded nanoparticles) made from these transition metals (and their oxides) have provided a rich playground to study the physics of magnetism due to the fascinating differences in properties from their bulk counterparts.[1].

The aim of this thesis is to provide insight into the importance and impact of inter-

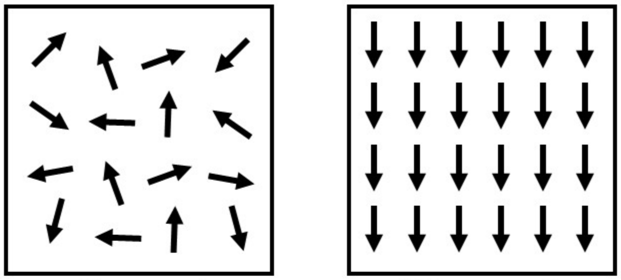

a) Paramagnet

b) Ferromagnet

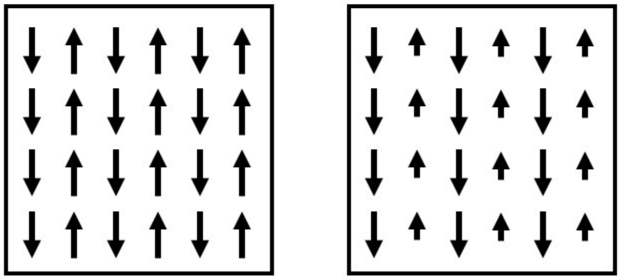

c) Antiferromagnet

d) Ferrimagnet

Figure 1.1: Schematic of the magnetic moment orientations for different types of magnetic materials (in zero applied field).

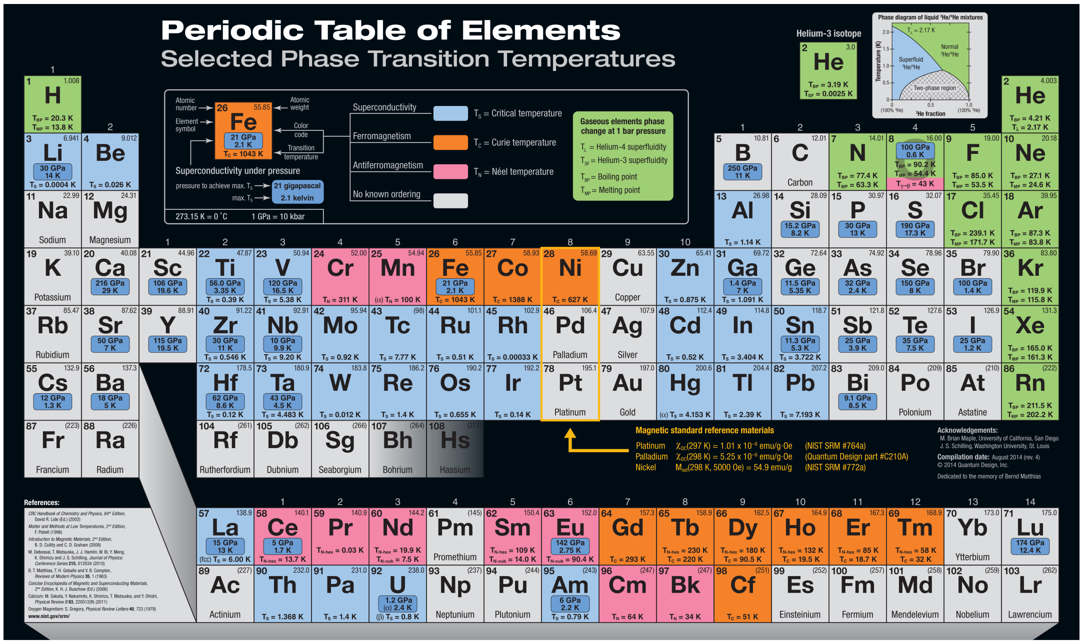

Figure 1.2: Magnetic periodic table of the elements[2].

facial atoms on the nanomagnetism of core/shell nanoparticles and nanocrystallites in thin films. Magnetic nanomaterials have become ubiquitous with todays technologies and can be found in a wide range of applications, from information storage[3] to drug delivery[4]. Core/shell nanoparticles have played an important role in our understanding of nanomagnetism. Formed most easily through the passive oxidation of the surface of a (magnetic) nanoparticle, this leads directly to the discovery of the exchange anisotropy in Co/CoO core/shell nanoparticles[5], which gives the exchange bias field loop shift and its use as the "biasing field" in hard-drive read/write heads central to the information revolution.

In this thesis, the nanoparticle cores' materials were chosen specifically to understand the physics of the nanomagnetism caused by the formation of an interfacial phase(s) that results in different types of exchange interactions between core and shell or nanocrystallite and matrix. γ-Fe_2O_3 (Fig. 1.3) nanoparticles have a large number of vacancies in the octahedral B-sites and significant surface disorder which make them ideal for exploring the effects on the magnetism of an interfacial phase on the surface atoms. In addition, it has been shown previously that doping atoms preferentially occupy B-sites[6; 7], which can be explored through element specific and atomic spectroscopy techniques. As a comparison, multiphase FeCo nanoparticles were chosen as they do not suffer from vacancies or surface disorder. Finally, Fe nanocrystallites were chosen as they represent the most straightforward case; no vacancies or surface disorder and single phase. Therefore, the evolution of the magnetism from the formation of an interfacial phase can be followed along a path where indirect exchange interactions dominate (Fe/Cu nanostructured thin films) to one where superexchange interactions dominate (Cu/γ-Fe_2O_3 nanoparticles).

The outline of this thesis begins with a brief introduction to nanoparticle magnetism, interparticle and intraparticle interactions, direct and indirect exchange interactions, and dipolar interactions. Chapter 2 describes the different experimental and analysis techniques used in this thesis. Chapters 3, 4, and 5 contain the bulk of my work on Cu/γ-Fe_2O_3 nanoparticles, undoped and V-doped SiO_2/FeCo nanoparticles, and Fe/Cu nanostructured thin films, respectively. Included in each chapter is a description of their synthesis, a detailed composition and microstructure analysis, overall magnetism, atomic magnetism, and elemental magnetism. An overall discussion of the experimental results is presented in Chapter 6 and conclusions are presented in Chapter 7.

At the nanoscale, the physics of the magnetism of the core/shell nanoparticles or nanocrystallites studied in this thesis are affected significantly by intraparticle and interparticle interactions. Intraparticle exchange interactions occur between the magnetic nanoparticle core and the non-magnetic surface. Interparticle interactions can be from dipole-dipole interactions or exchange interactions (described below). The dipole-dipole energy varies as $1/r^3$ where r is the interparticle separation. Dipole-dipole interactions alter the energy barrier to superparamagnetism[8] and these interactions will alter the magnetic properties of nanoscale systems. Due to the reduced length scales, finite size and surface effects dominate the nanomagnetism. Finite size effects result from the reduced length scales comparable to that of the electron's wavelength and quantum confinement effects become increasingly relevant. This results in the sensitivity of nanoparticle properties to changes in composition or morphology.

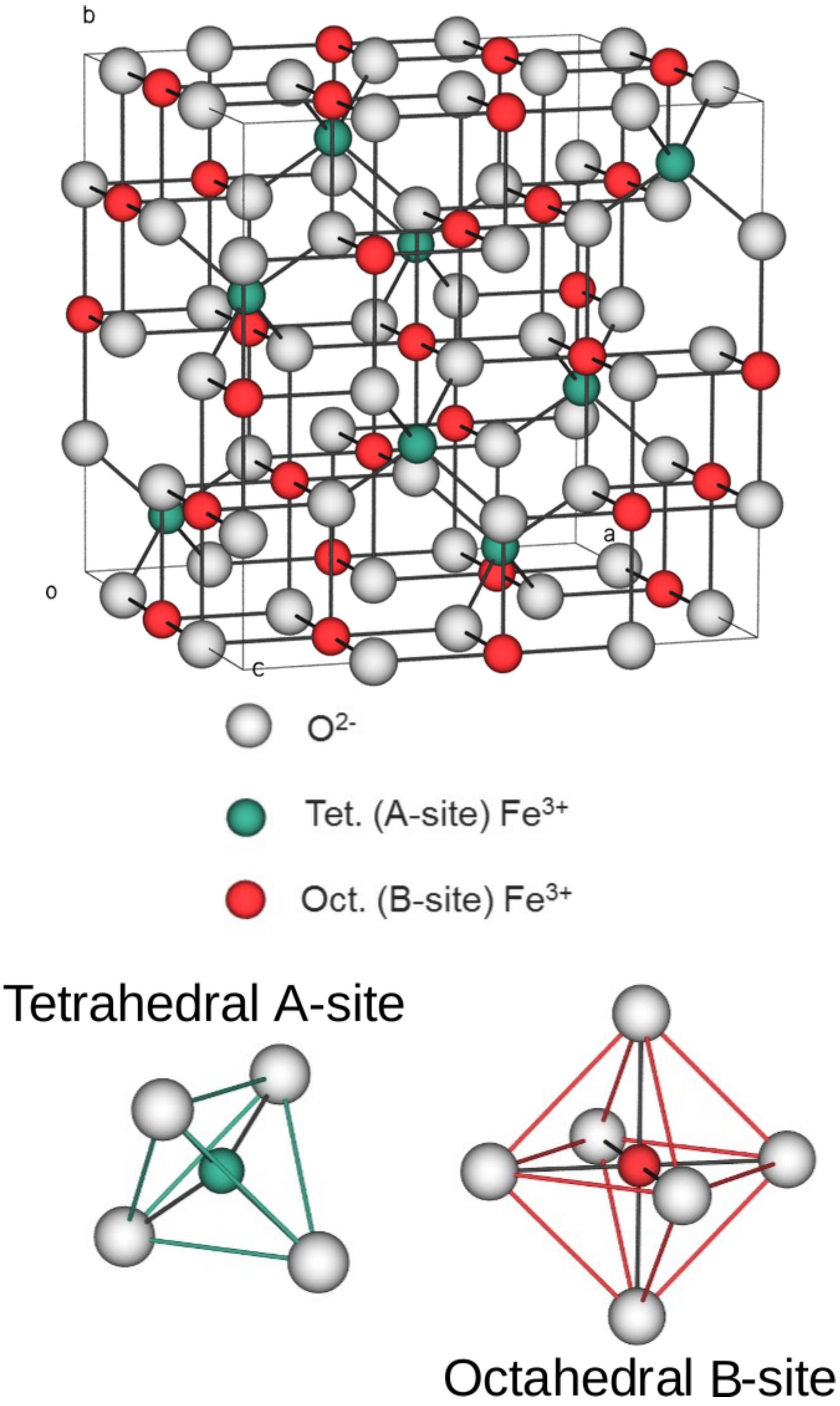

Figure 1.3: Crystal structure of γ-Fe_2O_3 showing both the tetrahedral Fe^{3+} A-sites and the octahedral Fe^{3+} B-sites. For maghemite, all the vacancies are located at the B-sites which provides a preferred location for the doping ions to go.

Surface effects (neglected at bulk scale where the surface area is small compared to the volume) play a significant role on the magnetism as the ratio of surface atoms to core atoms is large. For example, these surface atoms make up roughly 1-3% of a 100 nm diameter nanoparticle, 15-30% of a 10 nm diameter nanoparticle, and 30-60% of a 5 nm diameter nanoparticle[1].

Consider the surface atoms of a nanoparticle. These atoms (or ions) have a different environment than those of the core atoms having fewer neighboring atoms, thus their electronic and magnetic environments differ from that of the core atoms. The reduced number of magnetic neighbors can lead to frustrated surface spins with a canted magnetization leading to a reduction in the overall magnetism[9; 10]. In addition, the reduced symmetry at the surface of a nanoparticle can result in an enhanced surface anisotropy which can further influence the surface spins' orientation. This additional anisotropy modifies the energy barrier to superparamagnetic spin flips described by Stoner and Wohlfarth[8]. For an assembly of non-interacting single-domain nanoparticles, with uniaxial anisotropy, the energy barrier (Fig. 1.4) for the coherent reversal of the magnetization is; $E_B = KV \sin^2 \theta$, where K is the magnetic anisotropy, V is the volume of the nanoparticle, and θ is the angle between the moment and the nanoparticle's easy axis. This additional surface anisotropy from the frustrated surface spins alters the energy barrier. Attempts to control or alter these surface effects have been made[11] through the fabrication of core/shell morphologies. This morphology has been shown to provide an excellent route for obtaining magnetic properties not available to single phase nanoparticles[12]; not necessarily a simple combination of the magnetic properties of the core and shell materials.

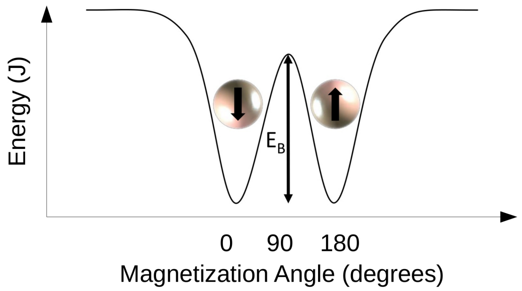

Figure 1.4: Energy barrier to superparamagnetic spin flips. Height of the barrier is proportional to KV.

This core/shell morphology provides a mechanism to understand the role that different types of exchange interactions (e.g. superexchange and direct exchange) have on the magnetism through the formation of an interfacial phase. Three nanoscale systems have been fabricated in order to answer this question. Core/shell nanoparticles of Cu/γ-Fe_2O_3 nanoparticles experience superexchange interactions with the ferrimagnetic core and also between the core and the interfacial phase of copper doped maghemite. Undoped and V-doped SiO_2/FeCo nanoparticles were synthesized using a metal halide reduction. These nanoparticles experience both indirect exchange interactions from the nanoparticle core and superexchange interactions between the FeCo core and the metal silicate interfacial phase. In addition, the V-doped SiO_2/FeCo nanoparticles provide an additional source of exchange interactions due to the formation of an antiferromagnetic vanadium oxide. Fe/Cu nanostructured films have been grown using a dual ion beam deposition system. Only indirect exchange interactions are present between the Fe nanocrystallites and the Cu matrix mediated through the formation of an interfacial FeCu alloy.

Magnetic properties of materials are influenced basically by two factors: exchange interactions and spin-orbit $(L - S)$ coupling. Spin-orbit coupling dictates the ori-

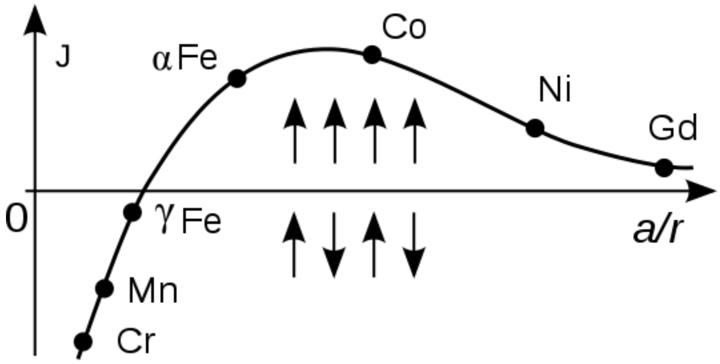

Figure 1.5: Bethe-Slater curve showing the magnitude of the exchange interaction as a function of atomic distance[13].

entation of the magnetization within materials whilst exchange interactions between atoms (or ions) determine how magnetic moments will align. These interactions will require the magnetic moments to be either parallel (positive exchange integral, J >0) or anti-parallel (negative exchange integral, J <0). The amount of energy involved depends on the electron orbital overlap. Direct, indirect, and superexchange are the three types of exchange interactions.

Direct exchange interactions are the result of wavefunction overlapping of magnetic atoms. In all cases, nature attempts to minimize the Coulombic interaction energy. Therefore, for atoms (or ions) that are close together, the Coulombic interaction is minimized when the electrons are located between the nuclei and have opposite spin; antiferromagnetic ordering. For atoms that are of sufficient distance apart, the electron configuration that best minimizes the Coulombic interaction energy is that of electrons localized near their nuclei and aligned parallel, ferromagnetic ordering. The magnitude of the direct exchange integral as a function of atomic distance is shown in the Bethe-Slater curve (Fig. 1.5). For direct exchange interactions, the exchange integral J can be either positive or negative.

Indirect exchange interactions couple magnetic moments over large distances through their interactions with conduction electrons. This type of exchange dominates in metals where there is very little overlap between the electron orbitals (i.e. electrons are localized). These exchange interactions, also known as Ruderman-Kittel-Kasuya-Yosida[14; 15; 16] (RKKY) have an exchange integral that oscillates between positive and negative as a function of the distance between the magnetic ions (Fig. 1.6). These effects have been observed readily in thin films of Fe/Cr/Fe[17; 18] and Co/Cu/Co[19]

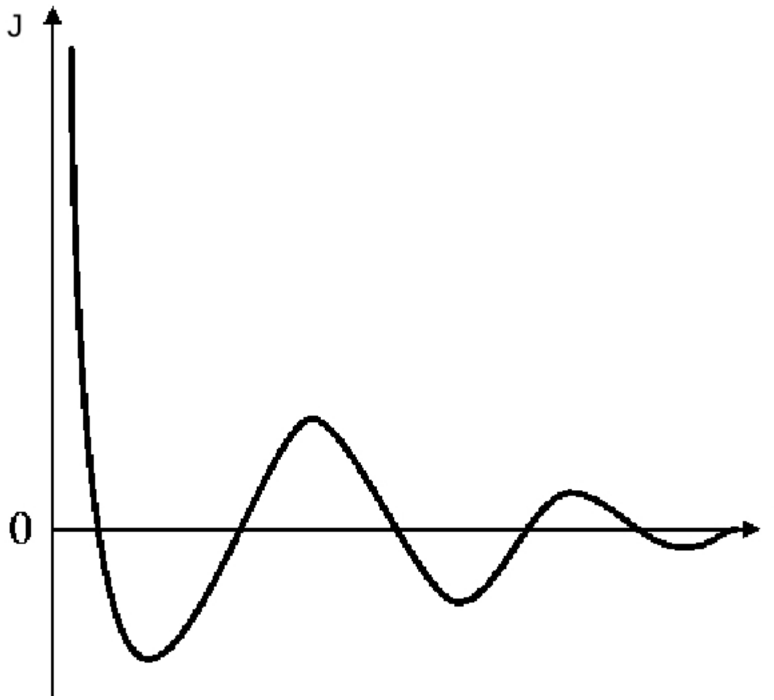

Figure 1.6: Variation of the indirect exchange interaction as a function of atomic spacing.

Superexchange interactions are the coupling of magnetic cations through a non-magnetic anion due to the overlap of their respective electron orbitals (Fig. 1.7). The sign of the exchange integral, J, depends on several factors; the bond lengths, the bond angles, the involved d-orbitals, and the amount of hybridization with the

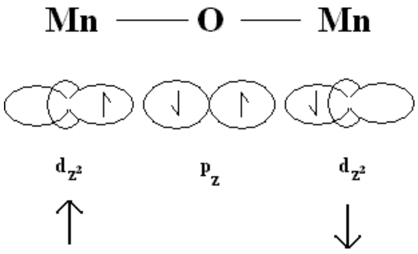

Figure 1.7: Superexchange of Mn^{2+} cations through an O^{2-} anion[20].

anions electron orbitals. The rules that govern this were determined by Goodenough and Kanamori[21]. Kramers first observed the superexchange interaction effects in MnO[22]. Here, the Mn-O-Mn exchange interactions have 180° orbital symmetry (which results in strong superexchange) and yields antiferromagnetic coupling (J <0). Another example, one relevant to this thesis, is magnetic ordering in maghemite (γ-Fe_2O_3). Three exchange interactions (J_{AA}, J_{BB}, and J_{AB}) exist due to the two lattice sites (A- and B-sites). Because of the specific geometry set by the spinel crystal structure, J_{AB} dominates the exchange, followed (in magnitude) by J_{BB} and J_{AA}. Resulting directly from these exchange integral terms, the arrangement of spins within the maghemite spinel crystal lattice is such that the ions of the A- and B-sites are aligned antiferromagnetically, and the ions within the A-site and the B-site are aligned ferromagnetically. As there are more iron ions in the B-sites, the net magnetic moment is non-zero. Thus, maghemite is a ferrimagnetic material, an antiferromagnetic configuration with ferromagnetic behaviour.

Spin-orbit ($L-S$) coupling gives rise to the magnetocrystalline anisotropy (K). As discussed previously, exchange interactions determine the magnetic ordering, while the magnetocrystalline anisotropy sets the orientation of the magnetization (with respect to the the crystal lattice). Here, the crystallographic axis that results in the lowest anisotropy sets the easy axis, and it costs energy to rotate the magnetocrystalline anisotropy away from this axis. The magnetocrystalline anisotropy is an intrinsic property of the magnetic material in question, and its magnitude therefore affects directly the magnetizations' field response.

Other types of anisotropy are shape anisotropy and surface anisotropy. Shape anisotropy is the result of magnetostatic energy and is therefore an extrinsic property of the system[23]. For the core/shell nanoparticles and the Fe nanocrystallites in a Cu matrix, their shapes are, to first order, spherical and therefore have no shape anisotropy. Surface anisotropy results from the reduced coordination of surface atoms (or ions) with respect to core atoms[24]. This surface anisotropy is crystal-field-like and from the surface atomic disorder, local crystal-fields with easy axes normal to the surface form[25]. As a result of these effects, magnetic spins at the nanoparticle surface are often canted or disordered and do not align with the core spins, sometimes forming a magnetically "dead" layer. In this thesis, we have altered directly these surface spins by coating the nanoparticles with a non-magnetic shell, resulting in the formation of a magnetically active interfacial phase.

The magnetism of a nanoscale system is influenced significantly by the different environment of the surface/interfacial spins relative to the core spins. The effects of these spins are evident in the temperature dependence of the saturation magnetization ($M_S(T)$). Consider a ferromagnetic material in the ground state ($T = 0$). Such a system has all of its spins ($S = 1/2$, $g = 2$) aligned parallel. Now, with a small increase in temperature ($T < T_C$), allowing only a single spin to reverse orientation

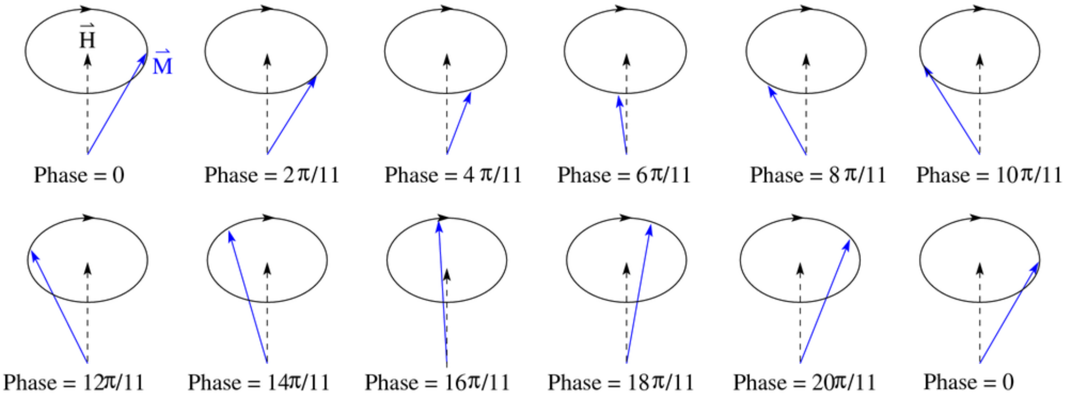

Figure 1.8: Illustration of a spin-wave. The precessing spins at a given phase and with a wavelength $\lambda = 11a$ are shown[26].

(lowest excited state), each electron has equal probability of being the source of this reversal suggesting that this reversed spin will not remain localized. The propagation of this reversed spin through a crystal is known as a spin-wave or magnon, a particle describing the collective excitation of an electron spin structure (Fig. 1.8). The energy of this spin-wave is given by[27]:

$$E - E_0 = E_K = Jk^2a^2 \tag{1.1}$$

Where J is the exchange constant, k is the wave-vector, and a is the lattice spacing. For a wave, the energy for a particle wave-vector k is simirlar to that of a harmonic oscillator, $E = n_k E_k = n_k \hbar\omega_k$. Since a spin-wave can behave as a particle (with an energy and a momentum) that obeys Bose-Einstein statistics, the average number of spin-waves for a certain wave-vector and temperature is then

$$\bar{n_k} = \frac{1}{e^{E_k/k_BT} - 1} \tag{1.2}$$

The total number of spin-waves ($\bar{n}$) is then determined by the sum over all possible k's of $\bar{n_k}$. Recall that the energy of a spin-wave (magnon) is given by $E_k = Jk^2a^2$, $\bar{n}$

is then

$$\bar{n} = \frac{V}{4\pi^2}\left(\frac{1}{a^2J}\right)^{3/2}\int_0^\infty \frac{E^{1/2}dE}{e^{E_k/k_BT}-1} \tag{1.3}$$

Solving this integral, we obtain

$$\bar{n} = 0.1174V\left(\frac{k_BT}{a^2J}\right)^{3/2} = BT^{3/2} \tag{1.4}$$

where B is the Bloch constant and depends on the volume (V), lattice spacing (a), and exchange constant (J). The thermal evolution of the saturation magnetization is then the Bloch-$T^{3/2}$ law[28]:

$$\frac{\Delta M_S}{M_S(0)} = \frac{\bar{n}}{N} \tag{1.5}$$

$$\frac{M_S(T)}{M_S(0)} = 1 - BT^{3/2} \tag{1.6}$$

As discussed above, the effects of the surface/interfacial spins affect significantly the thermal evolution of the saturation magnetization. Experimentally, this is observed as a rapid increase in $M_S(T)$ at low temperatures ($T < 100$ K), and becomes more pronounced with decreasing nanoparticle size. Currently, no definitive theoretical model is available. Recently, it has been suggested that the increased magnetization is due to Bose-Einstein condensation at low temperatures[29], however, this description does not take into account the finite size of the particles[30; 31] and the effect of the surface/interfacial spins[32]. In this thesis, we will show that the saturation magnetization's temperature dependence is well described by the modified Bloch-$T^{3/2}$ law which includes a phenomenological term that describes uniquely the effects of these surface/interfacial spins on the saturation magnetization is given by[30]:

$$\frac{M_S(T)}{M_S(0)} = \left[(1-A)\left(1-BT^{3/2}\right) + Ae^{-T/T_F}\right] \tag{1.7}$$

where A and T_f are experimental parameters determined *a priori* and are material and nanoparticle size dependent. A scales with the number of frozen surface spins and T_f represents the temperature at which these surface spins freeze.

A complete understanding of the composition and microstructure is paramount to understanding fully the magnetic properties of a nanoscale system. The size scales relevant for nanomagnetism provide several interesting experimental challenges that must be overcome. To that end, multiple experimental techniques must be used in order to determine fully the composition and microstructure of a core/shell nanoparticle or nanostructured thin film. To complicate the composition and microstructure determination further, the reduced length scale over which the interfacial phase forms makes its direct observation typically problematic. For example, in the studies of the Cu/γ-Fe_2O_3 nanoparticles, it became evident that the interfacial phase could be no more then 0.2 Å in thickness (the minimum resolution of the high-resolution transmission electron microscope used). There exists several experimental techniques with the sensitivity to observe the changes in the electronic environment due to this interfacial phase.

Characterization of the effects of these interfacial phases and the different exchange interactions on the nanomagnetism required the overall magnetic properties for the nanoscale systems to be explored using temperature and field dependent magnetometry and susceptometry. To compliment these experiments, both the temperature and field dependent elemental and atomic magnetism were measured using x-ray magnetic circular dichroism and Mössbauer spectroscopy. To understand the origin of the measured magnetism, comprehensive structural and compositional characterization and analysis were undertaken using x-ray diffraction, electron microscopy, x-ray photoelectron and absorption spectroscopy and Mössbauer spectroscopy.

The microstructure of the nanoscale systems studied within this thesis was determined from Rietveld refinements of the x-ray diffraction patterns that revealed the systems space group, lattice constants, crystallite size and texture (where present). Electron diffraction experiments provided complimentary results and supplemented the diffraction patterns at d-spacings not accessible with conventional x-ray diffraction. Transmission electron microscopy images in both the plane-view and cross-sectional view (for the Fe/Cu films) help identify the morphology and provide the average crystallite diameter and distribution of diameters (important for understanding the overall magnetism). X-ray absorption and photoelectron spectroscopy experiments were performed to identify the coordination environment and oxidation state of the transition metal atoms (or ions) within the nanoscale materials. In addition to the x-ray spectroscopy experiments, Mössbauer spectroscopy experiments provide information about the local environment around the Fe nuclei.

The effects of the magnetically active interfacial phase on the blocking behaviour were be determined from both *ac* and *dc* susceptibilities. Evidence of interparticle interactions was determined from the spin-glass-like field-cooled temperature dependent magnetization and the frequency dependence of the blocking temperature. The saturation magnetization's temperature dependence provided insight into the effects of this interfacial phase on the surface moments of the core nanoparticles/nanocrystallites. In addition, the temperature dependence of the coercivity and exchange bias loop shift identified how the interfacial phase had altered the surface anisotropy. X-ray magnetic circular dichroism and resonant scattering experiments provided insight into the elemental magnetism and provided an indication of the origins of the induced magnetism in the interfacial phase. The atomic magnetism of the Fe nuclei was measured using both transmission and conversion electron Mössbauer spectroscopy providing, for example, evidence of a magnetic transition from the formation of an FeCu alloy in the Fe/Cu nanostructured films.

Chapter 2

Experimental Methods

To understand fully the magnetic properties of the nanoscale samples studied within this work, it was necessary to determine completely their structural and compositional properties. The microstructure of these nanoscale materials was determined from diffraction experiments using both x-rays (x-ray diffraction and grazing incident x-ray diffraction) and electrons (selective area electron diffraction), as well as x-ray reflectometry and transmission electron microscopy. The composition of these materials was verified from x-ray photoelectron spectroscopy and x-ray absorption spectroscopy. Using circularly polarized (right and left) x-rays to collect absorption spectra, we can determine element specific magnetic properties via the magnetic circular dichorism. Probing the local environment around the ^{57}Fe nucleus using the Mössbauer effect (transmission and conversion electron spectroscopies) allowed us to determine compositional properties in addition to the hyperfine parameters. The temperature, field, and frequency dependence of the overall magnetic properties of these nanoscale samples were characterized using magnetometry and susceptometry experiments. We will describe these experimental techniques in the following sections.

2.1 X-ray Diffraction and Reflectometry

X-ray diffraction and reflectometry are non-destructive (depending on the x-ray energy used) experimental techniques that elucidate the structural and morphological properties of materials. The typical x-ray diffraction and reflectometry experiment begins with x-rays generated from a sealed x-ray tube (a Cu source for all x-ray diffraction and reflectometry experiments was used) which then pass through a set of primary optics (e.g. Göbbel mirror or anti-scatter slits such as fixed slits) and interact via coherent scattering with the sample (incoherent scattering and absorption processes are ignored as their contributions are minimized through proper sample and measurement preparation). The diffracted beam then passes through a series of secondary optics (e.g. anti-divergence slits) and was collected by a scintillation or position sensitive detector (strip) detector. The type of sample being studied (powder or thin film) will dictate the geometry and the optics necessary to acquire a diffraction pattern suitable for Rietveld refinement (section 2.1.3).

The integrated intensity of an x-ray diffraction pattern results from several key factors such as the atomic structure. The integrated intensity can then be expressed as the following product[33]:

$$I_{hkl} = b + K * p_{hkl} * L_\theta * P_\theta * A_\theta * T_{hkl} * E_{hkl} * |F_{hkl}|^2 \tag{2.1}$$

Here, b is the function that describes the background, K is the overall scale factor for a given phase, p_{hkl} is the multiplicity factor which accounts for the number of symmetrically equivalent points (FullProf[34], the software used for refinements, calculates these factors from the given space group), L_θ and P_θ are the Lorentz multiplier and the polarization factor that take into account the angular dependence of the geometry of diffraction and the partial polarization of the diffracted x-ray beam, A_θ is the absorption multiplier, T_{hkl} is the preferred orientation factor, E_{hkl} is the extinction multiplier and lastly, $|F_{hkl}|^2$ is the structure factor which defines the details of the crystal structure (i.e. type and location of atoms and their distribution (occupancy) about the different lattice sites). Preferred orientation occurs when there is a relatively large amount of a diffraction sample that is oriented in a specific crystallographic direction. The factor T_{hkl} used in the Rietveld refinements in this thesis is the March-Dollase function[35]:

$$T_{hkl} = G_2 + (1 - G_2)\left[(G_1 \cos\alpha_h)^2 + \frac{\sin^2\alpha_h}{G_1}\right]^{-3/2} \tag{2.2}$$

where G_1 and G_2 are refined parameters. For $G_1 < 1$, the sample has plate-like (platy habit) orientation and the angle α_h defines the acute angle between the scattering vector and the direction normal to the crystallites. When $G_1 > 1$, the sample has a needle-like orientation and α_h defines the acute angle between the scattering vector and the direction the long axis of the fibre. For $G_1 = 1$, there is no preferred orientation. In addition, G_2 represents the fraction of the sample that is not textured.

In the following sections, a description of the x-ray diffraction experiments used to study the nanosystems within this thesis (Chapters 3, 4, and 5) as well as the requisite data analysis techniques (Section 2.1.3 and 2.1.5) will be discussed. These experiments are the so-called standard θ-θ scans, also known as x-ray powder diffraction, grazing incident x-ray diffraction (GIXRD), and x-ray reflectometry (XRR).

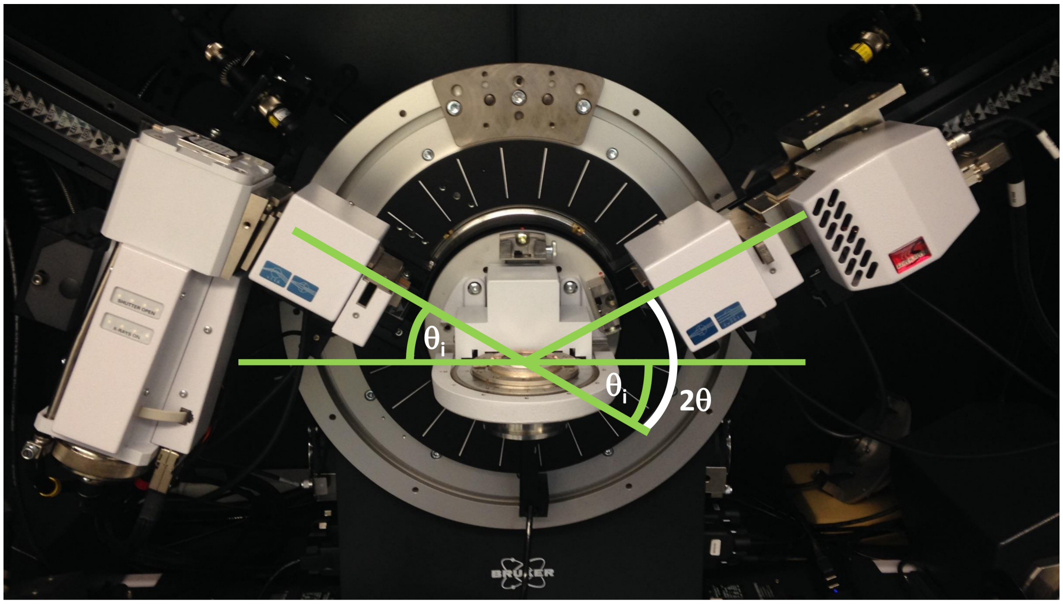

Figure 2.1: Bruker x-ray diffractometer

2.1.1 Powder X-ray Diffraction ($\theta/2\theta$)

Powder x-ray diffraction (XRD) patterns were collected by varying together the incident (θ_i) and scattered (2θ) angles to satisfy Bragg's Law (Fig. 2.1),

$$n\lambda = d\sin(\theta) \tag{2.3}$$

where n is the integer number of wavelengths (here $n = 1$), λ is the wavelength of the x-rays, in this case $\lambda = 1.540460$ $\mathring{A}$ and 1.544400 $\mathring{A}$ for Cu $K_{\alpha 1}$ and $K_{\alpha 2}$, d is the distance between crystal planes with Miller indices (hkl), and θ is the angle between the incident x-rays and the scattering plane. This geometry is ideally suited for powder samples as the penetration depth of x-rays is on the order of microns for the angles often studied (2θ = 10-120°) and the thickness of samples are a few microns or thicker. Although the powder diffraction geometry can be applied to thin films, one must take great care not to saturate the detector when single crystal substrates (e.g. STO[100]) are used. Within this thesis, Cu/γ-Fe_2O_3 nanoparticles were studied using a PANalytical X'Pert Pro System diffractometer. Here, a monochromator and Ni filter between the sample and the detector were used to remove the unwanted Cu K_β and K_{α_2} characteristic x-ray contributions to the diffraction pattern, and this diffractometer used a scintillation detector. FeCo and $Fe_{49\%}Co_{49\%}V_{2\%}$ nanoparticles with and without SiO_2 shells as well as Fe/Cu nanostructured thin films were studied using a Bruker D8 Advance DaVinci diffractometer. Primary and secondary optics were selected to maximize the quality of the collected diffraction patterns and the Lynxeye detector (a PSD) was used. For the Lynxeye detector, it was possible to adjust the discriminator settings to minimize the fluorescence when measuring Cu, Co, or Fe. For the Bruker, the K_β x-rays were removed by a either a Ni filter or the Göbel mirror which was capable of filtering out the K_β x-rays via destructive interference.

2.1.2 Grazing Incident X-ray Diffraction

For thin samples (thicknesses $\leq 1\ \mu$m), determining the crystal structure from the standard $\theta/2\theta$-scan is problematic as the penetration depth of x-rays (at all angles relevant for the diffraction experiment) is much deeper than the sample is thick. This results in the diffraction pattern being that of the substrate primarily and not the sample, as the substrate is orders of magnitude thicker than the sample (in our case we used ~0.5 mm thick SiO_2 substrates). In these cases, by fixing the incident angle at or slightly above the critical angle for total external reflection ($0.4^\circ \leq \theta \leq 0.8^\circ$), we were able to increase the volume of sample x-rays scatter off of and decrease substantially the penetration depth of the x-rays. To then satisfy Bragg's Law, we scanned the detector between 5° and 90° 2θ. The optics best suited for this type of experiment are the Göbbel mirror which produces a perfectly parallel beam of x-rays with minimal equatorial divergence coupled with an axial Sollar slit. This geometry, allow for high quality diffraction patterns to be collected for very thin films, on the order of tens of nanometers thick. For the Fe/Cu nanostructured thin films studied within this thesis, diffraction patterns were collected using a 1.0 mm anti-scatter slit with a Göbbel mirror, and a 5.0 mm anti-scatter slit for the primary and secondary optics, respectively.

2.1.3 X-ray Diffraction Pattern Analysis

X-ray diffraction patterns can be analyzed either by matching, as closely as possible, the reflections to a database of known x-ray diffraction patterns (pattern matching), or by a systematic analysis of the pattern using a full pattern refinement method (Rietveld refinement). Pattern matching provides qualitative insight into the crystal structure and lattice parameters of the collected diffraction pattern. However, there remains a significant amount of ambiguity with this method as there can be several database entries for a single structure resulting in a distribution of lattice parameters. For example, the spinel Fe_3O_4 (magnetite) has 105 entries in the Pearson database[36]. Also, there are ambiguities associated with different materials having similar diffraction patterns, which become increasingly difficult to determine uniquely at the nanoscale (e.g. Fe_3O_4, γ-Fe_2O_3, and other ferrites). Alone, this technique does not provide enough information to make a claim about the structural properties. However, pattern matching is a good place to start when looking to perform a quantitative analysis of x-ray diffraction patterns (e.g. Rietveld refinement).

Initial refinement techniques were developed for the complete pattern refinement of single crystal diffraction data. However, it is often difficult or impossible to obtain a large enough single crystal of a material to collect such a diffraction pattern. Thus, with his seminal works in 1967[37] and 1969[38], H. M. Rietveld was able to apply the refinement process to powder diffraction neutron data, for the first time. This opened the door for determining the structural properties for many polycrystalline materials. This method has since been refined and applied to the x-ray diffraction patterns with great success. The Rietveld refinement process is built upon the minimization, via the non-linear least squares fitting process, of Φ, where;

$$\Phi = \sum_{i=1}^{n} w_i (Y_i^{obs} - Y_i^{calc}) \tag{2.4}$$

Here, w_i is the weight assigned to the i^{th} data point, and Y_i^{calc} is the calculated intensity (see 2.1) at the i^{th} data point. This refinement process allowed for the unique quantitative determination of structural properties requisite for the complete understanding of the samples magnetic properties. For example, the determination of the location, type, and occupancy of the atoms at the different lattice sites within a material as well as the amount of each phase present for multi-phase samples.

2.1.4 X-ray Reflectometry

X-ray reflectometry (XRR) is a surface sensitive experimental technique. Here, x-rays are reflected from the surface of the sample (or interface for multilayer or superlattice films) and the changes in intensity as a function of 2θ in the specular direction (incident and reflected angle are the same) is measured. If, for example, the sample's surface or interface(s) is(are) rough, then the measured angular dependent intensity will deviate from that predicted by Fresnel reflectivity[39]. All the information about the sample's structure and morphology can be found from these deviations.

Lymann Parratt first applied this technique to copper coated glass. The analysis of the XRR patterns has subsequently been based on this work[40]. The relationship that describes the reflectivity for a rough interface with an average electron density given by $\rho_e(z)$ is:

$$\frac{R(Q)}{R_F(Q)} = \left| \frac{1}{\rho_\infty} \int_{-\infty}^{\infty} \exp(iQz) \left(\frac{dp_e}{dz} \right) dz \right|^2 \tag{2.5}$$

$$Q = 4\pi \sin(\theta)/\lambda \tag{2.6}$$

Here, $R(Q)$ is the reflectivity, λ is the wavelength of the x-rays used, ρ_∞ is the electron density deep within the sample (the sample is approximated as infinitely thick) and θ is the incident angle of the x-rays. By comparing models constructed using Eqn. 2.5 with the collected pattern, the thickness, roughness, and electron density of the material can be determined.

This method can be extended to samples with multiple interfaces, such as multilayered thin films or superlattices. These patterns show visible oscillations of the intensity as a function of 2θ. These oscillations are related directly to the thickness of the layers and the amplitude of the oscillations is related to the roughness of the interface. Thus, by including these parameters into the model we can further describe the structure and morphology of the materials being studied.

2.1.5 Modeling of Reflectometry Data

The Leptos[41] software package was used to model the XRR patterns collected. Similar to the Rietveld method, a theoretical structure must be introduced. The calculated intensity of the pattern is based on the work of Parratt[40]. For this software in particular, this involved fabricating a theoretical thin film where we set initial conditions for the electron density, thickness, and roughness. If there are multiple layers or a superlattice, we must also include these parameters for each layer. Therefore, some understanding of the composition of the material must be known beforehand in order to obtain physical fits. By adjusting the thickness, roughness, and electron density (not simultaneously) of the theoretical model using a built in genetic algorithm or a simulated annealing technique (global minimization techniques), the calculated intensity as a function of angle can be produced. The fitting of the calculated pattern to the collected pattern allows the physical properties of the sample to be determined. For multi-layered and superlattice films, it is possible to determine the thickness of each individual layer. The Fe/Cu nanostructured thin films described in Chapter 5 were fit using the simplest model to describe the observed pattern. For the samples that showed distinct layers from cross-sectional transmission electron microscopy images, the fitting succeeded. However, the majority of the samples did not have distinct layers but instead consisted of Fe nanocrystallites embedded in a copper matrix. As a result of this morphology, the XRR patterns could not be described using this method. However, the total film thickness could still be determined by assuming that the entire film was a single layer with an electron density less then iron but greater then copper, and the values obtained were in good agreement with cross-sectional TEM images.

2.2 Transmission Electron Microscopy

Transmission Electron Microscopy (TEM) images were collected to determine physical properties such as the average size and size distributions of nanoparticles/nanocrystallites as well as thin film thickness for nanostructured thin films. The images for the Cu/γ-Fe_2O_3 nanoparticles were collected by Dr. Hao Ouyang and his graduate student C.-C. Lin (see Appendix A), the images for the undoped and V-doped SiO_2/FeCo nanoparticles were collected by Dr. Taghi Daroudi (see Appendix A), and the images for the Fe/Cu nanostructured thin films were collected by Dr. K.-W. Lin and his graduate students C. Shueh and H.-F. Hsu (see Appendix A). Several different experimental techniques fall under the umbrella of TEM. These include plane-view and cross-sectional experiments using both bright and dark field images. Electron diffraction images are also collected using the transmission electron microscope.

2.2.1 Plane-View TEM

Images for the Cu/γ-Fe_2O_3 core/shell nanoparticles and the Fe/Cu nanostructured thin films were collected using a JEOL 2100F operating at 200 kV while images for the undoped and V-doped SiO_2/FeCo core/shell nanoparticles were collected using a Hitachi 9500 operating at 120 kV (Ch 4). There are two types of images that were collected using the plane-view geometry. Bright field images were collected by placing an aperture at the focal plane of the TEM's objective lens allowing only direct beam to pass and be collected. The image is then created by the reduction of the beam intensity as it interacts with the sample. In such an image, the difference in contrast is a result of the thickness (mass-thickness) and diffraction. Thicker areas, areas with higher Z atoms, and crystalline areas therefore appear darker. Dark field images were produced by blocking the direct beam with an aperture allowing only diffracted beam to pass and be collected. Bright field images are well suited for observing the contrast between elements with different Z's, whereas, dark field images are ideal for observing the planar defects, stacking faults, and for the cases studied within, the average particle size[42].

2.2.2 Cross-sectional TEM

Cross-sectional TEM images are used to determine a thin films total thickness as well as to determine the thickness of individual layers in multi-layered thin films. Samples are prepared by gluing together two pieces of the same film, face-to-face, and then polishing them until they are thin enough (a few hundred nm) to allow for the transmission of electrons. Using image analysis software such as ImageJ[42] we are able to determine the total film thickness of the Fe/Cu nanostructured thin films. For the Fe/Cu nanostructured thin films where there remains a multi-layered structure, the individual layer thicknesses can be determined as well.

2.2.3 High Resolution TEM

High resolution TEM (HRTEM) images are a two-dimensional projection of the crystal structure and provide structural information at resolutions better than 0.2 nm[43]. For the work in this thesis, HRTEM images were collected using a JEOL 2100F microscope at 300 kV. For images collected along a specific low-index direction[44], we observe all of the atoms on top of each other (see Fig. 2.2). HRTEM allows for imaging of the atomic structure of crystalline samples. Also, for core/shell nanoparticles (e.g. γ-Fe_2O_3/Cu core/shell nanoparticles) where there is a distinct difference in the density (Z), phase-contrast, structure, or crystallinity of the core and the shell, allow the direct measurement of the shell thickness.

HRTEM, in principle, is a simple extension of the wave nature of electrons. However, in practice, the interactions of the electron beam with the sample is quite complex[45]. Simply, each electron will interact with the sample. Outside the sample, the electrons can be approximated as a plane wave incident on the sample. Within the sample, the electrons are attracted by the atomic potentials of the atoms and will be channeled along the aligned atomic columns of the lattice. Simultaneously, interactions between the electrons in different atomic columns leads to diffraction. Therefore, as the electron wave exits the sample, the objective lens recombines the plane wave and diffracted waves and their interference leads to an enlarged image[45].

2.2.4 Selective Area Electron Diffraction

Selective area electron diffraction (SAED) experiments were performed using the same instruments used to collect TEM images. Typically, electrons with energies between

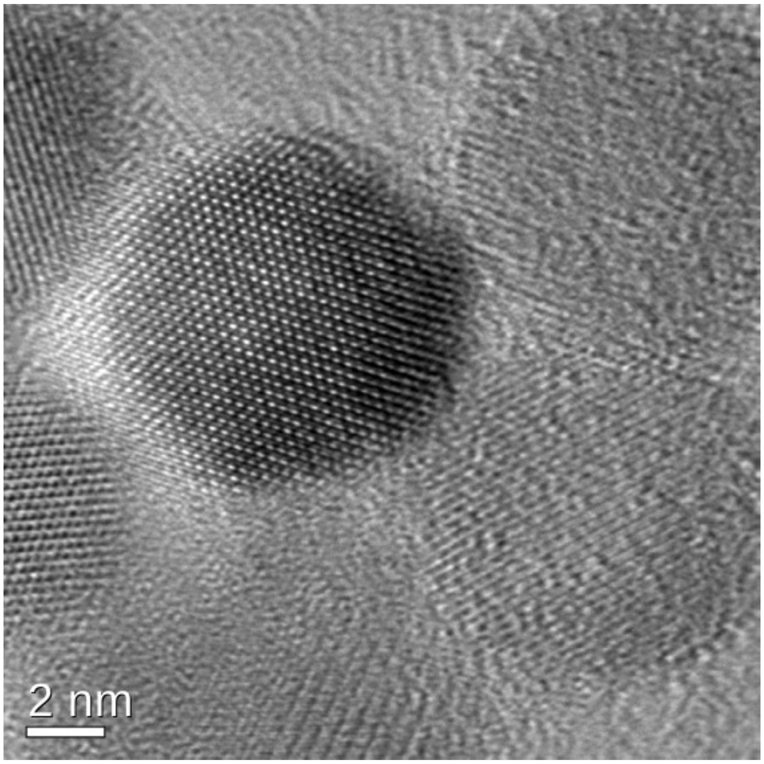

Figure 2.2: HRTEM image of Cu[1.0 nm]/γ-Fe_2O_3 core/shell nanoparticles. The image was collected along a low-index direction such that the atoms are all aligned on top of each other in a hexagonal closed packed structure producing sharp contrast.

80 and 120 keV pass through the sample (which is nanoparticles deposited on a TEM grid or nanostructured thin films grown on TEM grids). For these experiments, the wave-like electrons with wavelengths of a few hundredths of an nanometer interact with the atoms in the sample which are spaced angstroms apart (e.g. $\sim$8.387 Å for maghemite). Thus, the sample being studied acts essentially as a diffraction grating for the incident electrons where some satisfy the diffraction condition of the sample and are thus diffracted while the remaining electrons pass straight through. As a result of these interactions, a pattern will be produced dependent on the nature of the sample. For example, a single crystal will produce a diffraction pattern consisting

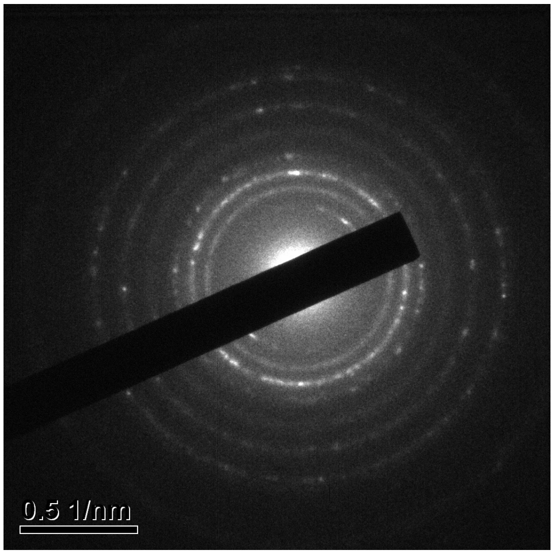

Figure 2.3: Selective area electron diffraction image of an Fe(15s) $V_{EH} = 50$ V nanostructured thin film. The complete rings indicate that the sample is polycrystalline. The bright spots located on a ring suggest the presence of texturing.

of a series of bright spots corresponding to unique diffraction conditions (a unique set of Miller indices) and a polycrystalline sample (see Fig. 2.3) will produce a series of concentric rings corresponding to the satisfied diffraction conditions. Unlike a single crystal or polycrystalline sample, an amorphous sample will produce a series of diffuse diffraction rings because of the structural disorder within the sample. These differences allow us to describe the nature of the sample (i.e. degree of polycrystallinity) from the structure of the diffraction rings as a completely polycrystalline sample will show distinct fully resolved concentric rings, a single crystal will show unique diffraction points (intense spots), and an amorphous material will show diffuse diffraction rings. Therefore, if we are certain that our system is polycrystalline or amorphous (from other diffraction experiments), the appearance of bright spots suggests the presence of texture (e.g. preferred orientation).

To determine the crystal structure of the samples being investigated from the electron diffraction patterns, one must determine the radius of the rings. From the image analysis of the SAED pattern and knowing the instrumental parameters, it is possible to determine the *d*-spacing of each observed feature (ring or bright spot). Then, with a comparison to known *d*-spacing values from a diffraction database, identification of likely candidates for the structure and composition is possible. Image analysis of the diffraction rings provides a mechanism for determining the *d*-spacing as it is proportional to the radius of the ring. However, SAED on its own is not enough to identify uniquely the structure as there are large inherent uncertainties in the analysis. These are largely the result of the "thickness" of the diffraction rings in the image which can introduce a significant range of possible values for the *d*-spacing for a single ring (10-20% variation).

2.3 X-ray Spectroscopy

Several types of x-ray spectroscopy experiments were performed to determine the composition, oxidation state, and coordination environment of the nanoscale samples studied. Both x-ray photoelectron (XPS) and x-ray absorption spectroscopy (XAS) experiments were performed. Simulations of the spectra for transition metal ions and their coordination environment using, for example, the CTM4XAS software package enable a more robust matching of the collected spectra when determining the ions electronic environment. A description of these two spectroscopic techniques along with the requisite analysis of the collected spectrum follows.

2.3.1 X-ray Photoelectron Spectroscopy

XPS is a surface sensitive technique (0-10 nm, based on escape depth of excited electron) that allows for the quantitative determination of the elemental composition, oxidation state, and coordination environment of a samples surface. Spectra are collected by exciting photoelectrons with an incident x-ray from a monochromatic Al K_α source (systems are not limited to only an Al source;bi Mg sources are also used) and measuring their kinetic energy. Thus, the binding energy, E_B, can be calculated,

$$E_B = E_\gamma - (E_K - \Phi) \tag{2.7}$$

where E_γ is the energy of the incident x-ray (Al K_α = 1486.7 eV), E_K is the kinetic energy of the photoelectron, and Φ is the work function that depends on the instrument and the sample. Each element produces a characteristic x-ray spectrum whose peaks are located at binding energies corresponding to specific electronic configurations (e.g. 1s, 2s, 2p, 3s). A comparison between the spectral features observed within the material and those from a database such as the one from NIST[46] allow for the determination of the oxidation state and coordination environment of the element being studied. Furthermore, the intensity of the spectral peaks is directly proportional to the amount of that element within the sample. More specifically, the amount of that element within the area of the sample being measured.

During the XPS measurement, approximately only the top 20 atomic layers contribute to the observed spectral features (∼10 nm into the sample). This is significant for thin film samples where often the sample is much thicker. However, for the nanoparticle samples studied (e.g. Ch. 4), these restrictions are less severe as the diameter of the largest sample was ~16 nm. Therefore, the collected spectra remain representative of the bulk of the sample. For thick samples, it is possible to access areas deeper into the sample by argon ion beam bombarding the sample, essentially drilling (or etching) into the sample using argon ions. However, this will inevitability alter the chemical environment of the sample, affecting the spectroscopic properties measured.

2.3.2 XPS data analysis

Using software such as CASAxps[47] or MultiPak[48], we can fit XPS spectra with an appropriate lineshape to determine quantitative properties of the materials being studied. The correct choice of lineshape depends on many factors. For example, if the material being studied is a metal, then an asymmetric lineshape would be expected[49]. However, for an oxide, a combination of Gaussian or Lorentzian lineshape may be necessary. Furthermore, instrumental and physical effects must also be considered when determining the ideal lineshape model. For example, the response of the electron analyzer may be asymmetric or the intrinsic life-time broadening of the core-level hole state is assumed to be Lorentzian. These are two possible instrumental and physical effects that must be considered when determining the ideal line-shape model to describe the observed XPS spectra.

When fitting XPS spectra, the first step is to calibrate the binding energies. This is often done by measuring the binding energy of the advantageous C 1*s* peak and fixing its binding energy to 285 eV. Alternatively, Au is also used as a binding energy calibrant. Secondly, the background of the area being fitted must be accounted for, generally by using an iterated Shirley function[50]. The spectral features are then deconvoluted to determine the composition. For example, for an FeCo spectrum, the $2p^{3/2}$ peak is twice as intense as the $2p^{1/2}$ peak. The remaining spectral features describe the formation of interfacial metal silicates, a result of the silica shell on these core/shell nanoparticles. The small changes in binding energy resulting from the silica shells were used to identify each spectral feature.

2.3.3 X-ray Absorption Spectroscopy

X-ray absorption spectroscopy (XAS) is a technique that yields information about the electronic structure (e.g. oxidation state) and the coordination environment (e.g. octahedral or tetrahedral) of the elements being studied. Furthermore, when circularly polarized light is used, we are capable of determining the element specific magnetic properties. For a successful XAS experiment, we need the ability to obtain circularly polarized photons and tune the energy of these photons. Also, these experiments were carried out at temperatures between 10 and 300 K and B = 0-7 T. It is for these reasons that we performed the XAS (and subsequent XMCD) experiments at beamline 4-ID-C at the Advanced Photon Source (APS) located within Argonne National Laboratory.

During an XAS experiment, we wish to determine the absorption coefficient μ. This is easily done in the transmission geometry, however, due to the nature of our samples (e.g. nanoparticles or thin films) and the experimental setup at the Advanced Photon Source, the transmission geometry can not be used. Therefore, we must rely on measuring the induced current within the sample to determine μ as the number

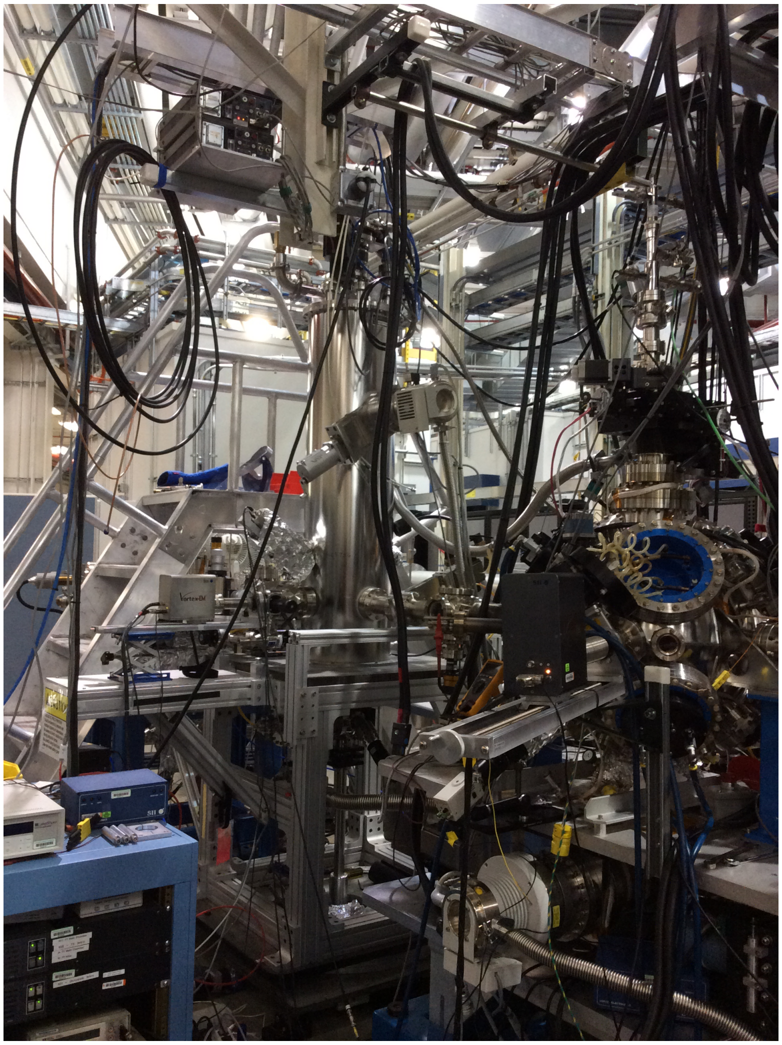

Figure 2.4: Photograph of the magnet system used for XAS and XMCD experiments at beamline 4-ID-C at the Advanced Photon Source in Argonne National Laboratory.

of emitted photo-electrons (the induced current) is proportional to μ.

Two types of experiments were performed at the APS (Fig. 2.4). The total electron yield (TEY) and the total fluorescence yield (TFY) where intensities as a function of energy were measured. The TEY is directly proportional to μ; for example, a typical metallic iron spectrum reveals two distinct features. A peak at ∼707 eV from the $2p^{3/2}$ transition, and ∼721 eV from the $2p^{1/2}$ transitions. These spectral features are known as the L_3 and L_2 absorption edges, respectively. In the TEY experiment, due to the finite escape depth of electrons, we measure primarily the surface of the sample. That is, although the incident photons are able to penetrate up to several hundred of nanometers, the contribution to the TEY decreases drastically with depth. Typically, TFY experiments suffer from self absorption as the fluorescence photons attempt to escape from deep within the material ($\sim$100 nm). As a result, often steps must be taken to account correctly for this loss in energy dependent intensity. For the core/shell nanoparticles, the TFY collected suffered from self-absorption effects resulting in a reduced signal-to-noise, however, the nanostructured thin films samples are thin ($<$ 30 nm) and do not suffer from self-absorption so the measured TFY does not need to be corrected[51].

During the XAS experiment on transition metals, we are exciting core electrons from the $2p$ shell into unfilled $3d$ holes. Therefore, as the magnetism of transition metals is dictated by the electrons in the 3d shell, we are able to determine element specific magnetic properties from the spectral features of these transition metals. By using circularly polarized x-rays, we are able to excite core electrons while conserving their spin (see section 2.3.4).

The analysis of x-ray absorption spectra is much more complex compared to the analysis of x-ray photoelectron spectra. As the excitation of a core electron from the $2p$ shell into an unoccupied bound $3d$ shell has significantly more possible transitions then that compared with the single transition observed from XPS data. For example, the Fe^{3+} atomic configuration has a total of 25 possible transitions, however, only 23 of them are allowed due to selection rules[52]. The simulation of XAS spectra was performed using the CTM4XAS (charge transfer 4 x-ray absorption spectroscopy) software program[53]. The initial and final states of the excited core electron are calculated using atomic multiplet theory within the framework of a ligand field theory application to produce a theoretical x-ray absorption and magnetic circular dichroism spectrum. By manually adjusting the parameters that describe the spectral features as well as including a contribution from collected metallic spectra, it was possible to obtain reliable matches of XAS spectra collected on the nanoparticles and thin films studied.

2.3.4 X-ray Magnetic Circular Dichroism

X-ray magnetic circular dichroism (XMCD) is an element specific experimental technique that provides quantitative information about the ferro- or ferri-magnetism of the sample. By comparing artifact free XMCD with sum-rule analysis[54; 55; 56], it is possible to determine the spin and orbital magnetic moments. Artifact free XMCD spectra are obtained from the difference in absorption spectra when the applied field polarity is changed, removing all non-magnetic contributions to the XMCD spectrum.

The XMCD spectra studied are of the $L_{3,2}$ transitions for Fe, Co, Cu, and V. The $L_{3,2}$ transition corresponds to a 2p core electron excited into a 3d hole. Incident circularly polarized photons transfer their angular momentum to the 2p core electrons. As spin flips are forbidden in an electric dipole transition, electron spin remains unchanged during the core-hole transition. Thus, the absorption cross-section for the two polarizations differ, and the dichroic spectra results from this difference. The intensity of the measured spectral features is related directly to the spin and orbital magnetic moments.

2.3.5 X-ray Magnetic Resonance Scattering

X-ray magnetic resonance scattering (XMRS) is an extension of XAS and XMCD. During the measurement the energy of the incident photon is held fixed at a resonance energy for a specific transition (e.g. the L_3 transition of Fe). With the incident photon energy fixed, the field is swept from $+H_{app}$ to $-H_{app}$ and then back to $+H_{app}$ creating an element specific hysteresis loop. From these loops, the elemental coercivity can be determined. In addition, any shift from zero (horizontal or vertical) in the hysteresis loop suggests the presence of pinning of the magnetization.

2.4 Magnetometry and Susceptometry

Magnetometers based on a superconducting quantum interference device (SQUID) are capable of resolving changes in the magnetic field of $\sim 1\text{x}10^{-15}$ T, for example, the magnetic field produced by the electrical activity in the human brain is on the order of $\sim 10^{-12}$ T[57]. For this work, the magnetometer measures the static magnetic moment at various applied fields with constant temperature (isothermal), and temperatures with constant field (isofield). We have also used the magnetometer to measure the time-dependent magnetic moment by applying a small (0.25 mT) alternating (*ac*) magnetic field which allows for the extraction of the complex *ac* susceptibility at a frequency ν,

$$\chi(\nu, T) = \chi'(\nu, T) - i\chi''(\nu, T) \tag{2.8}$$

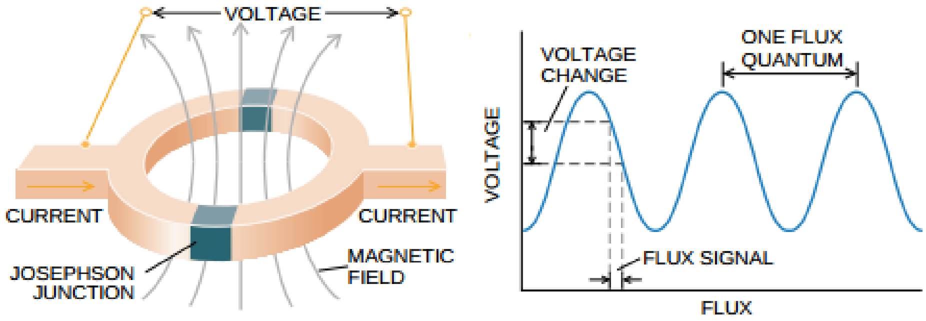

Figure 2.5: If a constant bias current is maintained in the SQUID, the measured voltage across the Josephson junction oscillates with a phase change which depends on the change in magnetic flux. By determining the number of oscillations, one can correlate that with the change in magnetic flux.[58]

where, $\chi'(\nu,\mathrm{T})$ and $\chi''(\nu,\mathrm{T})$ are the in- and out-of-phase contributions to the *ac* susceptibility, respectively.

Two fundamental principles are required for the operation of SQUID magnetometers; the quantization of magnetic flux, in units of $\Phi_0 = \frac{2\pi\hbar}{2e} \cong 2.0678\mathrm{x}10^{-15}$ Tm^2, within a superconducting ring, and the Josephson junction. A Josephson junction is a device that consists of a thin insulating material sandwiched between two superconductors (see Fig. 2.5). The thickness of the insulator is such that an electron wave in one superconductor is capable of tunneling (through the junction) and overlapping with the electron wave in the other superconductor.

The SQUID device within the magnetometer consists of a closed superconducting loop with two Josephson junctions in the current path of the loop. A direct result of the quantization of magnetic flux coupled with the non-linear behaviour of the Josephson junction allows for a SQUID magnetometer to resolve minute changes of the external magnetic field, while remaining operational in fields up to 7 T. During a measurement, a sample is moved through the superconducting coils which induces a current. When the current in the coils changes in response to the magnetic flux from the sample (as it moves through the coil), a phase difference across the Josephson junction occurs. The current through the coil is quantized, therefore, interference between the current of the two sides of the superconductor will occur changing the total current. These current changes can then be correlated to the magnetic flux.

Two types of DC magnetization experiments were performed. The first is the temperature dependent magnetization at constant field (isofield), $M_{DC}(T)$, and the second is the field dependent magnetization at constant temperature (isothermal), $M_{DC}(H)$. In this thesis, two different types of temperature dependent measurements were collected. A zero-field cooled (ZFC) measurement occurs when the sample was cooled from above a critical temperature (e.g. the onset temperature of superparamagnetism - blocking temperature) with zero applied field. At base temperature (e.g. 5 K), a DC field (generally small, $\leq$ 0.1 T) was applied and the magnetization was measured, with warming. A similar measurement where the sample was field-cooled (FC) was also performed, the difference being that the magnetization was measured as the sample was cooled, from above the critical temperature, with the applied DC field. Similarly, these two types of measurements, ZFC and FC were applied to the field dependent measurements as well. Frequency dependent susceptibility experiments were also performed with the samples in the ZFC state. At base temperature, a small AC field was applied at different frequencies ranging from 10 Hz to 1000 Hz and the susceptibilities ($\chi(\nu,\mathrm{T})'$ and $\chi(\nu,\mathrm{T})''$) were measured as the temperature was increased. The samples studied within this thesis were measured using a Quantum Design SQUID MPMS-XL magnetometer in the temperature range of 2 K to 400 K with applied fields ranging from -5 T to 5 T.

2.5 Mössbauer Spectroscopy

The Mössbauer effect requires the emission and resonant absorption of recoil-free γ-photons by atomic nuclei. The loss of energy associated with the recoil of the emitting and absorbing nuclei are avoided entirely, a process unique to Mössbauer spectroscopy compared to other resonant processes.

For resonant absorption experiments, it is assumed that the γ-photon emitted by the de-excitation of the nucleus of the absorber with energy $E_0 = E_e - E_g$ (the difference in energy between the excited and ground states, 14.4 keV for ^{57}Fe, the most common Mössbauer isotope) carries the full energy $E_\gamma = E_0$. However, for a free nucleus, this is not the case. When a photon is emitted from the free nucleus at rest, the nucleus must recoil in the opposite direction to ensure that momentum remains conserved. Thus, the energy of the emitted photon is reduced by this recoil energy,

$$E_\gamma = E_0 - E_R \tag{2.9}$$

where E_R is

$$E_R = \frac{E_\gamma^2}{2Mc^2} \tag{2.10}$$

Here, M is the mass of the recoiling nucleus and c is the velocity of light. To further complicate matters, the nucleus is rarely at rest, thus the photons energy is further reduced by the thermal energy of the emitting nucleus.

$$E_\gamma = E_0 - E_R - E_T \tag{2.11}$$

Where E_T is the thermal energy of the nucleus which will have a temperature dependent average value resulting from the velocity distribution of the nuclei. When the photon is absorbed by a nucleus, a similar situation occurs and the energy of the photon is then $E_\gamma = E_0 + E_R - E_T$. Thus, the energy separation of the emission and absorption is $2E_R$. Since $E_R \gg \Gamma$ (the characteristic line width) there will be no overlap between emission and absorption process, therefore no resonant absorption will be possible.

In 1957-58, Rudolph Mössbauer discovered[59] that resonant nuclear absorption can occur for the case when both the emitter and absorber are bound to a solid matrix (e.g. ^{57}Co in a Rh matrix source). Upon emission of a γ-photon, the recoil energy is transferred completely to the much more massive matrix ($M_{Matrix} \gg M_{Nucleus}$) creating quantized lattice vibrations, phonon. When this occurs in either the emitting or absorbing nuclei, nuclear resonant absorption can not occur. Fortunately, there remains a finite probability, known as the recoil-free fraction, for a γ-photon to be emitted and absorbed without loss of energy due to recoil as, in this case, E_R is less then the energy necessary to create a phonon. It is this recoil-free nuclear resonant absorption that forms the basis of the Mössbauer effect.

The Mössbauer transition's energy which describes the environment around the ^{57}Fe nuclei is described by the Hamiltonian:

$$H = H_0 + C_0 + M_1 + C_2 + ... \tag{2.12}$$

where H_0 is the terms that describes the Hamiltonian for the atom apart from the hyperfine interactions (e.g. dipole and exchange interactions), C_0 represents the Coulombic interactions, M_1 describes the magnetic hyperfine interactions and C_2 represents the electric quadrupole interactions. Each interaction affects the nuclear transition of the Mössbauer active nuclei (e.g. ^{57}Fe) influencing the energy, linewidths and intensities of spectral lines. The spectral lineshapes are set by the lifetime of the ^{57}Fe nuclei's exited state (97 ns), and therefore have a Lorentzian lineshape.

The simplest of these interaction between a nucleus and its environment results in a shift in the spectral feature relative to zero velocity (corresponding to 14.4 keV for the ^{57}Fe Mössbauer transition) from the differences in the electron density of the target nucleus relative to the source nucleus. This shift is called the isomer (chemical) shift. The magnitude of the isomer shift (δ) is described by:

$$\delta = \frac{Ze^2R^2c}{5\epsilon_0 E_\gamma}\left[\rho_a(0) - \rho_b(0)\right]\left(\frac{R_e - R_g}{R_{eff}}\right) \tag{2.13}$$

where R_{eff} is the effective nuclear radius, R_e and R_g are the radius of the nucleus in the excited state and the ground state, ϵ_0 is the permittivity of free space, e is the elementary charge, and ρ_a and ρ_b are the electron densities of the source and absorber atoms, respectively.

When an ^{57}Fe nucleus experiences a non-spherical charge distribution there is an electric field gradient resulting in a quadrupole moment. This electric field gradient causes a degeneracy in the energy levels with $I > \frac{1}{2}$ to be lifted. For ^{57}Fe the $I = \frac{3}{2}$ state splits into the $m_I = \frac{1}{2}$ and $m_I = \frac{3}{2}$ states (Fig. 2.6), resulting in the quadrupole splitting. The magnitude of this effect can be described by:

$$\Delta = eQV_{zz} = \frac{eQ}{4\pi\epsilon_0}\sum q_i r_i^{-3}\left(3\cos{\theta_i}^2 - 1\right) \tag{2.14}$$

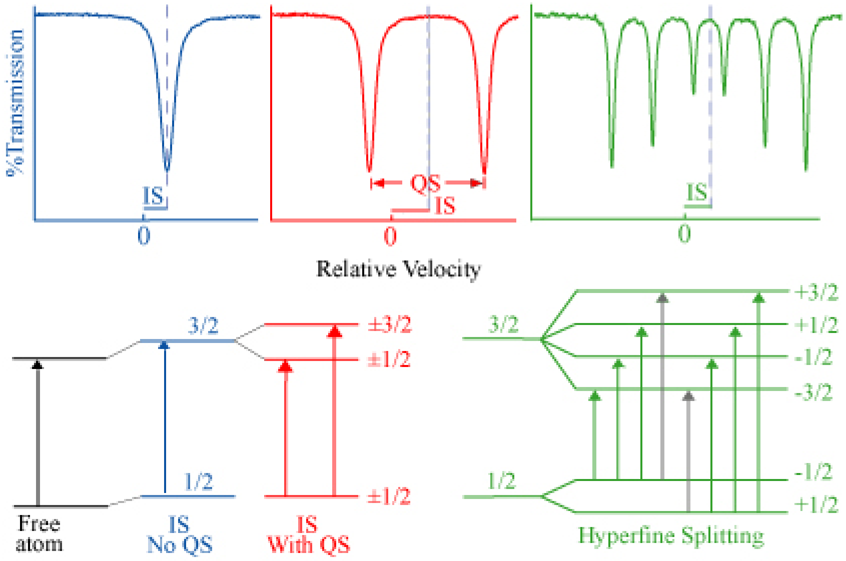

Figure 2.6: Characteristics of Mössbauer spectra related to nuclear energy levels. The transitions marked by grey arrows are forbidden due to selection rules.[60]

where V_{zz} is the largest component of the electric field gradient, r is the distance from the centre of the nucleus making an angle θ to the nuclear spin quantization axis. The relative intensities of the Lorentzian spectral lines resulting from quadrupole splitting is related to the probability of the two possible transitions occurring, 1:1.

Finally, when the target nuclei are in the presence of a magnetic field the degeneracy is lifted further by Zeeman splitting from I to $(2I+1)$ equally spaced substates where the relative line intensities correspond to the transitions probability (Fig. 2.6). Of the eight possible transitions from the $I = \frac{1}{2}$ to $I = \frac{3}{2}$ state only six are allowed due to selection rules (green arrows in figure 2.6) and these transitions have relative probabilities of 3:R:1:1:R:3, resulting in the six spectral lines shown in Fig. 2.6. The R value is related to the magnetization of the sample and can vary from zero (sample magnetized perpendicular to the γ-ray beam) to four (magnetized parallel to the γ-ray beam). For samples with no preferred magnetization direction, R=2 represents

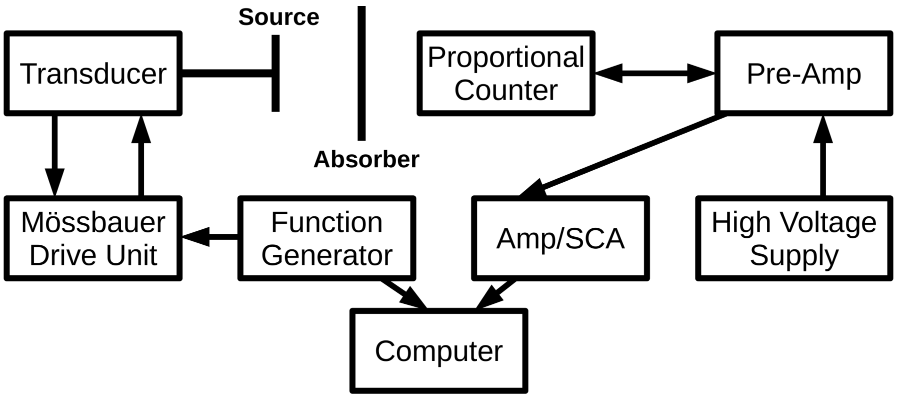

Figure 2.7: A schematic diagram of a transmission Mössbauer spectrometer

the powder average.

2.5.1 Transmission Mössbauer Spectrometer

A schematic diagram of the experimental setup used to collect transmission Mössbauer spectra is shown in Fig. 2.7). Here, a ^{57}Co**Rh** source (ranging from ~720 MBq to ~18 MBq, depending on experiment) was attached to a Wissel MDU MR-360 or MR-260 velocity transducer. ^{57}Co undergoes nuclear decay to ^{57}Fe in the $I = \frac{5}{2}$ state via electron capture (Fig.2.8). The velocity of the source was controlled using a Wissel DFG-1200 digital function generator. The function generator provides the drive unit with a triangle (constant acceleration) voltage waveform which was amplified such that the maximum and minimum voltages of the waveform corresponded to the largest positive and negative velocities of the transducer. γ-photons which pass through the sample were detected using a Xe with CO_2 filled (at 800 Torr) beryllium side window proportional counter (type 4546). The signal from the detector was amplified, and to accept only signal from the 14.4 keV photons, an ORTEC single-

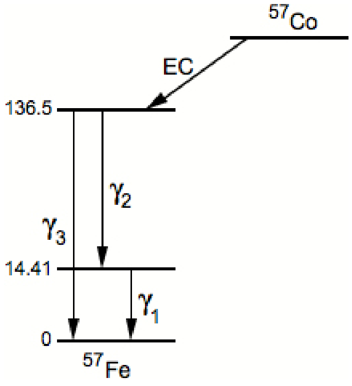

Figure 2.8: ^{57}Co decay scheme.

channel analyzer (SCA) was used. The output from the SCA was then sent to an ORTEC multi-channel scaling (MCS) acquisition card.

The transmission Mössbauer spectrometer was calibrated (velocity scale and isomer shift) using a $\sim$6 micron α-Fe foil (BCC structure with known μ_B) at room temperature as $B_{HF} = 33$ T is well known. Spectra of the Cu/γ-Fe_2O_3 nanoparticles were collected using a Janis SHI-850 closed cycle refrigeration system (CCR) from 5 K to 300 K. The isomer shifts of these spectra are given relative to α-Fe.

Non-linear least squares analysis was applied to all the transmission Mössbauer spectra presented here. These spectra were described using a Lorentzian line-shape sextet where the hyperfine interaction parameters described above set the absorption energies.

2.5.2 Conversion Electron Mössbauer Spectroscopy

Naturally occurring ^{57}Fe has an abundance of $\sim$2%, therefore, transmission Mössbauer spectroscopy experiments are not well suited to investigate thin films (e.g. Fe/Cu nanostructured thin films) due to the small amount of sample. For thin films, we

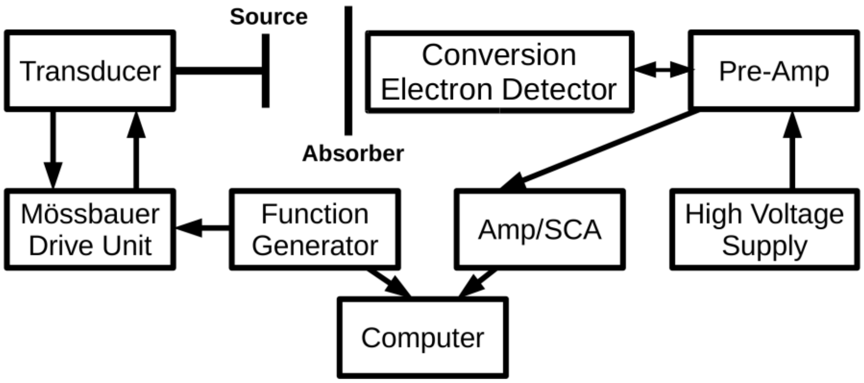

Figure 2.9: A schematic diagram of a conversion electron Mössbauer spectrometer

performed conversion electron Mössbauer spectroscopy (CEMS) experiments. CEMS involves the detection of conversion electrons, using a gas proportional counter, emitted during the de-excitation of the ^{57}Fe nuclei. De-excitation of the excited nuclei occurs either by the re-emission of a γ-photon or by the internal conversion and emission of an electron. The emission of the conversion electrons leave behind a hole that is subsequently filled by an outer shell electron, causing the emission of an Auger electron. For ^{57}Fe, internal conversion occurs with approximately 90% probability ($\sim$81% probability from 7.3 keV K-shell conversion electrons, $\sim$9% probability from 13.6 keV L-shell conversion electrons, and $\sim$1% probability from M-shell conversion electrons). Also, all conversion and Auger electrons produced resulted from a resonant γ-photon absorption, thus unlike transmission Mössbauer spectroscopy experiments, CEMS experiments do not require energy selection beyond that required to minimizing electrical noise.

A schematic diagram of the experimental setup used to collect conversion electron Mössbauer spectra is shown in Fig. 2.9). Here, a ^{57}Co**Rh** source (ranging from

$\sim$720 MBq to $\sim$18 MBq, depending on experiment) was attached to a Wissel MDU MR-360 velocity transducer. The CEMS experiment used the same electronic setup for the transmission Mössbauer experiment (see above). However, instead of a proportional counter, a Plexiglas body with a detachable face allowed for sample mounting. The inside of the detector was coated in aluminum to provide electrical continuity between the sample and the detector, and the sample was attached to the detachable face. Four gold coated tungsten anode wires inside the detector were connected to the pre-amplifer by a high voltage coaxial cable. The detector was connected to a gas bottle containing a mixture of helium (to act as the ionizing gas) and $\sim$4% methane (the quench gas).

Conversion electrons emitted from the sample ionized the surrounding helium gas filling the detector chamber. The ionization process continued until the energies of the emitted conversion electrons and secondary electrons became less than the ionization potential of the helium atoms, or until the ionizing electrons interacted with the quench gas (methane). A continuous flow of gas into the detector was necessary to replenish this quench gas. Conversion electrons, ionized helium atoms and secondary electrons were then attracted to the tungsten anode wires, which were held at high voltage (855 V). To further reduce the CED's response to lower energy photons (e.g. 6 keV x-rays from the decay of ^{57}Fe nuclei), a filter material (the Plexiglas body) was placed in front of the cathode.

CEM spectra of a $\sim$25 micron stainless steel foil were collected and the effect (ϵ) and counting time (t_{eff}) were calculated. A stainless steel sample (Fig. 2.10) was used for the tuning process because it produces a single line spectrum and is iron rich. The

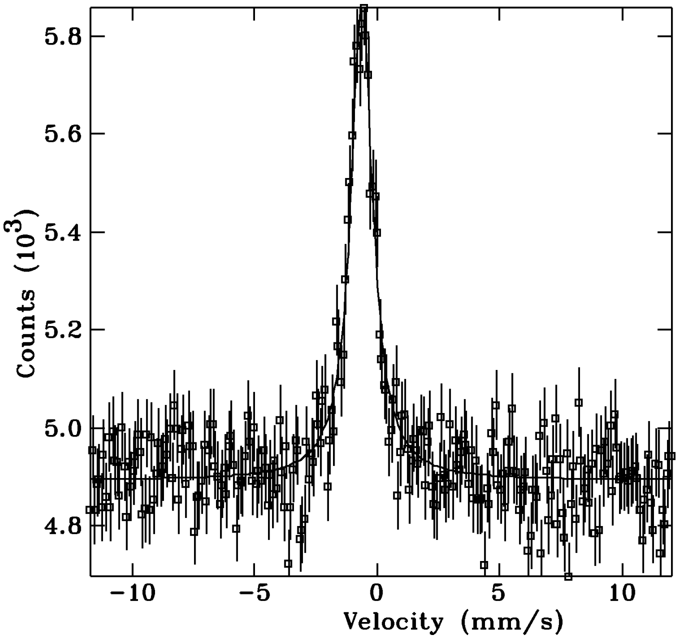

Figure 2.10: CEMS spectrum of a stainless steel foil collected using a LL setting of 0.7 V and a bias voltage of 855 kV.

detectors counting efficiency was optimized by tuning the bias voltage (BV) as well as the lower level (LL) discriminator settings (Figs. 2.11 and 2.12).

$$\epsilon = \frac{I}{I_\infty} \tag{2.15}$$

$$t_{eff} = \frac{2(\epsilon + 2)}{\epsilon^2 I_\infty} \tag{2.16}$$

where I is the peak intensity of the stainless steel singlet and I_∞ is the baseline. The settings which maximized the ϵ and minimized t_{eff}, a bias voltage of 855 eV and a LL of 0.7 V, were the optimal detector settings.

Similar to the transmission Mössbauer spectroscopy experiments, the CEMS spectra were described using non-linear least squares analysis. These spectra were described using a Lorentzian line-shape singlet or doublet where the hyperfine interaction parameters described previously set the absorption peak energies.

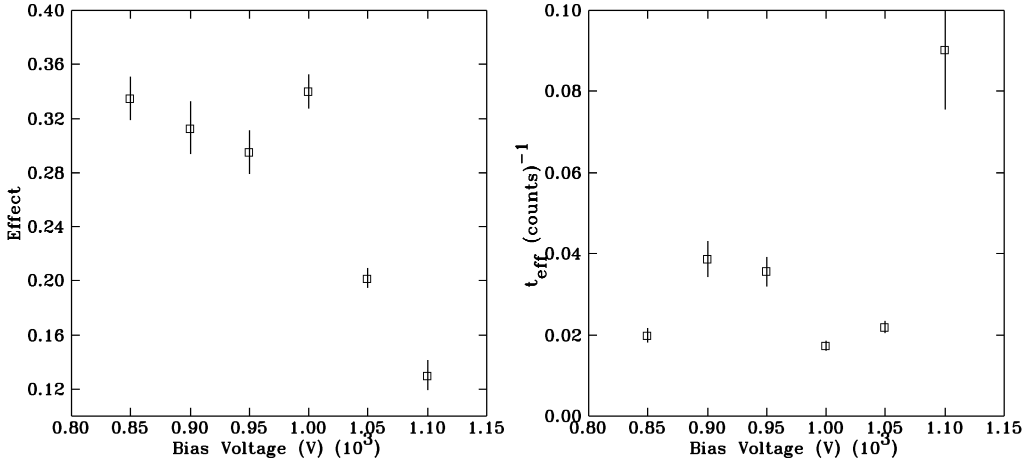

Figure 2.11: Left: ϵ as a function of bias voltage. Right: t_{eff} as a function of bias voltage

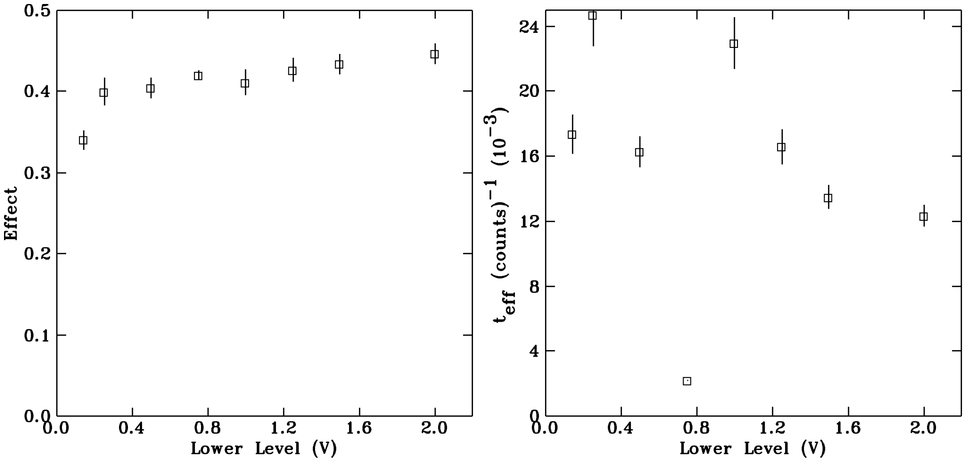

Figure 2.12: Left: ϵ as a function of lower level discriminator setting. Right: t_{eff} as a function of lower level discriminator setting.

Chapter 3

Maghemite Nanoparticles coated with a metal

3.1 Introduction

For the ferrite, γ-Fe_2O_3, at the nanoscale, finite size and surface effects play an increasing role in determining its magnetic and structural properties. Here, the finite size effects result from the length scale of the nanoparticle being comparable to that of the electron's wavelength at the Fermi level of an atom (e.g. quantum confinement). Surface effects arise from the increasing ratio of surface atoms to core atoms. These surface atoms have a different chemical and structural environment, enabling novel properties such as chemically induced magnetism for materials that otherwise exhibit no magnetic characteristics[32]. In this chapter, we explore the finite size and surface effects on the magnetism of γ-Fe_2O_3 with the addition of a thin ($\leq$1.0 nm) copper shell. By altering the thickness of this shell, we are able to demonstrate that intraparticle interactions between the core and the shell (mediated by the interfacial region) change significantly the surface spin environment of the γ-Fe_2O_3 nanoparticles. These changes in surface spin environment allow for the recapturing of frustrated surface moments leading to an increased magnetic performance.

3.2 Nanoparticle Synthesis and Characterization

Three copper coated maghemite (Cu/γ-Fe_2O_3) core/shell nanoparticle samples were synthesized using a two stage thermal decomposition process. First, γ-Fe_2O_3 nanoparticles were grown following the synthesis developed by Rockenberger *et. al*[61] in 1999. The parameters used for this synthesis have been described in detail in Shendruk *et. al*[62]. Coating the γ-Fe_2O_3 nanoparticles with copper shells of different thickness (the second stage of the synthesis) was accomplished by first heating the γ-Fe_2O_3 nanoparticle solution to 523 K (the thermal decomposition temperature of the Cu-cupferron - $Cu(C_6H_5N_2O_2)_2$) in an argon atmosphere. The copper cupferron complex was synthesized following the method described by Rockenberger *et al*[61]. 4 mL of Cu-cupferron was injected with a molar concentration of 0.2 mmol, 0.5 mmol, and 1.20 mmol to produce copper shells of $\sim$0.3 nm, $\sim$0.5 nm, and $\sim$1.0 nm, respectively. The complete solution was reacted at 498 K for 30 minutes, after which it was removed from the heat source and allowed to cool to room temperature, gradually.

Samples of the copper coated γ-Fe_2O_3 core/shell nanoparticles for x-ray powder diffraction (XRD), transmission electron microscopy (TEM), Mössbauer spectroscopy, x-ray absorption spectroscopy (XAS), and x-ray magnetic circular dichroism (XMCD) experiments were prepared by first removing any excess surfactant (oleic acid) as well as unreacted reagents by washing and magnetically separating the nanoparticles.

Magnetic separation was performed to remove any copper nanoparticles that may have formed during the synthesis. Once washed, the nanoparticles were allowed to dry in air, producing a powder sample. Magnetometry samples were prepared by mixing 20 μL of nanoparticle solution (washed and dispersed in a solvent) with 40 mg of melted paraffin wax to ensure that a comparison of the magnetic properties was made between samples of similar interparticle spacings.

TEM and electron diffraction images were collected by Dr. H. Ouyang (NTHU) and his graduate student C.-C. Lin using a JEOL 2100F microscope. The average particle size and size distribution of copper coated and the parent γ-Fe_2O_3 nanoparticles was determined from image analysis using the ImageJ[42] software. XRD patterns were collected using a PANalytical X'Pert Pro System utilizing a monochromatic Cu K_α beam and a nickel filter. Rietveld refinement of the collected diffraction patterns was accomplished using FullProf[34] software. X-ray absorption spectroscopy (XAS) and x-ray magnetic circular dichroism (XMCD) experiments were performed using the 7 T magnet system at the 4-ID-C beamline at the Advanced Photon Source located within Argonne National Laboratory. Magnetometry and susceptometry experiments were performed using a Quantum Design MPMS-XL in a temperature range of 2 to 300 K and with fields between ± 5 T.

3.3 Composition and Structure

TEM images of the bare and a copper coated γ-Fe_2O_3 nanoparticles are shown in figures 3.1 a-b). These bright field images allowed us to calculate the average nanoparticle diameter and distribution of diameters. We first determined the Feret diameter

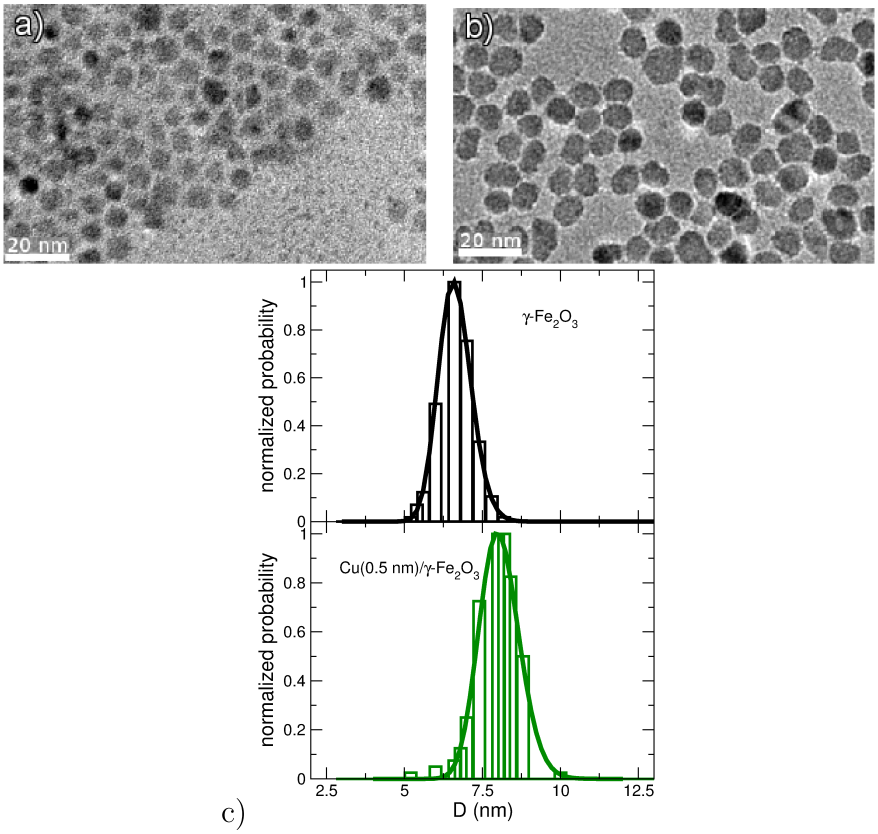

Figure 3.1: a) TEM image of parent γ-Fe$_2$O$_3$ nanoparticles, b) Cu(0.5 nm)/γ-Fe$_2$O$_3$ nanoparticles, c) particle size distribution of the parent (top) γ-Fe$_2$O$_3$ and Cu(0.5 nm)/γ-Fe$_2$O$_3$ (bottom) nanoparticles[32; 63]

.

of the nanoparticle (the diameter of a 3D object projected onto a 2D plane) then, we fit the normalized probability as a function of particle diameter (Fig. 3.1 c)) using a log-normal size distribution function,

$$\eta(D) = \frac{1}{\sqrt{2\pi} D \ln \sigma_D} \exp\left[\frac{-1}{2}\left(\frac{\ln D/\bar{D}}{\ln \sigma_D}\right)^2\right] \tag{3.1}$$

where D is the particle diameter, $\bar{D}$ is the geometric median particle diameter and σ_D is the dimensionless geometric log-normal standard deviation. $\bar{D}$ and σ_D were fitted parameters. The average nanoparticle diameter was determined to be 6.61 ± 0.04 nm, 7.8 ± 0.2 nm, 8.02 ± 0.03 nm, and 8.83 ± 0.04 nm for the parent, 0.2 mmol $Cu(Cup)_2$, 0.81 mmol $Cu(Cup)_2$, and 1.20 mmol $Cu(Cup)_2$ nanoparticles, respectively. The fitted log-normal standard deviation was $\ln(\sigma_D) = 0.05 \pm 0.01$ for all nanoparticle samples. For values of $\ln(\sigma_D) \leq 0.1$, the system is considered to be monodisperse[64]. For a monodisperse system of superparamagnetic nanoparticles the distribution of blocking temperatures is small allowing us to determine uniquely the magnetic properties free of obstruction due to a large volume distribution (the nanoparticle volume is proportional to the energy barrier to superparamagnetic rotation).

To further characterize the morphology and structure of these copper coated maghemite nanoparticles, high resolution TEM images were collected using the JEOL 2100F, by Dr. Ouyang and his group. The copper coated γ-Fe_2O_3 nanoparticle seen in figure 3.2 a-c) highlight the crystallinity of the cores. The uniform bright and dark fringes are a result of the atoms being aligned parallel to the electron beam. These well resolved lattice fringes indicated a high degree of crystallinity. Unlike the cores, the copper shells were not observed to have crystalline lattice fringes, indicating that the shells were amorphous. From the bright field HRTEM images, we observed differences in intensity representing the changes in element (higher Z elements will produce a darker image, whereas lighter elements, with lower Z, will produce a brighter image). Analysis of the intensity profile across the nanoparticles from core, through shell, to the carbon coated TEM grid provided a means to determine the average shell thickness. Inside the core, we observed well defined, periodic, changes in intensity as a result of the crystallinity of the nanoparticle cores. The copper shell, which was amorphous, presented a constant intensity as there were no observed lattice fringes. The

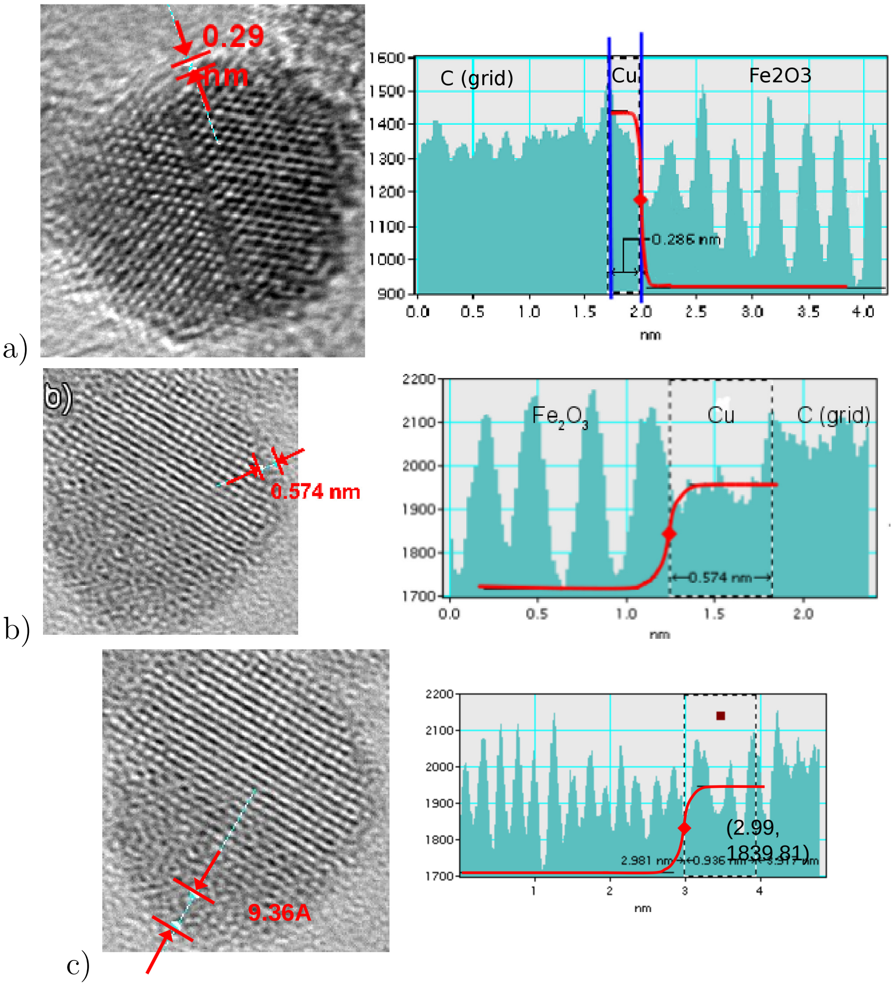

Figure 3.2: HRTEM figure of amorphous Cu-coated γ-Fe_2O_3 nanoparticles and their respective intensity mapping of the interplanar distances where the solid curved line represents the background differences between Cu and γ-Fe_2O_3. Cu(0.3 nm)/γ-Fe_2O_3 (a), Cu(0.5 nm)/γ-Fe_2O_3 (b), and Cu(1.0 nm)/γ-Fe_2O_3 (c) nanoparticles[65; 32].

TEM grids which are a carbon coated nickel mesh also showed a region of constant intensity, however, the intensity was markedly larger then that observed for the copper shell as carbon is a much lower Z element then copper. The average shell thicknesses determined from this method were 0.3 ± 0.2 nm, 0.5 ± 0.2 nm, and 1.0 ± 0.2 nm for the 0.2 mmol $Cu(Cup)_2$, 0.81 mmol $Cu(Cup)_2$, and 1.20 mmol $Cu(Cup)_2$ nanoparticles, respectively. The resolution limit of this instrument is ~0.2 Å, setting an upper

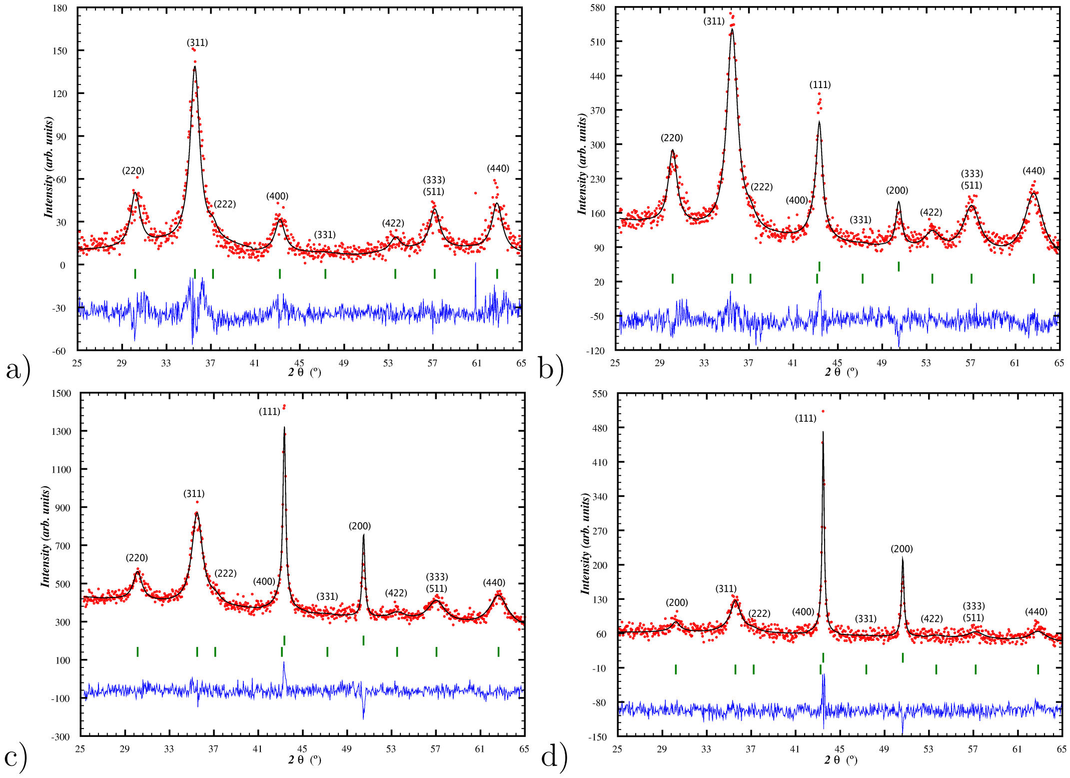

Figure 3.3: XRD pattern for the parent γ-Fe_2O_3 (a), Cu(0.3 nm)/γ-Fe_2O_3 (b), Cu(0.5 nm)/γ-Fe_2O_3 (c), and Cu(1.0 nm)/γ-Fe_2O_3 (d) nanoparticles. The solid black lines are the Rietveld refinements, with Bragg markers for the phases indexed. The top markers identify the metallic Cu (Fm$\bar{3}$m) phase and the bottom markers the γ-Fe_2O_3 (Fd$\bar{3}$m) phase. The solid blue lines represent the residuals[63].

limit on the thickness of any interfacial phase that may have formed spontaneously.

XRD patterns for the bare and copper coated γ-Fe_2O_3 nanoparticles shown in figure 3.3 a-d) were refined using FullProf[34]. The results of the Rietveld refinement for all of the samples identified the Fd$\bar{3}$m spinel phase of maghemite. The unit cell of maghemite has 16 Fe^{3+} ions in tetrahedral (A) sites, 8 Fe^{3+} ions in octahedral (B) sites, and 32 O^{2-} ions. The fitted lattice parameter of 0.838 ± 0.001 nm was typical of maghemite nanoparticles[66]. By including Scherrer broadening into the refinement, an average crystallite diameter of 6.5 ± 0.5 nm was determined for the spinel phase. The XRD patterns of the copper coated γ-Fe_2O_3 nanoparticles were refined with an additional phase representing the $Fm\bar{3}m$ phase of copper. Significant broadening of the copper reflections were observed. In addition to these broadened reflections of the copper shells, intense reflections from the (111) and (200) planes of the $Fm\bar{3}m$ phase of copper were observed. These reflections increased in intensity with the increasing, relative to the γ-Fe_2O_3 core, with increasing copper shell thickness suggesting that these reflections were from the copper shells. Although the shells were found to be quite thin (0.3 to 1.0 nm), similar diffraction patterns of the shell in core/shell nanoparticles have been observed[7]. Furthermore, it has been seen previously that for hollow nanoparticles, Scherrer analysis of the diffraction peaks yield sizes as if the nanoparticles were solid[67]. These results, although strange, are not to be unexpected, as the shells do have a thickness comparable to their diameter, tangent to the surface of the cores. Thus, crystallite sizes comparable to that of a nanoparticle with an average diameter of $core + shell$ is to be expected. We did not observed any reduction in relative intensity of the two copper reflections after several washes indicating that these reflections were not a result of copper nanoparticles but were from the copper shells. Also, no TEM images of copper nanoparticles (EDX and EELS) were observed.

Selective area electron diffraction images were collected for all three copper coated maghemite samples (Fig. 3.4 a-c)). These images show two distinct types of diffraction rings: sharp, well focused rings from the maghemite cores and diffuse, broadened rings from the amorphous copper shells. ImageJ analysis of the diffraction rings yielded d-spacings consistent with the $Fm\bar{3}m$ phase of maghemite and the $Fd\bar{3}m$ phase of

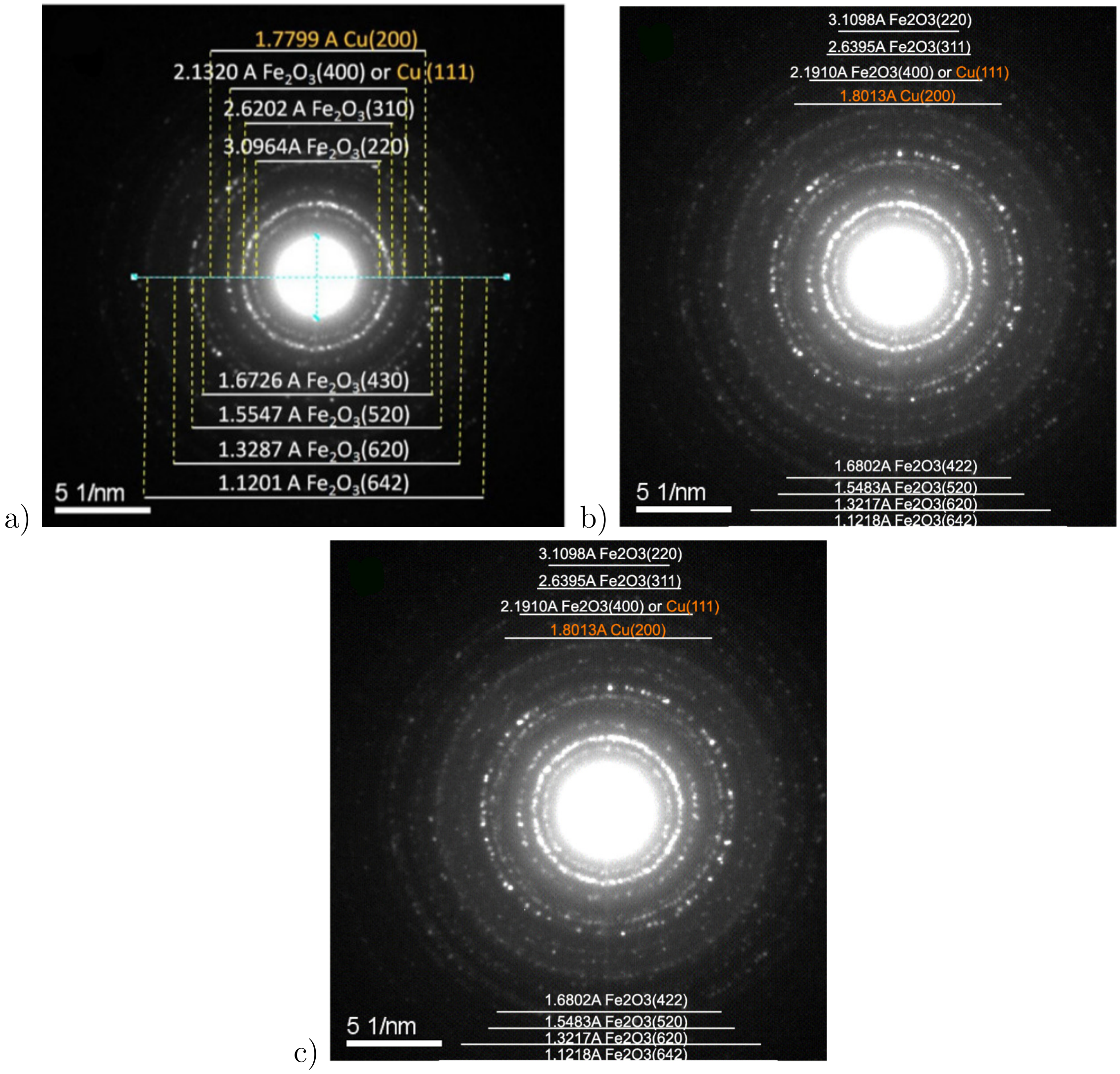

Figure 3.4: Selective area electron diffraction images for a) Cu(0.3 nm)/γ-Fe_2O_3 nanoparticles, b) Cu(0.5 nm)/γ-Fe_2O_3, and c) Cu(1.0 nm)/γ-Fe_2O_3[65].

copper, in agreement with Rietveld refinements of the x-ray diffraction patterns.

X-ray absorption spectroscopy experiments, an element specific spectroscopic technique, were performed to determine the oxidation state and coordination environment of the Fe (700-730 eV) and Cu (925-960 eV) atoms (Fig. 3.5). These spectra were collected over the $L_{3,2}$ transitions. The iron spectra for the three nanoparticle samples

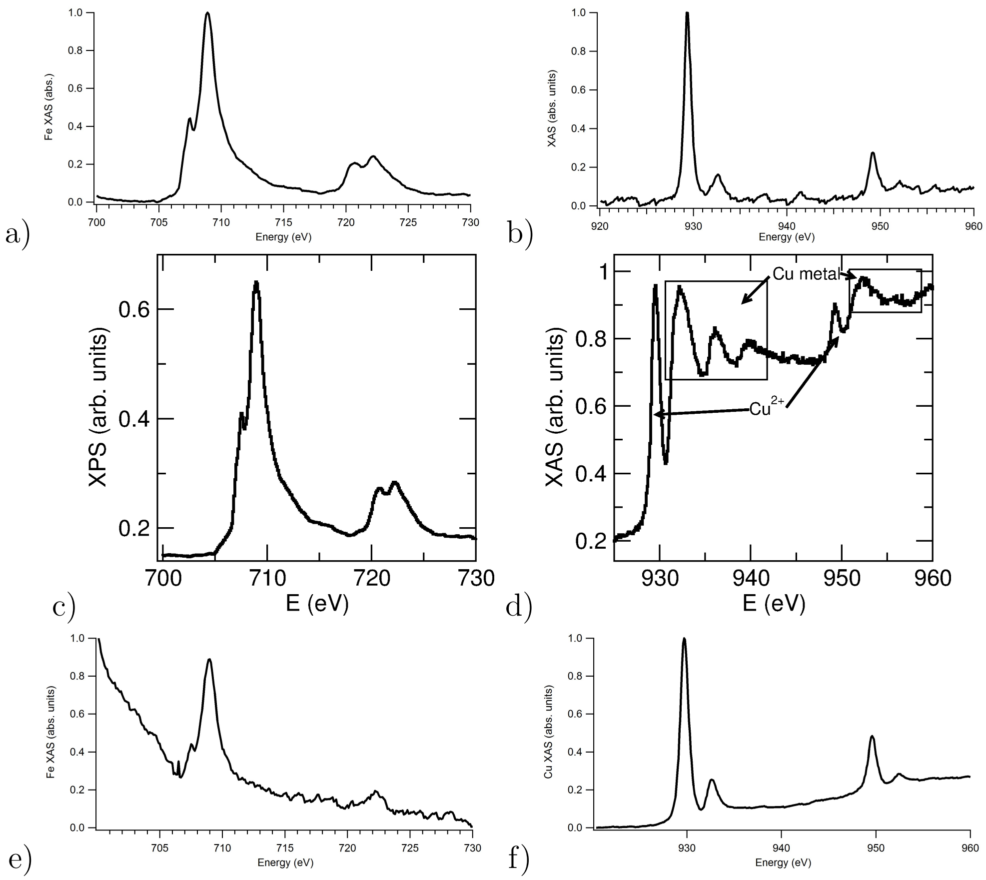

Figure 3.5: X-ray absorption spectroscopy at the $L_{3,2}$ transitions for Fe a), c), e), Cu(0.3 nm)/γ-Fe_2O_3, Cu(0.5 nm)/γ-Fe_2O_3, and Cu(1.0 nm)/γ-Fe_2O_3, respectively. $L_{3,2}$ transition edge for Cu; b), d), f) Cu(0.3 nm)/γ-Fe_2O_3, Cu(0.5 nm)/γ-Fe_2O_3, and Cu(1.0 nm)/γ-Fe_2O_3, respectively. The Fe XAS spectral features are consistent with γ-Fe_2O_3. Both metallic Cu and Cu^{2+} were present[32].

were similar. Two peaks observed at ∼707 eV and ∼721 eV from the $2p_{3/2}$ and $2p_{1/2}$ transitions (L_3 and L_2 transition edges). The L_3 spectral features were in agreement with Fe^{3+} in both an octahedral and tetrahedral coordination environment, similar to that observed in γ-Fe_2O_3[68]. The copper spectra was much more interesting. Not only was metallic copper present, as would be expected, but we also observed characteristic spectral features for Cu^{2+} in an octahedral coordination environment. These spectral features for Cu^{2+} are similar to what would be observed for CuO[69].

Furthermore, as the integrated area of the metallic copper spectral features increase with increasing amounts of copper; the Cu^{2+} observed must not be the result of surface oxidation. Thus, what is likely occurring is that with the copper coating, an interfacial phase of CuO has formed spontaneously.

3.4 Magnetism

The overall magnetic properties, that is, the magnetism representative of the bulk of the sample were determined from magnetometry and susceptometry experiments. These overall magnetic properties together with experiments to determine the elemental magnetism and the local atomic magnetism have allowed for us to elucidate the key role that the interfacial layer of CuO that has formed spontaneously between the maghemite core and copper shell has on the magnetism of copper coated maghemite nanoparticles. Below is a detailed discussion of our experimental results and analyses which have allowed us to expand our understanding of intraparticle interactions and the direct role that nanoparticle surface moments play in the magnetism.

The temperature dependent magnetization of copper coated maghemite nanoparticles embedded in paraffin wax was studied in both the zero-field cooled (ZFC) and field cooled (FC) states (Fig. 3.6). The magnetometry samples were prepared with similar interparticle separation between nanoparticles, allowing for a direct comparison of the magnetometry and susceptometry results. The ZFC state was set by cooling the nanoparticles from 300 K, a temperature above their superparamagnetic blocking temperature (T_B), to 10 K. This was done to ensure that the nanoparticles' magnetizations were aligned randomly, resulting in a zero, time-averaged, magnetization. Once

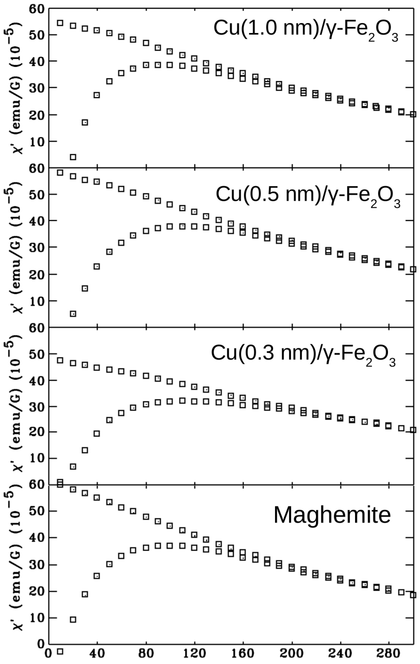

Figure 3.6: Temperature dependence of the magnetization in the ZFC and FC states with an applied field of 50 Oe (5 mT).

base temperature was reached, a small *dc* field of 5 mT was applied (resulting in a measurable magnetization) and the magnetization was measured with warming. Initially, a rapid increase in the *dc* susceptibility, $\chi_{DC}(T)$, was observed for the Cu(0.3 nm)/γ-Fe_2O_3 and the Cu(0.5 nm)/γ-Fe_2O_3 nanoparticle samples. This increase continued until a maximum was reached, T_B. A T_B of 96 ± 2 K and 113 ± 1 K was observed for the Cu(0.3 nm)/γ-Fe_2O_3 and Cu(0.5 nm)/γ-Fe_2O_3 nanoparticle samples, respectively. With continued warming, the magnetization decreased as the nanoparticles became superparamagnetic. This decrease continued until 300 K. The magnetization could not be measured above 300 K as the nanoparticles were embedded in a paraffin matrix and the melting point of paraffin is ~320 K. A different temperature dependence was observed for the Cu(1.0 nm)/γ-Fe_2O_3 nanoparticles (Fig. 3.6 top). Initially, with warming from the ZFC state, the magnetization decreased almost monotonically to 300 K. There was no observable T_B for this sample in the range of temperatures measured. At 300 K, we cooled the nanoparticle samples in the FC state while continuing to measure their magnetizations. Initially, the FC magnetization tracked the ZFC magnetization. This was to be expected as the nanoparticles were superparamagnetic. With continued cooling, the $\chi_{DC}^{FC}(T)$ tracked with the $\chi_{DC}^{ZFC}(T)$ until T_B was reached, at which point they diverged as the nanoparticle moments were no longer superparamagnetic and remained aligned with the applied field. Precise determination of T_B from $\chi_{DC}^{ZFC/FC}(T)$ was made problematic by the significant broadening of the maxima compared with the parent nanoparticles with similar diameters (and interparticle spacing). This broadening was evidence that the anisotropy of the maghemite core had been altered significantly by the copper coating since the energy barrier that describes the coherent spin reversal mechanism (superparamagnetism) is equal to KV and KV is proportional to T_B. To better understand the role that the copper coating had on the magnetism, time-dependent susceptibility experiments were performed.

ac susceptibility experiments were performed in the ZFC state. A small *ac* field of 0.25 mT was applied at frequencies from 10 to 1000 Hz are shown in figure 3.7. For the parent nanoparticles (uncoated γ-Fe_2O_3), after ZFC to 2 K, there was a gradual increase of χ_{AC}(T,ν) with warming, as thermal energy was added to the system which enabled the nanoparticle's magnetization to oscillate more rapidly. At these low temperatures, the nanoparticle's magnetization was fixed along its easy axis direction which was set by the uniaxial anisotropy. With warming, an increase in thermal energy, the moments oscillated around their easy axis direction increas-

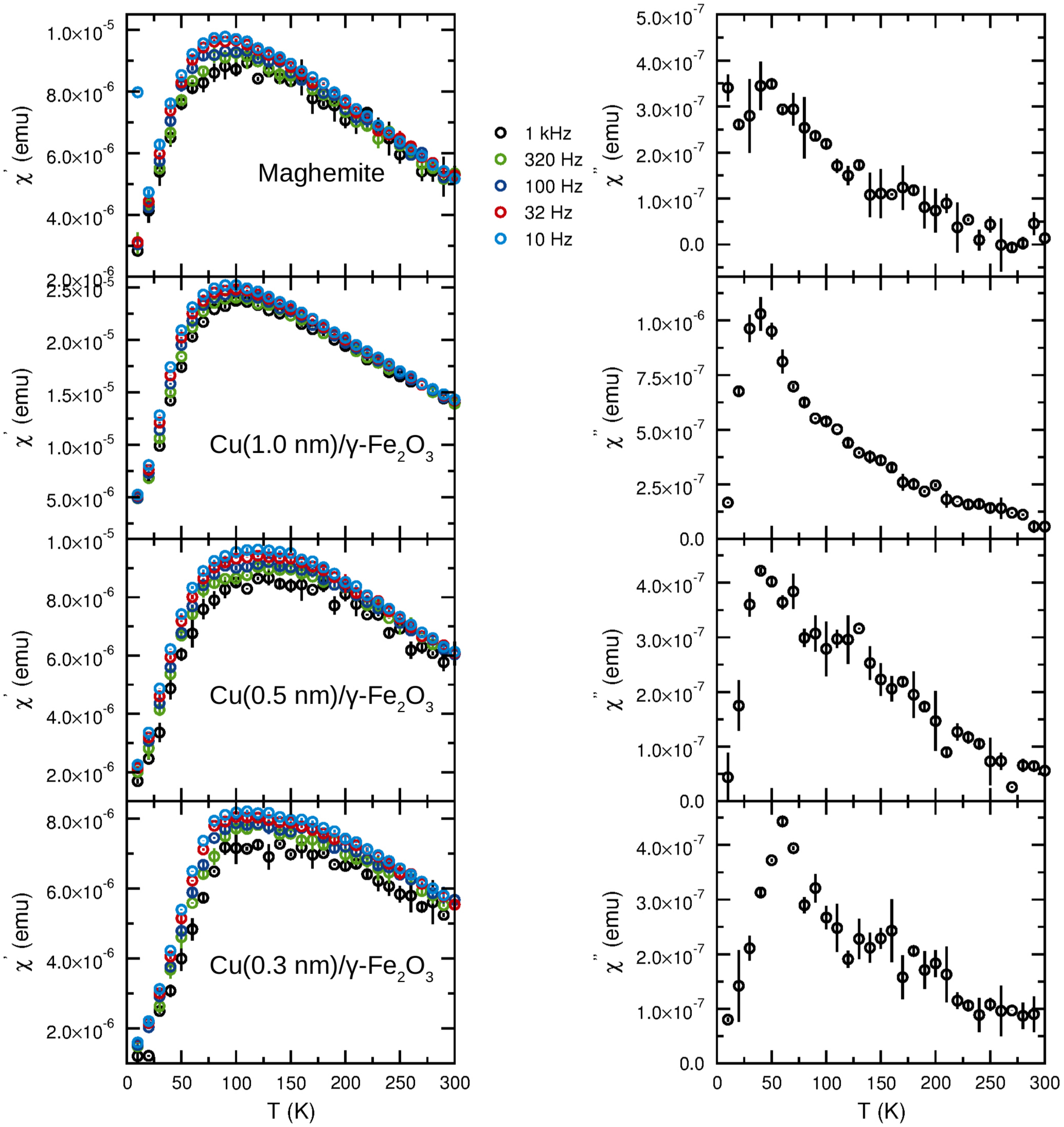

Figure 3.7: Temperature and frequency dependence of the in-phase (left) and out-of-phase (right) *ac* susceptibility in a 0.25 mT drive field.

ing the susceptibility resulting from the increased response to the oscillating applied magnetic field. With continued warming, the magnitude of the collective excitations increased, seen as an increased χ_{AC}(T,ν). At T_B of the nanoparticle system, the moments began to undergo 180° spin-flips becoming superparamagnetic. Here, at this temperature, the drive frequency was nearest to the oscillating frequency of the magnetization reversal seen as the frequency dependent maximum in χ'_{AC}(T,ν) and χ''_{AC}(T,ν). At temperatures above T_B, these superparamagnetic fluctuations increased in rate, the time-averaged magnetization decreased reflected by the gradual reduction in χ_{AC}(T,ν) coupled with its frequency independence. For the copper coated magnetite nanoparticles, similar trends in the frequency and temperature dependence of χ_{AC}(T,ν) were observed. Interestingly, there was significant broadening in temperature of the frequency dependent maxima which made the unique determination of $T_B(\nu)$ problematic. Furthermore, the convergence of the frequency dependent susceptibility was increased to a much higher temperature then compared with the parent γ-Fe$_2$O$_3$ nanoparticles ($\geq$150 K). These features were good indications that the γ-Fe$_2$O$_3$ core had been effected significantly by the copper coating, and since the energetics that described the moment fluctuation process (such as superparamagnetism) had been altered, the anisotropy of the copper coated maghemite nanoparticles was increased.

Field-cooled hysteresis loops ($\mu_0 H_{APP}$ = 2.5 T) were collected for the parent and copper coated maghemite nanoparticles showed, below T_B, magnetic hysteresis as the nanoparticles single-domains were static (Fig. 3.8). By ~1 T, the nanoparticles' magnetizations were saturated, and there was no observable high-field susceptibility. Above T_B, where these single-domains were superparamagnetic, no magnetic hysteresis was observed. The effects on the magnetism of the copper coating were seen in the differences of the behaviour of the hysteresis loops. For example, the loops of the

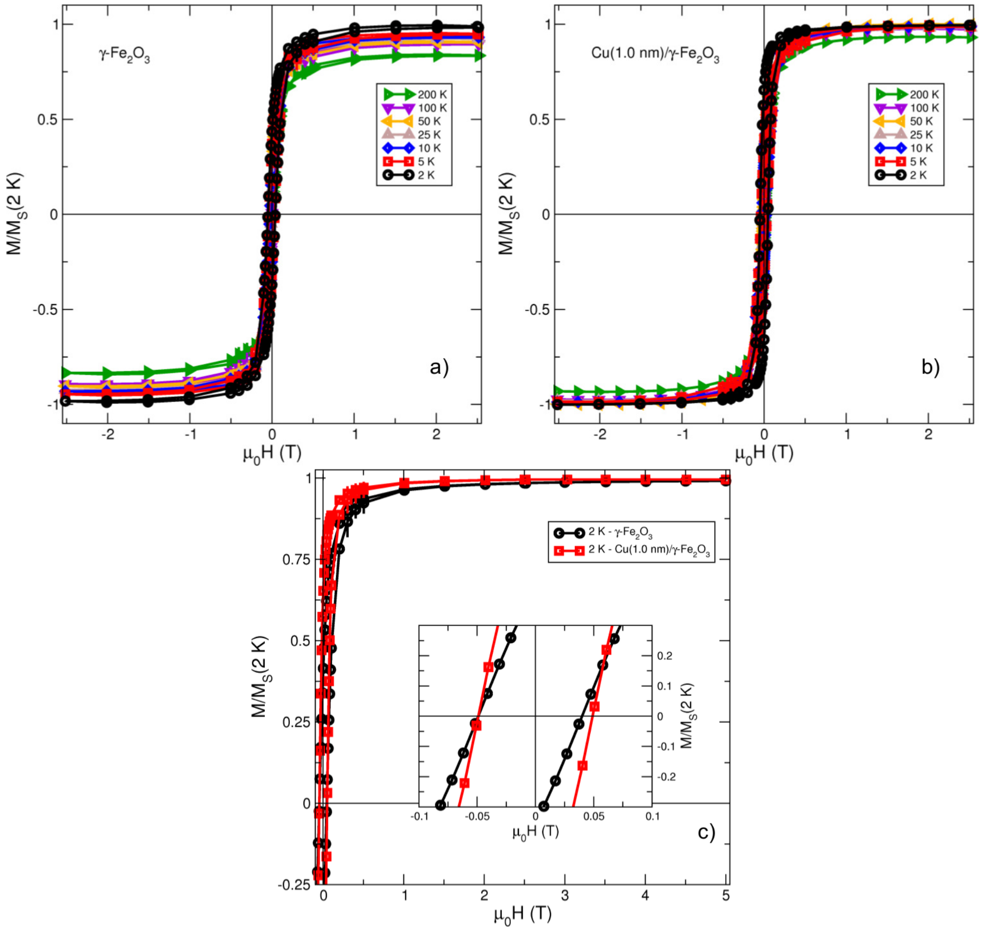

Figure 3.8: Typical field-dependent magnetization (M versus $\mu_0 H$ data for γ-Fe$_2$O$_3$ nanoparticles (left), Cu(1.0 nm)/γ-Fe$_2$O$_3$ nanoparticles (middle), and the 2 K M versus $\mu_0 H$ data showing the general differences between the hysteresis loops, with the inset focusing on the low-field regime (right)[32].

copper coated maghemite nanoparticles appeared to be more square (Fig. 3.8 b)), indicating changes in the magnetic anisotropy of the γ-Fe$_2$O$_3$ nanoparticle cores, consistent with the $\chi_{DC}(T)$ and χ_{AC}(T,ν) behaviour described above. In addition to the effects on the squareness of the hysteresis loops, the copper coating also effected significantly the coercivity as well as the saturation magnetization (Fig 3.8 a) and c)).

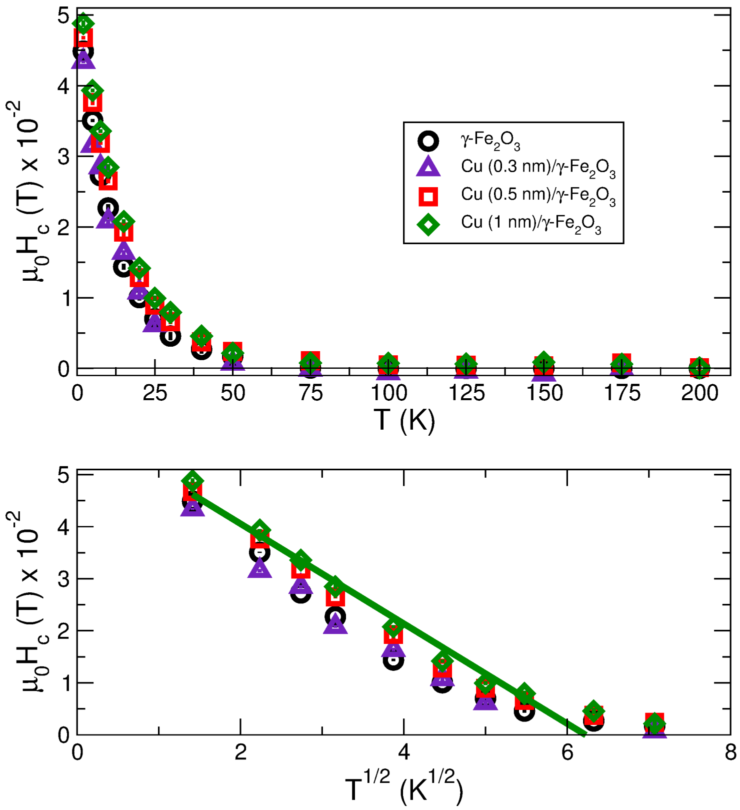

Figure 3.9: Temperature dependence of the coercivity, $\mu_0 H_C$ (top), and $\mu_0 H_C$ as a function of $\sqrt{T}$ (bottom) of the γ-Fe_2O_3, Cu(0.3 nm)/γ-Fe_2O_3, Cu(0.5 nm)/γ-Fe_2O_3, and Cu(1.0 nm)/γ-Fe_2O_3 nanoparticle systems[32].

The temperature dependence of the coercivity ($\mu_0 Hc(T)$) is shown in figure 3.9 for the parent and copper coated maghemite nanoparticles. All four samples presented $\mu_0 Hc(\mathrm{T} = T_B) = 0$ mT, in good agreement with susceptibility experiments. Generally, in the uniaxial anisotropy description of the energy barrier of which a nanoparticle's magnetization must overcome to flip orientations (180° spin-flip), $\mu_0 Hc(T)$ is found to follow:

$$\mu_0 H_C(T) = \frac{2K}{M_S}\left(1 - \sqrt{\frac{T}{T_B}}\right) \tag{3.2}$$

where K is the temperature independent anisotropy and M_S is the saturation magnetization. Figure 3.9) shows a plot of $\mu_0 Hc(\mathrm{T}^{1/2})$. With increasing copper coat-

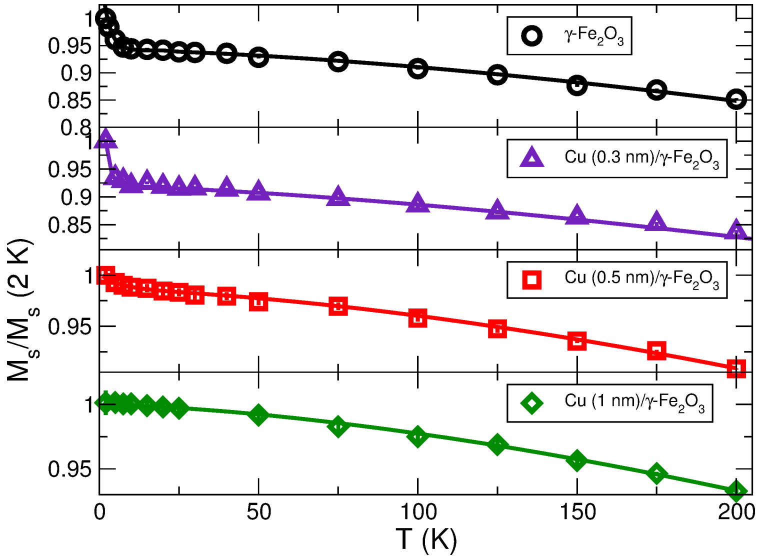

Figure 3.10: $M_S(T)$ for γ-Fe_2O_3, Cu(0.3 nm)/γ-Fe_2O_3, Cu(0.5 nm)/γ-Fe_2O_3, and Cu(1.0 nm)/γ-Fe_2O_3 nanoparticles determined from fits to field-cooled hysteresis loops. The solid lines are fits described in the text. Note that the error bars are smaller then the symbol size[32].

ing thickness, better agreement with the above model (eq. 3.2) was observed. The parent γ-Fe_2O_3 nanoparticles showed the largest disagreement with this model as a result of the significant surface spin disorder[62]. Further evidence for the alteration of K can be seen here as the thickness of the copper coating increased. The Cu(1.0 nm)/γ-Fe_2O_3 nanoparticle system showed a good fit using eqn: 3.2, indicating towards the core γ-Fe_2O_3 of the nanoparticle behaving like a 'simple' single-domain nanoparticle. From an application of (Eqn. 3.2), a fitted $T_B = 50 \pm 5$ K was in agreement with the T_Bs determined from susceptibility data, and assuming γ-Fe_2O_3 nanoparticles regained their bulk $M_S = 3.65 \times 10^5$ A m^{-1}[70], the fit yielded a $K = 2.5 \pm 0.2 \times 10^4$ J m^{-3}, in good agreement with the bulk values[70].

It is well established that finite size effects impact the magnetism of nanoparticles and any disorder (e.g. structural, chemical, or magnetic) will effect the magnetic response of the γ-Fe$_2$O$_3$ parent and core (of the copper coated maghemite nanoparticles) significantly[71]. A measure of this magnetic response is the temperature dependence of the saturation magnetization, $M_S(T)$. To determine $M_S(T)$, both the law of approach to saturation[72]

$$M(H) = M_S \left(1 - \frac{a}{H} - \frac{b}{H^2}\right) \tag{3.3}$$

where a and b are phenomenological constants, and linear fits to M versus $1/\mu_0 H$ of the high-field M behaviour where used, as a cross-check, to quantify $M_S(T)$ from the $M(\mu_0 H)$ data. Figure 3.10 shows the $M_S(T)$ for the parent and copper coated maghemite nanoparticles. Initially, at temperatures where the disordered spins were frozen, M_S decreased rapidly with warming for the parent γ-Fe$_2$O$_3$ nanoparticles, a result of the thawing surface spins[62; 30]. By comparison, the copper coated maghemite nanoparticles exhibited a much weaker decrease in $M_S(T)$ between 2 and ~15 K with warming due to fewer disordered surface spins. For example, the Cu(1.0 nm)/γ-Fe$_2$O$_3$ nanoparticles $M_S(T)$ was essentially constant until ~50 K, indicating that the surface spin disorder had been reduced significantly. The measured $M_S(T)$ permitted an indirect measure of trends from core/surface magnetism. We used a modified Bloch $T^{3/2}$ law that incorporated a term describing the temperature at which the surface spins freeze (T_F) to describe the temperature dependence of M_S[30]. We observed that at $T \geq 25$ K, $M_S(T)$ was well described by $M_S(\mathrm{T})/M_S(0) = (1 - BT^{3/2})$ where B was the Bloch constant. For lower temperatures, an exponential term, Ae^{-T/T_F}, with A a phenomenological constant that scale with the relative amount of frozen surface moments[30] compared with magnetically ordered core moments, was necessary.

Results of non-linear least squares fits to $M_S(T)$ (the solid lines in figure 3.10) are summarized in table 3.1. We observed good agreement of these fitted parameters for the γ-Fe_2O_3 parent nanoparticles to previous measurements on similar particles[62]. For the Cu(0.3 nm)/γ-Fe_2O_3 nanoparticles $M_S(T)$, T_F was reduced along with a decrease of ~7% in B. Similar reductions for Cu(0.5 nm)/γ-Fe_2O_3 and Cu(1.0 nm)/γ-Fe_2O_3 nanoparticles were observed. These trends indicated possible pinning effects of Fe moments with the reduction of the surface anisotropy describing the surface spin layer at a slightly stronger Fe-O-Fe exchange ($B \propto 1/J$, where J is the exchange constant[71]) of the surface spins, perhaps resulting from Cu-O-Fe superexchange. This stronger exchange by altering the surface magnetism of the γ-Fe_2O_3 cores was enhanced further in the Cu(1.0 nm)/γ-Fe_2O_3 nanoparticles where there was no evidence for surface spin freezing and B was decreased further (~10% compared to Cu(0.5 nm)/γ-Fe_2O_3 nanoparticles).

Further evidence of two spin populations (core and surface) was provided by the presence of a measurable exchange bias loop shift, $\mu_0 H_{EX}$ (Fig. 3.11). Since the core of the nanoparticles (γ-Fe_2O_3) had a T_C significantly larger then T_F[73], field-cooling from 300 K would have set a preferred orientation onto the surface spins. The single-

Table 3.1: Results of fit of $M_S(T)$ to the modified Bloch $T^{3/2}$ law described in the text

	B ($K^{-3/2}$)	**A**	**T_F (K)**
γ-Fe_2O_3	$2.82 \pm 0.07 \times 10^{-5}$	$1.09 \pm 0.06 \times 10^{-3}$	4.1 ± 0.5
Cu(0.3 nm)/γ-Fe_2O_3	$2.61 \pm 0.09 \times 10^{-5}$	$3.2 \pm 0.8 \times 10^{-1}$	1.5 ± 0.4
Cu(0.5 nm)/γ-Fe_2O_3	$2.26 \pm 0.02 \times 10^{-5}$	$2.73 \pm 0.03 \times 10^{-4}$	2.0 ± 0.1
Cu(1.0 nm)/γ-Fe_2O_3	$2.02 \pm 0.06 \times 10^{-5}$	$0.00 \pm 0.05 \times 10^{-4}$	0.0 ± 0.5

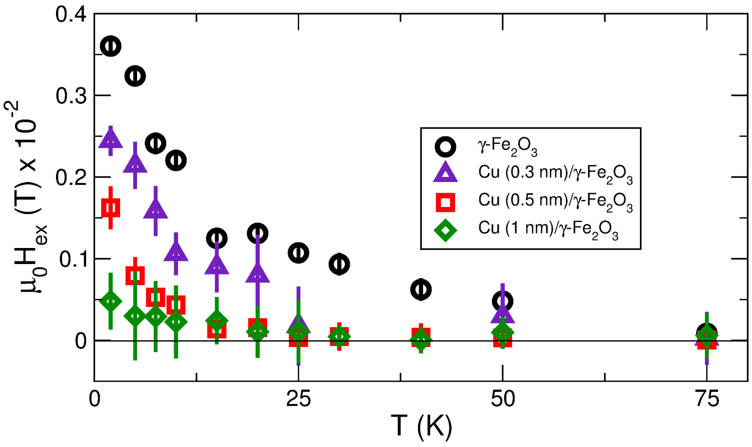

Figure 3.11: Temperature dependence of the exchange bias loop shift, $\mu_0 H_{EX}$, of the parent γ-Fe_2O_3 and Cu-coated γ-Fe_2O_3 nanoparticles[32].

domain γ-Fe_2O_3 cores then experienced the field generated by these frozen surface spins aligned with the applied field, and exchange coupling between the γ-Fe_2O_3 core and surface spins occurred. This exchange coupling set the uniaxial anisotropy resulting in a small H_{EX} (Fig. 3.11), in keeping with the ~6000 Fe sites in a γ-Fe_2O_3 nanoparticle with approximately 60% of these Fe sites being located on the surface[74]. The parent γ-Fe_2O_3 nanoparticles presented the largest $\mu_0 H_{EX}$, where $\mu_0 H_{EX}$ was observed to decrease significantly after 5 K, in agreement with the T_Fs determined from $M_S(T)$ fits. $\mu_0 H_{EX}$ continued to decrease with warming tracking with $M_S(T)$ and $\mu_0 H_{EX}(T > T_B) = 0$ mT was in good agreement with T_Bs described above. These results provided evidence that with warming, the number of available static surface spins decreased, therefore, fewer of these surface spins were able to couple to the ordered core spins, decreasing $\mu_0 H_{EX}$. The copper coated maghemite nanoparticles showed a reduced number of surface spins, decreasing $\mu_0 H_{EX}$. For the Cu(1.0 nm)/γ-Fe_2O_3 nanoparticles, an elimination of $\mu_0 H_{EX}$ altogether was observed. These trends indicated the presence of stiffer exchange and a reduced number of disordered surface

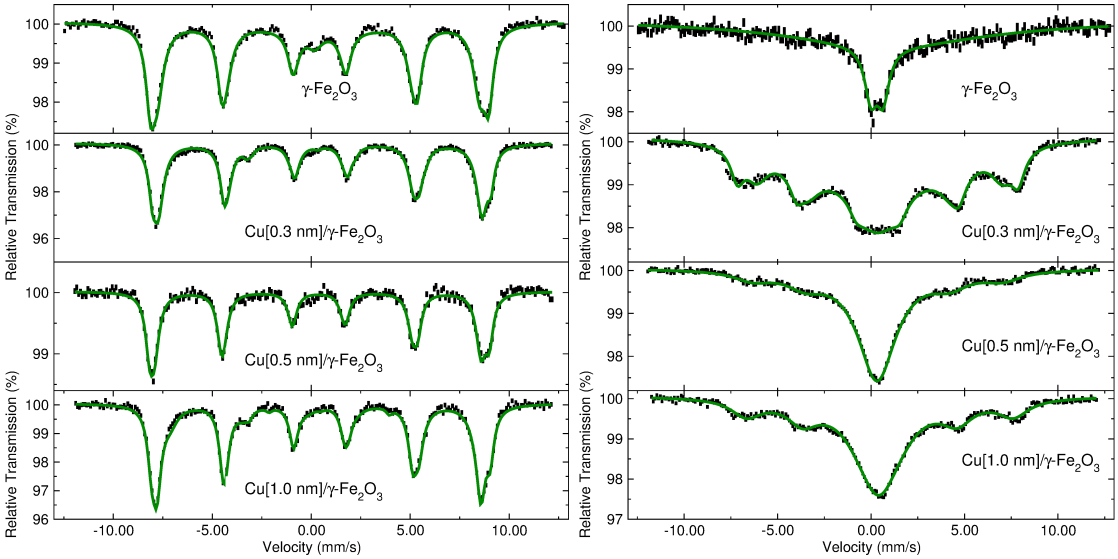

Figure 3.12: Transmission Mössbaur spectra at Left: 10 K and Right: 300 K. The solid line is a fit described in the text[32].

spins with increasing copper coating.

To provide further evidence for the interactions of the Cu ions in the copper shell with the Fe surface ions, Mössbauer spectroscopy experiments were performed at 10 K (T $< T_B$) and 300 K (T $> T_B$) (Fig. 3.12). The 10 K spectrum of the parent γ-Fe_2O_3 nanoparticles was described using two magnetic sites with hyperfine fields, B_{HF}, of 50.7 ± 0.1 T and 53.1 ± 0.1 T consistent with the A- and B-sites of γ-Fe_2O_3[75]. In addition, a singlet was necessary to obtain a good fit to the data. This singlet described the fluctuating surface Fe spins. For the copper coated maghemite nanoparticles, similar A- and B-site B_{HF}s were observed. However, the singlet necessary to describe the Fe surface spins was decreased significantly in intensity for the Cu(0.3 nm)/γ-Fe_2O_3 nanoparticle system, indicating that the previously fluctuating surface spins had become constrained on the time-scale of the Mössbauer measurement ($\sim$10 MHz). A further reduction of intensity for this spectral component for the Cu(0.5 nm)/γ-Fe_2O_3 nanoparticles was observed. This indicated that these Fe ions had become part of the spectrum between ± 4 mm s^{-1} and a component of a sextet that indicated slowly fluctuating Fe spins with a $B_{HF} \approx 22$ T[32]. With an increased copper coating thickness, the B_{HF} of the component describing these slowly fluctuating surface Fe ions increased to 25.0 ± 0.3 T for the Cu(1.0 nm)/γ-Fe_2O_3 nanoparticle samples. The variation of the ± 8 mm s^{-1} line intensities (lines 1 and 6 in the Mössbauer spectra) provided even further evidence of the effects of the copper coating on the surface Fe ions. These lines, becoming more intense with copper coating thickness suggested that the recoil-free fraction of the ^{57}Fe at the A- and B-sites of the γ-Fe_2O_3 was being altered resulting from the increased number of surface moments which had different Fe environments, the Fe exchange was being stiffened[59]. Also, a quadrupole shift, necessary to fit the parent γ-Fe_2O_3, could not be fitted to the copper coated maghemite nanoparticles' spectra, further indicating that the distorted coordination environment experienced by the parent γ-Fe_2O_3 nanoparticles was no longer present.

These results were mirrored in the Mössbauer spectra collected at 300 K. We observed clear evidence for the pinning of surface Fe moments by the copper coating. As reported previously, the spectrum of the parent γ-Fe_2O_3 nanoparticles was well described by a magnetic relaxation model that included both core and surface spins[76]. At 300 K, all spins fluctuated faster then the measurement time of the Mössbauer effect. This resulted in a time-averaged $B_{HF} \approx 0$ T. The sextet observed at 10 K had collapsed into a broad doublet with the same quadrupole shift of 0.43 ± 0.07 mm s^{-1}, consistent with a distorted coordination environment from Fe surface spins.

In keeping with the previous observations, the quadrupole doublet was not observed with the copper coated maghemite samples; evidence that the copper coating affected directly the Fe surface spins. Furthermore, the spectral component with a $B_{HF} \sim 45$ T, is likely the fully resolved sextet component that was only partially observed via the ∼25 T component at 10 K. This component had the same isomer shift, which described the A- and B-site Fe, identifying that a significant number of the Fe spins whose fluctuating rate had been slowed considerably at 300 K.

To better understand the link implied between the copper coating and the γ-Fe_2O_3 nanoparticle surface magnetism, temperature and field dependent elemental magnetic measurements were carried out over the $L_{3,2}$ transitions ($2p$ core to $3d$ hole) of Fe (700 to 730 eV) and Cu (925 to 960 eV). Both the total electron yield (TEY) and total fluorescence yield (TFY) x-ray magnetic circular dichroism (XMCD) experiments were performed. Typically, the TEY is a measure of the surface of the sample which depends on the escape depth of the electrons at the energies studied (e.g. ∼2 nm for Fe[77]) and the TFY is a measure of the photons that come from deep within the sample (e.g. on the order of 100 nm). Thus, TEY experiments are representative of the copper coating and the surface layers of the γ-Fe_2O_3 nanoparticle cores. In addition, no charging effects were observed during these experiments which indicates clearly that the nanoparticles were conductive.

Figure 3.13 shows the Fe TEY XMCD spectra for the different copper coating thicknesses. The spectral features at the Fe L_3 transition energies were consistent with γ-Fe_2O_3. Complementary results for the TFY XMCD Fe spectra were observed, although the signal-to-noise ratio was decreased significantly due to self absorption

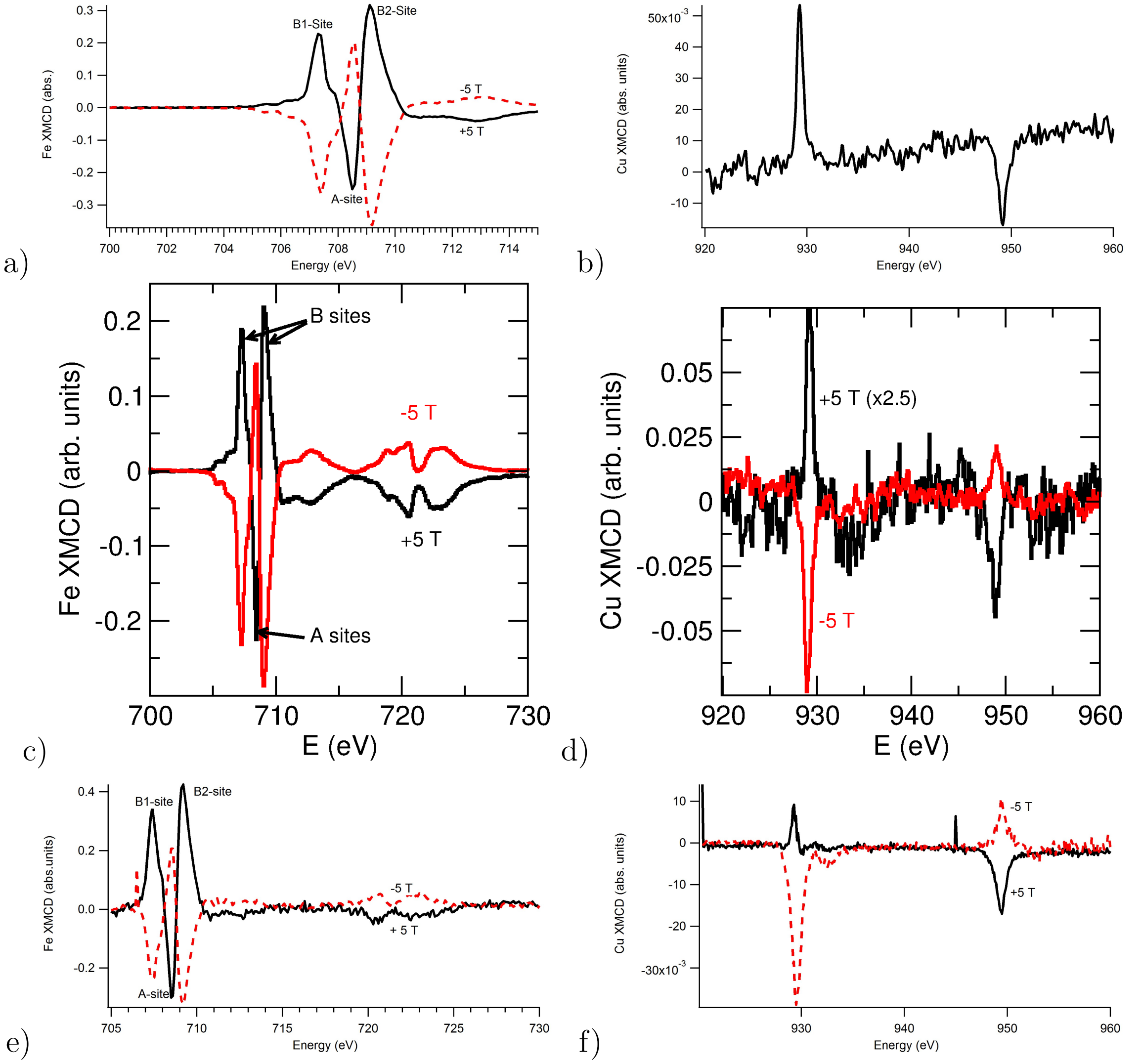

Figure 3.13: Left: L_3 edge normalized XMCD TEY signal of the Fe $L_{3,2}$ transitions at 10 K in +5 T (black) and -5 T (red) with the characteristic signature of the tetrahedral (A-sites) and octahedral (B-sites) of γ-Fe_2O_3 in a) Cu(0.3 nm)/γ-Fe_2O_3, c) Cu(0.5 nm)/γ-Fe_2O_3, and e) Cu(1.0 nm)/γ-Fe_2O_3. Right: L_3 edge normalized TFY XMCD of Cu in +5 T black, (signal multiplied by a factor of 2.5) and -5 T (red) showing clearly the presence of a magnetic moment on the Cu at 10 K for b) Cu(0.3 nm)/γ-Fe_2O_3, d) Cu(0.5 nm)/γ-Fe_2O_3, and f) Cu(1.0 nm)/γ-Fe_2O_3[32].

processes making quantitative analysis with the Fe TFY spectra problematic. At the L_3 transition energies, three peaks were observed ascribed to tetrahedral Fe^{3+} (a single peak) and the octahedral Fe^{3+} (two peaks) of γ-Fe_2O_3. As expected, the Fe^{3+}

moments set by the 5 T applied field at the A-site were antiferromagnetically coupled with the Fe^{3+} moments at the B-sites. All spectral features were observed to flip with a change in field polarity, as expected for magnetic γ-Fe_2O_3. This behaviour was also observed in the TFY Fe XMCD spectra. Interestingly, the XAS normalized Fe spectra had an ∼10% stronger XMCD signal with an applied field of -5 T compared to 5 T, unlike plain γ-Fe_2O_3[68], further evidence for possible pinning of the Fe surface moments.

Similar measurements were performed over the $L_{3,2}$ transitions energies of Cu in order to identify any magnetic exchange coupling between the Fe and Cu atoms (Fig. 3.13). The XMCD spectral features at the Cu $L_{3,2}$ transition were consistent with Cu^{2+} (CuO)[69]. Unexpectedly, a reversal of the Cu XMCD spectral feature with a change in field polarity was observed. Cu^{2+} in CuO, a simple antiferromagnet, would not show this behaviour as circularly polarized photons are unable to distinguish between the magnetization of equal numbers of parallel and antiparallel moments in an applied field irrespective of its polarity. These results show the Cu moments as being canted by the Fe moments with ∼0.05 μ_B/Cu spin in -5 T[78] at 10 K (compared with ∼1.2 μ_B/Fe spin[75]). Interestingly, the enhanced Fe and Cu magnetism was observed with the same field polarity in the Cu(0.5 nm)/γ-Fe_2O_3 nanoparticle systems, whilst the Cu(1.0 nm)/γ-Fe_2O_3 nanoparticle's elemental magnetism experienced no observable field polarity bias.

The temperature dependence of the elemental XMCD signal for both Fe and Cu are shown in figure 3.14. The spectral area of the magnetic XMCD peaks are proportional to the elemental magnetization (e.g. total Fe and Cu moments). To ensure

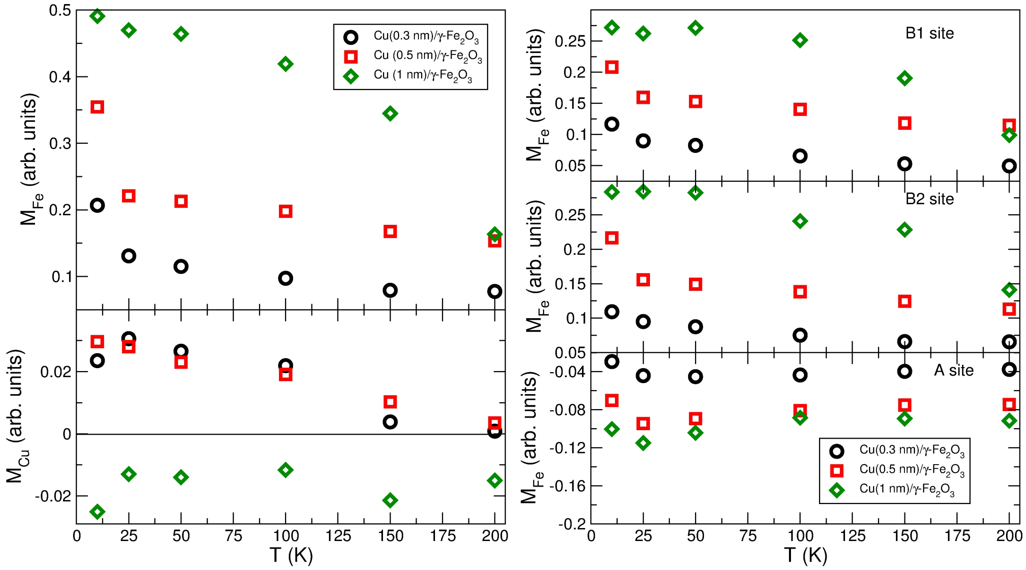

Figure 3.14: Left: Temperature dependence of the Fe magnetization determined from the TEY XMCD signal (sum of both A- and B-site components) and the Cu^{2+} interface coating magnetization from the TFY XMCD signal. Right: Temperature dependence of the Fe A- and B-site magnetization determined from the TEY XMCD signal[32].

that an appropriate comparison between the copper coated maghemite nanoparticle samples, we renormalized the XMCD spectra to the TEY XAS spectra. The Fe magnetization for the Cu(0.3 nm)/γ-Fe_2O_3 and Cu(0.5 nm)/γ-Fe_2O_3 nanoparticles (sum of A- and B-site components) decreased with warming, consistent with the observations of the surface and core magnetism behaviour of the atomic Fe magnetism from Mössbauer spectra and the overall magnetism described by the magnetometry and susceptometry. The changes in the Fe magnetism for the Cu(0.3 nm)/γ-Fe_2O_3 and Cu(0.5 nm)/γ-Fe_2O_3 nanoparticles were mirrored by the reduction in the Cu interfacial magnetization over the same range of temperatures. With warming, the Cu elemental magnetization decreased more rapidly, relative to that of Fe, becoming essentially zero by 200 K. The Cu magnetization was a small fraction of the total, therefore these changes in the elemental magnetization would not show in an as pronounced fashion in the magnetometry (e.g. overall magnetism). The effect on the temperature dependence of the elemental magnetism for the Cu(1.0 nm)/γ-Fe_2O_3 nanoparticle sample was readily observed. A significant increase of the Fe magnetization (∼40 % larger at 10 K) was observed. Furthermore, below 50 K, there was little change with temperature. $M_{Fe}(T)$ displayed the same basic $T^{3/2}$ behaviour previously observed in the $M_S(T)$ (Fig. 3.10). In addition, the Cu interfacial magnetism for these nanoparticles was different then that of the thinner copper coated samples. At all temperatures, $M_{Cu}(T)$ was negative and presented little variation with temperature. This change in polarity indicated that the Cu canting had changed (Fe-O-Cu interfacial exchange) and the weaker T dependence may result from an increased amount of interfacial CuO from the increased copper coating thickness so that we observed a more typical antiferromagnetic behaviour. The antiferromagnetic-like reorientation observed here may be the result of an enhanced interfacial exchange coupling similar to that observed in exchange-biased thin films[79]. Figure 3.14 shows the site-specific elemental magnetizations temperature dependence. The variation of the overall Fe magnetization with temperature was mirrored equally by the B-sites. The A-site magnetization was opposite in polarity (antiferromagnetically coupled to the B-site) and showed a small decrease in magnetization between to and 50 K, then becoming essentially unchanged with further warming. In the copper coated maghemite nanoparticles, the Cu magnetization was aligned with the B-site, likely due, in-part, to their larger numbers (∼1.6x) and they canted in the direction of the applied field[80] unlike the A-sites which remain collinear in γ-Fe_2O_3.

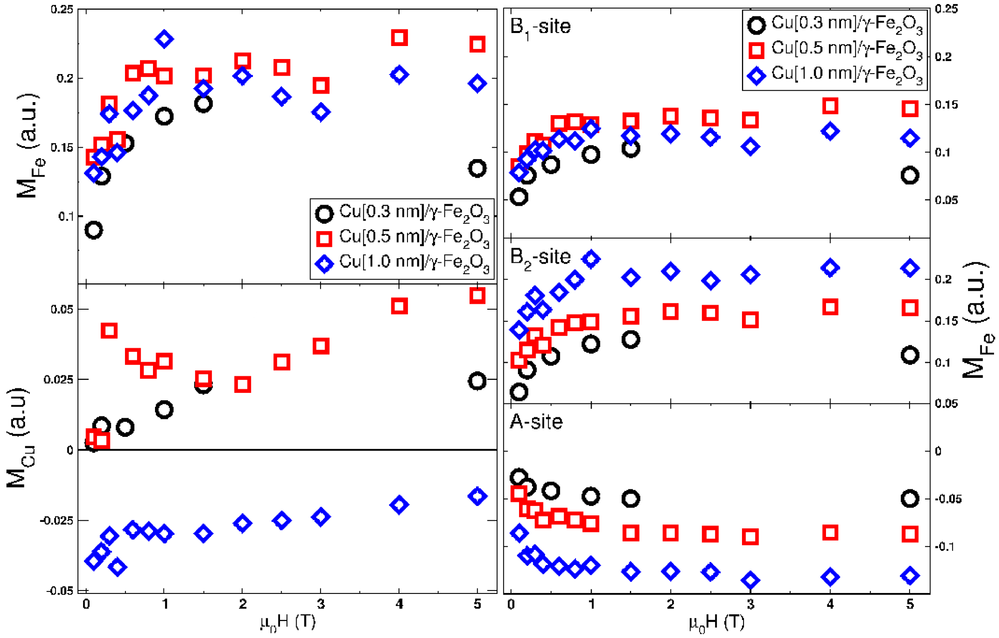

Figure 3.15: Left: Total elemental Fe^{3+} (top) and Cu^{2+} (bottom) magnetization as a function of applied field at 10 K for the three copper coated maghemite samples. Right: Elemental magnetization for the three copper coated maghemite samples of the individual Fe sites: B_1-site(top), B_2-site(middle) and A-site (bottom)[63].

The field dependence of the total elemental Fe and Cu magnetization are shown in figure 3.15. The Fe^{3+} magnetizations for the three copper coated maghemite nanoparticles showed a rapid increase in magnetization followed by a plateau as the Fe^{3+} magnetization became saturated with an applied field ≥ 1 T, in agreement with magnetometry experiments. The elemental Cu^{2+} magnetization for the Cu(0.3 nm)/γ-Fe_2O_3 sample saturated in an applied field of ∼1 T. The Cu(0.5 nm)/γ-Fe_2O_3 nanoparticle sample showed a continuous increase in magnetization which effected directly the Fe^{3+} sites such that they saturated in a slightly larger applied field and had a larger magnetization compared with the Cu(0.3 nm)/γ-Fe_2O_3 nanoparticles. The Cu(1.0 nm)/γ-Fe_2O_3 sample showed a rapid decrease in magnetization up to an applied field of ∼0.5 T, followed by a much more gradual temperature dependence, indicating a reduction in canting of the Cu^{2+} moments and a return to antiferromagnetic behaviour.

3.5 Conclusions

We have synthesized copper coated maghemite nanoparticles with copper coatings of thicknesses between 0.3 and 1.0 nm. At the interface between the γ-Fe_2O_3 core and Cu shell, a thin ≤ 0.2 Å(upper limit set by HRTEM) layer of CuO has formed spontaneously. The Cu^{2+} in the interfacial CuO layer alters directly the γ-Fe_2O_3 cores surface Fe spins allowing for the recapture of these once frustrated spins. This process allows for the magnetization of the γ-Fe_2O_3 core to be fully realized, as the effects of the magnetically dead surface layer from the frustrated surface spins were reduced. A complete understanding of the intraparticle interactions that mediate these changes in the magnetization is necessary in order to fully realize the potential of these nanoparticle systems. To further this goal, the intraparticle interactions resulting from an inorganic shell coating magnetic nanoparticles will be explored.

Chapter 4

Metallic Nanoparticles Coated with an Inorganic Shell

4.1 Introduction

Current trends in electronic components point toward their continuous decrease in size[81; 82], along with nanoparticles and their composites being developed for many technological applications[83]. Of significant interest, superparamagnetic nanoparticles for applications such as low-loss transformer cores[84; 85], ultra-high density computer memories[3], and rare-earth-free permanent magnets[86]. Quite often, to stabilize these nanoparticles within their composite materials, inorganic anti-diffusion layers are used, such as a silica matrix[87; 88; 89] or shell[90; 91; 92]. However, a detailed study of the effects of such intimate contact between metallic nanoparticle and the assumed inert inorganic anti-diffusion layer has been lacking. As discussed in Chapter 1, the description of the overall magnetism observed in a core/shell nanoparticle is typically that of an interpolation from a distinct core and shell, a direct result of the difficulties in determining uniquely the microstructure and composition of the interface. In this chapter, we present our work on undoped and V-doped SiO_2/FeCo nanoparticles, where vanadium has been added in small quantities to improve the ductility of the FeCo nanoparticle core for processing, and the effects on the magnetism of even a 2% *at. wt.* V-doping are explored. What are nominally assumed to be structurally simple core/shell magnetic nanoparticles, with distinct cores and shells, are in fact complex multiphase nanostructures containing a spontaneously formed magnetically active metal silicate interfacial layer.

4.2 Nanoparticle Synthesis and Preparation

Nanoparticles of binary FeCo and V-doped FeCo coated with SiO_2 were synthesized using a scalable metal halide reduction synthesis. The parent undoped and V-doped FeCo nanoparticles for comparison with the SiO_2 coated nanoparticles were also synthesized. All metal salts, reagents, and solvents were purchased from Sigma-Aldrich and used as received. All water used was DI water, and ethanol was >99.5% pure anhydrous 200 proof. All solvents used were nitrogen bubbled to remove any trapped oxygen to prevent unintended oxidation of the undoped and V-doped FeCo nanoparticles prior to the addition of the silica shells. A five neck flask was attached to an argon Schlenk line to provide an oxygen free environment for the nanoparticle synthesis. A solution of 4.200 g of $FeCl_2{\cdot}4H_2O$, 4.764 g of $CoCl_2{\cdot}6H_2O$, 0.199 g of NaOH, and 2.394 g of tetraoctylammonium bromide were added to 210 mL of ethanol (0.0763 g of VCl_3 was added to create 2% at. wt. V-doped nanoparticles). The metal salt solution was added to the flask and stirred vigorously using a Teflon coated paddle stirrer under Ar to ensure there was no trapped O_2 present. The disassociation of the metal salts was catalyzed by adding slowly a solution of 4.864 g of $NaBH_4$ dissolved in 180 mL of ethanol. The product was then washed several times with a 400 mL mixture of 30 % H_2O and 70 % Ethanol to remove any unreacted salts.

The silica coating process was accomplished using a modified Stöber reaction. The synthesized nanoparticles were first dispersed in a mixture of 252 mL H_2O and 3.3 mL of triethylamine (TEA), a catalyst for the silica coating process. To this, a solution of 596 μL tetraethyl orthosilicate (TEOS) in 156 mL of ethanol was added slowly and allowed to react, coating the nanoparticles completely in silica. The duration of the reaction was varied, allowing for the systematic control of the thickness of the silica shells. A one minute reaction time produced a shell of $\sim$3 nm thick, whilst reactions of 10 minutes and 20 minutes produced shells of $\sim$4 nm and $\sim$6 nm thickness, respectively.

The final product was washed several times with ethanol and separated magnetically to remove any unreacted reagents. The washed nanoparticles were then transfered to a glove box with an argon atmosphere and allowed to dry completely for $>$ 12 hours at $\sim$50 °C. This unique synthesis allows for pristine undoped and V-doped FeCo and SiO_2/FeCo nanoparticles. Oxygen contamination did not occur as such an event would have been readily observable from the magnetometry (see below), and as these nanoparticles are highly pyrophoric, the oxidation would have resulted in a rapid exothermic reaction. Furthermore, the nanoparticles undergo a colour change upon oxidation, changing from a deep black to a light grey. This colour change was observable even after only a few seconds of air exposure.

Samples for x-ray diffraction were prepared by covering completely the nanoparticles with polyamide tape to prevent oxidation during the experiment. Samples for transmission electron microscopy (TEM) experiments were prepared by using a controlled oxidation method by first freezing a small amount of sample in liquid nitrogen to prevent nanoparticle growth when exposed to the air resulting from the exothermic pyrophoric reaction. This “low temperature oxidation” prevents nanoparticle growth, thus, the sizes obtained are comparable to those of the pristine nanoparticles. X-ray photoelectron spectroscopy (XPS) and x-ray absorption spectroscopy (XAS) samples were transfered from an argon glove-box using an air free sample chamber to the PHI Versaprobe II and to the liquid helium cryostat, respectively. Magnetometry and susceptometry samples were prepared by encapsulating completely the nanoparticles with TEM resin within a polycarbonate gelcap.

4.3 Composition and Structure

To determine the average nanoparticle diameter and the distribution of diameters, TEM images were collected by Dr. Taghi Darroudi of the Electron Microscope Facility at Clemson University using a Hitachi 9500 operating at 120 kV. Figure 4.1 shows the collected TEM images of the FeCo and V-doped FeCo nanoparticles with and without SiO_2 shells. Analysis of the TEM images was done using ImageJ[42] to determine the average nanoparticle diameter and the distribution of diameters from fits of the data to a log-normal size distribution. All TEM images showed large agglomerations of nanoparticles which was to be expected as the synthesis was designed to fabricate nanoparticles in gram quantities necessary for applications (i.e. synthesis was performed in the concentrated reagent limit). The typical “frog egg”-like TEM image often seen in publication (e.g. Desautels, *et. al.*[65; 32]) are of nanoparticles that were synthesized in the dilute reagent limit using very strong surfactants (i.e. Oleic acid) to prevent agglomeration specifically, however, the yield of these syntheses is on the order of micro-gram quantities and it is nearly impossible to remove all of the surfactant[93]. Therefore, for applications, this dilute limit synthesis is not feasible. For the SiO_2 coated FeCo and V-doped FeCo nanoparticles, the difference in contrast (difference in atomic Z) between the nanoparticle core and SiO_2 was used to determine the average diameter of the nanoparticles and the average thickness of the SiO_2 shells. For all samples, the average diameter was determined to be 4 ± 1 nm, indicating a high degree of reproducibility of the nanoparticle core synthesis. The thickness of the SiO_2 shells which coated completely the undoped and V-doped FeCo nanoparticles was found to be 3 ± 1, 4 ± 1, 6 ± 1 (FeCo), and 5 ± 1 nm (V-doped FeCo) for the respective Stöber reaction times. The samples will be referred to as SiO_2(3 nm)/FeCo, SiO_2(4 nm)/FeCo, SiO_2(6 nm)/FeCo, and SiO_2(5 nm)/$Fe_{49}Co_{49}V_2$

X-ray diffraction patterns were collected between 10° and 120° 2θ using the standard Bragg-Brantano geometry on the Bruker diffractometer. The XRD patterns, for all the nanoparticle samples, indicated that the undoped and V-doped FeCo nanoparticles with and without SiO_2 shells were amorphous. Figure 4.2 shows the typical diffraction patterns for SiO_2 coated and uncoated FeCo nanoparticles. All samples show a large broad reflection centred at 20° 2θ from the polyamide tape used to ensure the samples remain uncontaminated by oxygen. In addition, the SiO_2 amorphous reflections occur at a similar 2θ. Low intensity reflections broadened significantly were

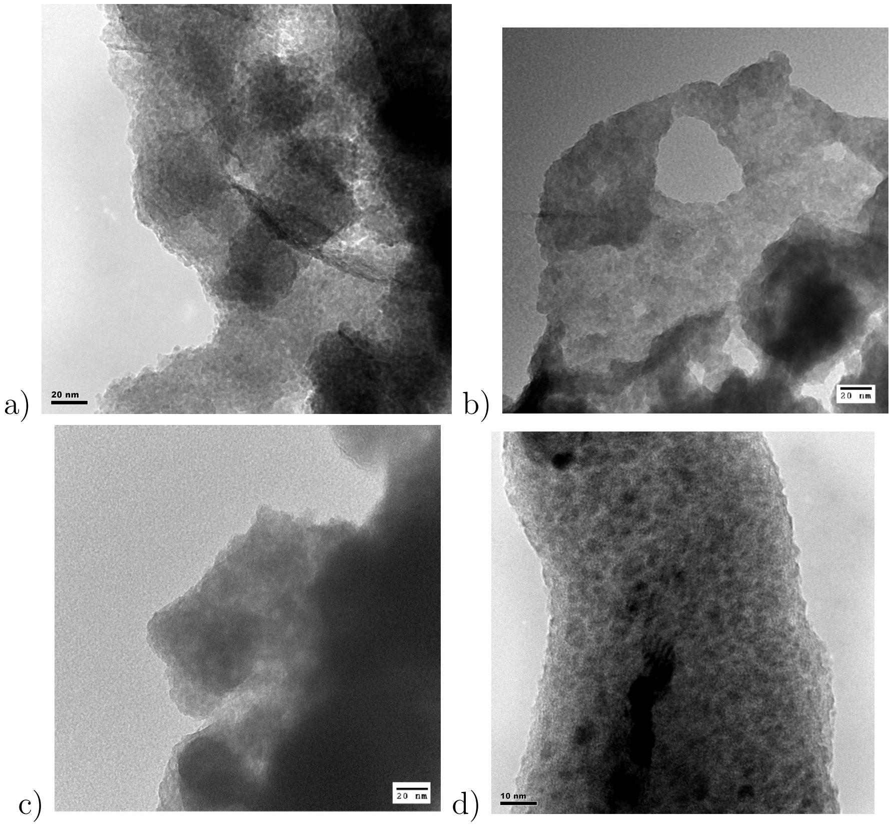

Figure 4.1: Bright-field TEM images for a) FeCo/SiO_2(3 nm), b) FeCo/SiO_2(4 nm), c) FeCo/SiO_2(6 nm), and d) FeCoV/SiO_2(5 nm)

observed at 2θ angles in agreement with the bulk Im$\bar{3}$m phase of FeCo (similar reflections were observed in the V-doped FeCo and SiO_2/FeCo nanoparticles). These reflections were only observable as a change in the slope of the background, as expected for amorphous nanoparticles.

To determine the composition of the undoped and V-doped FeCo/SiO_2 nanoparticles (and their parent nanoparticles), x-ray photoelectron spectroscopy (XPS) experiments were performed. XPS is well suited to determine the oxidation state and coordination environment from the measured kinetic energy of the core electrons ejected from the surface (top 20 atomic layers, approximately) of the sample when

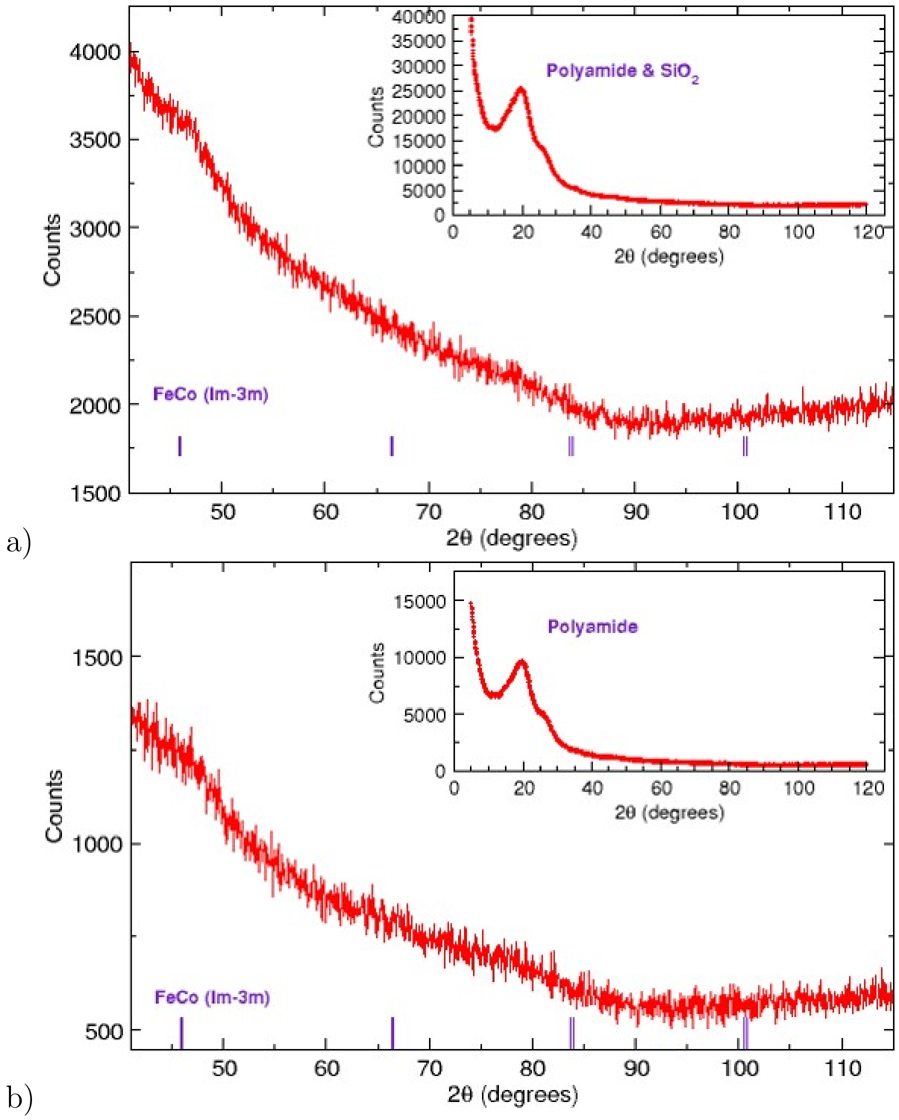

Figure 4.2: X-ray diffraction images of undoped and V-doped FeCo nanoparticles

compared with a database of calculated binding energies for different compounds (e.g. NIST XPS Database[46]). Spectra collected of the Fe, Co, and V 2p photoelectrons are shown in figures 4.3. To determine uniquely the binding energies, E_{bind}, the spectra were corrected for charging effects using the 285 eV C 1s peak[94] from adsorbed carbon on the surface of the samples always present. Quantitative analysis of the collected spectra was performed by fitting the spectral features with individual Gaussian-Lorentzian peaks with constrained widths and shapes with an iterated Shirley background function[95]. The collected Fe spectra also showed the characteristic metallic Co Auger peak (the Co Auger peak overlaps with the Fe photoelectron peaks and *vice versa* when using an Al K_α source). In addition to these spectral features, we observed additional peaks representative of Fe in a higher oxidation state (e.g. Fe^{3+}); a result of the spontaneous formation of Fe-silicates at the interface between the FeCo or V-doped FeCo nanoparticles and the SiO_2 surrounding them. Similar spectral features were observed in the Co spectra (Fig. 4.3); metallic Co and Co-silicates with no observed cobalt oxides. A comparison of the relative integrated areas of metallic Fe and Co indicated that Co-silicate formed preferentially over Fe-silicate (see Table 4.1). Unlike the Fe and Co 2p XPS spectra, the V spectra (Fig 4.3) did not show the characteristic metallic peak at ∼712 eV. The observed features were from a higher oxidation state (e.g. V^{4+}). A comparison of the V spectra for the uncoated and coated nanoparticles yields interesting results. For the uncoated nanoparticles, the V spectrum appears to be a mixture of V^{2+} and V^{3+} likely a result of the altered electronic environment of the vanadium atom due to the alloying with Fe or Co. However, the coated V-doped nanoparticles spectrum shows only V^{4+}. This drastic change in vanadium oxidation state points towards the silica coating process "sucking" all the V from within the doped nanoparticle onto the surface where it is being oxidized completely by the SiO_2 shell. For comparison with the SiO_2 coated undoped and V-doped FeCo nanoparticles, the parent nanoparticles XPS spectra (Fig. 4.3) show the characteristic metallic Fe and Co spectral features along with the representative Auger peaks. There remains spectral features often attributed to higher oxidation states of Fe and Co, however, there was no experimental evidence for oxygen contamination of these nanoparticle samples (as discussed above), therefore, these higher oxidation state spectral features must be the result of the alloying itself. It has been shown previously that alloying of Fe and Co results in a change in the local chemical environment surrounding the Fe nucleus and this effect is proportional to the relative amount of Co in the system[96]. A similar affect on the Co atoms is therefore inferred. Also, as will be discussed in Chapter 5, a similar effect was observed for alloying for Fe and Cu. This change in chemical environment would alter the binding energies between Fe-Fe, Fe-Co, Fe-V, and Co-V atoms, resulting in a shift in the XPS spectral features.

X-ray absorption spectra (XAS) were collected over the $L_{3,2}$ transition edges of Fe (700-740 eV), Co (770-815 eV), and V (505-530 eV) for the undoped and doped FeCo and FeCo/SiO_2 coated nanoparticles. To identify the observed spectral features (e.g. their oxidation state and coordination environment) beyond matching our spectra with spectra collected previously, simulations of the XAS spectra were performed using CTM4XAS[53]. The simulations were carried out using a fourfold symmetry

Table 4.1: Relative integrated areas of the metallic Fe and Co spectral components from quantitative analysis of the XPS spectra

	% Area Fe	% Area Co
FeCo/SiO_2(3 nm)	7 ± 1	27 ± 1
FeCo/SiO_2(4 nm)	14 ± 1	40 ± 1
FeCo/SiO_2(6 nm)	7 ± 1	28 ± 1

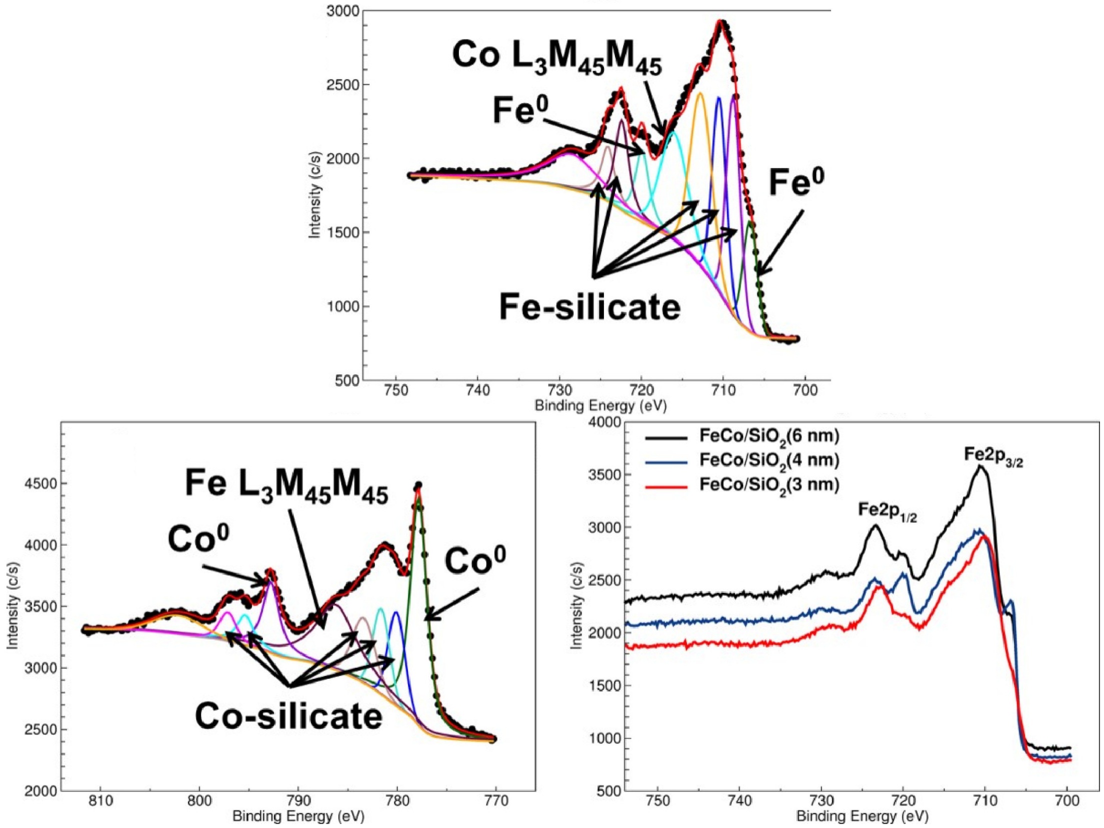

Figure 4.3: X-ray photoelectron spectra for the undoped and V-doped FeCo/SiO$_2$ nanoparticles.

(C$_4$), which was necessary in order to obtain XMCD spectra, and crystal field parameters of 10Dq = 1.2 eV[97] and an exchange field splitting of 10 meV. The simulated spectra for Fe^{3+} and Co^{2+} in addition to collected metallic Fe and Co spectra[97] were used to provide evidence for these species in our collected XAS spectra. The Fe XAS spectra for the parent FeCo and V-doped FeCo nanoparticles showed peaks centred at ~708 eV and ~721 eV from the L$_3$ ($2p^{3/2} \rightarrow 3d$) and L$_2$ ($2p^{1/2} \rightarrow 3d$) transitions, respectively. The Fe L$_3$ transition (Fig. 4.4) for both undoped and V-doped FeCo nanoparticles showed two spectral features. A large peak centred at 707 eV is followed by a much smaller peak at 710 eV. From the simulations, the observed L$_3$

edge comprises a component from metallic Fe (Fe^0) and octahedral (O_h) Fe^{3+}. The Fe^{3+} component is the result of a change in the electronic environment around the Fe atoms, as seen in XPS (described above), as no oxygen contamination was observed. Similar spectral features were observed for the Co L_3 spectra (Fig. 4.5). However, unlike the Fe spectrum which contained Fe^{3+}, the Co spectra appears to contain O_h Co^{2+}. In both cases, the O_h component is in the minority. The V L_3 transition for the doped FeCo nanoparticles appears to consist of a combination of V^{2+} and V^{3+}, in agreement with XPS results presented above.

The Fe XAS spectra for both the undoped and V-doped SiO_2/FeCo nanoparticles (Fig. 4.4) showed similar structures at the $L_{3,2}$ transitions as their parent nanoparticles. However, unlike the parent nanoparticles, the O_h components were the majority phase (seen as an increased peak intensity). The Fe XAS spectra (Fig. 4.4) shows that the O_h component decreases in intensity with an increase in the SiO_2 thickness, indicative of the preferred formation of Co-silicates, in agreement with the XPS results discussed above. Fe-oxides which contain Fe^{3+} such as maghemite or magnetite were not observed here as spectral features unique to these oxides were absent. Magnetite contains Fe^{2+} which has a very different spectrum compared to Fe^{3+} and maghemite (see Ch. 3) has a unique spectral pre-peak feature absent here. To compare the relative change in the ratio of metallic Fe to O_h Fe^{3+}, the spectra were normalized to the Fe^{3+} peak and matched to a linear combination of the O_h and metallic Fe spectra. The use of the previously collected metallic Fe spectrum (and Co spectrum used below) allows for only a qualitative comparison between samples to be performed as the experimental setup will differ resulting in instrument dependent variations in

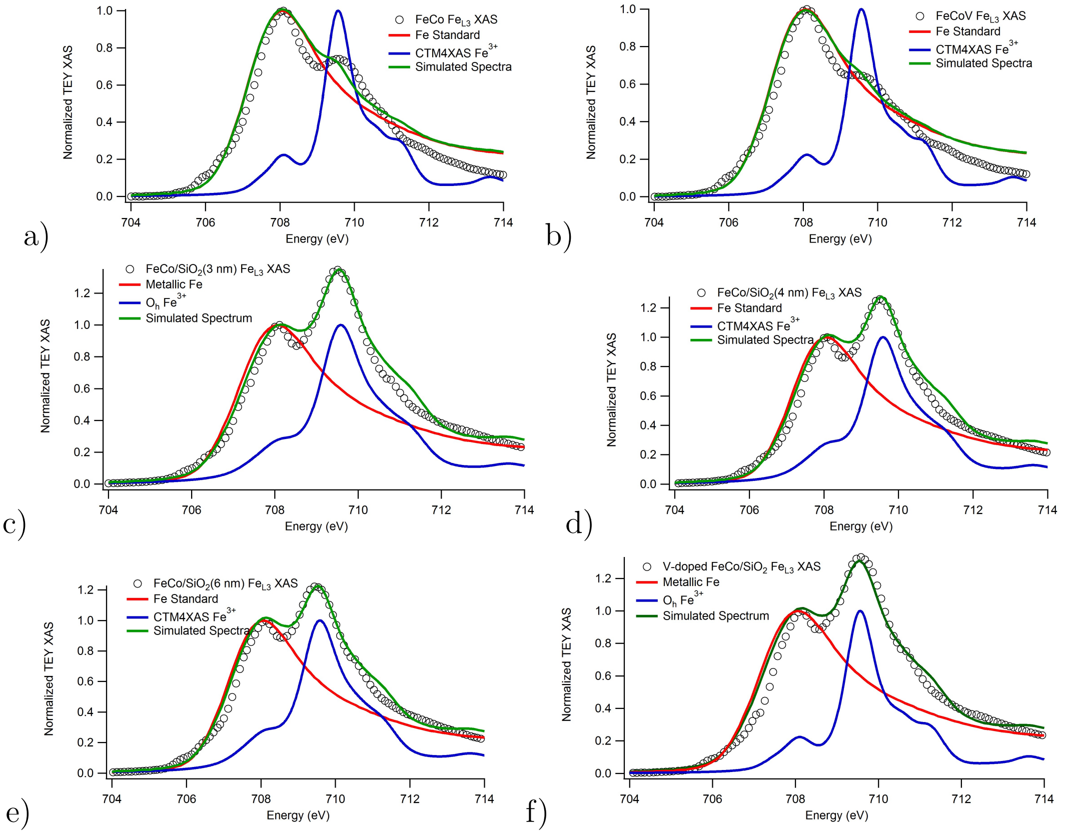

Figure 4.4: X-ray absorption spectra collected at the Fe L_3 transition edge. Black circles are the collected XAS spectra. Solid green lines are the matched spectrum. Blue lines are the simulated octahedral Fe^{3+} spectrum. Red lines are the metallic Fe standard. a) FeCo nanoparticles b) FeCoV nanoparticles c) FeCo/SiO_2(3 nm) nanoparticles d) FeCo/SiO_2(4 nm) nanoparticles e) FeCo/SiO_2(6 nm) nanoparticles f) FeCoV/SiO_2(5 nm) nanoparticles

the collected spectra (e.g. spectral width broadening). Similar spectral features were observed for the Co spectra (Fig. 4.5); peaks at ∼779 eV and ∼794 eV from the L_3 and L_2 transitions, respectively. Simulations for O_h Co^{2+} and collected metallic Co were used to match to the Co XAS experimental data. To determine the evolution of the O_h component with SiO_2 content, the Co spectra were normalized to the Co^{2+} component and a linear combination of the simulated and metallic spectra were matched to the Co XAS experimental data. Unlike the results found for the Fe spec-

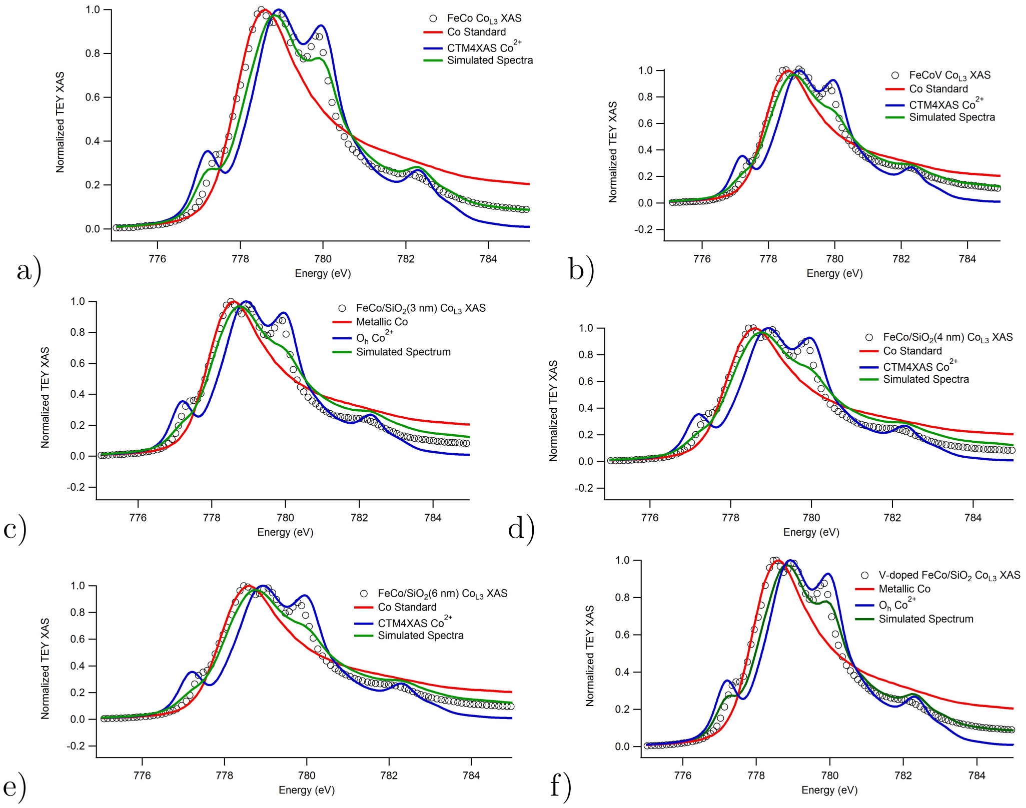

Figure 4.5: X-ray absorption spectra collected at the Co L_3 transition edge. Black circles are the collected XAS spectra. Solid green lines are the matched spectrum. Blue lines are the simulated octahedral Co^{2+} spectrum. Red lines are the metallic Fe standard. a) FeCo nanoparticles b) FeCoV nanoparticles c) FeCo/SiO_2(3 nm) nanoparticles d) FeCo/SiO_2(4 nm) nanoparticles e) FeCo/SiO_2(6 nm) nanoparticles f) FeCoV/SiO_2(5 nm) nanoparticles

tra, the O_h Co^{2+} component increased with SiO_2 content indicating that the amount of Co-silicates increased with increasing SiO_2 content and formed preferentially over the Fe-silicates, in agreement with the XPS results discussed previously.

A similar approach was taken for the V $L_{3,2}$ edge transition in the V-doped FeCo/SiO_2 and parent nanoparticles (Fig. 4.6). However, unlike the Fe and Co spectra, there was no indication of V metal in the collected spectra, in agreement with XPS experiments. The V L_3 transition for the parent nanoparticles (Fig. 4.6) showed

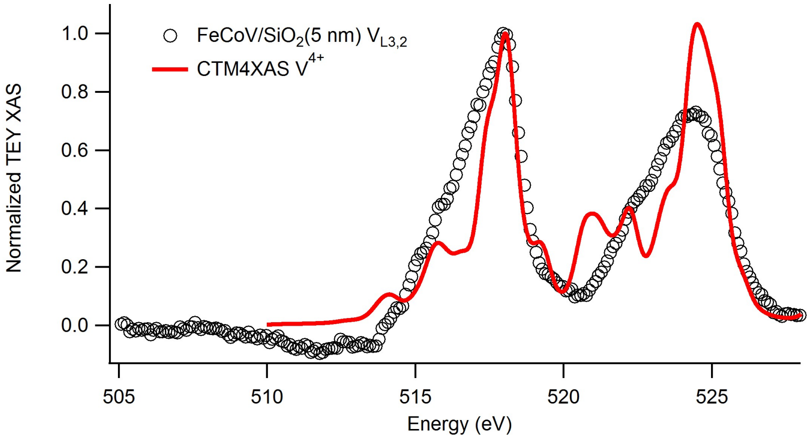

a)

Figure 4.6: X-ray absorption spectra collected at the V $L_{3,2}$ transition edge for the V-doped SiO_2/FeCo nanoparticles. Black circles are the collected XAS spectra. Red lines is the simulated V^{4+} spectrum.

the presence of spectral features consistent with V^{2+} or V^{3+} from the alloying process. The SiO_2 coated V-doped FeCo nanoparticles showed only the V^{4+} component. This change is the result of all of the V present within the FeCo nanoparticle being “sucked” to the surface and interacting with the SiO_2, and being further oxidized. The V spectrum of the SiO_2 coated nanoparticles was consistent with simulated data for O_h V^{4+}, also indicating that the silica deposition on the nanoparticle surface had induced further oxidation of the V atoms. The differences between the simulated and experimental spectra could be the result of instrumental linewidth broadening.

4.4 Magnetism

We have seen previously with nanoparticles coated with a metal shell (Ch. 3) how significant an impact on the magnetism the interface between a nanoparticle core and shell can have. For undoped and V-doped FeCo nanoparticles coated with SiO_2,

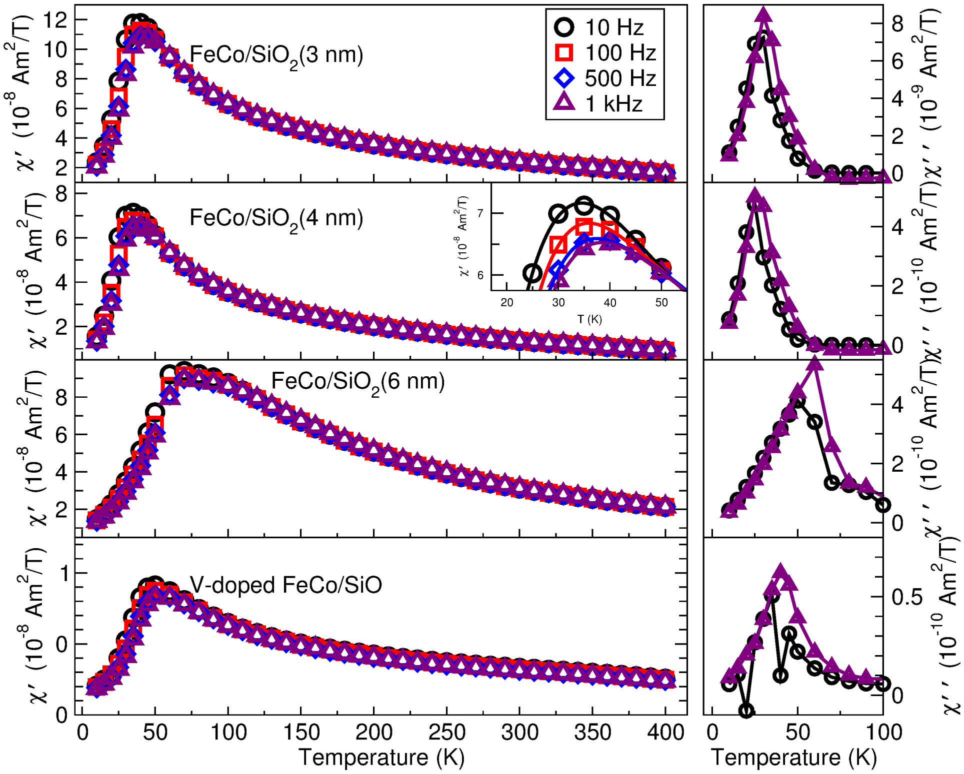

Figure 4.7: Left: in-phase *ac* susceptibility as a function of temperature for the undoped and V-doped FeCo/SiO$_2$ nanoparticles. The inset for FeCo/SiO$_2$(4 nm) highlights the frequency dependence of the maximum in the susceptibility Right: out-of-phase *ac* susceptibility as a function of temperature.

an interfacial metal silicate layer formed spontaneously during the coating process. It follows from the previous nanoparticle study that this interfacial layer will affect significantly the magnetism. To verify this, a combination of magnetometry, susceptometry and element specific magnetic circular dichroism experiments were performed showing the significant effects this interfacial phase has on the magnetism. Below is a detailed description of these results indicating how fundamental the interface between core and shell can be for the complete understanding of the magnetism of a core/shell nanoparticle system.

ac susceptibility experiments ($\chi_{AC}(T,\nu)$) using a 0.25 mT drive field at frequen-

Table 4.2: Blocking temperatures for the undoped and V-doped SiO_2/FeCo nanoparticles

	T_B (K)
FeCo/SiO_2(3 nm)	40 ± 3
FeCo/SiO_2(4 nm)	35 ± 3
FeCo/SiO_2(6 nm)	70 ± 3
FeCoV/SiO_2(5 nm)	45 ± 3

cies between 10 and 1000 Hz (Fig. 4.7)were performed to determine the effects of the interfacial metal silicates on the overall magnetocrystalline anisotropy of the core/shell nanoparticle system. All undoped and V-doped FeCo/SiO_2 nanoparticles showed, after an initial zero-field cooling (ZFC) down to 10 K, a gradual increase in the in-phase component of the susceptibility, $\chi'_{AC}(T,\nu)$ and mirrored in the out-of-phase component, $\chi''_{AC}(T,\nu)$, with warming as thermal energy (k_BT) was added to the system. The increased energy within the system enabled the single-domain nanoparticles' magnetizations to oscillate more rapidly. At the nanoparticles' blocking temperature (Table 4.2), which was determined from the maximum in the frequency-dependent $\chi'_{AC}(T,\nu)$ and $\chi''_{AC}(T,\nu)$, the nanoparticles' magnetizations became superparamagnetic, undergoing 180° spin-flips. With the further addition of thermal energy, these 180° spin-flips occurred more often, resulting in a decreased time-depend averaged nanoparticle magnetization observed as the gradual reduction in the measured $\chi_{AC}(T)$. Furthermore, no observable frequency dependence remained since these superparamagnetic fluctuations occurred beyond the measuring time window of the experiment. Interparticle interactions in the undoped and

V-doped FeCo/SiO_2 nanoparticle systems were quite strong (observed in the temperature dependence of the *dc* susceptibility, described below). Attempts to describe the magnetocrystalline anisotropy using the Nèel-Brown model[24] resulted in non-physical attempt frequencies (e.g. 5×10^{18} Hz) due to the interparticle distances set by the SiO_2 shell thicknesses. Therefore, the typical Neél-Arrhenius law could not be applied to obtain the magnetocrystalline anisotropy from the frequency dependence of T_B. However, results observed over the entire range of $T_B(\nu)$ from *dc* ($\nu = 0.01$ Hz) and *ac* (ν = 10, 100, 500, and 1000 Hz) susceptibilities using the Vogel-Fulcher law[98], $\nu = \nu_0 e^{-[KV/k_B(T_B - T_0)]}$, permitted the nanoparticles' overall anisotropy, K, to be calculated. Here, T_0 describes the local nanoparticles' magnetization correlation temperature (the onset temperature of these correlations or interactions among particle magnetizations), ν_0 represents the attempt frequency of the 180° spin-flips, and KV is the energy barrier to these spin-flips. As the nanoparticle volumes are known (from TEM images), the overall anisotropies, K, were calculated from the above fit (see Table 4.3). For the Vogel-Fulcher analysis, the $T_B(\nu)$'s used were determined from the maximum of a Chebychev polynomial used to describe the temperature evolution near the maximum of $\chi'_{AC}(T)$ for each frequency measured. This approach allowed for a consistent method for determining T_B for all four SiO_2 coated nanoparticles. The overall K values were then calculated from a fit of the Vogel-Fulcher law to a plot of $1/T_B$ vs $\ln(\nu)$ (Fig. 4.8)

The fitted attempt frequency, $\nu_0 \approx 4 \times 10^{12}$ Hz, was typical for nanoparticles[1]. The progression of T_0 to larger values with an increased SiO_2 shell thickness was to be expected as $T_0 \sim M_S^2$ and M_S was observed to increase with SiO_2 shell

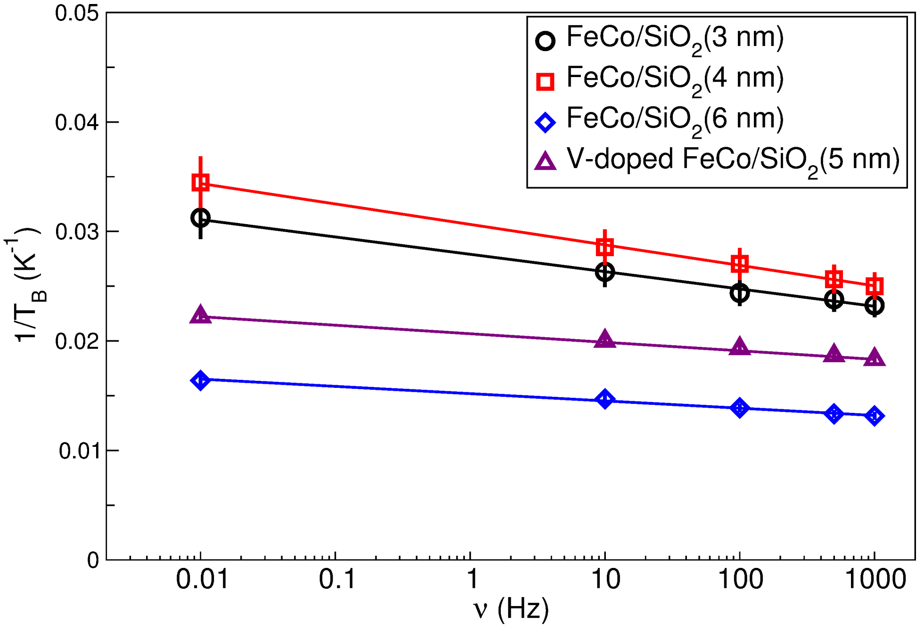

Figure 4.8: Plot of T_B^{-1} as a function of $\ln \nu$ and the straight line is a fit to the data as described in the text.

thickness (described below). Clearly, the results from the above analysis indicate that the overall anisotropy increased as the thickness of the SiO_2 shell increased, of which a component from the interfacial anisotropy (responsible for the high field paramagnetic susceptibility, see below) increased, a clear indication that the metal silicate interfacial layer affected significantly the overall magnetism of the undoped

Table 4.3: Fit parameters from Vogel-Fulcher analysis of $\chi'_{AC}(T)$ data

	K (10^5 J/m^3)	T_0 (K)
FeCo/SiO$_2$(3 nm)	3.2 ± 0.2	9 ± 1
FeCo/SiO$_2$(4 nm)	3.0 ± 0.2	8 ± 1
FeCo/SiO$_2$(6 nm)	4.5 ± 0.2	29 ± 1
FeCoV/SiO$_2$(5 nm)	2.6 ± 0.2	26.5 ± 0.5

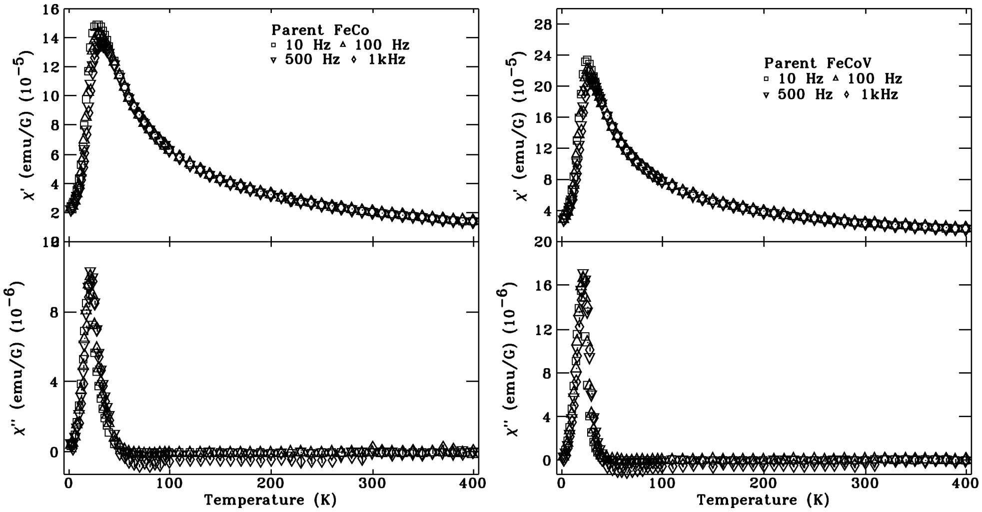

Figure 4.9: *ac* susceptibility of parent FeCo and FeCoV nanoparticles.

and V-doped FeCo nanoparticle core. As a comparison, undoped and V-doped FeCo nanoparticles χ_{AC}(T,ν) seen in figure 4.9 showed a similar temperature dependence to the SiO_2 coated nanoparticles, however, a reduced T_B and frequency dependence from the increased interparticle interactions was observed.

In addition to the above description, low field (5 mT) *dc* susceptibility (Fig. 4.10 and Fig. 4.11) $\chi_{DC}(T)$ experiments were performed. The susceptibility was measured in both the ZFC ($\chi_{DC}^{ZFC}(T)$) and FC ($\chi_{DC}^{FC}(T)$) states. Initially, the nanoparticle systems were cooled from 400 K, a temperature well above the superparamagnetic blocking temperature (T_B) ensuring that the nanoparticles' magnetizations were oriented randomly along their easy axes (set by the intrinsic magnetocrystalline anisotropy) so that no preferred orientation was set[1]. With warming (the addition of thermal energy) from 2 K, a rapid increase in the measured $\chi_{DC}^{ZFC}(T)$ occurred as the nanoparticles' magnetizations aligned with the applied magnetic field. With additional warming, the nanoparticles' magnetization underwent 180° spin-flips with

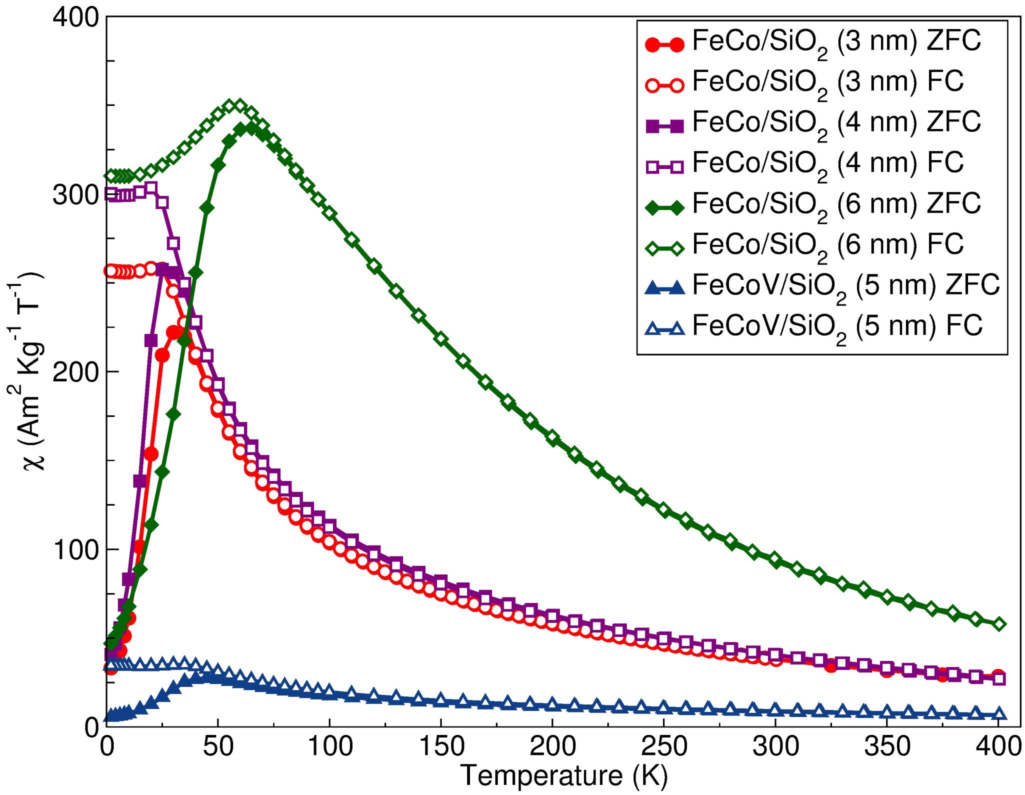

Figure 4.10: *dc* susceptibility for the undoped and V-doped FeCo/SiO$_2$ nanoparticles.

respect to their intrinsic magnetocrystalline anisotropy axis, occurring more rapid then the time-scale of the measurement resulting in a maximum in $\chi_{DC}^{ZFC}(T)$. Again, as further warming occurred, the larger nanoparticles became superparamagnetic and a decrease in $\chi_{DC}^{ZFC}(T)$ was observed as the time-averaged measured susceptibility decreased. This temperature evolution of the $\chi_{DC}^{ZFC}(T)$ was observed for the uncoated and SiO$_2$ coated, undoped and V-doped, FeCo nanoparticles. In general, for non-interacting single-domain nanoparticles, T_B is indicated by the maximum in $\chi_{DC}^{ZFC}(T)$ = $\chi_{DC}^{FC}(T)$. As all of the nanoparticle systems studied here have a similar size distribution which indicated that they were reasonably monodisperse (from TEM), the observed differences between $\chi_{DC}^{ZFC}(T)$ and $\chi_{DC}^{FC}(T)$ around what should be a T_B must be the result of dipole-dipole interactions occurring between the nanoparticles. The observed maxima in $\chi_{DC}^{ZFC}(T)$ and $\chi_{DC}^{FC}(T)$, T_P, would therefore be representative of the temperature where the dipole-dipole interaction energies are equivalent to that provided by the applied field to reorient the nanoparticles' magnetization at that temperature. The observed T_B's were determined from the maxima in $\chi_{DC}^{ZFC}(T)$. T_B's of 40, 35, 45, and 70 K were determined for the undoped SiO_2(3 nm)/FeCo, SiO_2(4 nm)/FeCo, SiO_2(6 nm)/FeCo, and V-doped SiO_2(5 nm)/FeCo nanoparticles, respectively. The T_B's were observed to increase with SiO_2 shell thickness, an indicator of an increased magnetic anisotropy due to the metal silicate interfacial layer which likely altered the surface spin environment of the undoped and V-doped FeCo nanoparticle cores. A reduced surface spin disorder of the undoped and V-doped FeCo nanoparticle cores of the SiO_2/FeCo would result in an increased magnetic volume compared to the uncoated nanoparticles where the surface moments were disordered. The observed spin-glass-like behaviour of $\chi_{DC}^{FC}(T)$ (e.g. the decreased $\chi_{DC}^{FC}(T)$ below T_B) is likely an indication of a combination of spin-glass-like disorder resulting from the random nature of the nanoparticle orientations (magnetizations during ZFC) and interparticle interactions[1; 99]. In addition, as the thickness of the silica shells was increased so to was the total volume of the interfacial metal silicate phase. As a result, the interfacial spins suffered further magnetic frustrated interactions.

Hysteresis loops (Fig. 4.12) were collected for the undoped and V-doped FeCo/SiO_2 nanoparticles after initially field-cooling with an applied field of 5 T from 300 K (a temperature well above T_B). Field-cooling was done to establish whether even a monolayer of Fe-, Co-, or V-oxide not otherwise associated with a silicate structure,

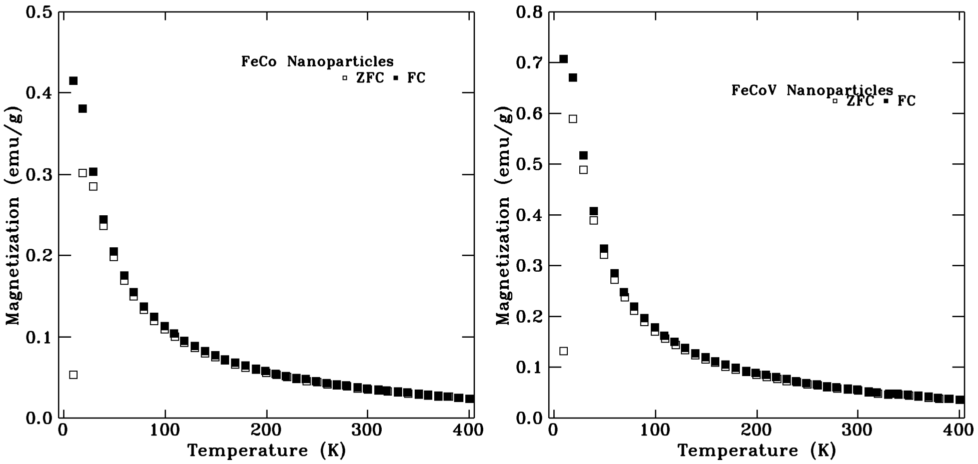

Figure 4.11: *dc* susceptibility of parent FeCo and FeCoV nanoparticles.

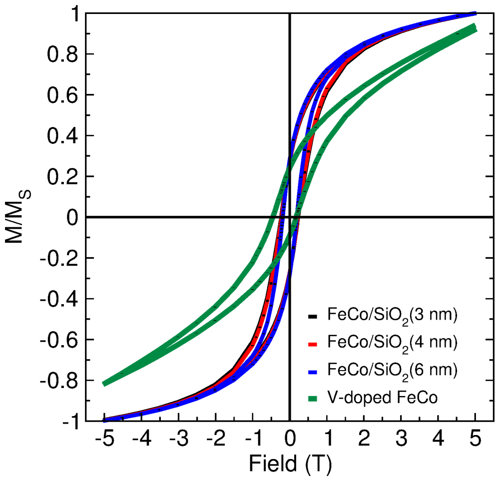

Figure 4.12: Magnetization as a function of field normalized to the saturation magnetization at 5 K.

had formed around the FeCo nanoparticles' core. Such an oxidation would have resulted in an exchange bias field shift ($H_{C1} \neq H_{C2}$) of the collected hysteresis loops; a measurable exchange bias field shift was observed for only the V-doped FeCo/SiO$_2$ nanoparticles (Fig. 4.13). The lack of an exchange bias field shift for the undoped FeCo/SiO$_2$ nanoparticles indicated clearly that oxidation had not occurred from a source other then the SiO_2 shell and that the Fe-O-Co interfacial bonds were sufficiently disordered to keep a ferrimagnetic or antiferromagnetic phase from forming. Interestingly, the hysteresis loops of the undoped and V-doped FeCo/SiO_2 nanoparticles had a paramagnetic-like component at high fields, attributable to a large interfacial anisotropy[100]. At applied fields larger then those needed to saturate the nanoparticle systems, any measured susceptibility reflects only the paramagnetic contribution (no diamagnetic contribution was observed). A small increase in the high-field susceptibility with increased SiO_2 shell thickness was measured (see Table 4.4) indicative of a large interfacial anisotropy. For these undoped and V-doped FeCo/SiO_2 nanoparticles, the SiO_2 shells represent ~80% of the mass and ~90% of the volume, indicating that the diamagnetic contribution from the SiO_2 shells was being suppressed by the paramagnetic/ferromagnetic-like magnetization of the nanoparticles. We used a modified Bloch $T^{3/2}$ law that incorporated a term describing the temperature at which the surface spins freeze (T_F) to describe the temperature dependence of M_S[30]. We observed that for the undoped FeCo/SiO_2 nanoparticles, $M_S(T)$ was well described by

$$\frac{M_S(T)}{M_S(0)} = (1 - BT^{3/2}) \tag{4.1}$$

where B was the Bloch constant and where $B \propto 1/J$ with J representing the exchange constant[71] ($J \propto T_C$). For the V-doped SiO_2/FeCo nanoparticles, an exponential term, Ae^{-T/T_F}, with A a phenomenological constant that scales with the relative amount of frozen surface moments[30] compared with magnetically ordered core moments, was necessary to describe fully the observed $M_S(T)$ (Fig. 4.14). Results of the above description of the $M_S(0)$ are shown in table 4.4. As the thickness

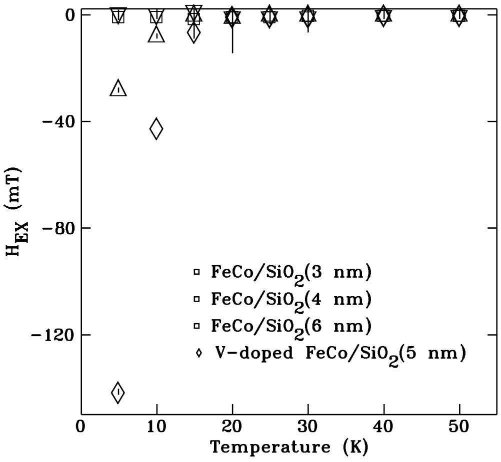

Figure 4.13: Exchange bias field shift for undoped and V-doped FeCo/SiO_2 nanoparticles.

of the SiO_2 shell increased, $M_S(T)$ increased as well. The values obtained here are similar to typical bulk ferrites (e.g. $M_S(CoFe_2O_4) = 80$ Am^2/kg, $M_S(NiFe_2O_4) =$ 55 Am^2/kg, and $M_S(\gamma\text{-}Fe_2O_3) = 74$ Am^2/kg). These results indicate that as the SiO_2 shell thickness increases, the magnetization becomes more bulk-like recovering any "lost" surface spins with Fe-O and Co-O coordination being reinforced by the thickening SiO_2 shell. Furthermore, an increase in the Bloch constant with an increase in the SiO_2 shell thickness indicates a weaker exchange constant. The fitted Bloch constants for the undoped and V-doped FeCo/SiO_2 nanoparticles was much larger than that of bulk iron ($B \approx 3.3$ x 10^{-6} $K^{2/3}$) but in keeping with previously measured nanoparticles[101]. These trends in $M_S(T)$ resulted in an $\sim$10% increase in the overall high-field susceptibility corresponding to an increase in the interfacial anisotropy term[102].

To determine the effects of the SiO_2 shell and the metal silicate interfacial phase on the temperature dependence of the coercivity (H_C) (Fig. 4.15), the measured coer-

Table 4.4: Measured paramagnetic susceptibilities at high-fields, and fit results of the temperature dependence of the saturation magnetization

	χ (Am^2/kgT)	B (10^5 K$^{2/3}$)	A	T_F (K)	$M_S(0)$ (Am^2/kg)
FeCo/SiO$_2$(3 nm)	2.7 ± 0.1	4.9 ± 0.2	0	0	52.1 ± 0.8
FeCo/SiO$_2$(4 nm)	2.6 ± 0.1	5.61 ± 0.09	0	0	54.1 ± 0.6
FeCo/SiO$_2$(6 nm)	2.9 ± 0.1	1.56 ± 0.06	0	0	65.8 ± 0.2
FeCoV/SiO$_2$(5 nm)	2.7 ± 0.1	4.9 ± 0.2	0	0	7.0 ± 0.2

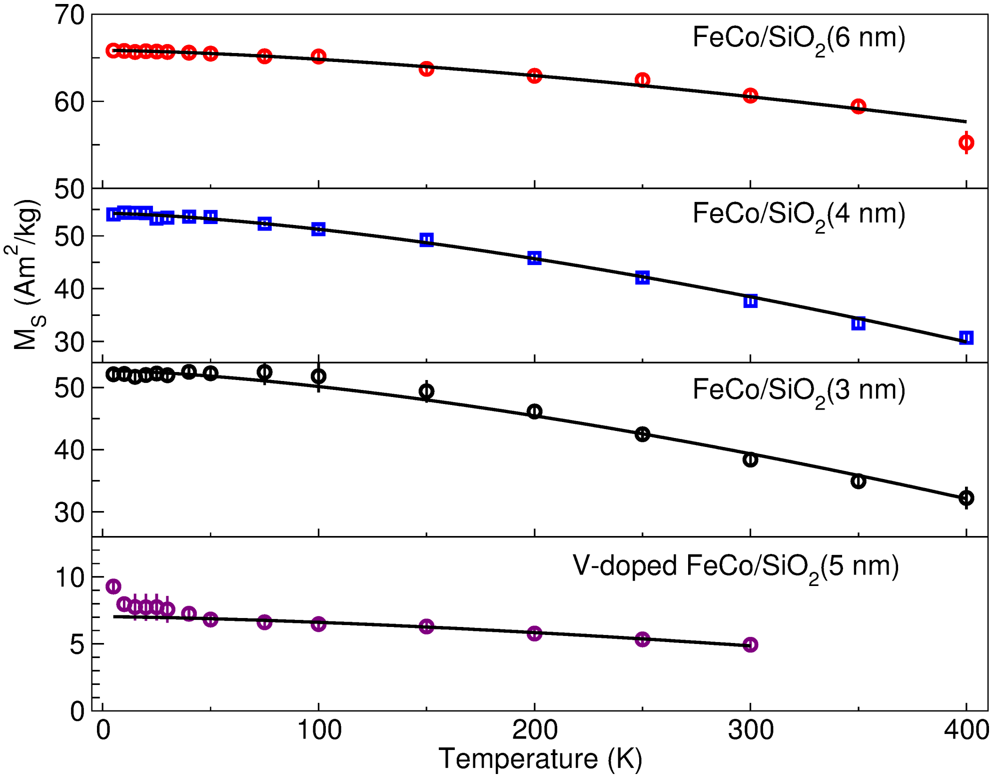

Figure 4.14: Saturation magnetization as a function of temperature. Lines through the data are fits described in the text.

civities have been normalized to their respective T_B's to take into account the different intrinsic and extrinsic magnetism (e.g. energy scales due to the intrinsic differences in K, described above). $H_C(T/T_B)$ for the undoped and V-doped SiO$_2$/FeCo nanoparti-

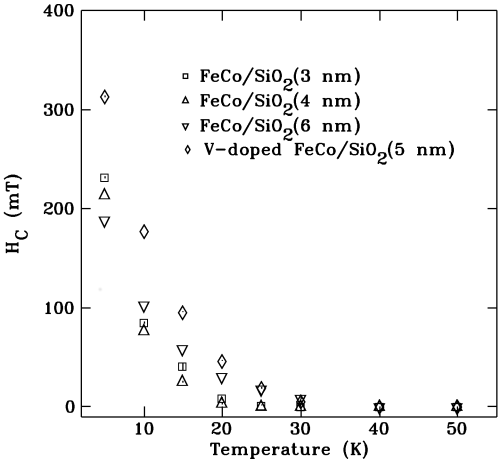

Figure 4.15: Coercivity as a function of temperature for the undoped and V-doped FeCo/SiO$_2$ nanoparticles

cles decreased rapidly with warming, and $H_C(T = T_B) = 0$ mT was in good agreement with χ_{AC} results. As the thickness of the silica shell increased, the measured coercivities increased over the intermediate temperature region $0.5 < \mathrm{T}/\mathrm{T}_B < 1.0$. This occurs just below the transition from superparamagnetism due to the increased magnetic volume of the undoped and V-doped FeCo nanoparticle core as more Fe and Co atomic spins were recaptured providing additional magnetic response. At the lowest temperatures, spin-glass-like behaviour from the interparticle interactions alters the energy landscape which results in the larger observed coercivities for the thinner SiO$_2$ shell samples (3 and 4 nm) compared with FeCo/SiO$_2$(6 nm) nanoparticles. The V-doped FeCo/SiO$_2$ nanoparticles had a considerably increased coercivity at all temperatures relative to the undoped FeCo/SiO$_2$ nanoparticles due to the increased anisotropy and reduced saturation magnetization.

To ascertain more clearly the roll of the interfacial metal silicates on the magnetism of these undoped and doped FeCo/SiO$_2$ nanoparticles, temperature and field

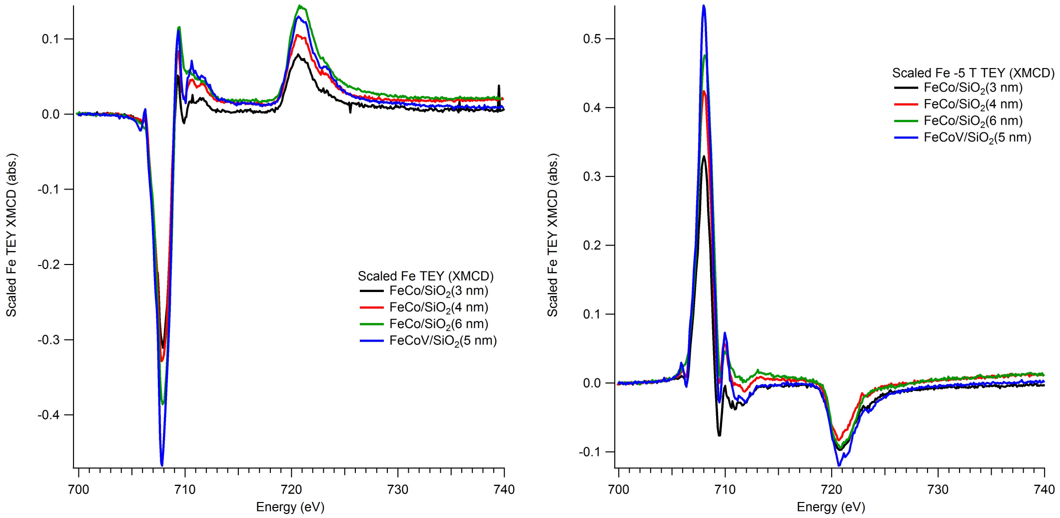

Figure 4.16: TEY XMCD collected at the Fe $L_{3,2}$ transition edge of Fe.

dependent elemental magnetic measurements were performed over the $L_{3,2}$ transitions of Fe, Co, and V. In all cases, both the total electron yield (TEY) and total fluorescence yield (TFY) x-ray magnetic circular dichroism (XMCD) experiments were performed. TEY is typically a surface sensitive technique as it is dependent on the electron escape depth at the studied energies (e.g. ∼2 nm for Fe[77]). Whereas the TFY is a measure of the photons from deep within the sample (e.g. order of 100 nm). Thus, TEY experiments are representative of the interfacial metal-silicates and the surface layers of the undoped and V-doped FeCo/SiO_2 nanoparticles.

The TEY XMCD collected at the Fe $L_{3,2}$ transition (Fig. 4.16). Here we observe spectral features centred at ∼708 eV and ∼721 eV from the L_3 and L_2 transition edges, respectively. At the L_3 edge of Fe, a peak at ∼708 eV corresponds with the metallic Fe spectral feature observed from the XAS experiments described above. Furthermore, a second spectral feature at ∼710 eV corresponds with Fe^{3+} also ob-

Table 4.5: Observed pinning in undoped and V-doped SiO_2/FeCo nanoparticles from XMCD spectra as measured by the percent difference in the L_3 transition edge intensity with a change in field polarity.

	Fe (%)	Co (%)
FeCo/SiO_2(3 nm)	6 ± 1	15± 1
FeCo/SiO_2(4 nm)	29± 1	36± 1
FeCo/SiO_2(6 nm)	23± 1	23± 1
FeCoV/SiO_2(5 nm)	17± 1	13± 1

served in the XAS Fe spectrum. These two spectral features are aligned antiparallel to each other indicating that they are antiferromagnetically coupled. With a change in the applied field polarity, all the spectral features flip orientations indicating that they are magnetic as to be expected for metallic Fe (ferromagnetic) and Fe-silicate (ferrimagnetic). Complementary results for the Fe $L_{3,2}$ TFY XMCD spectra were observed, however, the signal-to-noise ratio was reduced significantly due to the self absorption process making quantitative analysis from the Fe TFY (and the Co TFY) spectra problematic. Interestingly, with the change in field polarity, there were differences in the value of the peak maximum, which is proportional to the magnetization, indicating possible pinning of the Fe surface moments of the undoped and V-doped FeCo nanoparticle core (Table 4.5). These differences of the observed maximum with field polarity increased with SiO_2 thickness, further evidence that the Fe-silicates affected directly the surface Fe moments.

To observe the effects of the spontaneously formed Co-silicates on the magnetism of the nanoparticles, XMCD experiments at the Co $L_{3,2}$ transition edge were performed (Fig. 4.17). Spectral features centred at ~779 eV and ~794 eV, characteristic

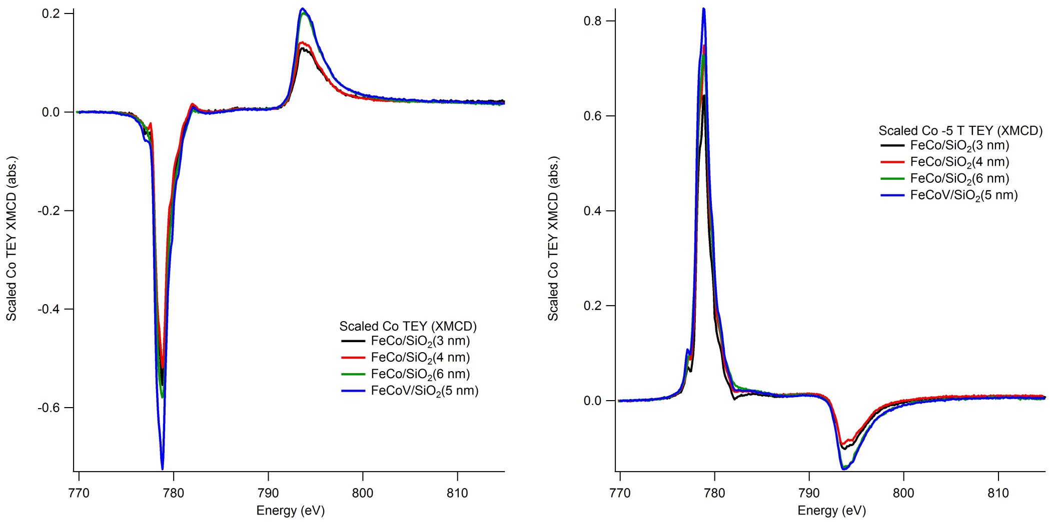

Figure 4.17: TEY XMCD collected at the Fe $L_{3,2}$ transition edge of Co.

of the L_3 and L_2 transition edges, were observed. At the L_3 transition edge, a single maximum was observed, centred at ~779 eV, corresponding to a combination of the metallic Co and O_h Co^{2+} (from the Co-silicates) spectral components. Unlike the observed antiferromagnetic coupling between the metallic Fe and Fe-silicate components, the metallic Co and Co-silicate components appear to be aligned ferromagnetically, and also coupled ferromagnetically with the metallic Fe component. Similar to the observed pinning in the Fe XMCD spectral features, the Co and Co^{2+} spectral features appear to be pinned as well. The change in field polarity results in a flip of all the Co L_3 spectral features, however, the magnitude of the maximum is decreased with an applied field of 5 T, similar to the Fe L_3 transition edge.

Applying sum-rule analysis[56] to the Fe and Co XMCD spectra (there was no measurable V XMCD spectrum), the ratio of the orbital (m_l) to spin (m_s) moments were calculated using:

$$\frac{m_l}{m_s} = \frac{2q}{9p - 6q} \tag{4.2}$$

where p and q are the integrated XMCD intensities over the L_3 and $L_3 + L_2$ transition edges, respectively. For all XMCD spectra, an increase of the integrated XMCD intensity from an offset from zero in the XMCD signal at the highest energies (energies greater then those for the L_2 transition edge) were observed. Considering that *d*-orbitals are highly localized and should not contribute to an XMCD spectrum beyond the L_2 transition edge, the observed spectral intensity may be the result of excited, polarized, *s*-electrons[103; 104]. Fortunately, these *s*-states due not contribute to the calculations of m_l/m_s, therefore q was terminated where there was a minimum in the slope of the XMCD intensity (e.g. 730 eV for Fe and 810 eV for Co). Considering the above, together with the possibility of there being mixing between the L_3 and L_2 transition edges (observed as a non-zero XMCD intensity between these transitions), a comparison of only the relative values of m_l/m_s between samples (following the same integration procedure) were made. The observed m_l/m_s values calculated for Fe and Co are shown in table 4.6. The calculated values for the Fe m_l/m_s are in agreement with those calculated for bulk Fe[56], indicating that the observed interfacial Fe-silicate has altered the elemental Fe magnetism as previous experiments on nanoscale Fe has shown a larger calculated $m_l/m_s \approx 0.1$[105]. The calculated Co m_l/m_s was observed to be enhanced significantly from that of bulk Co (e.g. 0.078 for fcc Co and 0.099 for hcp Co[56]), also seen in the enhanced magnetization measured by XMCD.

The field dependence of the Fe and Co magnetizations are shown in figure 4.18. These values were determined from the maximum of the Fe and Co L_3 transition edge

Table 4.6: m_l/m_s calculated values for the undoped and V-doped FeCo/SiO$_2$ nanoparticles

	Fe m_l/m_s	Co m_l/m_s
FeCo/SiO$_2$(3 nm)	0.026	0.160
FeCo/SiO$_2$(4 nm)	0.071	0.202
FeCo/SiO$_2$(6 nm)	0.053	0.140
FeCoV/SiO$_2$(5 nm)	0.039	0.154

which is proportional to the magnetization. The observed Fe magnetization, which is a combination of the metallic Fe and O_h Fe^{3+} components, showed a gradual increase with field (up to 5 T). The elemental Co magnetizations, which is a combination of metallic Co and the O_h Co^{2+} components, had a similar field dependence as the Fe

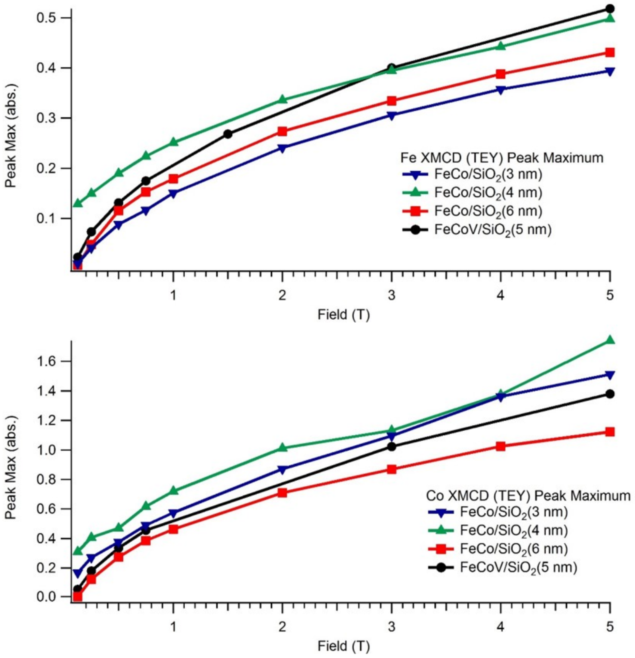

Figure 4.18: XMCD field dependence of the Fe (top) and Co (bottom) L$_3$ transition edge. The solid line is a guide to the eye.

magnetization. Both elemental magnetizations were in agreement with those observed for the overall sample from the collected hysteresis loops. Due to the nature of the elemental peak magnetization, decoupling the contribution from the metallic and metal-silicate components was not possible. As a result of this, identifying uniquely the component(s) responsible for the paramagnetic-like increase in magnetization with field was problematic. However, as we know that this effect is likely the result of an increased surface anisotropy[106], it is reasonable to suggest that the metal-silicate components (e.g. Fe^{3+} and Co^{2+}) are the cause.

4.5 Conclusions

We have synthesized undoped and V-doped FeCo nanoparticles coated with different thickness of SiO_2 between 3 and 6 nm. We have demonstrated, for the first time, that at the interface between these undoped and V-doped FeCo nanoparticle cores and the SiO_2 shells, a layer of metal-silicates has formed spontaneously. Furthermore, by tuning the thickness of the SiO_2 shell, we demonstrated the ability to tune all the technologically relevant magnetic properties (e.g. blocking temperature, magnetocrystalline anisotropy, coercivity, and saturation magnetization). From element specific experiments, we observed that O_h Fe^{3+} and Co^{2+} from this metal-silicate interfacial layer alter directly the core nanoparticles surface spins allowing for the complete recapture of these once frustrated spins. Through this process of coating undoped and V-doped FeCo nanoparticles with a nominally inert SiO_2 shell results in the formation of an interfacial phase that is relevant magnetically. To further understand the direct consequences of these interfacial metal-silicates, a study to identify uniquely the Fe-silicates formed using Mössbauer spectroscopy should be done. Also, to understand the mechanism by which the vanadium dopant appears to be “sucked” out of the entire FeCo nanoparticle to reside on the surface during the SiO_2 coating process, attempts to dope with other materials with larger enthalpy (e.g. Ni) of formation for metal-silicates will be attempted.

Chapter 5

Nanostructured Thin Films of Iron Nanocrystallites Embedded in a Conductive Matrix

5.1 Introduction

An increased awareness of our dependence on non-renewable resources is driving the need for more energy efficient technologies, and new functional magnetic materials are essential components for the development of these technologies. Furthermore, with the rapid nanoscale miniaturization of our technology taking place currently, there is an increased need to understand fully the magnetism that may arise due to interactions at the nanoscale such as; interactions between nanoparticles or nanocrystallites (interparticle) and interactions within the nanoparticle or nanocrystallite (intraparticle). Nanostructured thin films of magnetic crystalline nanoparticles (nanocrystallites) embedded in a conductive matrix provide an ideal system for the study of the interactions between (interparticle) and within (intraparticle) nanocrystallites. To understand the role of these interactions, a series of nanostructured thin films of iron nanocrystallites embedded in a copper matrix have been created. By controlling carefully the deposition conditions (e.g. deposition time of iron and copper and the in-situ ion-beam bombardment energy), thin films with morphologies ranging from a multilayered Fe/Cu film to dispersions of iron nanocrystallites embedded in a copper matrix have been grown. These systems have enabled a systematic study of the effects of interactions on the magnetism; for example, temperature and frequency dependent susceptibility experiments to study the effects of interparticle interactions and element specific x-ray magnetic circular dichroism and x-ray absorption spectroscopy experiments to study the results of intermixing between nanocrystallite and matrix provide insight into the intraparticle interactions.

5.2 Film Deposition

To investigate the effects of these interactions (inter- and intra-particle) on the magnetism, we have fabricated thin films of Fe and Cu using Dr. Ko-Wei Lin's (Appendix A) dual ion-beam deposition system (Fig. 5.1).[107] This system is equipped with two types of ion-beam guns.[108] A Kaufman type used to argon ion bombard target metal atoms of Fe or Cu, and an End-Hall argon ion-beam which provides a mechanism to alter the deposition conditions promoting intermixing between the deposited Fe and Cu (forming preferentially interfacial FeCu alloy) or by forming Fe nanocrystallites embedded in a copper matrix. These conditions allow for the fabrication of a range of film morphologies providing rich physics to explore, influenced by these inter- and intra-particle interactions.

These nanostructured thin films were deposited onto thermally annealed silica (SiO_2) substrates. The substrates were prepared by sectioning a SiO_2 wafer into quarters and washing them three times; once in acetone, once in methanol, and once in deionized water, each for ten minutes within an ultrasonic bath. This process removed any dust or oils left on the substrates that could prevent adhesion of the

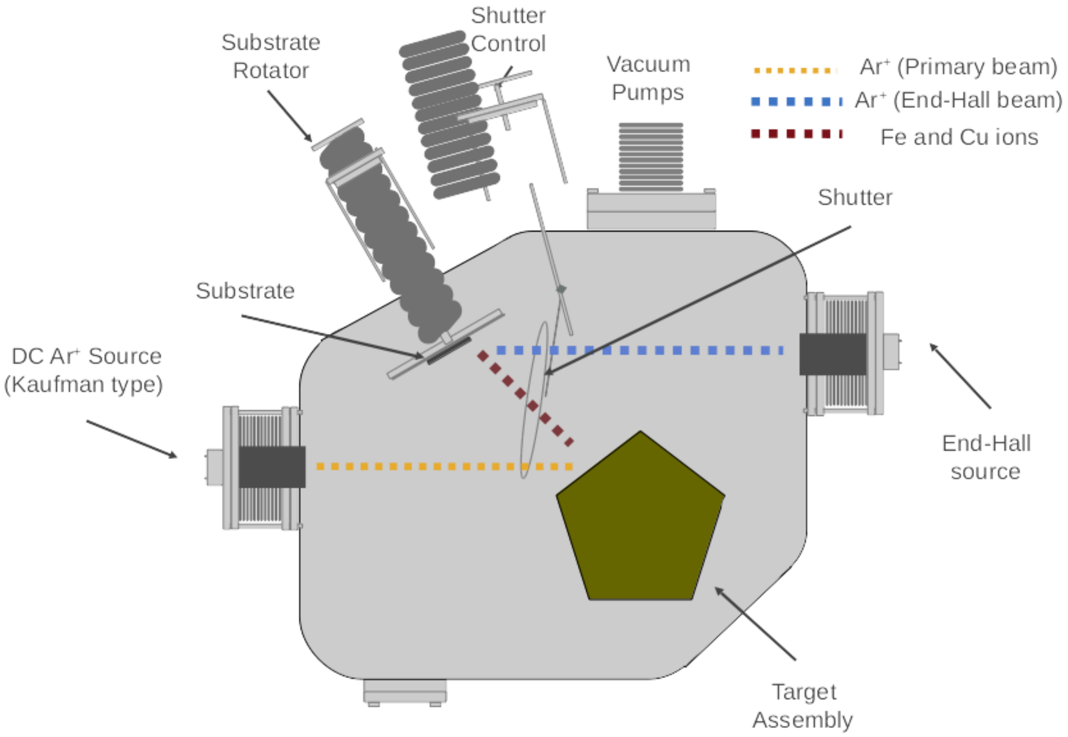

Figure 5.1: Schematic of the dual ion-beam assisted deposition (IBAD) chamber. The primary, Kaufman type, ion gun shoots argon ions towards the metal targets (e.g. Fe or Cu). The ejected metal ions are directed towards the SiO_2 substrate. The secondary, End-Hall type, ion gun shoots argon ions towards the substrate where they interact with the ejected metal ions and the substrate, providing a means of supplying additional kinetic energy to the system. This additional kinetic energy alters the deposition conditions of the iron atoms, increasing significantly the amount of intermixing that occurs between iron and copper.

deposited film. Once washed, the substrates were annealed, in air, at 900 °C for four hours. A warming rate of ∼10 °C/min and a cooling rate of ∼3 °C/min were used. A single quarter of the thermally oxidized silica substrate was then mounted onto the rotating sample holder inside the dual ion-beam deposition chamber using Kapton tape (see figure 5.1 for a diagram of the system). A carbon coated TEM grid was also mounted next to the substrate, during deposition of the film, for plane-view and SAED experiments on the deposited film.

To ensure an air-free environment for the deposition process, the chamber was evacuated to a vacuum pressure of 2.2×10^{-6} torr. Experimental evidence for oxygen contamination occurring during film growth (e.g. the formation of iron or copper oxides throughout the nanostructured film) was not observed in, for example, x-ray absorption spectra of the films, nor with magnetometry experiments (e.g. no measurable exchange bias field shift), see sections 5.3 and 5.4, respectively. Prior to film deposition, the metal targets[1] were pre-cleaned (*in situ* sputtering with Ar^+ from the primary ion gun) for 10 minutes ensuring no cross-contamination from oxidized metal or from other metals. In addition, a two minute cleaning was performed after each target change, to further protect against possible cross-contamination. The primary, Kaufman type, argon ion-beam sputtered target metal ions in the direction of the silica substrate and was operated at a constant beam voltage of 804 V, acceleration voltage of 120 V, and a three standard cubic centimeters per minute (3 sccm) Ar gas flow. To ensure reproducible film thicknesses, the Ar^+ ion-beam current was fixed at 7.5 mA (e.g. ∼0.2 Å/s for Fe and ∼0.3 Å/s for Cu). The secondary End-Hall Ar^+ ion-beam, used to provide additional control over the films microstructure and

---

[1] 99.99% pure Fe and Cu targets were purchased from Homogeneity Company, Taiwan.

morphology, was directed towards the silica substrate and *in situ* ion-beam bombarded metal atoms emerging from the target assembly achieved by a constant argon gas flow, through the End-Hall gun, of 7.0 sccm (End-Hall voltage, $V_{EH} = 35$ V), 3.6 sccm ($V_{EH} = 50$ V), and 3.1 sccm ($V_{EH} = 70$ V) for the end-hall source.

In total 12 nanostructured thin films and a bilayer film, for comparison, were grown. The deposition of the nanostructured films was as follows. First a layer of iron was deposited where the deposition time was 15, 30, or 60 seconds (the iron deposition time was kept constant during the sample growth, but varied systematically between samples). During the iron layer deposition, *in situ* ion-beam bombardment using the secondary End-Hall source provided additional kinetic energy to the iron ions. The End-Hall voltage, was also kept constant during the sample growth, but varied between samples. An End-Hall voltage (V_{EH}) of 0, 35, 50, or 70 V was used, where 0 V implies that there was no *in situ* ion-beam bombardment. Second, a layer of copper was deposited where the deposition time was 60 seconds. The deposition time of the copper layer was the same for all samples. This process was repeated for a total of five repetitions (10 total layers). The bilayer was grown by depositing iron and copper for 300 s each. Throughout this chapter, the following naming convention has been adopted, Fe(deposition time) $V_{EH} =$ (End-Hall Voltage) (see Table 5.1 for a list of fabricated samples), since the copper deposition conditions were unchanged between samples, it is omitted from the naming convention.

Table 5.1: List of samples fabricated by the dual-ion beam deposition process described above.

Fe60s $V_{EH} = 0$ V	Fe30s $V_{EH} = 0$ V	Fe15s $V_{EH} = 0$ V
Fe60s $V_{EH} = 35$ V	Fe30s $V_{EH} = 35$ V	Fe15s $V_{EH} = 35$ V
Fe60s $V_{EH} = 50$ V	Fe30s $V_{EH} = 50$ V	Fe15s $V_{EH} = 50$ V
Fe60s $V_{EH} = 70$ V	Fe30s $V_{EH} = 70$ V	Fe15s $V_{EH} = 70$ V
	Fe300s $V_{EH} = 0$ V (bilayer)	

5.3 Composition and Structure

A complete and thorough determination of the thin films microstructure, morphology, and composition is necessary in order to understand fully their magnetism. Therefore, a detailed study of the microstructure using grazing incident x-ray diffraction (GIXRD), transmission electron microscopy (TEM), and x-ray reflectometry (XRR) was performed. Coupled with the microstructure analysis, the composition was determined from x-ray absorption spectroscopy (XAS) experiments and the morphology was identified from cross-sectional TEM image analysis. Conversion electron Mössbauer spectroscopy (CEMS) experiments were performed to support the identification of the formation of an interfacial alloy as well as provide additional evidence for the lack of oxygen contamination during the deposition process.

GIXRD experiments were performed on the nanostructured thin films and the bilayer film using a Bruker D8 Advance with DaVinci. The deposition conditions described above fabricate thin films with thicknesses ∼30 nm or less, therefore, the standard $\theta/2\theta$ Bragg-Brantano geometry would not be appropriate as the penetration depth of x-rays from a Cu source is on the order of microns, leading to a diffraction pattern of the SiO_2 substrate primarily. In order to collect a diffraction pattern of the film, the grazing incident geometry was adopted. By fixing the incident angle at an angle near the critical angle, the Bragg condition can be satisfied while simultaneously removing the majority of the substrate from the diffraction pattern. The primary optics for these experiments were a Göbel mirror, an engineered multilayered nanostructured mirror which produces highly parallel, monochromatic (Kα only), x-rays which have a divergence significantly reduced when compared to a standard line-focus (providing better quality patterns) and a 1.0 mm physical slit to further reduced beam divergence perpendicular to the goniometer axis (equatorial divergence). The samples were mounted on a Eulerian cradle stage with a manual z-axis control, allowing for the adjustment of the sample height relative to the focal plane of the x-ray beam. A secondary 1.0 mm physical slit was used to minimize the divergence of the diffracted x-rays. These x-rays were collected using a Lynxeye position sensitive detector (PSD) operating in the 0D mode with its slit opened fully (13 mm).

Figures 5.2 to 5.4 show the Rietveld refined (FullProf[34]) GIXRD patterns for the nanostructured thin films and the bilayer film. From these patterns, we observe reflections which have been broadened significantly, to be expected for nanoscale crystallites with reduced structural long-range order[33; 109]. To further complicate the refinements of these patterns, the structures of iron, copper, and an FeCu alloy are all cubic with very similar lattice constants. This combination of broadened reflections and similar structures makes the unique determination of the structures and compositions described by x-ray diffraction problematic. Taking this into account, the refinements (solid black lines in figures 5.2 to 5.4) were accomplished using, at most,

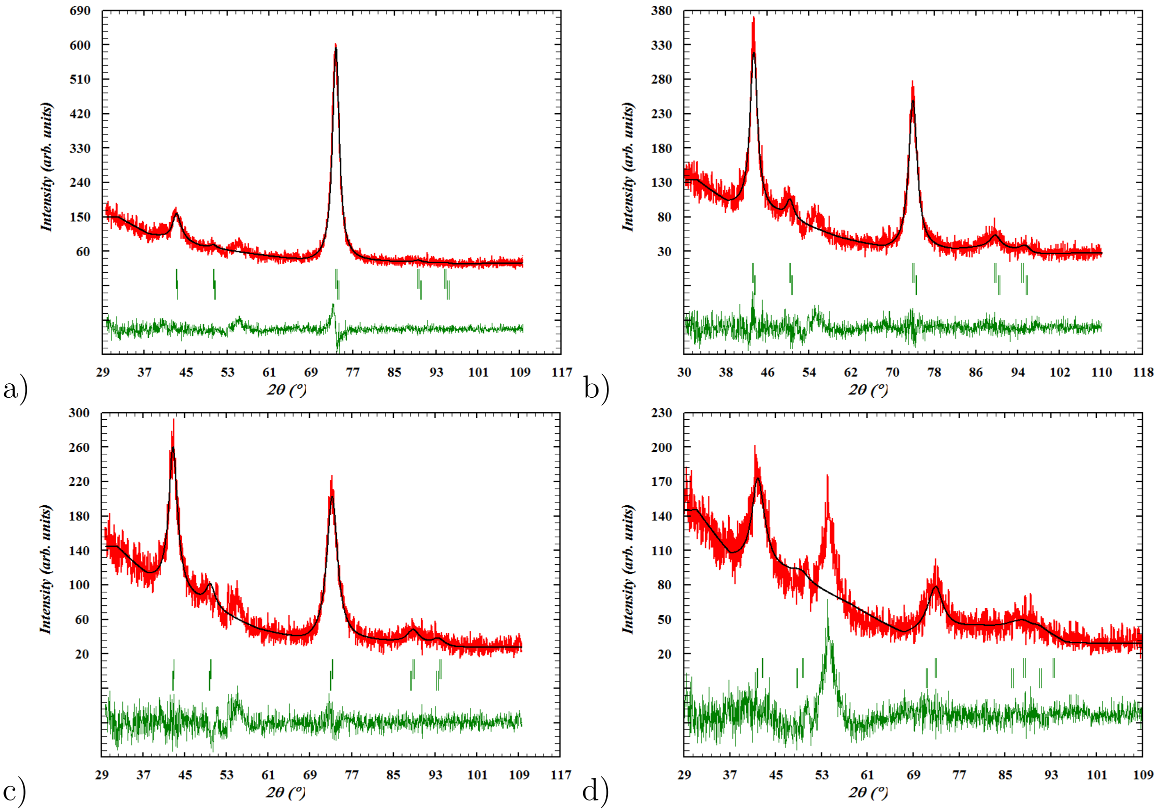

Figure 5.2: GIXRD pattern of the Fe60s series of films (red dots). a) Fe(60s) V$_{EH}$ = 0 V film, b) Fe(60s) V$_{EH}$ = 35 V film, c) Fe(60s) V$_{EH}$ = 50 V film, and d) Fe(60s) V$_{EH}$ = 70 V film. Rietveld refinement (solid black line) using FullProf indicated that the film was composed of a combination of cubic copper, iron, and FeCu alloy. Region omitted near ∼54 °2θ contains the SiO$_2$ substrate reflection. Bragg markers for the cubic copper (top) and iron (bottom) are shown as vertical bars.

two phases. A single phase with the cubic Fm$\bar{3}$m space group and an amorphous phase which describes the iron nanocrystallites or the FeCu interfacial alloy. An attempt to refine all three phases was made, however, as there were only five reflections, and these reflections were broadened significantly, a non-linear least squares fitting procedure resulted always in the reduction of the intensity of two of the three phases to zero.

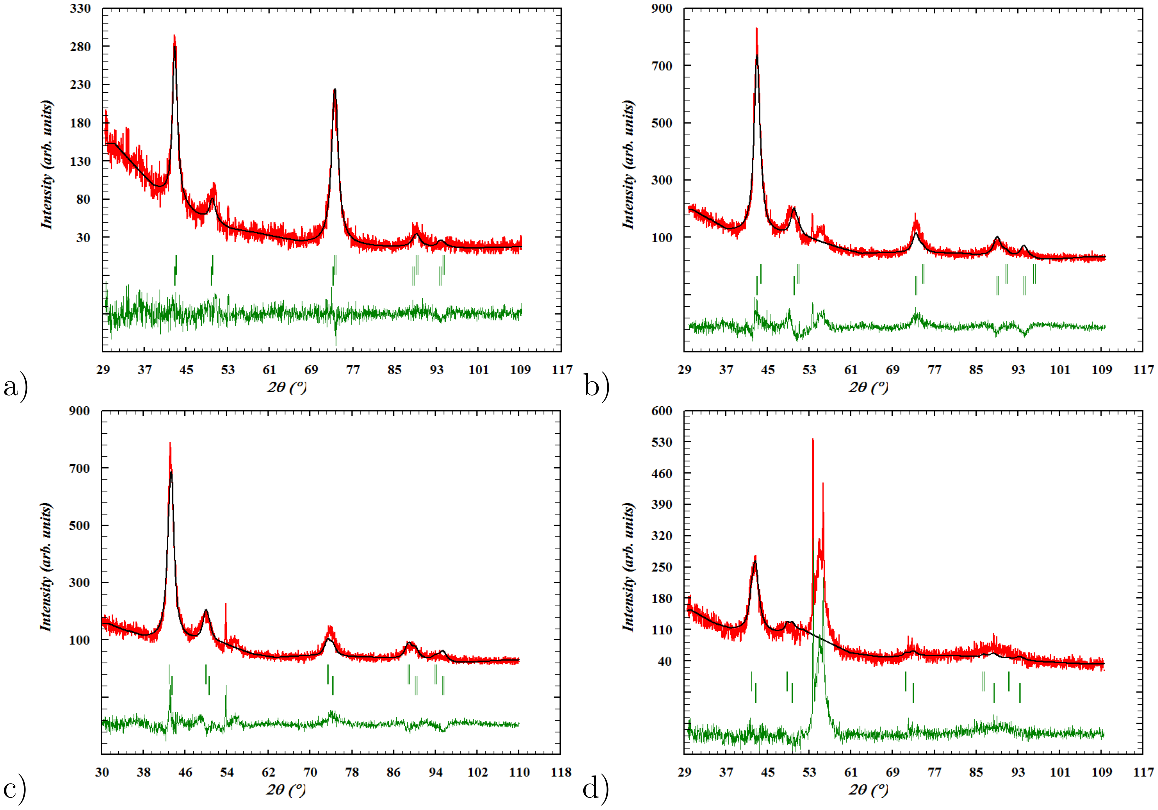

Figure 5.3: GIXRD pattern of the Fe30s series of films (red dots). a) Fe(30s) V_{EH} = 0 V film, b) Fe(30s) V_{EH} = 35 V film, c) Fe(30s) V_{EH} = 50 V film, and d) Fe(30s) V_{EH} = 70 V film. Rietveld refinement (solid black line) using FullProf indicated that the film was composed of a combination of cubic copper, iron, and FeCu alloy. Region omitted near ∼54 °2θ contains the SiO_2 substrate reflection. Bragg markers for the cubic copper (top) and iron (bottom) are shown as vertical bars.

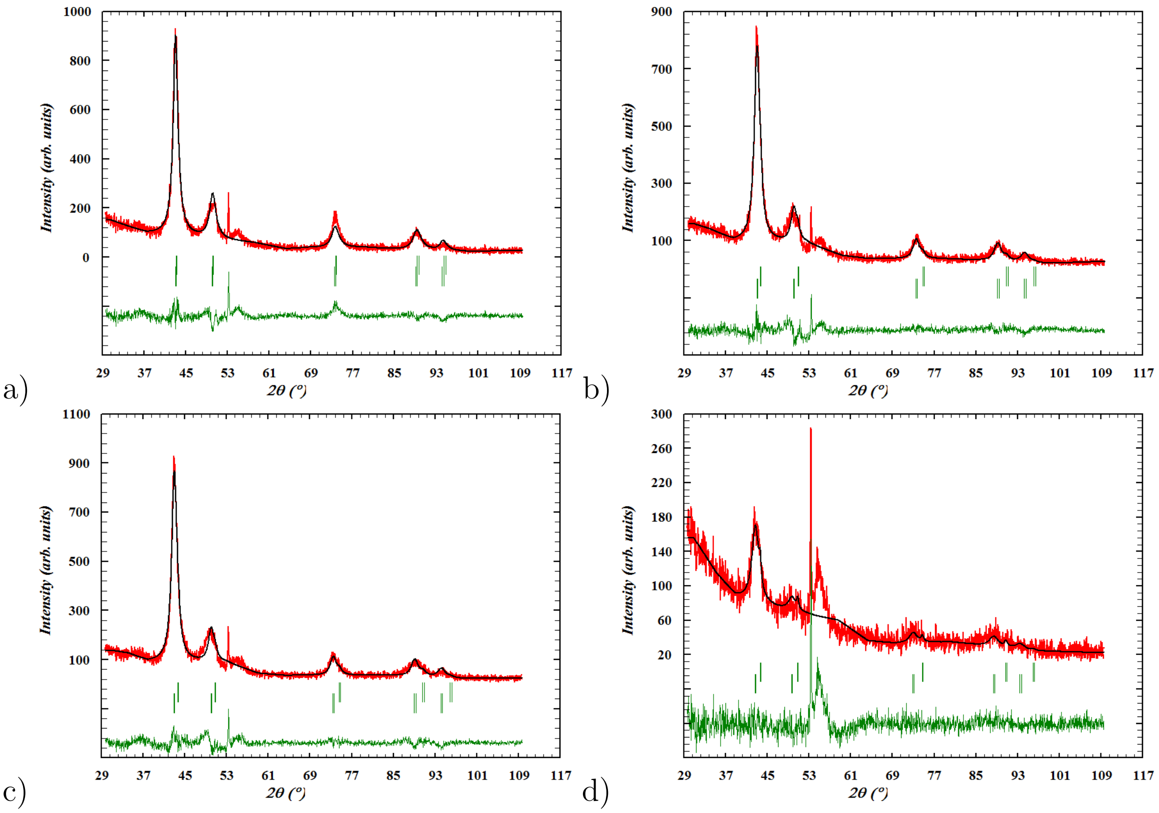

Figure 5.4: GIXRD pattern of the Fe15s series of films (red dots). a) Fe(15s) V$_{EH}$ = 0 V film, b) Fe(15s) V$_{EH}$ = 35 V film, c) Fe(15s) V$_{EH}$ = 50 V film, and d) Fe(15s) V$_{EH}$ = 70 V film. Rietveld refinement (solid black line) using FullProf indicated that the film was composed of a combination of cubic copper, iron, and FeCu alloy. Region omitted near ∼54 °2θ contains the SiO$_2$ substrate reflection. Bragg markers for the cubic copper (top) and iron (bottom) are shown as vertical bars.

A comparison of the collected diffraction patterns to the diffraction patterns of iron, copper, or FeCu alloy in the Pearson database[36] provides evidence for a preferred orientation as the ratio of intensities between the (220) reflection and the others was altered. A preferred orientation is likely the result of the mechanism of growth during the dual ion-beam deposition process and was not unexpected. As can be seen from the diffraction patterns, the intensity ratio between the (220) and (111) reflections centred at ~74 and ~43° 2θ, respectively, decreases with increasing V_{EH}. This indicates that the films become more isotropic as the intermixing increased. The refinements of the diffraction patterns included Scherrer broadening in order to

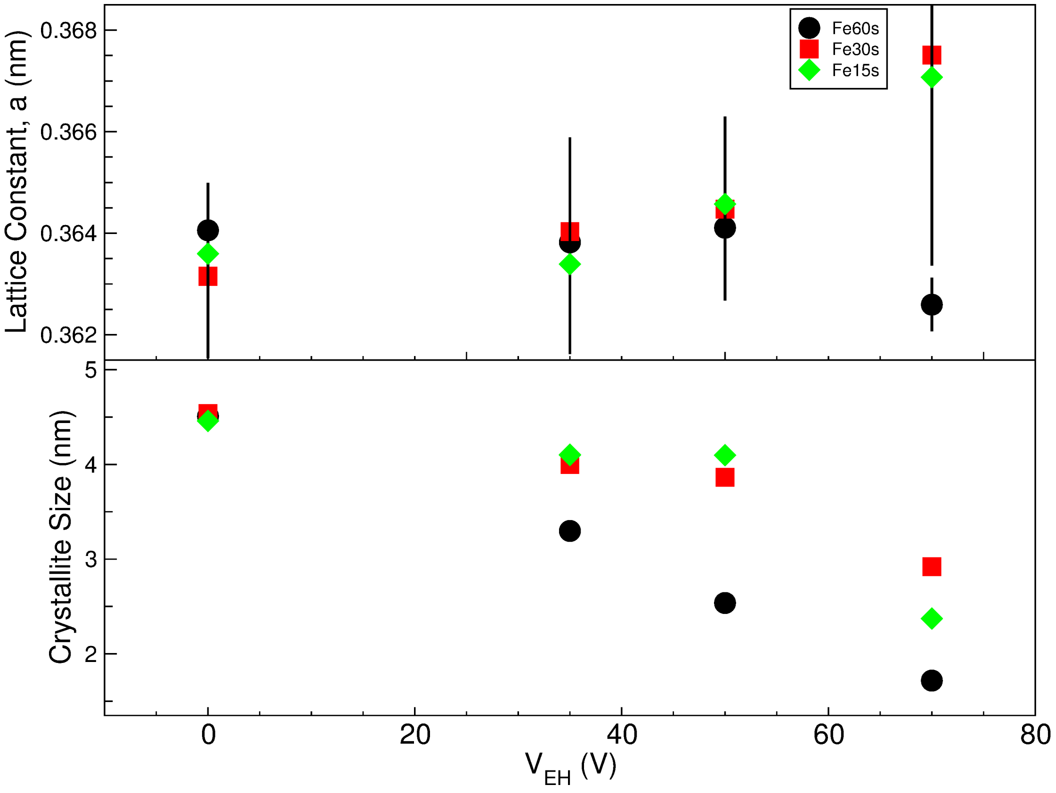

a)

Figure 5.5: Top: Lattice constant (a) as a function of V_{EH} and Bottom: Average crystallite size as a function of V_{EH} for the iron deposition times of 60s, 30s, and 15s.

obtain an average crystallite size. The refined lattice constants and crystallite sizes are shown in figure 5.5, and were in good agreement with TEM results (Table 5.2). To observe the effects of the *in situ* ion-beam bombardment on the microstructure of these thin films, plots of the lattice constants as a function of End-Hall voltage (V_{EH}) are also provided in figure 5.5. We observe that for the Fe60s, Fe30s, and Fe15s series of films, the lattice constants remain unchanged for all $V_{EH} < 70$ V. The observed changes in the lattice constant for the $V_{EH} = 70$ V films is likely the result of the significant increase in the intermixing between the Fe and Cu, and highlights the difficulties in refining the diffraction patterns with a single phase when multiple phases are present. A decrease in the average crystallite sizes with V_{EH} was also observed, again, due to the increased intermixing.

Planar TEM images collected by Dr. Ko-Wei Lin's group, using a JEOL 2100F operating at 200 kV were used for microstructural analysis (see Figs 5.6 to 5.8). The average nanocrystallite diameter (both the iron and copper nanocrystallites) and distribution of diameters was determined using image analysis software (ImageJ[42]) of the dark field images, and was well described by a log-normal size distribution (see Table 5.2). Cross-sectional TEM images (see Figs. 5.9 to 5.11) were collected by Dr. Ko-Wei Lin's group by gluing with epoxy two pieces of a nanostructured film together (face-to-face) and polishing this sandwich such that the resulting sample was thin enough that electron transmission could occur, allowing an image to be collected.

These images provide information about the total film thickness, and where possible, the thickness of each deposited layer. Of all the samples fabricated, only the Fe60s $V_{EH} = 0$ V (Fig 5.9a) sample showed clearly any indication of a multilayered

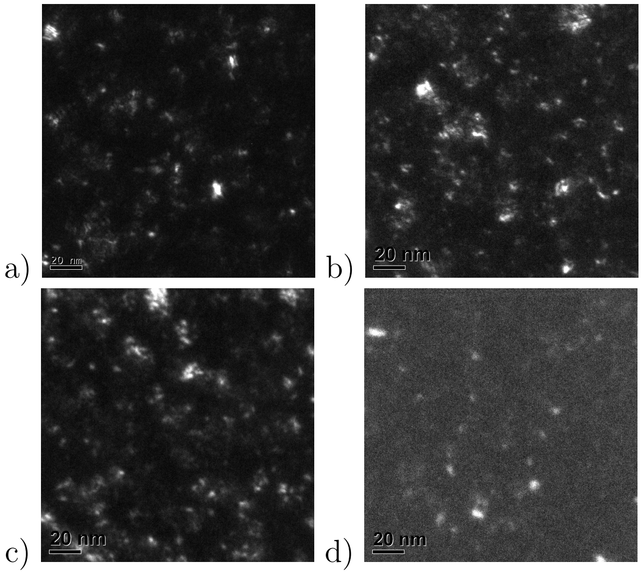

Figure 5.6: Planar dark-field TEM images of a) Fe60s $V_{EH} = 0$ V, b) Fe60s $V_{EH} = 35$ V, c) Fe60s $V_{EH} = 50$ V, d) Fe60s $V_{EH} = 70$ V

structure, however, the Fe30s and Fe15s $V_{EH} = 0$ V films showed a similar multi-layered structure in their XRR patterns. The remainder of the cross-sectional TEM images showed that the nanostructured films had significant intermixing resulting in a iron nanocrystallite embedded in a copper matrix morphology, supported by the XRR patterns discussed below.

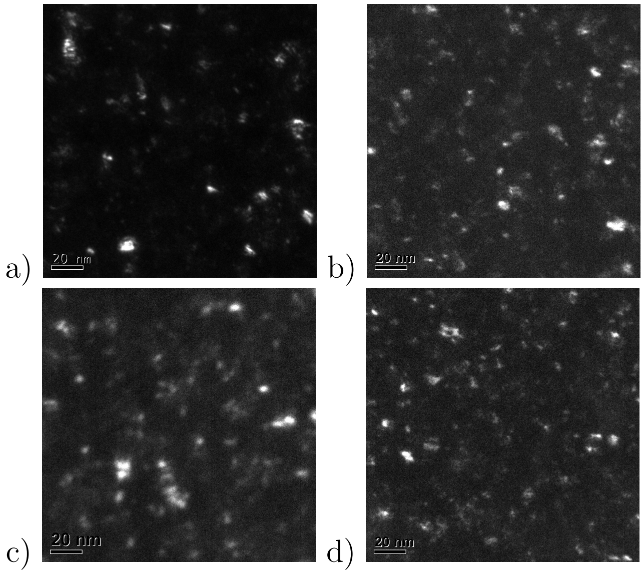

Figure 5.7: Planar dark-field TEM images of a) Fe30s $V_{EH} = 0$ V, b) Fe30s $V_{EH} = 35$ V, c) Fe30s $V_{EH} = 50$ V, d) Fe30s $V_{EH} = 70$ V

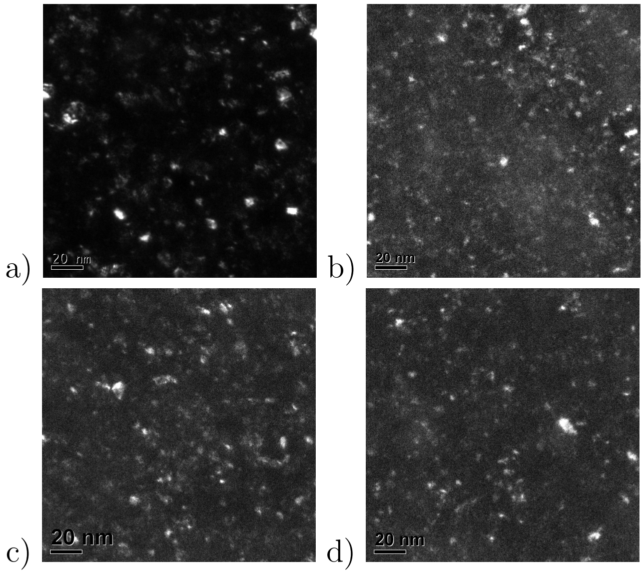

Figure 5.8: Planar dark-field TEM images of a) Fe15s $V_{EH} = 0$ V, b) Fe15s $V_{EH} = 35$ V, c) Fe15s $V_{EH} = 50$ V, d) Fe15s $V_{EH} = 70$ V

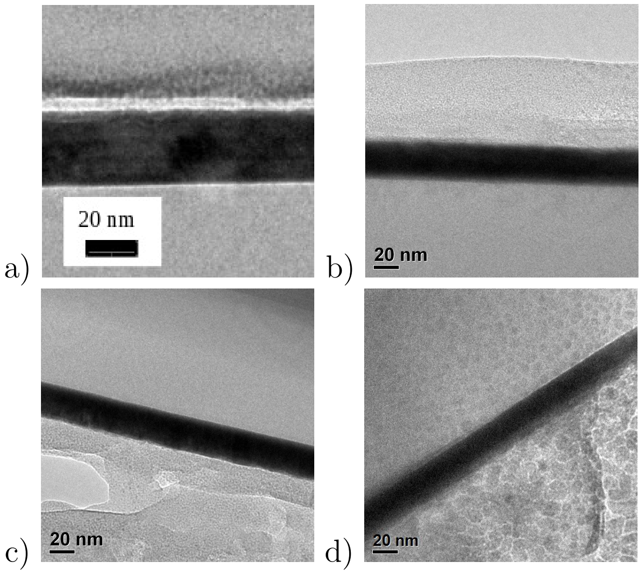

Figure 5.9: Cross-sectional TEM images of a) Fe60s $V_{EH} = 0$ V, b) Fe60s $V_{EH} = 35$ V, c) Fe60s $V_{EH} = 50$ V, d) Fe60s $V_{EH} = 70$ V

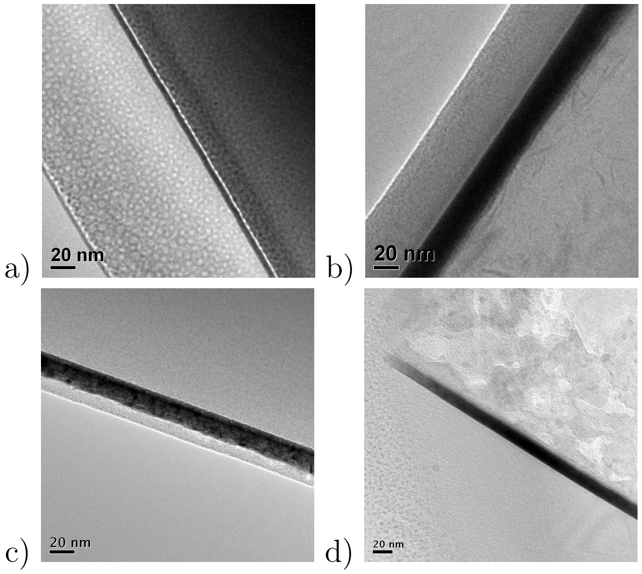

Figure 5.10: Cross-sectional TEM images of a) Fe30s $V_{EH} = 0$ V, b) Fe30s $V_{EH} = 35$ V, c) Fe30s $V_{EH} = 50$ V, d) Fe30s $V_{EH} = 70$ V

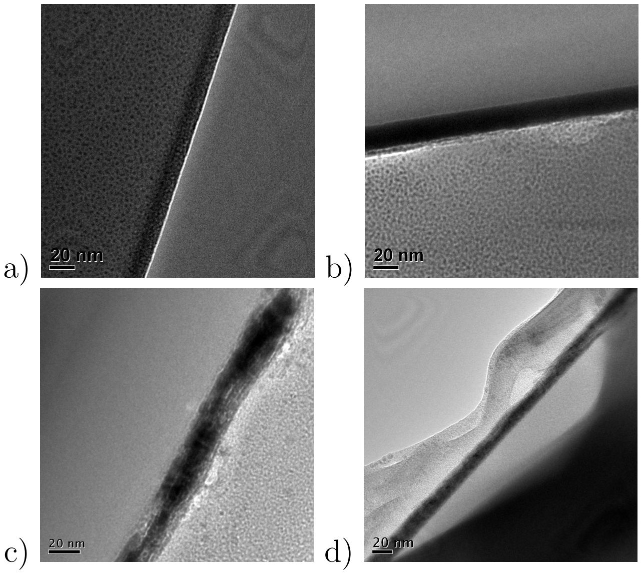

Figure 5.11: Cross-sectional TEM images of a) Fe15s $V_{EH} = 0$ V, b) Fe15s $V_{EH} = 35$ V, c) Fe15s $V_{EH} = 50$ V, d) Fe15s $V_{EH} = 70$ V

Table 5.2: Average nanocrystallite size (σ) and film thickness (d) determined from Rietveld refinement of the GIXRD patterns, ImageJ analysis of in-plane dark field TEM images, and Leptos fitting of the XRR patterns.

	V_{EH} (V)	σ_{XRD} (nm)	σ_{TEM} (nm)	d_{TEM} (nm)	d_{XRR} (nm)
Fe(60s)	0	5 ± 1	2 ± 1	26 ± 1	24 ± 1
	30	3 ± 1	2 ± 1	27 ± 1	28 ± 1
	50	3 ± 1	2 ± 1	27 ± 1	27 ± 1
	70	2 ± 1	2 ± 1	18 ± 1	16 ± 2
Fe(30s)	0	5 ± 1	2 ± 1	13 ± 1	20 ± 2
	30	4 ± 1	2 ± 1	20 ± 1	23 ± 1
	50	4 ± 1	3 ± 1	24 ± 1	24 ± 1
	70	3 ± 1	3 ± 1	11 ± 1	15 ± 2
Fe(15s)	0	4 ± 1	3 ± 1	17 ± 1	20 ± 1
	30	4 ± 1	3 ± 1	17 ± 1	19 ± 1
	50	4 ± 1	3 ± 1	22 ± 1	21 ± 1
	70	2 ± 1	2 ± 1	10 ± 1	8 ± 3

Selective area electron diffraction (SAED) images were collected to further determine the microstructure of the thin films (Figs. 5.12 - 5.15). The d-spacings obtained from the diffraction rings using ImageJ[42] (see Section 2.2.4) were in good agreement with the reflections obtained from GIXRD patterns. Furthermore, no evidence for copper or iron oxides was observed. For all of the nanostructured thin films, broadened polycrystalline rings were observed, consistent with the morphology of iron nanocrystallites (with reduced structural long-range order) embedded in a cop-

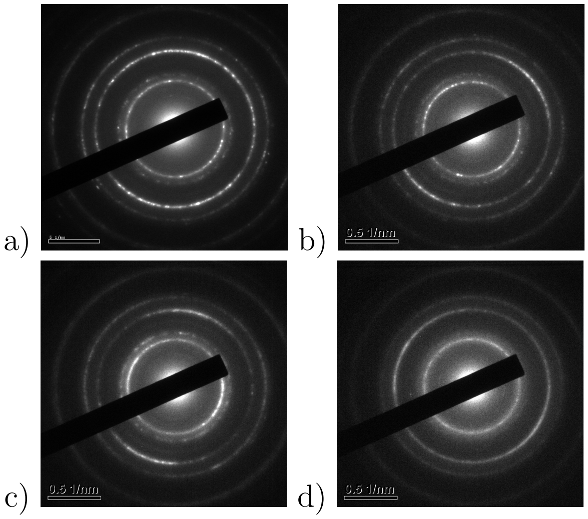

Figure 5.12: Selective area diffraction of a) Fe60s V$_{EH}$ = 0 V, b) Fe60s V$_{EH}$ = 35 V, c) Fe60s V$_{EH}$ = 50 V, and d) Fe60s V$_{EH}$ = 0 V,

per matrix, in addition to the increased amount of intermixing between the iron and copper phases, in agreement with XRR and cross-sectional TEM images.

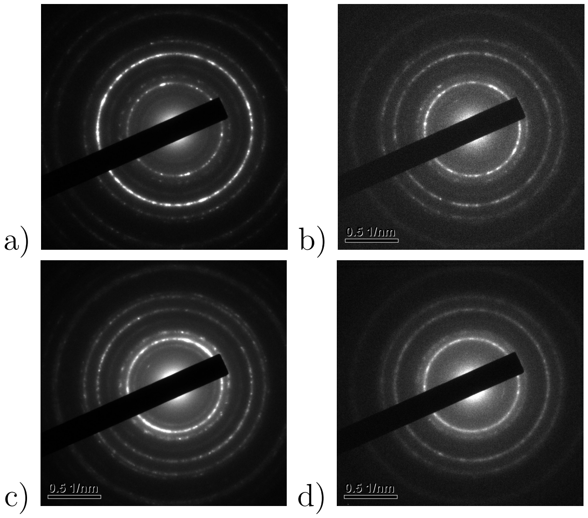

Figure 5.13: Selective area diffraction of a) Fe30s V$_{EH}$ = 0 V, b) Fe30s V$_{EH}$ = 35 V, c) Fe30s V$_{EH}$ = 50 V, and d) Fe30s V$_{EH}$ = 0 V,

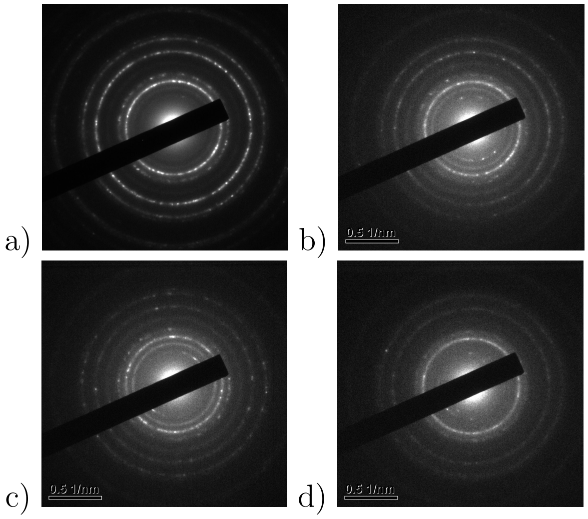

Figure 5.14: Selective area diffraction of a) Fe15s V$_{EH}$ = 0 V, b) Fe15s V$_{EH}$ = 35 V, c) Fe15s V$_{EH}$ = 50 V, and d) Fe15s V$_{EH}$ = 0 V,

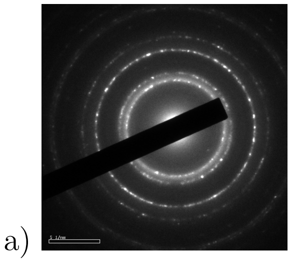

Figure 5.15: Selective area diffraction of the bilayer thin film

X-ray reflectometry (XRR) patterns (see Figs 5.16 to 5.19), using specular reflections, were collected between 0.2 and 6° 2θ and fit using the Leptos[41] software package. For the V$_{EH}$ = 0 V nanostructured films, fits to the data indicated that a multilayered structure was present. However, for the remainder of the films, the fits to the data using a multilayered structure was not possible, in agreement with cross-sectional TEM images (Fig. 5.9 - 5.11). The model used for the analysis of the V$_{EH}$ = 0 V film was of a unit consisting of an iron layer covered by a copper layer, repeated five times. The fit parameters allowed to vary were the thicknesses of the iron and the copper layers, where each iron(copper) layer thickness was coupled, as well as the interface roughness between these layers in addition to the silica/iron and copper/air interfaces. The thicknesses of each layer, determined from the fits were 2.43 ± 0.02 nm and 2.35 ± 0.02 nm for the copper and iron layers, respectively, in agreement with cross-sectional TEM. The remainder of the films could not be described using this simple model due to the lack of a multilayered structure (Fig. 5.20). Therefore, a modified "theoretical" sample was used where the sample's thickness was the total film thickness and the electron density was set as a weighted average depending on the ratio of iron to cobalt. The free parameters for these fits were the total thickness and the film/SiO_2 and film/air roughness. For all samples, the fitted total film thickness was in good agreement with the cross-sectional TEM images. The difficulties associated with describing the XRR patterns of the non-multilayered nanostructured films highlight the effects of the intermixing between the iron and copper atoms (the formation of FeCu alloy at the interface) indicating that both the amount of deposited iron and the *in situ* ion-beam bombardment had altered significantly the thin films morphology; these films were of iron nanocrystallites embedded in a copper matrix with an interfacial FeCu alloy.

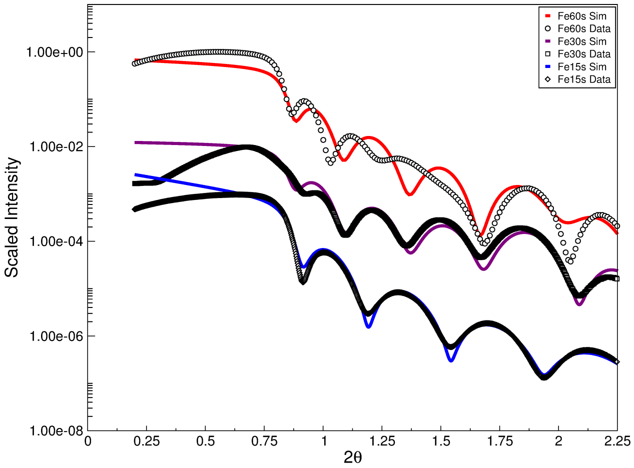

Figure 5.16: XRR scan of the $V_{EH} = 0$ V series of films. Simulations of the data were performed and the total film thickness obtained was in agreement with TEM results. Differences between the data and the fits are the result of difficulties in modeling the sample using only a multilayered structure. This model does not take into account the intermixing between the Fe and Cu forming an FeCu alloy.

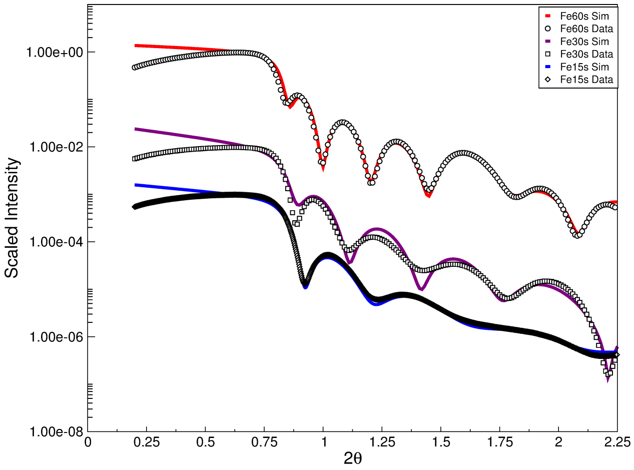

Figure 5.17: XRR scan of the $V_{EH} = 35$ V series of films. Simulations of the data were performed and the total film thickness obtained was in agreement with TEM results. Differences between the data and the fits are the result of difficulties in modeling the sample using a single layer with an electron density that is a weighted sum of Fe and Cu. This model does not take into account the microstructure of the films correctly and shows the limitations of XRR for studying non-multilayered films.

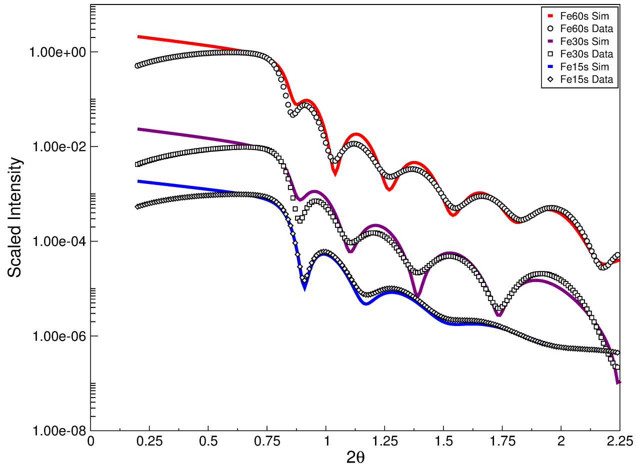

Figure 5.18: XRR scan of the $V_{EH} = 50$ V series of films. Simulations of the data were performed and the total film thickness obtained was in agreement with TEM results. Differences between the data and the fits are the result of difficulties in modeling the sample using a single layer with an electron density that is a weighted sum of Fe and Cu. This model does not take into account the microstructure of the films correctly and shows the limitations of XRR for studying non-multilayered films.

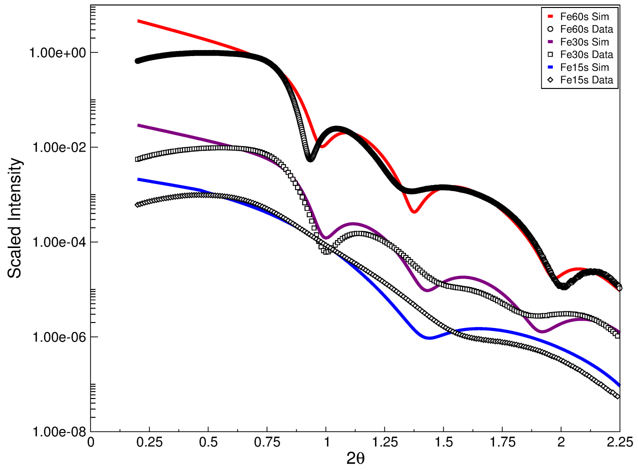

Figure 5.19: XRR scan of the $V_{EH} = 70$ V series of films. Simulations of the data were performed and the total film thickness obtained was in agreement with TEM results. Differences between the data and the fits are the result of difficulties in modeling the sample using a single layer with an electron density that is a weighted sum of Fe and Cu. This model does not take into account the microstructure of the films correctly and shows the limitations of XRR for studying non-multilayered films.

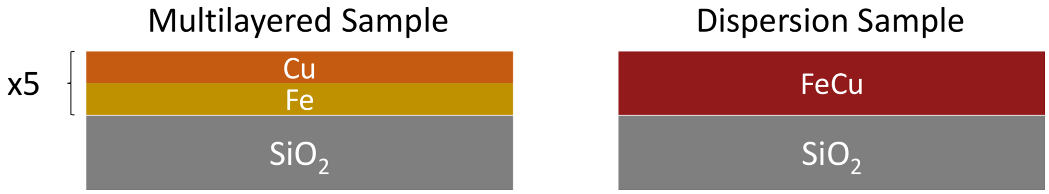

Figure 5.20: Left: model used to fit the multilayered samples. Right: model used to fit all other samples.

The microstructural analysis of these nanostructured thin films presented above indicate that these films fall into one of three categories: a multilayered film ($V_{EH} = 0$ V series), a nanostructured dispersion (e.g. amorphous iron nanocrystallites embedded in a copper matrix) ($V_{EH} = 70$ V series), and an intermediate series ($V_{EH} = 35$-50 V series) of films where some multilayered character remains and amorphous iron nanocrystallites are present. The composition from several samples from each of these categories will be explored in more detail using γ-ray and x-ray spectroscopic techniques (CEMS and XAS). These experiments will provide further insight into the effects of the *in situ* ion-beam bombardment on the microstructure and composition of these nanostructured thin films.

Conversion electron Mössbauer spectroscopy (CEMS) experiments were performed, at room temperature, on five of the nanostructured thin films to further identify the nature of the interfacial alloy and definitively establish or exclude the presence of an iron oxide phase. These five films represent the three different morphologies observed from the microstructural investigations: two multilayered samples (Fe60s $V_{EH} = 0$ V and Fe30s $V_{EH} = 0$ V), a film with a dispersion morphology (Fe60s $V_{EH} = 70$ V), and two intermediate films (Fe15s $V_{EH} = 0$ V and Fe15s $V_{EH} = 50$ V). Spectra were collected between a velocity scale of ± 6 mm s^{-1} in order to identify any possible ferro- or ferri-magnetic iron oxide present as well as to observe α-Fe, if present. This velocity scale was chosen so that the six line sextet ($B_{HF} = 33$ T) of α-Fe would be observable, in addition; this velocity scale was large enough to show the presence of a ferro- or ferri-magnetic iron oxide. Due to the nanocrystalline nature of these films, one needs to rule out the presence of superparamagnetic iron oxides. As seen in the collected spectra (Fig. 5.21), there was no evidence for a measurable sextet indicating that α-Fe was not present. Furthermore, the characteristic hyperfine field parameters of ferro- or ferri-magnetic iron oxides were not present, indicating definitively that the films did not contain these oxides; superparamagnetic iron oxides, such as maghemite (γ-Fe_2O_3) and magnetite (Fe_3O_4) have unique isomer (δ) and electric quadrupole (Δ) shifts which enables their identification[59]. To determine the hyperfine parameters of the observed spectra, they were described using Lorentzians to represent singlets or doublets (as described in 2.5.2, relative to a $\sim$6 μm foil of α-Fe), the results of these fits are summarized in table 5.3.

The hyperfine parameters, determined from the fits of the CEMS spectra, as a function of intermixing (e.g. film disorder) are plotted in figures 5.22. Two spectral features, two doublets (Δ_1 and Δ_2) or a doublet (Δ_1) and a singlet (δ_1), were necessary to fit the multilayered and intermediate sample's spectra, whilst only a doublet (Δ_1) was necessary to fit the dispersion film. As the disorder of the films increased from an increased *in situ* ion-beam bombardment energy or the reduced amount of deposited iron (reduced formation of individual iron nanocrystallites), the fitted Γ (Fig. 5.22) increased. This broadening of the spectral features is the result of the increased number of inequivalent Fe sites, similar to those found in amorphous FeCu alloys (in agreement with GIXRD patterns).[96]. The δ and Δ for the first spectral component (δ_1 and Δ_1, Fig. 5.22) are equivalent with that of paramagnetic Fe in a disordered FeCu alloy, and do not agree with those observed for the iron oxides.[59] With increased film disorder, an increase of δ and Δ was observed suggesting that the FeCu alloy component becomes increasingly disordered, in agreement with the observed effects of the secondary *in situ* ion-beam bombardment or the reduced amount of deposited iron which increased the amount of intermixing between the iron nanocrystallites and the copper matrix. The second spectral com-

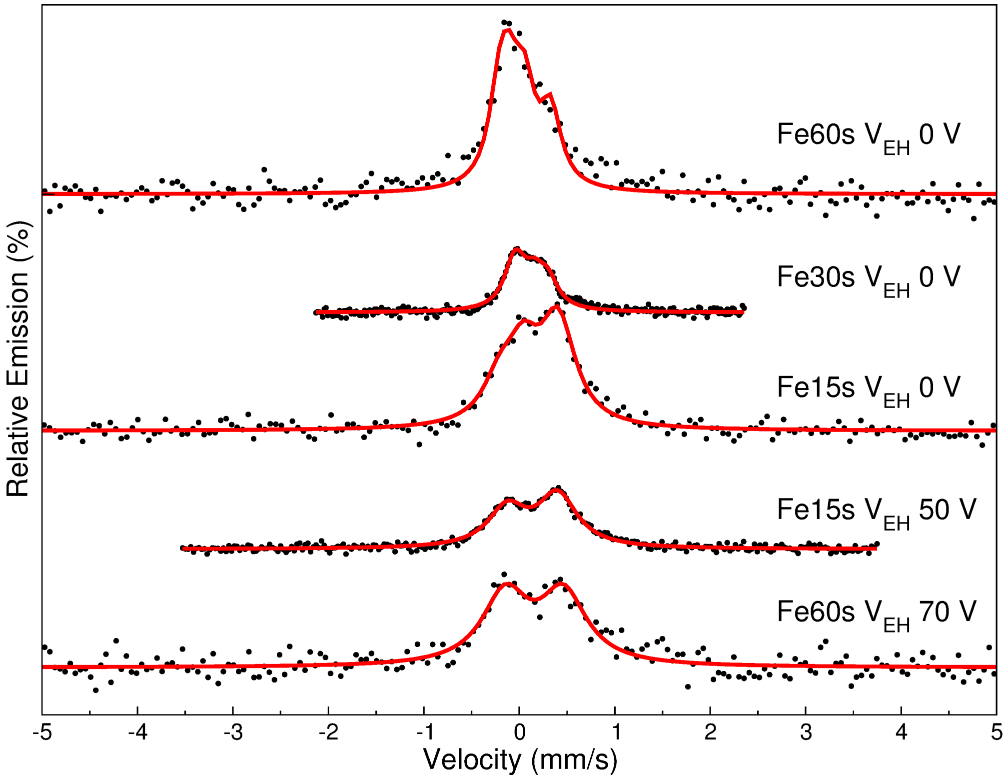

Figure 5.21: CEMS spectra collected at 300 K plotted as relative emission as a function of velocity. A direct comparison of the relative emission between samples was not possible as the distance of the source-absorber-detector system was different from sample to sample due to the thickness of the sample, and the detector efficiency may have been different between samples.

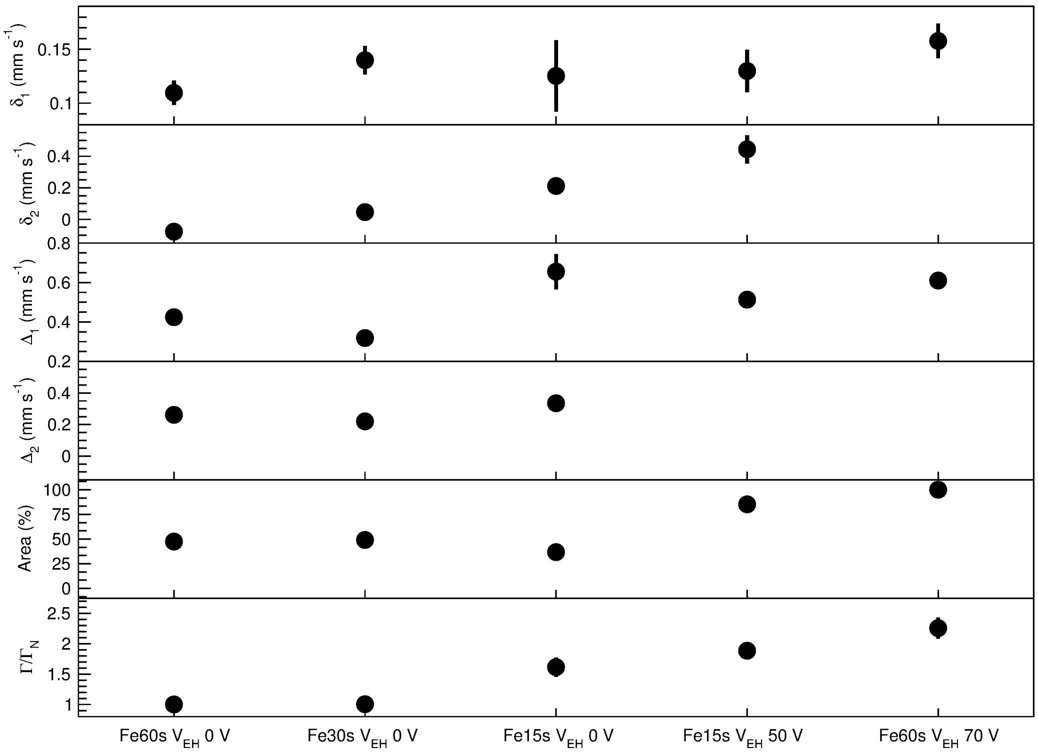

Figure 5.22: Hyperfine parameters obtained from fits of the CEMS spectra as described in the text as a function of the disorder in the film. The area of the first spectral component as a function of nanocrystallite disorder is shown above. The area of the second spectral component is $100 - x$, where x is the area of the first spectral component. The Γ has been normalized to the natural linewidth of the source, Γ_N. An increase in Γ/Γ_N indicates an increase in disorder.

ponent represents the iron nanocrystallites in the form of γ-Fe (δ_2 and Δ_2). This γ-Fe component is only observed in the Fe60s $V_{EH} = 0$ V and Fe30s $V_{EH} = 0$ V films. For the Fe15s $V_{EH} = 0$ V, the fitted hyperfine parameters indicate that the formation of γ-Fe nanocrystallites had been hindered due to the reduced amount of deposited iron, and only the disordered FeCu alloy formed. The two doublets needed to fit correctly this spectra represent the effects of the number of Fe nearest neighbors. The doublet with a $\delta = 0.21 \pm 0.02$ mm s^{-1} and $\Delta = 0.34 \pm 0.05$ mm s^{-1} is representative of the Fe atoms with a majority (3 to 5) of Fe nearest neighbors while the doublet with $\delta = 0.13 \pm 0.03$ mm s^{-1} and $\Delta = 0.66 \pm 0.09$ mm s^{-1} is representative of the Fe atoms with a minority (1 or 2) of Fe nearest neighbors (e.g. a more disordered Fe component)[110]. The Fe15s $V_{EH} = 50$ V spectra shows clearly that two components are needed to describe it correctly. The hyperfine parameters of the doublet component are similar to the other films; Fe in a disordered FeCu alloy. The singlet which has $\delta = 0.44 \pm 0.09$ mm s^{-1} is likely that of Fe in FeCu alloy with more then 5 Fe nearest neighbors. Although this δ is similar to that of Hematite ($\delta = 0.38$ mm s^{-1})[59], a $\Delta = 0.12$ mm s^{-1} for Hematite was not present. For the dispersion film (Fe60s $V_{EH} = 70$ V), only a single doublet was necessary to describe the spectrum completely, indicating that the Fe in the FeCu alloy was in a completely disordered state (largest Γ too).

The observed spectral features from the fitted CEMS spectra show clearly that with increased secondary ion-beam bombardment energy (V_{EH}) or with the reduction in deposited iron, the nanostructured films transform from a multilayered morphology to a dispersion-like morphology. Furthermore, these CEMS spectra show definitively that iron oxides have not formed during film deposition or afterwards.

Table 5.3: Conversion electron Mössbauer spectra fit results. Two spectral components were used to fit the collected spectra. The line width (Γ), isomer shift (δ), and the quadrupole shift (Δ) were fit parameters.

	Component	Γ (mm/s)	δ (mm/s)	Δ (mm/s)
Fe60s $V_{EH} = 0$ V	Doublet	0.13	0.11 ± 0.01	0.42 ± 0.02
	Doublet	0.13	-0.08 ± 0.01	0.26 ± 0.02
Fe30s $V_{EH} = 0$ V	Doublet	0.131 ± 0.008	0.14 ± 0.01	0.32 ± 0.02
	Doublet	0.131 ± 0.008	0.05 ± 0.01	0.22 ± 0.02
Fe15s $V_{EH} = 0$ V	Doublet	0.21 ± 0.02	0.13 ± 0.03	0.66 ± 0.09
	Doublet	0.21 ± 0.02	0.21 ± 0.02	0.34 ± 0.05
Fe15s $V_{EH} = 50$ V	Doublet	0.25 ± 0.01	0.13 ± 0.02	0.61 ± 0.03
	Singlet	0.25 ± 0.01	0.44 ± 0.09	0
Fe60s $V_{EH} = 70$ V	Doublet	0.29 ± 0.02	0.16 ± 0.02	0.51 ± 0.03

To characterize the Fe and Cu coordination environments and element-specific magnetism, XAS and XMCD experiments were performed over the Fe (700-740 eV) and Cu (920-970 eV) $L_{3,2}$ ($2p \rightarrow 3d$) transition edges ($L_{3,2}$-edges), using TEY and TFY, for the Fe60s $V_{EH} = 0$ and 35 V samples, the Fe30s $V_{EH} = 0$, and 70 V samples, and the Fe15s $V_{EH} = 0$ and 50 V samples. These samples represent the different morphologies observed from GIXRD, TEM, SAED, and cross-sectional TEM experiments and provide an overview of the elemental magnetism for all the samples studied by magnetometry and susceptometry. For these element-specific experiments, both the TEY and TFY spectra were collected at 10 K. No charging effects were observed indicating that the films were conductive. The TEY spectra is a surface sensitive probe of the absorption spectra (penetration depth of 2-3 nm at these energies)[77] and the TFY spectra is capable of probing deeper into the sample (a few hundred of nanometers). Generally, for thick samples, TFY suffers from self-absorption effects that decrease the relative spectral intensities associated with the different transitions that are measured[51]. However, for thin samples such as these nanostructured thin films (thicknesses < 30 nm), self-absorption is not an issue, and the TFY spectra are representative of the entire film.

The XAS collected at the Fe edge (TEY and TFY) showed two groups of spectral features; peaks at $\sim$710 eV and $\sim$725 eV from the L_3- and L_2-edges, respectively. The collected Fe TEY spectra were similar to that of Fe^{3+} in either an octahedral or tetrahedral coordination environment. A comparison to a collected Fe TEY spectra of γ-Fe_2O_3 showed significant overlap (Fig. 5.23). These spectral features typically suggest that an iron oxide was present, having formed potentially from the passive

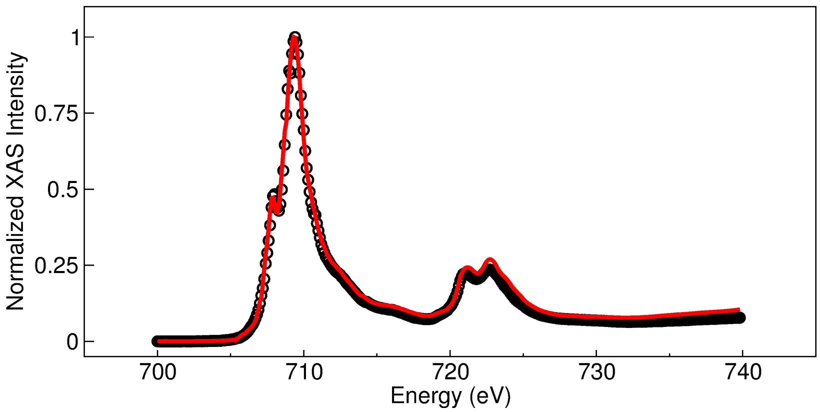

Figure 5.23: Comparison plot of XAS spectra of Fe60s $V_{EH} = 0$ V (black) and a maghemite (red) XAS spectra collected previously. The significant overlap indicates clearly that the Fe in the Fe60s film is Fe^{3+} in an octahedral or tetrahedral coordination environment.

oxidation of the surface of the sample. However, such an interpretation would contradict the other microstructural and magnetic experiments performed on these films which indicated that there was no iron oxide present. A straightforward experiment that can be performed to exclude the presence of an iron oxide near the surface of the film is to perform angular dependent Fe TEY XAS scans. These spectra were collected with incident angles between 20° and 60° measured relative to the plane of the film (Fig. 5.24). For the observed spectral features to be the result of surface oxidation, we would expect that as the x-rays penetrate deeper into the sample from the increased incident angle (a more normal incident angle) the spectral features corresponding to iron with an oxidation state compared to metallic iron would decrease in intensity. However, we observed no change in the shape or intensity of the spectral features for Fe with incident angle, indicating clearly that these effects were not due to surface oxidation. The Cu TEY spectra measured over the same range of incident angles similarly showed no change in the shape of the spectral features indicating sim-

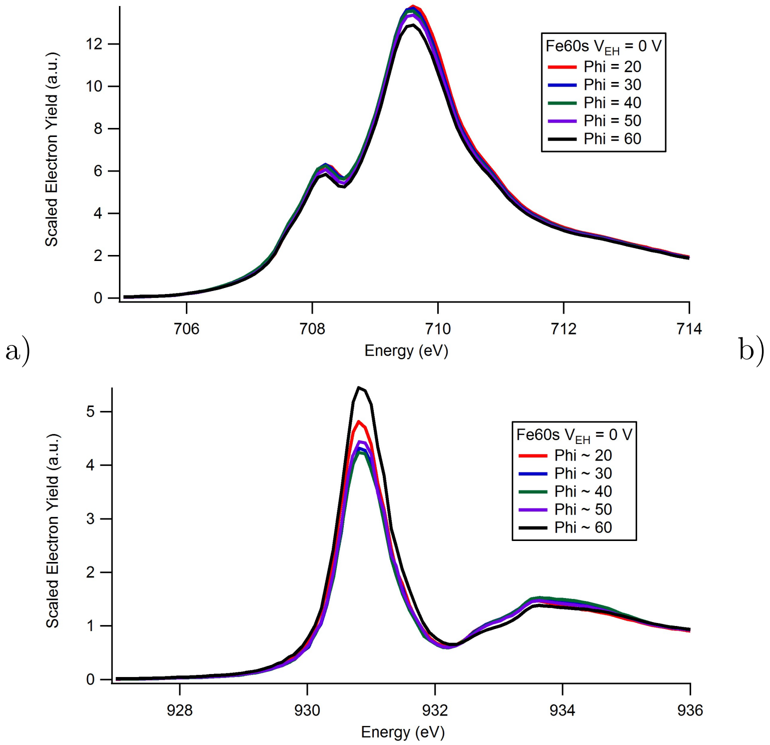

Figure 5.24: Angular dependence of the a) Fe and b) Cu TEY XAS.

ilar effects. These results suggest that the Fe^{3+} and Cu^{2+} character was continuous throughout the measurable component of the film by TEY. For the observed spectral components to be due to oxidized Fe throughout the film, oxygen would have to have been present during the film deposition. If this were to have occurred, Fe-oxides such as maghemite (γ-Fe_2O_3) and magnetite (Fe_3O_4) having spinel crystal structures which differ from the simple cubic structures of metallic Fe significantly would have been readily observable with GIXRD and SAED experiments. Furthermore, for iron oxides, the relative intensities of the maxima at ~707 eV (Iα) and ~710 eV (Iβ), which vary with A- an B-site occupancies, provide compositional information. An Iα/Iβ of 0.33 and 0.62 has been measured for γ-Fe_2O_3 and Fe_3O_4, respectively[111].

A measured Iα/Iβ of ∼0.5 supports our claim that the observed Fe TEY XAS spectra is not from an iron oxide (Fig. 5.25a), consistent with the other compositional information. Therefore, we conclude that the Fe^{3+} observed in the Fe TEY (and TFY) spectra are the result of the alloying of Fe and Cu resulting in an alteration of the local electronic environment around the Fe atoms.

The Fe TFY XAS L$_3$-edge (Fig. 5.25c) for the iron rich samples (Fe60s and Fe30s samples) appears to be predominately that from metallic Fe (spectral feature at ∼707 eV), however, a small component from iron in the FeCu alloy is present (∼710 eV). Unlike the Fe TEY experiments which show no change in the relative intensities of these two components as the relative amounts of copper compared with iron near the surface of the films was altered, the TFY spectral features changed significantly with iron content or *in situ* ion-beam bombardment. With the reduction in iron content, or an increase in the amount of intermixing from the increased V$_{EH}$, the

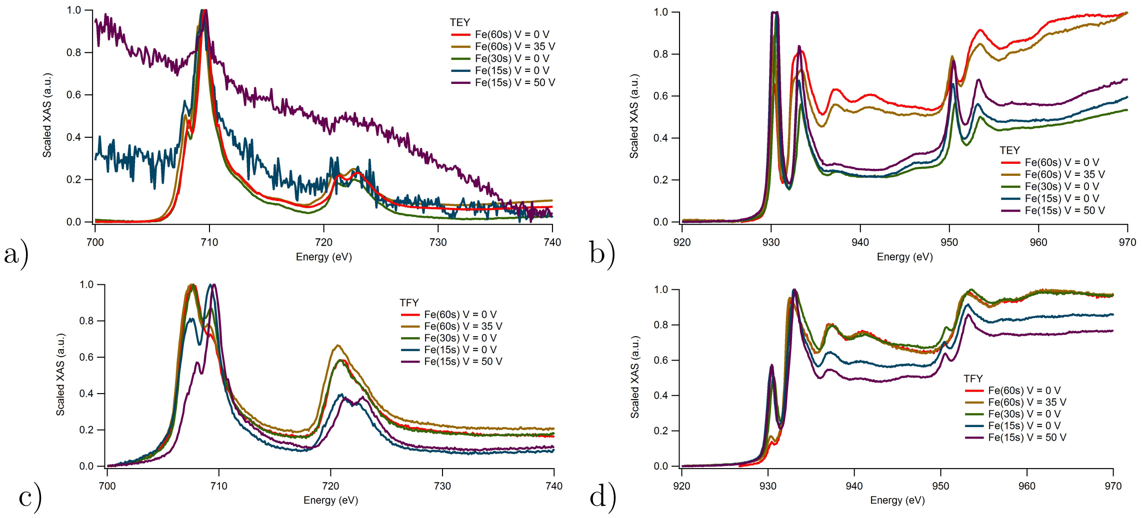

Figure 5.25: Scaled XAS spectra for a) Fe TEY, b) Cu TEY, c) Fe TFY, and d) Cu TFY.

TFY spectra become less metallic-like as the Fe^{3+} component increased in intensity relative to the metallic Fe component. These changes in the Fe TFY spectral features were the result of the increased intermixing promoted by the larger V_{EH} during the *in situ* ion-beam bombardment which resulted in the increased formation of the interfacial FeCu alloy component.

The Cu XAS spectra collected using both the TEY and TFY are shown in figure 5.25b and d. Similar to the Fe spectra, the Cu spectra show two groups of spectral features at ~930 eV and ~950 eV from the L_3 and L_2 transition edges, respectively. The Cu TEY and TFY L_3-edge spectra were a combination of metallic Cu and Cu^{2+} with the Cu^{2+} spectral features likely being a combination of Cu in the FeCu interfacial alloy and a small component from surface oxidized copper not measurable by GIXRD or SAED (e.g. CuO). As the amount of copper at the surface of the nanostructured thin films was the same for all samples (a copper capping layer was deposited for 60s for all samples), the change in the intensity of the Cu^{2+} spectral feature was likely the result of a change in the amount of interfacial FeCu alloy formed as the amount of deposited iron decreased or the V_{EH} increased. Furthermore, the metallic Cu component decreased in intensity with the increased formation of FeCu alloy.

5.4 Magnetometry and Susceptometry

As has been shown previously (Ch. 3), the magnetism of γ-Fe_2O_3 nanoparticles was affected significantly by a copper shell. Here we study the effect of a copper matrix on the magnetism of iron nanocrystallites in the form of a nanostructured thin film.

In this case, iron was used so that the effects of the intimate contact between iron and copper could be explored in a relatively straightforward system that didn't suffer from broken coordination at the surface such as with the γ-Fe_2O_3 nanoparticles. In keeping with the theme presented in chapters 3 and 4, the interface effects between the iron nanocrystallites and the copper matrix were studied in detail.

The temperature dependence of the susceptibility ($\chi_{DC} = M/\mu_0 H$) was measured in the zero-field-cooled (ZFC) and field-cooled (FC) states with an applied field of 10 mT (see Figs. 5.26 - 5.28). For all samples, the susceptibilities' temperature dependent behaviour was phenomenological similar. For the multilayered films (Fe60s, Fe30s, and Fe15s at $V_{EH} = 0$ V), the initial temperature dependence of the susceptibility, after ZFC, increased rapidly with warming as the magnetization of the iron nanocrystallites began to align with the applied field. At 40 K (Fe30s and Fe15s $V_{EH} = 0$ V) or 50 K (Fe60s $V_{EH} = 0$ V) a maximum in the $\chi_{DC}^{ZFC}(T)$ was reached. Here, the majority of the iron nanocrystallites magnetization was aligned with the applied field. With further warming, the magnetization of the iron nanocrystallites began to fluctuate faster than the time-window of the *dc* experiment resulting in a decrease in the time-averaged susceptibility. The temperature at which this decrease begins to occur is frequency dependent as observed from χ_{AC} susceptibility experiments (see Figs. 5.32 - 5.34). Furthermore, as we will discuss later in this section, the coercivity (Fig. 5.38) and remnant magnetizations (see Figs. 5.35 - 5.37) above this temperature are zero. Altogether, these results indicate that this temperature dependent behaviour describes the blocking of the iron nanocrystallites. As the system is warmed further, the susceptibility continued to decrease. This decrease was monotonic for the Fe60s $V_{EH} = 0$ V film until ∼300 K. Above this temperature, the susceptibility decreased rapidly as the interfacial FeCu alloy (observed from XAS experiments) became paramagnetic and marks a Curie temperature of the alloy, $T_{C,Alloy}$. However, a small measurable $\chi_{DC}(T)$ from the smallest, exchange coupled, iron nanocrystallites no longer being pinned by the interfacial FeCu alloy interactions again contribute to the overall susceptibility measured. The $T_{C,Alloy}$ for all of the nanostructured thin films was determined from the minimum in the calculated $d\chi_{DC}^{ZFC/FC}(\mathrm{T})/dT$ (see Figs. 5.29 - 5.31), and the $T_{C,Alloy}$'s are consistent with their composition and microstructure. For the Fe30s $V_{EH} = 0$ V film, a change in slope at ∼175 K is the result of increased overlap of the dynamical freezing nanomagnetism associated with the blocking behaviour of the iron nanocrystallites and the $T_{C,Alloy}$ of the interfacial FeCu alloy (mirrored in the $\chi_{AC}(\mathrm{T},\nu)$ susceptibility scans). Above this temperature, the susceptibility decreases rapidly, similar to the Fe60s $V_{EH} = 0$ V film. This overlap between these two competing processes is further enhanced in the Fe15s $V_{EH} = 0$ V film, T_B and $T_{C,Alloy}$ overlap completely and can no longer be distinguished uniquely (also observed in $\chi_{AC}(\mathrm{T},\nu)$ susceptibility scans). The $\chi_{DC}^{FC}(T)$ traced the $\chi_{DC}^{ZFC}(T)$ down to T_B where the two curves diverged as the iron nanocrystallites' magnetizations were no longer superparamagnetic and remained aligned with the applied field. For the intermediate films (Fe60s, Fe30s, and Fe15s with $V_{EH} = 35$ and 50 V), the $\chi_{DC}(T)$ behaves similar to the multilayered films. For these films, T_B is reduced slightly (∼10 K) to temperatures between 30 and 40 K and $T_{C,Alloy}$ is reduced also, resulting in a significant increase in the region of overlap of these two phenomena. The maximum in the $\chi_{DC}^{ZFC}(T)$ is broadened relative to the $V_{EH} = 0$ V series of films indicating that the increased intermixing promoted by the increased V_{EH} has likely altered the iron nanocrystallites volume distribution resulting in an increased distribution of blocking temperatures. We see this broadening increased further in the dispersion series of films (V_{EH} = 70 V).

$\chi_{DC}(T)$ susceptibility experiments on the nanostructured thin films has shown that the amount of intermixing induced by the *in situ* ion-beam bombardment has altered significantly the temperature dependence of the susceptibility. For the multilayered samples (V_{EH} = 0 V series), it is possible to identify uniquely both the T_B and the $T_{C,Alloy}$. However, with increased intermixing ($\mathrm{V}_{EH} > 0$ V), we observed an increase in the width of the $\chi_{DC}^{ZFC}(T)$ maximum, indicating that the distribution of the iron nanocrystallite volumes has been altered resulting in the increased distribution of blocking temperatures. With this increased distribution of blocking temperatures (interparticle magnetism), there begins to occur significant overlap between the blocking behaviour of the iron nanocrystallites and the transition to paramagnetism of the FeCu alloy. As a result of this overlap, it becomes increasingly difficult to separate these two processes. This overlap becomes complete in the V_{EH} = 70 V series of films. Similar effects are observed when considering the reduction in the amount of deposited iron (Fe60s to Fe30s to Fe15s, while keeping V_{EH} fixed). Here, the amount of iron affects the total volume of FeCu alloy in the film and as a result, the interfacial FeCu alloy is thinner resulting in an overall decreased $T_{C,Alloy}$ and an increased overlap between this temperature and T_B.

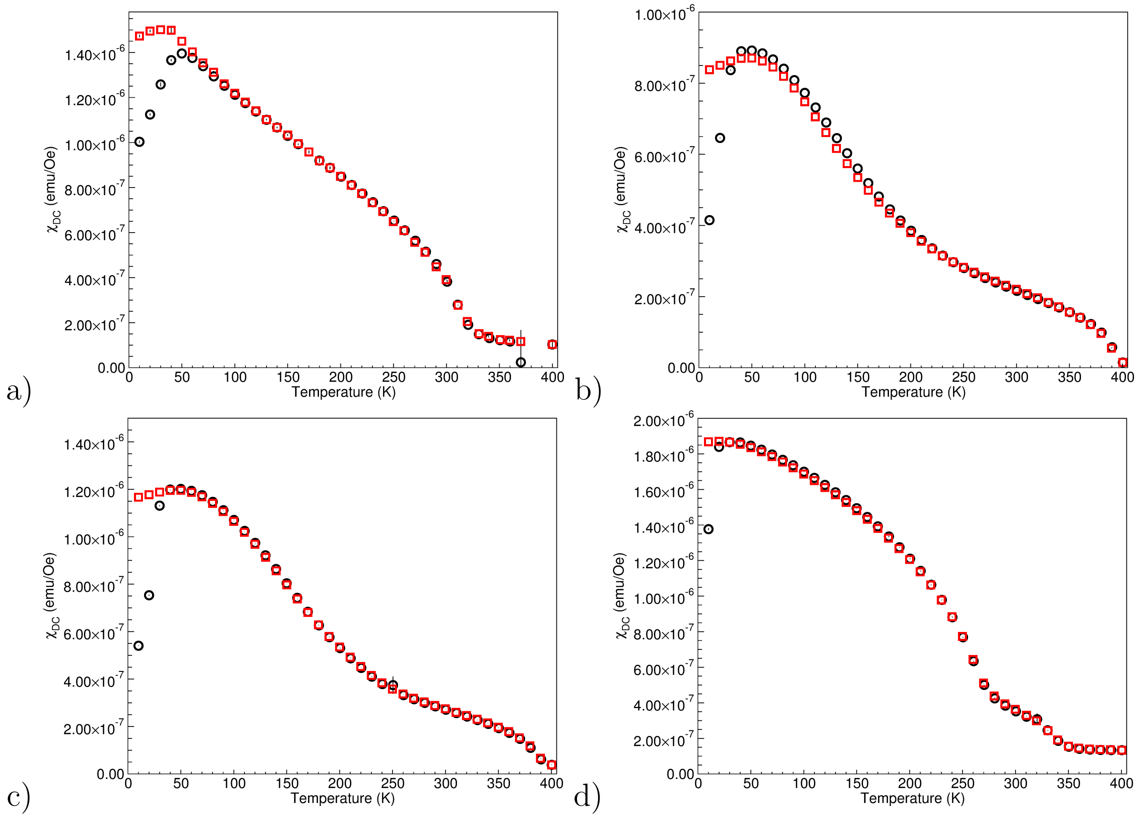

Figure 5.26: Temperature dependence of the χ_{DC}^{ZFC} (○) and χ_{DC}^{FC} (□). a) Fe60s V$_{EH}$ = 0 V, b) Fe60s V$_{EH}$ = 35 V, c) Fe60s V$_{EH}$ = 50 V, d) Fe60s V$_{EH}$ = 70 V

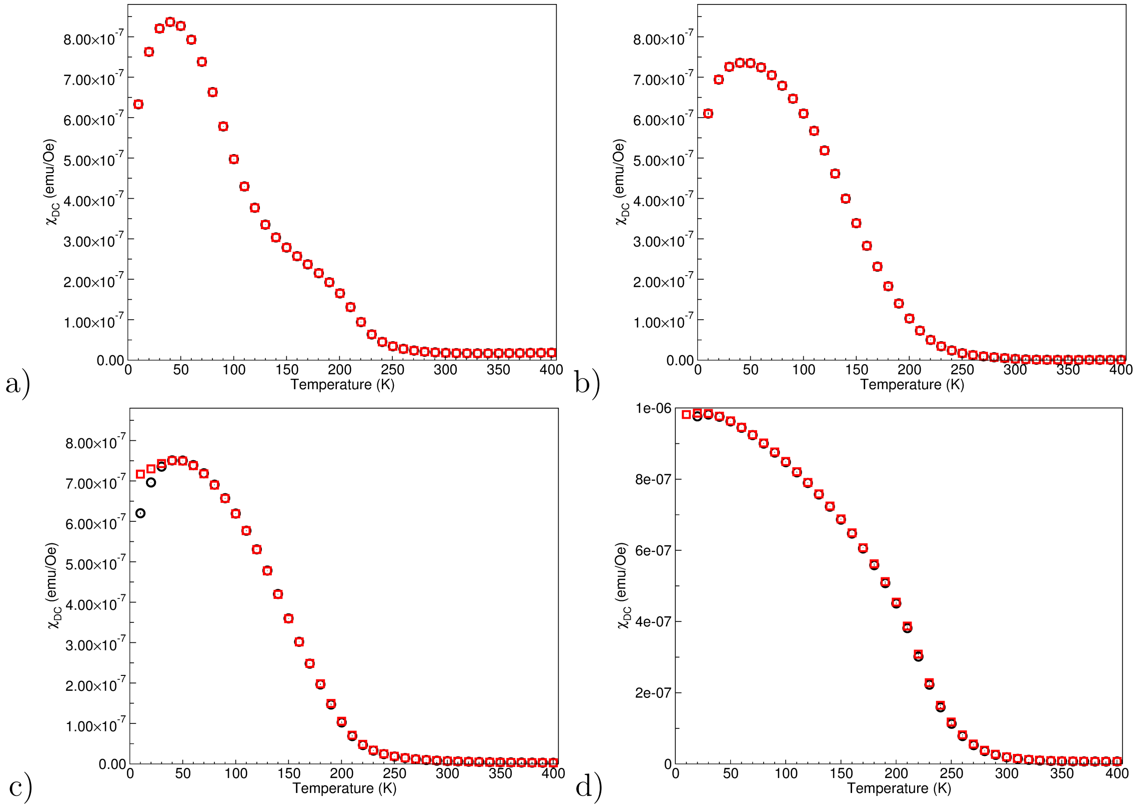

Figure 5.27: Temperature dependence of the χ_{DC}^{ZFC} (□) and χ_{DC}^{FC} (△). a) Fe30s $\mathrm{V}_{EH} = 0$ V, b) Fe30s $\mathrm{V}_{EH} = 35$ V, c) Fe30s $\mathrm{V}_{EH} = 50$ V, d) Fe30s $\mathrm{V}_{EH} = 70$ V

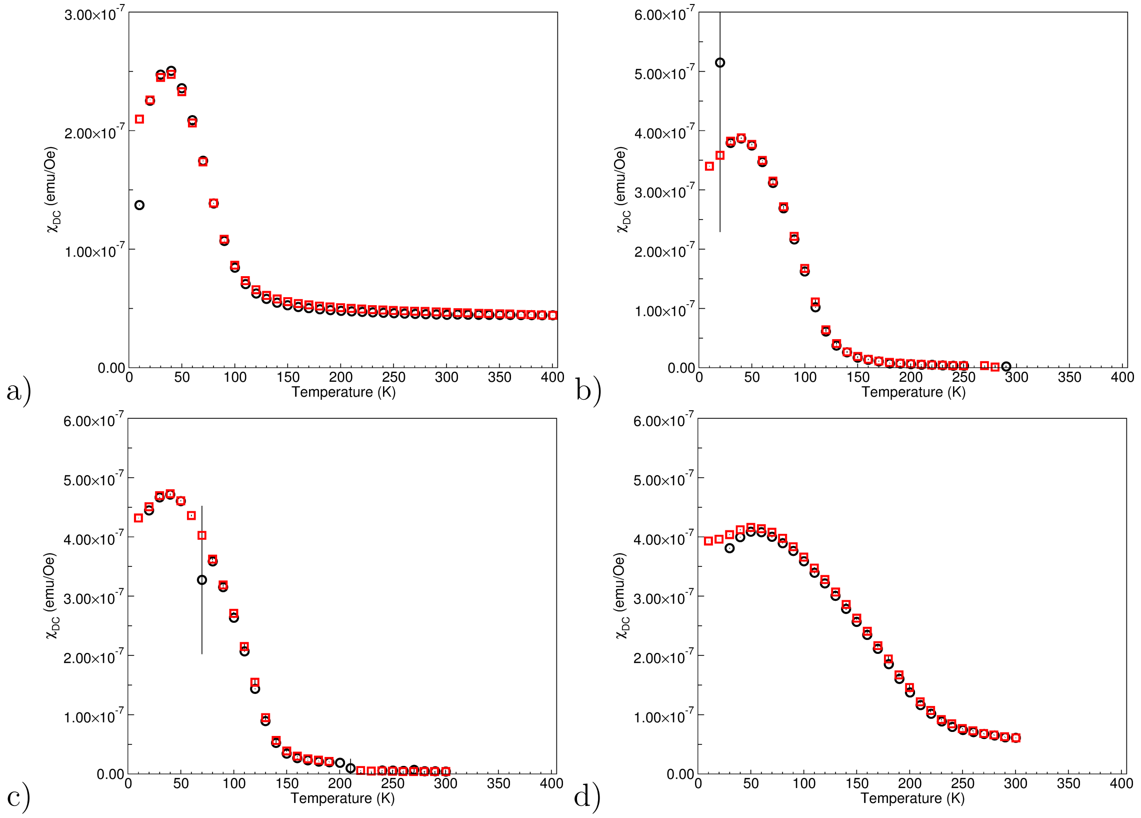

Figure 5.28: Temperature dependence of the χ_{DC}^{ZFC} (□) and χ_{DC}^{FC} (△). a) Fe15s V$_{EH}$ = 0 V, b) Fe15s V$_{EH}$ = 35 V, c) Fe15s V$_{EH}$ = 50 V, d) Fe15s V$_{EH}$ = 70 V

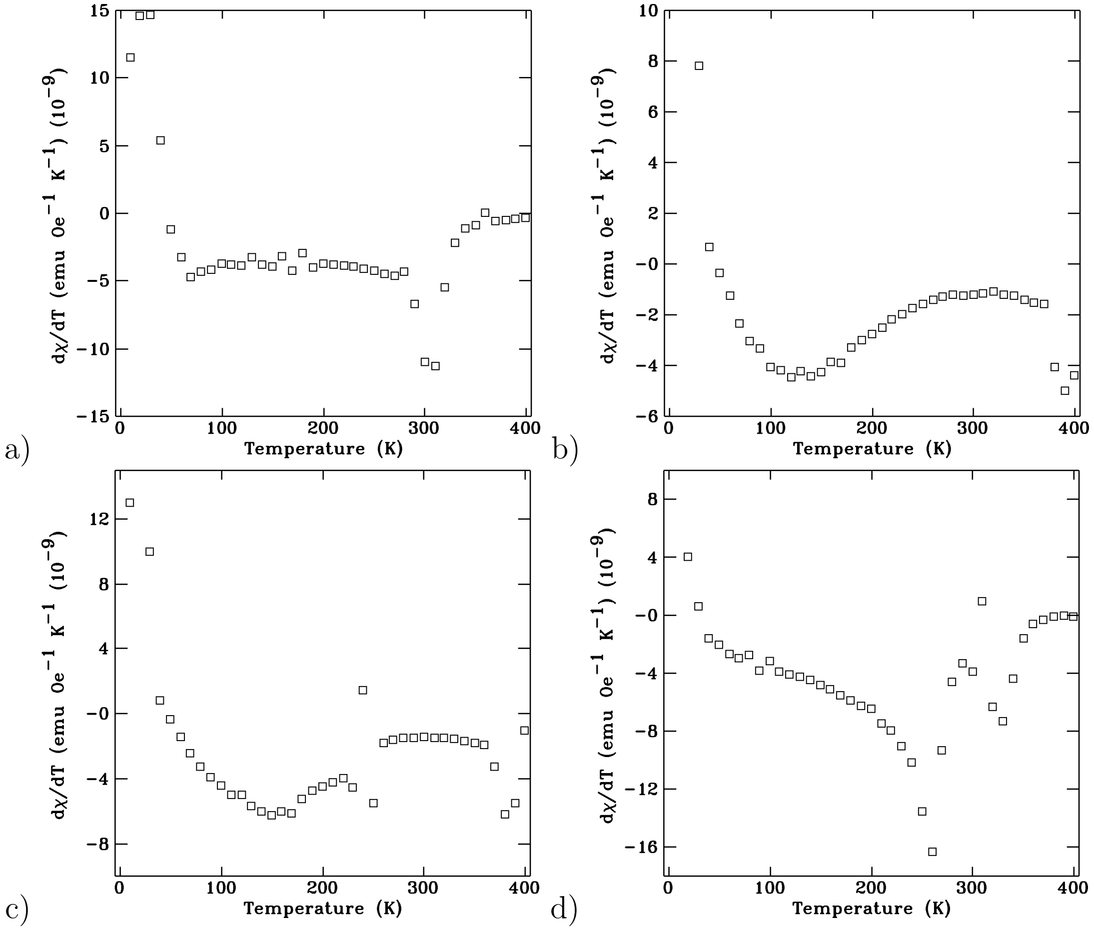

Figure 5.29: Temperature derivative of $\chi_{DC}(T)$ as a function of temperature for a) Fe60s V$_{EH}$ = 0 V, b) Fe60s V$_{EH}$ = 35 V, c) Fe60s V$_{EH}$ = 50 V, d) Fe60s V$_{EH}$ = 70 V,. The minimum occurs at $T_{C,Alloy}$ of the FeCu alloy.

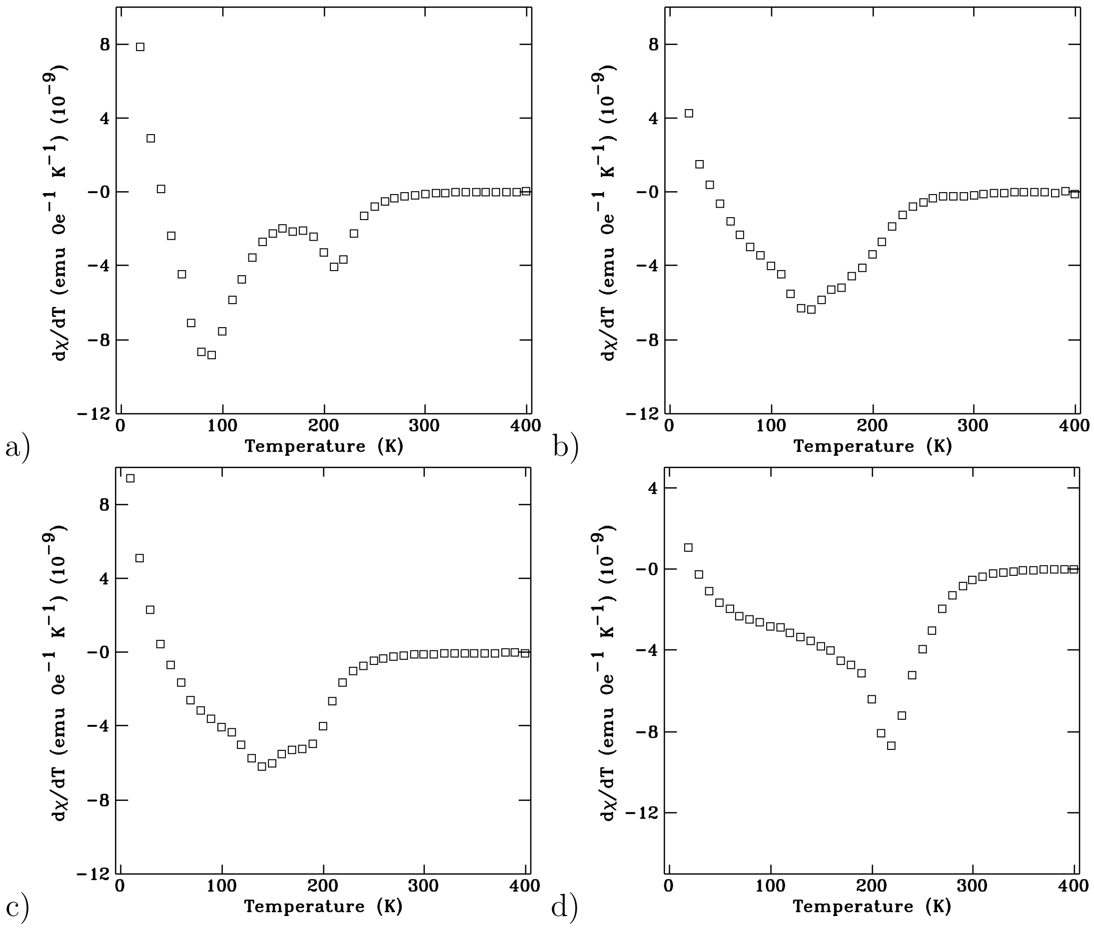

Figure 5.30: Temperature derivative of $\chi_{DC}(T)$ as a function of temperature for a) Fe30s V$_{EH}$ = 0 V, b) Fe30s V$_{EH}$ = 35 V, c) Fe30s V$_{EH}$ = 50 V, d) Fe30s V$_{EH}$ = 70 V,. The minimum occurs at $T_{C,Alloy}$ of the FeCu alloy.

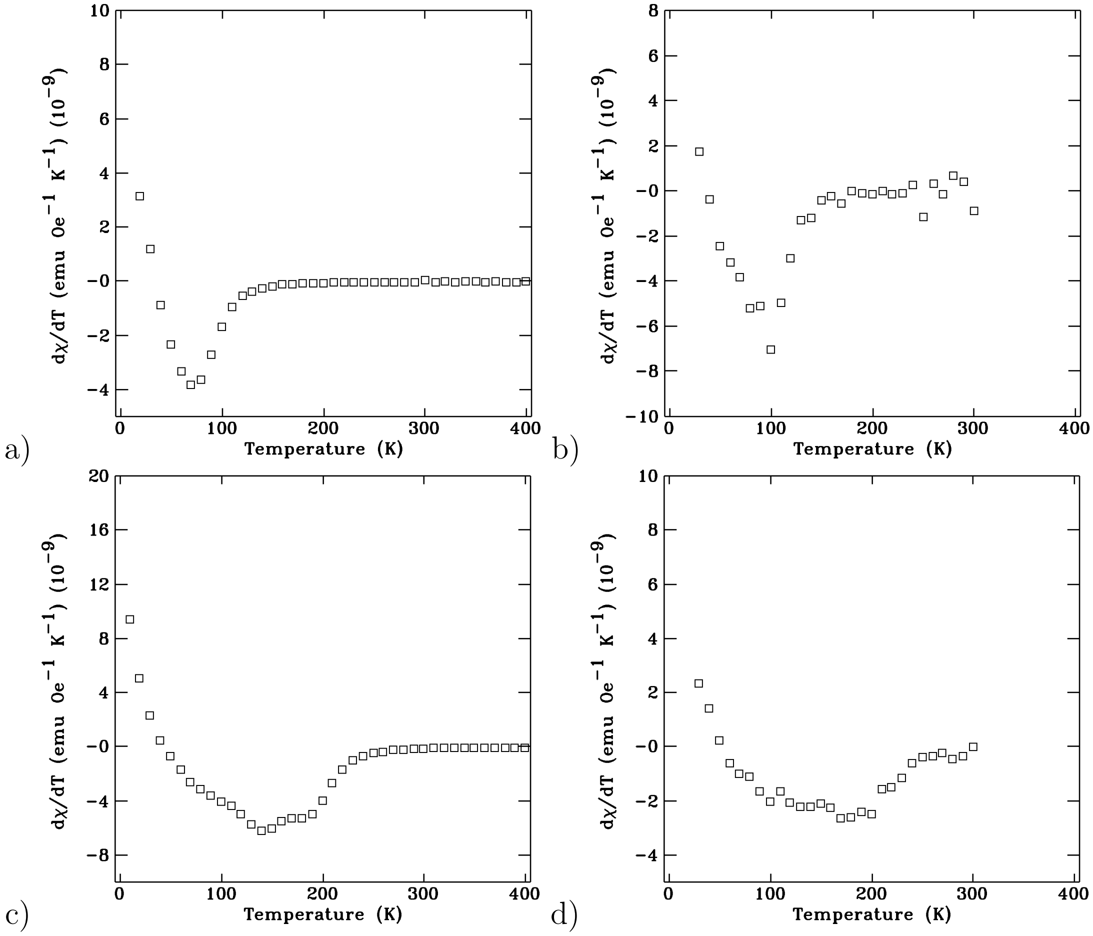

Figure 5.31: Temperature derivative of $\chi_{DC}(T)$ as a function of temperature for a) Fe15s V$_{EH}$ = 0 V, b) Fe15s V$_{EH}$ = 35 V, c) Fe15s V$_{EH}$ = 50 V, d) Fe15s V$_{EH}$ = 70 V,. The minimum occurs at $T_{C,Alloy}$ of the FeCu alloy.

To better ascertain the nature of the dynamical freezing associated with the nanostructured thin films T_Bs due to interparticle interactions, and the spin (moment) dynamics around $T_{C,Alloy}$ from intraparticle interactions, χ_{AC}(T,ν) measurements (after initially ZFC the system) using a 0.25 mT drive field at frequencies from ν = 10 to 1000 Hz were collected (see Figs 5.32 - 5.34). For the multilayered films (Fe60s, Fe30s, and Fe15s with V$_{EH}$ = 0 V), a gradual, frequency dependent increase of the in-phase component of the susceptibility (χ'_{AC}(T,ν)) with warming was observed. This is from the increased thermal energy which enabled the single-domain iron nanocrystallites' magnetizations to oscillate more rapidly around their easy axis direction (set by the uniaxial anisotropy). With continued warming, χ_{AC}(T,ν) increased in magnitude and became frequency dependent. T_B of these nanostructured films was determined from the maximum in the in-phase *ac* susceptibility. Above T_B, the nanocrystallites magnetizations' became superparamagnetic, and as these fluctuations increased with warming, the measured time-averaged magnetization decreased as the fluctuations became faster than the time-window of the drive (measuring) field, as observed by the frequency independent decrease of the in-phase component. With further warming, χ'_{AC}(T,ν) was reduced significantly as $T_{C,Alloy}$ was approached, above which there was no measurable in-phase susceptibility. The observed T_Bs and $T_{C,Alloy}$s for these nanostructured thin films are in agreement with χ_{DC} scans. Additional evidence of interparticle interactions was observed in the out-of-phase (χ''_{AC}(T,ν)) susceptibility for the nanostructured thin films which showed a single maxima with a strong frequency dependence near T_B, indicating that the maximum energy dissipation occurs when the *ac* drive field is comparable to the time scale of magnetization reversal below T_B.

A shift in the maxima to lower temperatures with reduced Fe content ($V_{EH} = 0$ V), indicates clearly a decrease in T_B, in agreement with $\chi_{DC}(T)$ scans. Additionally, the $T_{C,Alloy}$ also decreases to lower temperatures with a reduction in the amount of deposited Fe. For the Fe15s $V_{EH} = 0$ V film, both T_B and $T_{C,Alloy}$ overlap completely. The observed reduction in T_B is the result of the reduced iron nanocrystallite volume distribution (less deposited Fe results in smaller iron nanocrystallites) and with regards to the intraparticle interactions, the reduced $T_{C,Alloy}$ is likely the result of a reduction in the amount of intermixing between Fe and Cu due to the smaller iron nanocrystallite volume. The intermediate series of films (Fe60s, Fe30s, and Fe15s with V_{EH} = 35-50 V) show significant broadening of the χ'_{AC}(T,ν) maximum indicating that the increased intermixing has altered the anisotropy of the films. We also observe a reduction in the frequency dependent nature of the χ'_{AC}(T,ν) maximum compared with the multilayered films. Furthermore, this increased intermixing has resulted in a significant decrease in the out-of-phase component indicating a reduction in the energy dissipation; less hysteresis *inside* the Fe nanocrystallites. The overlap between T_B and $T_{C,Alloy}$ is also significantly increased due to more FeCu intermixing. The dispersion films (Fe60s, Fe30s, and Fe15s with $V_{EH} = 0$ V) show no measurable out-of-phase component and a significantly reduced frequency dependence of the maximum at T_B.

These susceptometry experiments provide further evidence that these nanostructured thin films consist of superparamagnetic iron nanocrystallites embedded in a copper matrix with an interfacial FeCu alloy. As the amount of intermixing is increased, a significant decrease in the frequency dependence of the χ'_{AC}(T,ν) was observed. Furthermore, the reduction in χ''_{AC}(T,ν) indicates that the energy dissipation is altered significantly by the increased intermixing.

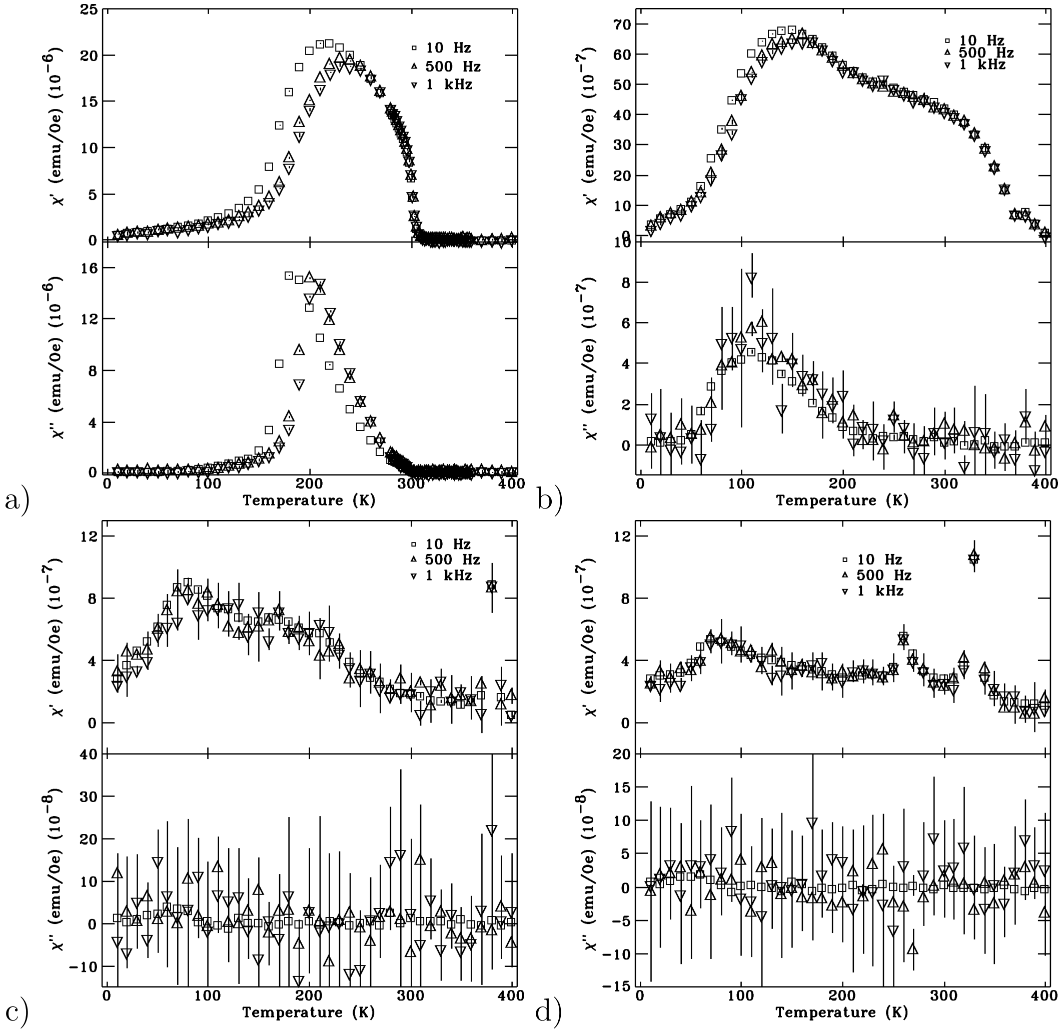

Figure 5.32: Temperature dependence of the in-phase $(\chi'_{ac})(T))$ and the out-of-phase $(\chi''_{ac})(T))$ for a) Fe60s V$_{EH}$ = 0 V, b) Fe60s V$_{EH}$ = 35 V, c) Fe60s V$_{EH}$ = 50 V, d) Fe60s V$_{EH}$ = 70 V. The frequency dependent maximum occurs at the blocking temperature (T_B) of the iron nanocrystallites.

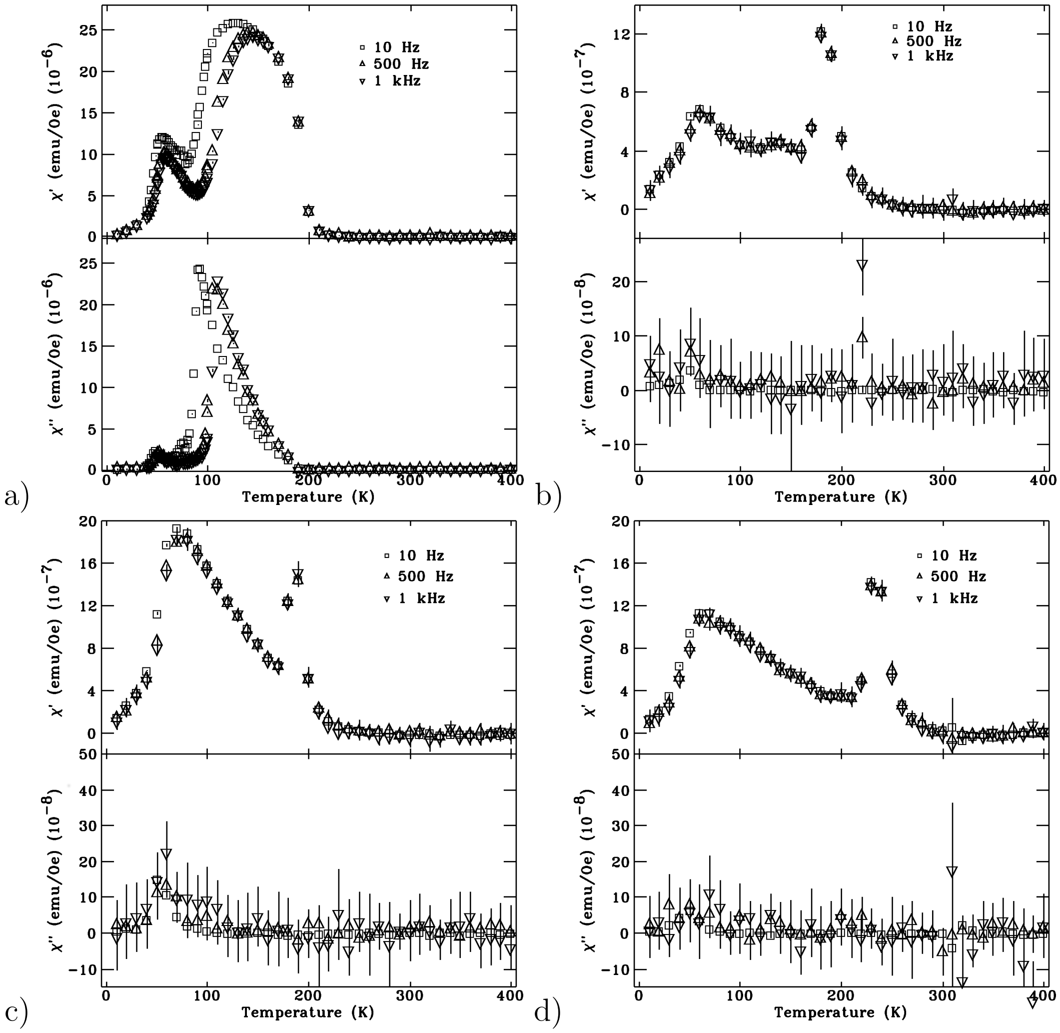

Figure 5.33: Temperature dependence of the in-phase $(\chi'_{ac})(T)$) and the out-of-phase $(\chi''_{ac})(T)$) for a) Fe30s V$_{EH}$ = 0 V, b) Fe30s V$_{EH}$ = 35 V, c) Fe30s V$_{EH}$ = 50 V, d) Fe30s V$_{EH}$ = 70 V. The frequency dependent maximum occurs at the blocking temperature (T_B) of the iron nanocrystallites.

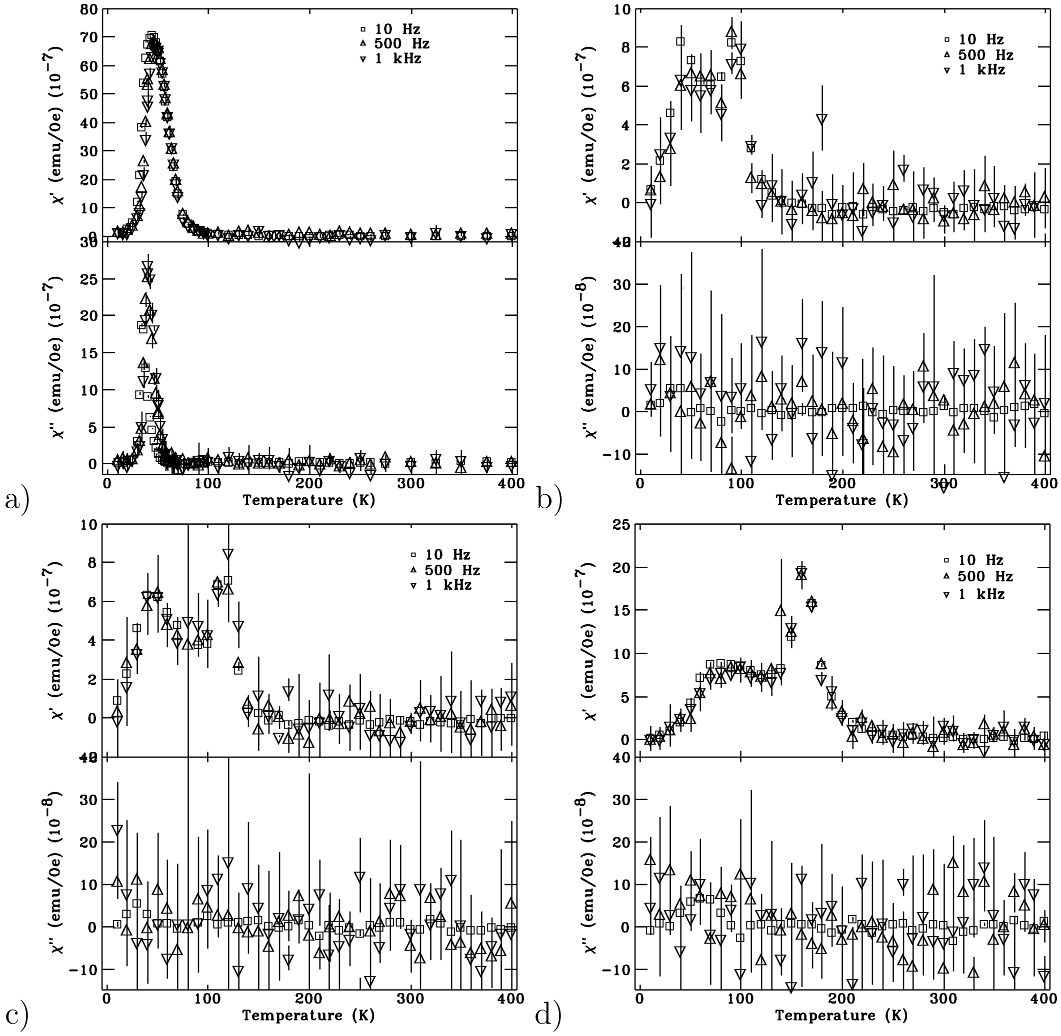

Figure 5.34: Temperature dependence of the in-phase $(\chi'_{ac})(T))$ and the out-of-phase $(\chi''_{ac})(T))$ for a) Fe15s V$_{EH}$ = 0 V, b) Fe15s V$_{EH}$ = 35 V, c) Fe15s V$_{EH}$ = 50 V, d) Fe15s V$_{EH}$ = 70 V. The frequency dependent maximum occurs at the blocking temperature (T_B) of the iron nanocrystallites.

To examine the static magnetic properties of the nanostructured thin films, hysteresis loops were collected from 10 K to 400 K (after initially FC the sample in a 0.5 T field). No measurable exchange bias field shifts were observed, further indicating that the formation of magnetic (e.g. antiferromagnetic or ferromagnetic) oxides had not occurred[63], in agreement with the composition and microstructure experiments. While the 10 K loop of the bilayer film showed simple single-phase magnetism, the 10 K loops of all the nanostructured thin films were “wasp-waisted”, consistent with the presence of two magnetic phases; magnetization from the iron nanocrystallites with the larger anisotropy and the interfacial FeCu alloy with its reduced anisotropy and lower field response (see Figs 5.35 - 5.37). Above T_B of the iron nanocrystallites, the hysteresis loops no longer show a coercivity and the remnant magnetization is zero as expected for superparamagnetic nanocrystallites. The coercivities temperature dependence [$H_C(T)$] (Fig. 5.38) for all of the nanostructured films behaved similarly. With warming from 10 K, a rapid decrease in $H_C(T)$ was observed. At T_B of the iron nanocrystallites, $H_C(T) = 0$ T. Interestingly, while the bilayer film whose $H_C(T) = 0$ T at all temperatures since $T_B \approx 10$ K, all the nanostructured thin films presented a coercivity at elevated temperatures ($T \gg T_B$); a rapid increase in $H_C(T)$ followed by a plateau up to 400 K was observed. This significant increase in $H_C(T)$ is likely the result of intraparticle exchange interactions between the soft FeCu alloy and the population of the smallest iron nanocrystallites (intraparticle interactions) that are magnetically ordered through exchange coupling, not measurable with χ_{AC}(T,ν) since no magnetism fluctuations would occur, but measurable, in the small $\chi_{DC}(T)$ above $T_{C,Alloy}$ which, at its largest, makes up ∼10% of $\chi_{DC}(T)$. Above $T_{C,Alloy}$, where the interfacial FeCu alloy is paramagnetic, the exchange coupled iron nanocrystallites were no longer pinned by the alloy interactions and can once again contribute to $H_C(T)$. Such a trend is similar to rapid increases, with warming, of $H_C(T)$ observed in nanocrystallite ferromagnets via magnetic hardening behaviour through nanocrystallite decoupling[112]. The coercivity was observed to increase as the iron content decreased or V_{EH} increased, a result of the altered anisotropy due to the enhanced intermixing occurring between iron and copper, in agreement with $\chi_{AC}(\mathrm{T},\nu)$. Since the bilayer film did not have coupled or no iron nanocrystallites surrounded by interfacial FeCu alloy (that had $T_{C,Alloy} \gg T_B$ of the iron nanocrystallites) no $H_C(\mathrm{T} > T_B)$ was observed.

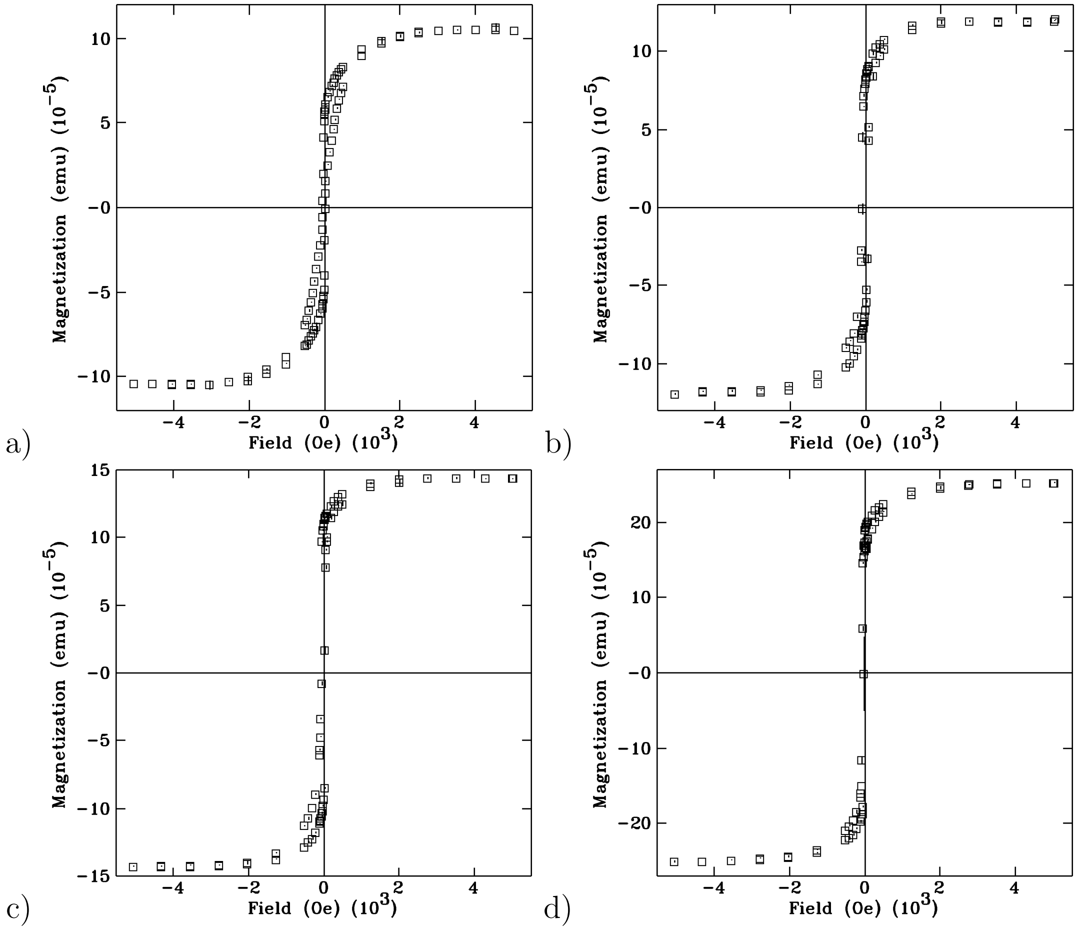

Figure 5.35: Magnetization as a function of field at 10 K for a) Fe60s $V_{EH} = 0$ V, b) Fe60s $V_{EH} = 35$ V, c) Fe60s $V_{EH} = 50$ V, d) Fe60s $V_{EH} = 70$ V. All loops have had the diamagnetic contribution from the combination of the SiO_2 substrate, gel cap, and straw subtracted.

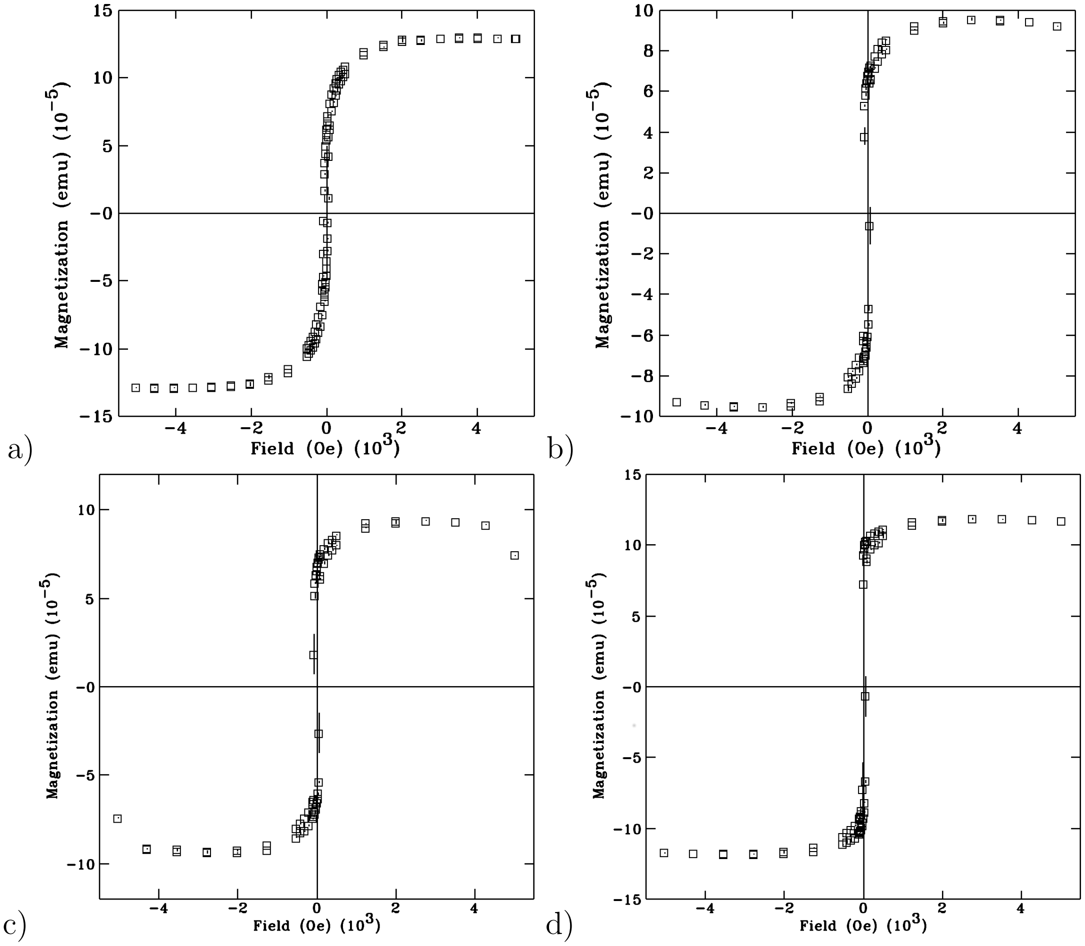

Figure 5.36: Magnetization as a function of field at 10 K for a) Fe30s $V_{EH} = 0$ V, b) Fe30s $V_{EH} = 35$ V, c) Fe30s $V_{EH} = 50$ V, d) Fe30s $V_{EH} = 70$ V. All loops have had the diamagnetic contribution from the combination of the SiO_2 substrate, gel cap, and straw subtracted.

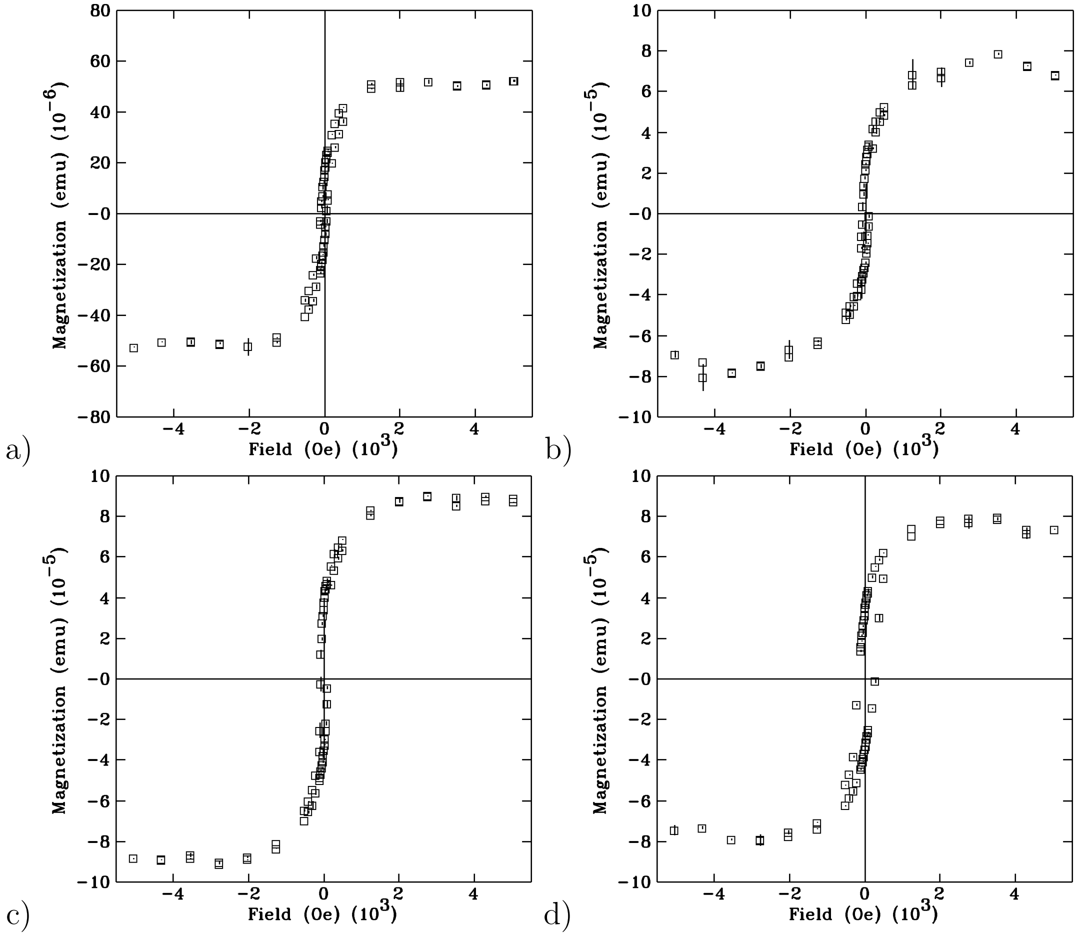

Figure 5.37: Magnetization as a function of field at 10 K for a) Fe15s $V_{EH} = 0$ V, b) Fe15s $V_{EH} = 35$ V, c) Fe15s $V_{EH} = 50$ V, d) Fe15s $V_{EH} = 70$ V. All loops have had the diamagnetic contribution from the combination of the SiO_2 substrate, gel cap, and straw subtracted.

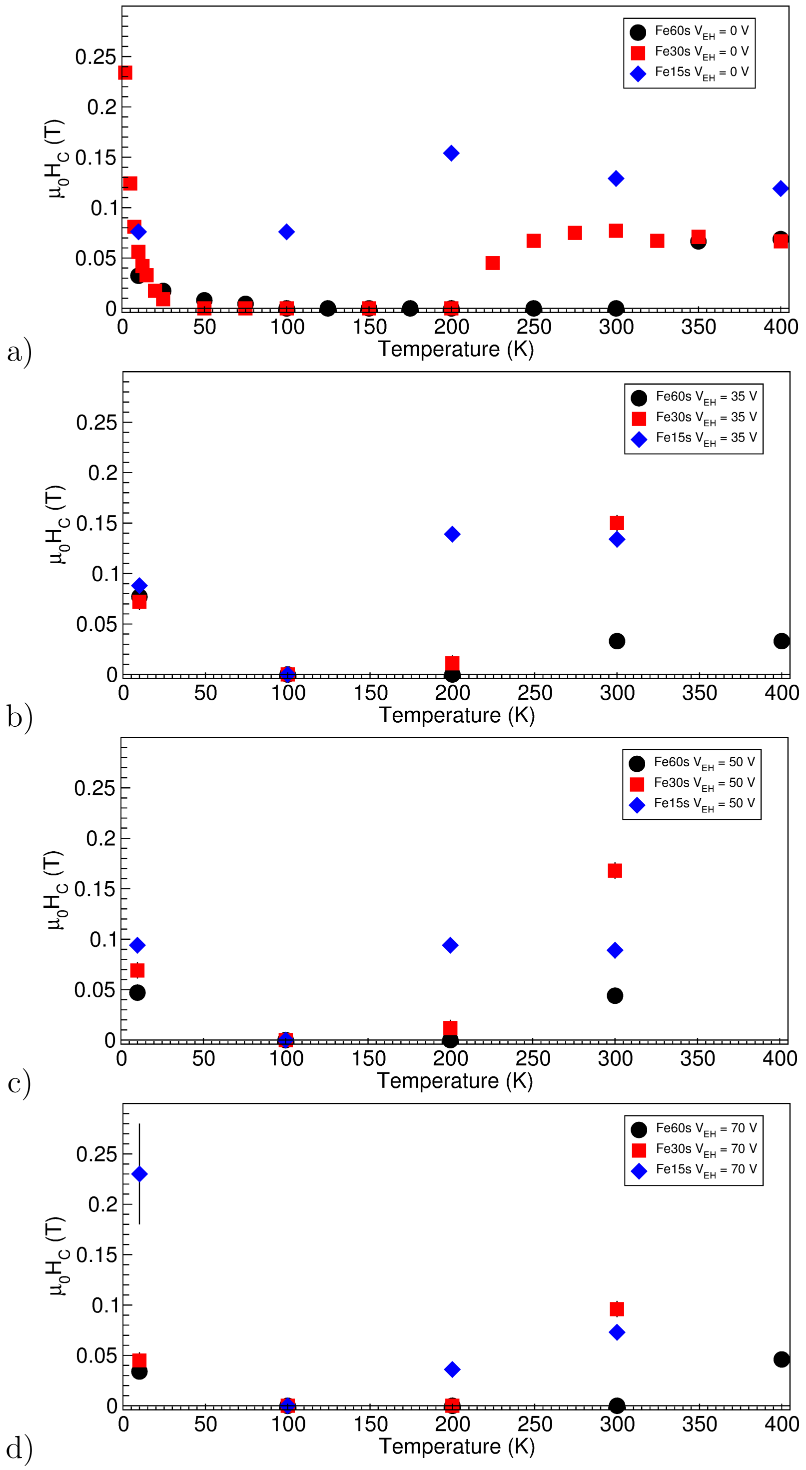

Figure 5.38: Temperature dependence of the coercivity for a) $V_{EH} = 0$ V, b) $V_{EH} = 35$ V, c) $V_{EH} = 50$ V, d) $V_{EH} = 70$ V. $H_C(T) = 0$ for $T_B < T < T_{C,Alloy}$ is in good agreement with χ_{DC} and χ_{AC} experiments. At $T_{C,Alloy}$, a rapid increase in $H_C(T)$ followed by a plateau up to 400 K was observed.

The XMCD spectra, similar to the XAS spectra, are characteristic of the coordination environment surrounding the Fe and Cu atoms (or ions). However, the intensity of the XMCD spectral transitions are proportional to the magnetization of these ions (Fe and Cu) and thus provides site-specific magnetization. The results obtained from XMCD experiments further support the claim that an iron oxide has not formed. Iron oxides such as maghemite and magnetite have characteristic XMCD spectra that these films do not present. The Fe XMCD spectra collected using both TEY and TFY (see figs. 5.39 to 5.44) were consistent with the above description provided from the XAS experiments. With a change in field polarity from 5 T to -5 T, all the spectral features of the Fe TEY and TFY XMCD spectra flip orientation, indicating that they are all magnetic in origin. A difference in the magnitude of the peak intensities with a change in field polarity also indicated that the magnetization of an Fe component was being pinned. The Fe TEY XMCD spectra for the Fe60s $V_{EH} = 0$ V sample shows three spectral features similar to maghemite, however, the TFY XMCD spectra only shows one component similar to metallic iron. As was discussed above, there was no evidence for the formation of iron oxide near the surface of these films, therefore, the XMCD spectral features are the result of Fe in a coordination environment similar to that of maghemite (octahedral or tetrahedral Fe^{3+}) due to the formation of the interfacial FeCu alloy. Similar spectra were observed for the other films, however, with decreased iron content or increased V_{EH}, the character of the Fe TEY XMCD began to change, becoming more metallic like, mirroring that of the Fe TFY XMCD. This change of spectral features suggested that with a decrease in iron content, the contribution to the magnetism of the interfacial FeCu was diminished.

Copper, a non-magnetic material, will not produce an XMCD spectra. Furthermore, any surface oxidized Cu (CuO) would be antiferromagnetic, and will also not produced an XMCD spectra as circularly polarized photons are unable to differentiate between equal number of parallel and anti-parallel moments in an applied field irrespective of its polarity. Although it has been shown previously[32] that with sufficient pinning, oxidized copper (Cu^{2+}) can provide an XMCD spectra through an induced magnetism from Fe^{3+}, in this case, there is significant amounts of metallic copper between the iron nanocrystallites and the surface of the nanostructured thin films (the copper capping layer was approximately 2 nm thick). Thus, the copper in the FeCu alloy was responsible for all the spectral features observed in the Cu TEY and TFY XMCD spectra. For all samples, a Cu XMCD spectral component was observed (see figs. 5.39 to 5.44) which was ferromagnetically coupled to the metallic Fe component observed in both the TEY and TFY XMCD, indicating that the moments on the Fe and Cu atoms in the interfacial FeCu alloy were ferromagnetically coupled.

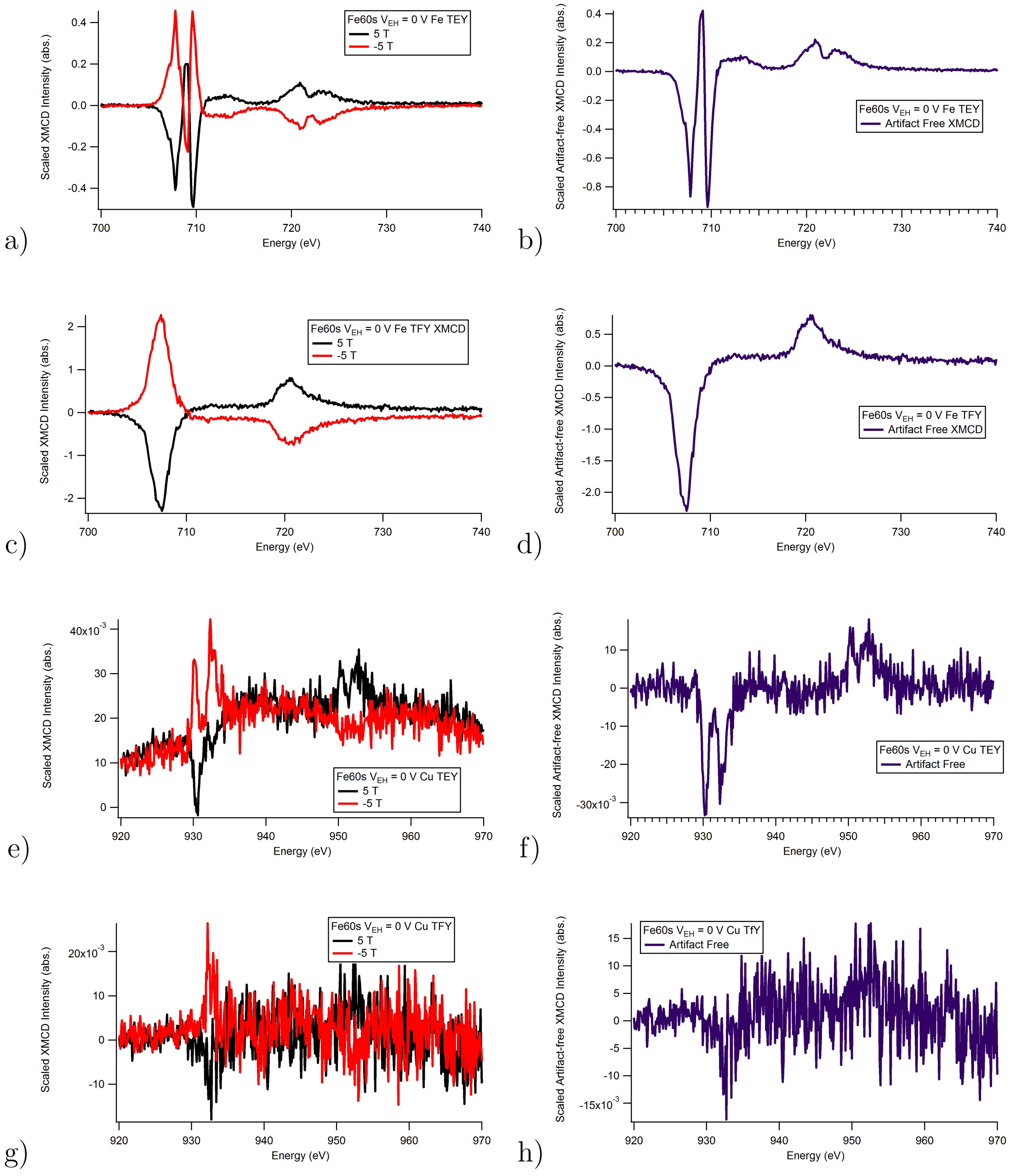

Figure 5.39: Figures on the left show the difference between an applied field of ±5 T. Evidence for pinning was observed as the intensity of the L_3-edge differs between field polarities. Figures on the right show the artifact-free XMCD which shows only the magnetic contribution to the XMCD spectra. All features in the artifact-free XMCD spectra are magnetic in origin.

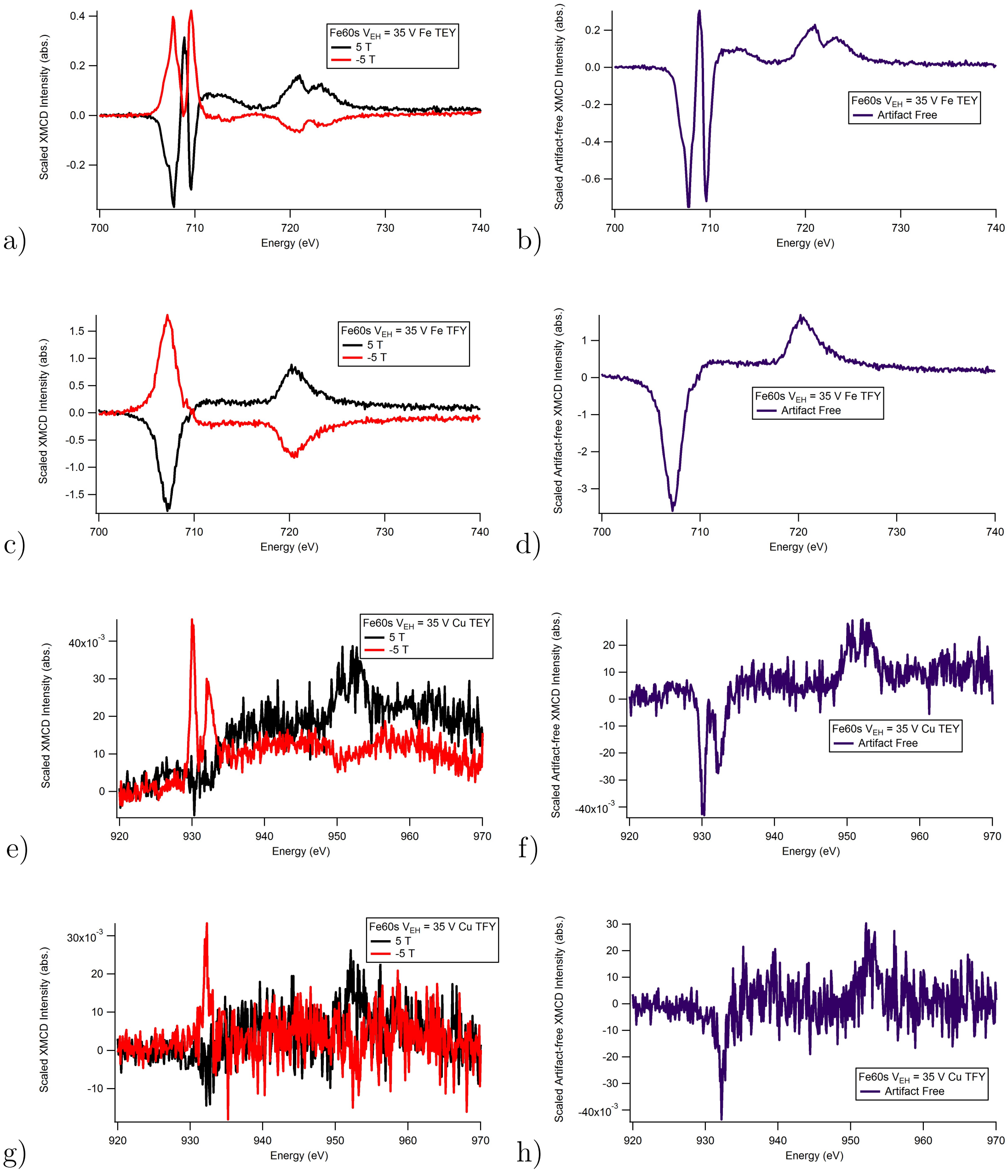

Figure 5.40: Figures on the left show the difference between an applied field of ±5 T. Evidence for pinning was observed as the intensity of the L_3-edge differs between field polarities. Figures on the right show the artifact-free XMCD which shows only the magnetic contribution to the XMCD spectra. All features in the artifact-free XMCD spectra are magnetic in origin.

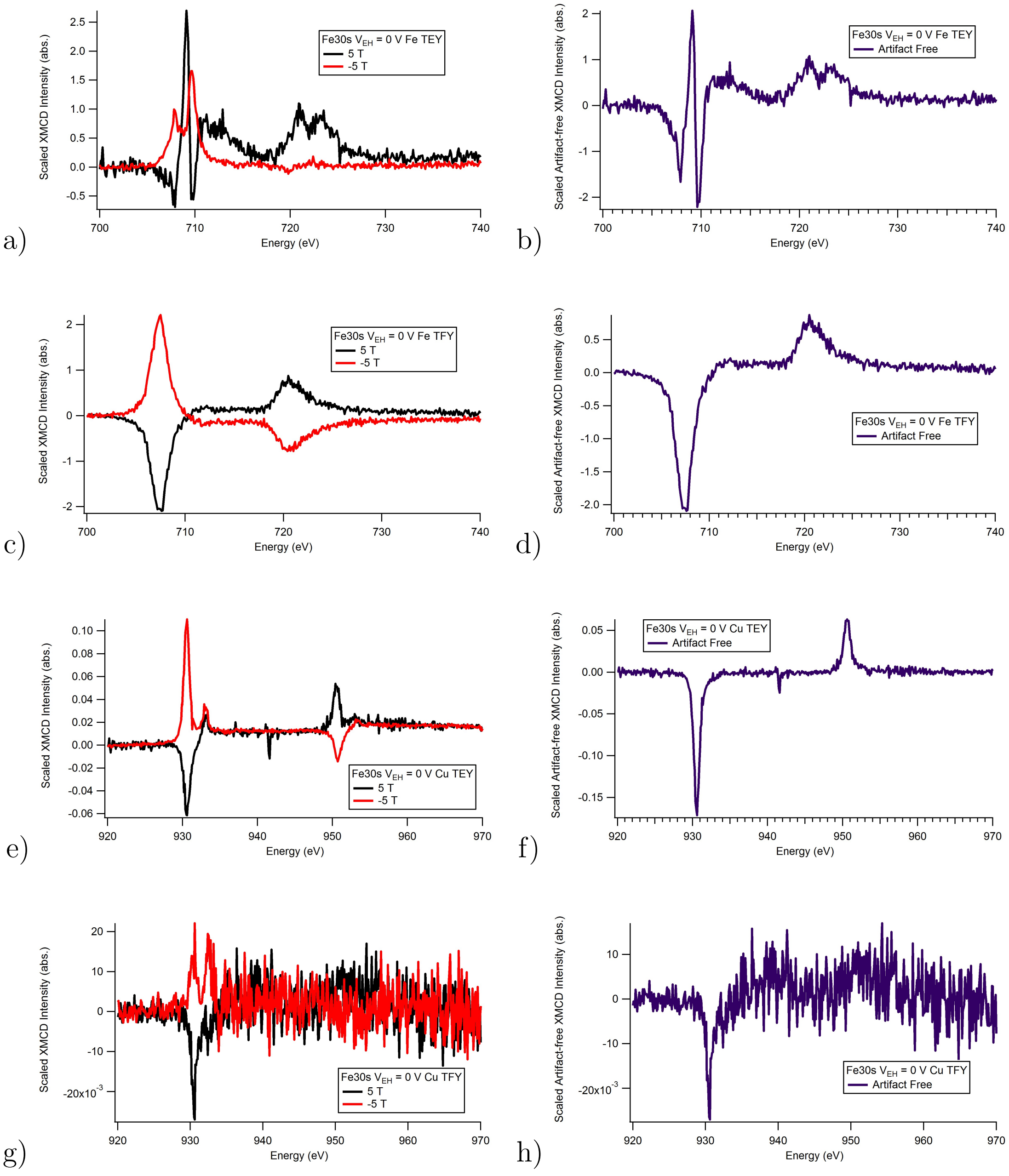

Figure 5.41: Figures on the left show the difference between an applied field of ±5 T. Evidence for pinning was observed as the intensity of the L_3-edge differs between field polarities. Figures on the right show the artifact-free XMCD which shows only the magnetic contribution to the XMCD spectra. All features in the artifact-free XMCD spectra are magnetic in origin.

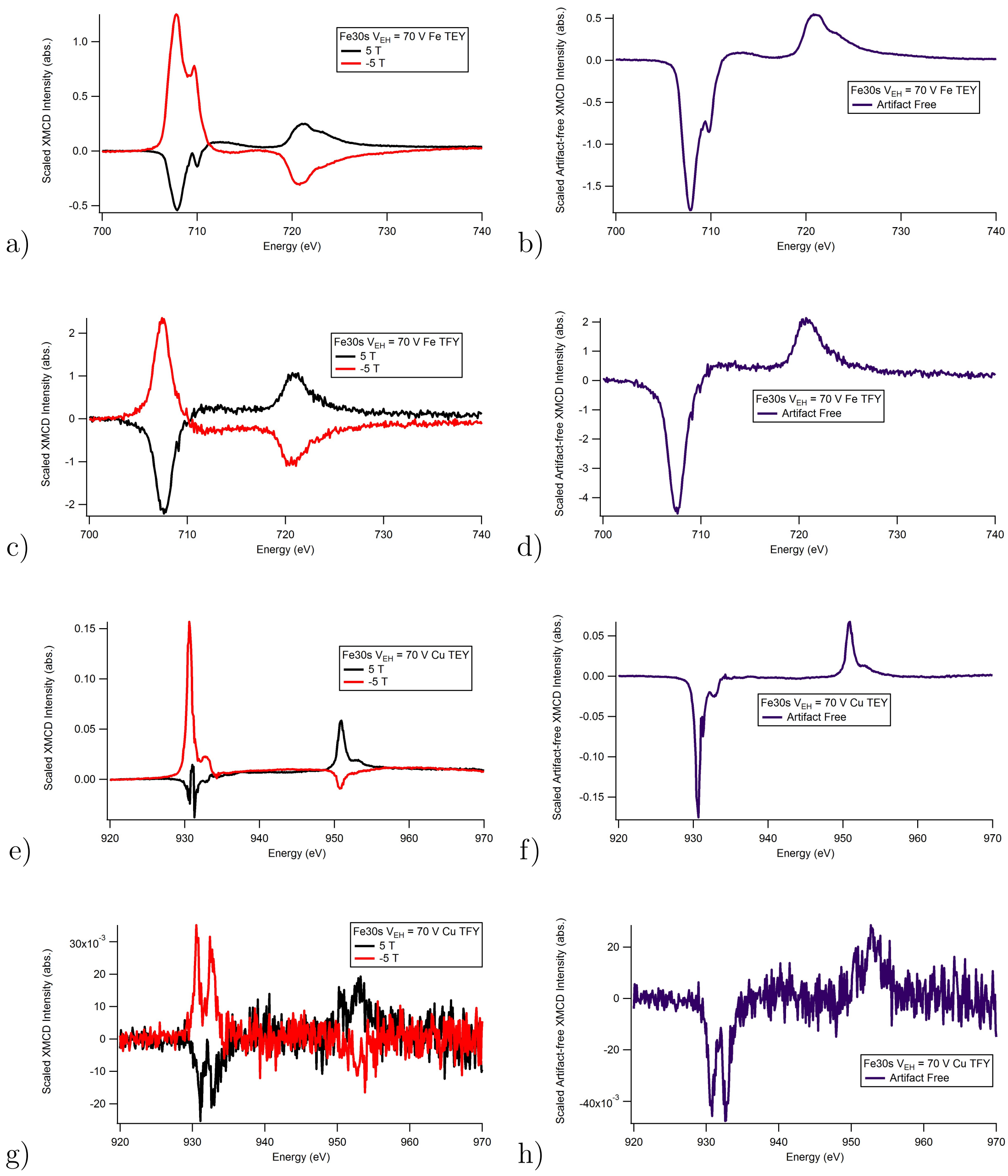

Figure 5.42: Figures on the left show the difference between an applied field of ±5 T. Evidence for pinning was observed as the intensity of the L_3-edge differs between field polarities. Figures on the right show the artifact-free XMCD which shows only the magnetic contribution to the XMCD spectra. All features in the artifact-free XMCD spectra are magnetic in origin.

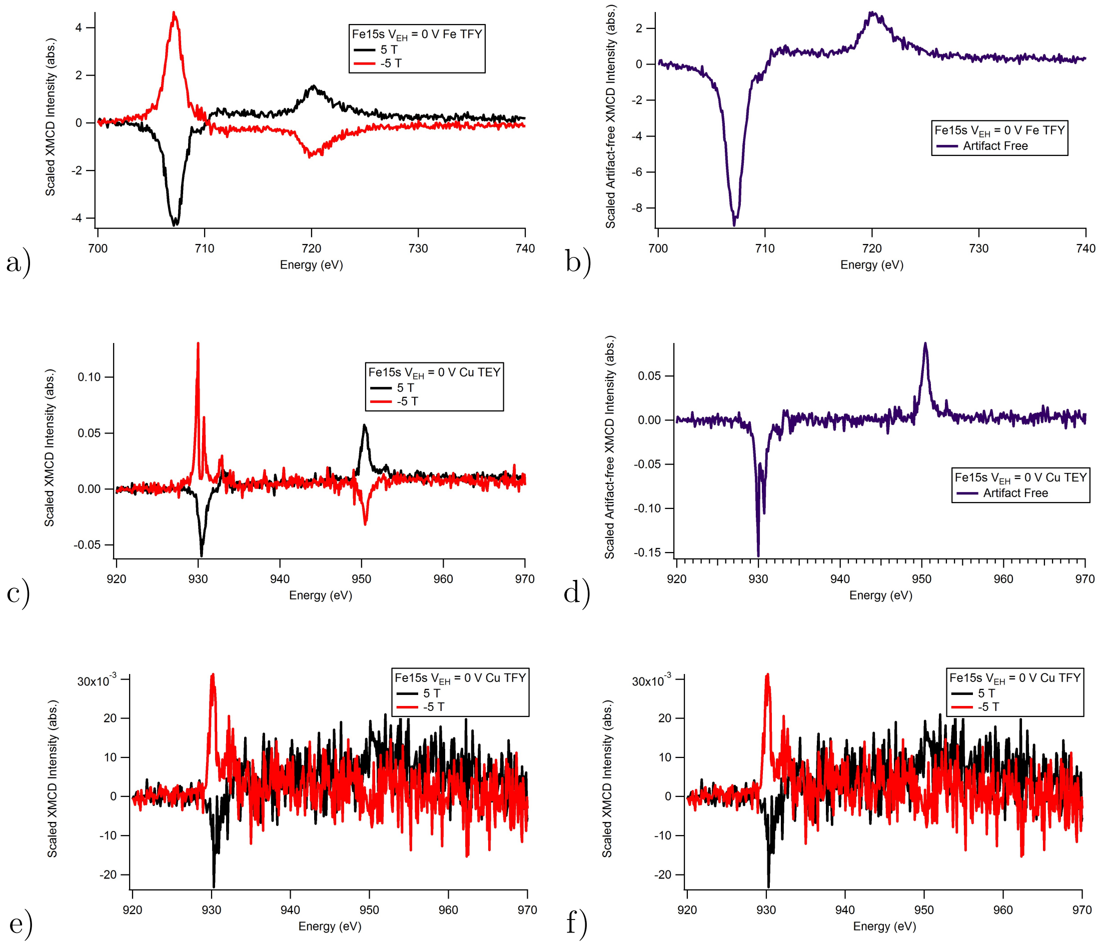

Figure 5.43: Figures on the left show the difference between an applied field of ±5 T. Evidence for pinning was observed as the intensity of the L_3-edge differs between field polarities. Figures on the right show the artifact-free XMCD which shows only the magnetic contribution to the XMCD spectra. All features in the artifact-free XMCD spectra are magnetic in origin.

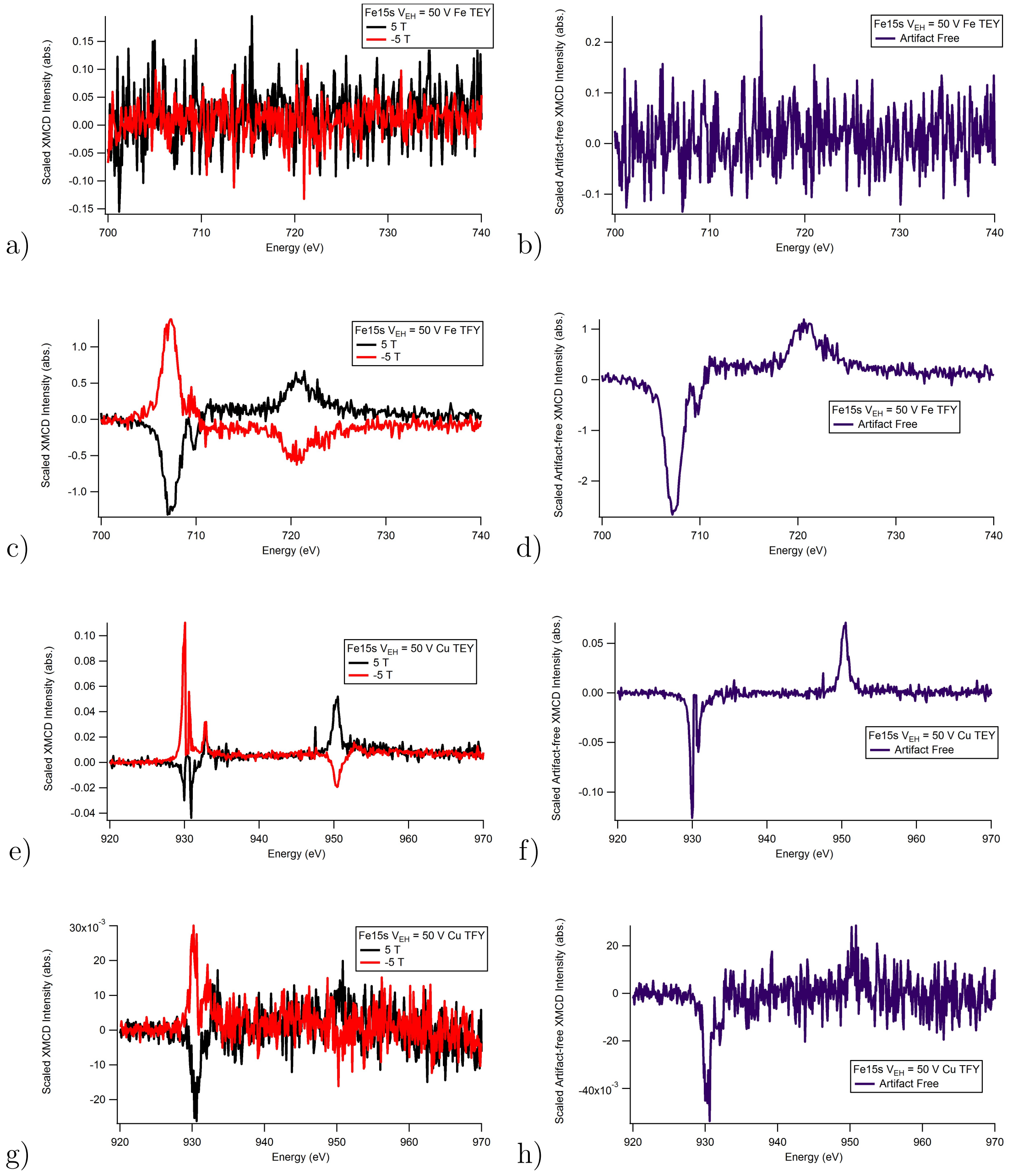

Figure 5.44: Figures on the left show the difference between an applied field of ±5 T. Evidence for pinning was observed as the intensity of the L_3-edge differs between field polarities. Figures on the right show the artifact-free XMCD which shows only the magnetic contribution to the XMCD spectra. All features in the artifact-free XMCD spectra are magnetic in origin.

The ratio of orbital (m_{orb}) to spin (m_{spin}) magnetic moments for Fe and Cu were determined by using sum-rule analysis.[56] From this sum-rule analysis,

$$\frac{m_{orb}}{m_{spin}} = \frac{2q}{9p - 6q}, \tag{5.1}$$

where p and q are the integrated XMCD intensities over the L$_3$-edge and the combined L$_{3,2}$-edges, respectively. At high energies, an increase in the integrated XMCD intensity due to an increased offset from zero in the XMCD spectrum was observed for all nanostructured thin films studied. These results were observed for artifact free XMCD spectra, obtained by reversing both the incident photon helicity and the polarity of the applied field, indicating that these effects were not instrumental in origin. As the *d*-orbitals are localized and should not be a contributing factor to the XMCD intensity at these energies, the observed non-zero XMCD intensity may be the result of delocalized *s*- and *p*-electrons[103] which should not be relevant for the calculations of m_{orb}/m_{spin}. Therefore, the integral (q) was terminated at the energy where there was no longer a slope in the XMCD intensity (736.31 eV for Fe). To ensure a reliable comparison between nanostructured films, the energy where p and q were terminated for Fe was kept constant at 717 eV and 736.31 eV, respectively. For the Fe spectra, we observed a non-zero m_{orb}/m_{spin}, approximately an order of magnitude larger then that observed for bulk Fe[105], and relatively unchanged between samples, independent of the amount of deposited Fe (see Table 5.4). This increased m_{orb}/m_{spin} (relative to bulk Fe) is likely due to the intraparticle interactions between the iron nanocrystallite and the FeCu alloy, as evidenced by the observed pinning of the Fe^{3+} magnetization from the XMCD analysis. A similar analysis was applied to the Cu XMCD spectra for the V$_{EH}$ = 0 V series of films where p and q where fixed at 947 eV and 959.4 eV, respectively. Cu, which is non-magnetic should have an m_{orb}/m_{spin} of zero, however, due to the induced magnetism in the FeCu alloy, a non-zero m_{orb}/m_{spin} resulted. The majority of Cu XMCD spectra had a poor signal-to-noise ratio making sum-rule analysis problematic. The calculated m_{orb}/m_{spin} differed significantly from sample to sample (see Table 5.4) and for the Fe30s and Fe15s $V_{EH} = 0$ V films m_{orb}/m_{spin} was comparable to that of the Fe in these films. These results suggest that as the amount of intermixing is increased, the Fe (metallic Fe and Fe^{3+}) magnetization remains constant while the contribution to the magnetism due to the Cu^{2+} increases. That is to say, that the induced magnetism on the Cu plays a more significant role for the films where the amount of deposited iron has been reduced.

Table 5.4: Calculated m_{orb}/m_{spin} for Fe and Cu from the XMCD spectra. For the spectra where there was no measurable XMCD or the XMCD spectra was very noisy, no calculable m_{orb}/m_{spin} was observed (NM).

Sample		Fe m_{orb}/m_{spin}	Cu m_{orb}/m_{spin}
Fe60s V$_{EH}$ = 0 V	TEY	0.19984	0.07423
	TFY	0.21943	NM
Fe30s V$_{EH}$ = 0 V	TEY	-0.01942	0.34849
	TFY	0.20974	NM
Fe15s V$_{EH}$ = 0 V	TEY	NM	0.23333
	TFY	0.20315	NM
Fe60s V$_{EH}$ = 35 V	TEY	0.23486	NM
	TFY	0.23202	NM
Fe30s V$_{EH}$ = 70 V	TEY	0.23460	NM
	TFY	0.23000	NM
Fe15s V$_{EH}$ = 50 V	TEY	NM	NM
	TFY	0.23167	NM

A ferromagnetic-to-paramagnetic (or ferrimagnetic-to-paramagnetic) transition can be characterized using x-ray magnetic resonance scattering (XMRS) above and below the transition temperature, T_C. To explore the nature of the Fe^{3+} and Cu^{2+} behaviour observed in the XAS and XMCD spectra, XMRS experiments were performed using the total electron yield at the resonance energies of $Fe^0 = 707$ eV, $Fe^{3+} = 710$ eV, $Cu^0 = 933$ eV and $Cu^{2+} = 930$ eV. Below the so-called $T_{C,Alloy}$ of the FeCu interfacial alloy, the Fe^{3+} and Cu^{2+} components should be ferro- or ferrimagnetic (a typical antiferromagnetic material would have no XMCD or XMRS spectra), therefore, by scanning the field between ±0.35 T (an applied field large enough to saturate the magnetization), the element-specific hysteresis loops will be observed. The loop obtained from the difference in the measured electron yield from left- and right-circularly polarized x-rays, is proportional to the magnetization of the element under observation. Furthermore, the element-specific coercivity is then a measure of the energy required to rotate the magnetization of that specific component (e.g. Fe^{3+}). We observed from dc and ac susceptibility experiments that below $T_{C,Alloy}$ the magnetization of the FeCu alloy pinned the smallest of the iron nanocrystallites magnetizations, not allowing them to contribute to the overall magnetization. Above $T_{C,Alloy}$ where the FeCu alloy was paramagnetic, these previously pinned magnetizations could contribute freely to the overall magnetization of the nanostructured thin film. By studying the temperature dependence of the x-ray magnetic resonance scattering, the transition of the FeCu alloy to paramagnetism can be explored.

At 50 K, the hysteresis loop from metallic Fe of the Fe60s $V_{EH} = 0$ V film appears similar to the hysteresis loops measured of the entire sample (see Figs. 5.45 - 5.51).

With warming, a decrease in the saturation magnetization was observed up to 250 K. A vertical loop shift of ∼15% was measured indicating that pinning of the metallic Fe magnetization was present, in agreement with the XMCD spectra. A temperature dependent elemental coercivity was observed which decreased with warming from 50 K to 250 K. The Fe^{3+} component's saturation magnetization (taken from the maximum of the hysteresis loop) also decreased with warming, and the metallic Fe components coercivity decreased with warming until 250 K where it was small, but not zero, in agreement with the observed $T_{C,Alloy}$ from susceptometry experiments. 250 K was well below the observed $T_{C,Alloy}$ for the FeCu interfacial alloy in this film; however, the coercivity, as measured by magnetometry (which measures the sample as a whole) had a coercivity of zero at 250 K. The elemental hysteresis loops for the Fe30s $V_{EH} = 0$ V and Fe15s $V_{EH} = 0$ V film showed similar temperature dependent behaviour of the saturation magnetization and coercivity. However, as the $T_{C,Alloy}$ of the FeCu interfacial alloy of these films was reduced compared to the Fe60s $V_{EH} = 0$ V film, no elemental coercivity was measured above this temperature. The hysteresis loop obtained from the Fe^{3+} transition energy shows a significant difference in the shape of the loop. The loop for the $V_{EH} = 0$ V series of films is flipped along the field axis (instead of tracing the magnetization from the 1st to 2nd to 3rd to 4th and back to the 1st quadrant) these loops trace the magnetization from the 2nd → 1st → 4th → 3rd and back to the 2nd. This indicates that the difference between the circularly polarized photons electron yield has changed sign, further evidence for pinning of the Fe^{3+} component[79]. The temperature dependence of the elemental coercivity decreases with temperature more rapidly than the metallic Fe component and is zero above $T_{C,Alloy}$. The remaining films share similar temperature dependencies of the magnetization and coercivity for the metallic Fe and Fe^{3+} components. These XMRS results suggest that both the metallic Fe and Fe^{3+} components are pinned. Also, the measured elemental coercivity of the metallic Fe component persists at temperatures above where the elemental coercivity of the Fe^{3+} component was zero (above $T_{C,Alloy}$), strengthening our argument that the smallest iron nanocrystallites were being pinned by the FeCu alloy and above $T_{C,Alloy}$ where the FeCu alloy has become paramagnetic, these previously pinned moments are now able to contribute to the overall magnetization as seen in the temperature dependent coercivity (Fig. 5.38) and dc susceptibility (see Figs. 5.26 - 5.28).

The copper hysteresis loops (Cu^0 and Cu^{2+}) are shown in figures 5.45 - 5.51. The Cu^{2+} loops at 50 K show evidence of pinning as a significant vertical loop shift was observed. Hysteresis loops for the Cu^{2+} component of the Fe30s $V_{EH} = 70$ V, Fe15s $V_{EH} = 0$ V and 50 V were not measurable. The metallic Cu component shows clear evidence for induced magnetism. Here, the magnetic Cu component that we observe is the copper found in the FeCu alloy, indicating that not all the Cu is Cu^{2+}; a significant amount is Cu. This suggests that there is a distribution of local electronic environments leading to a distribution of oxidation states for copper (and likely for iron as well) and not discrete Cu and Cu^{2+}. Additionally, the signal-to-noise of the copper hysteresis loops is increased significantly compared with that of the iron loops. This difference in signal-to-noise is the result of the reduced magnetism of the copper compared to that of the iron as the iron nanocrystallites make up a significant portion of the sample (up to 50%, by mass) and are a much more efficient scatterer then the copper as only the Cu^{2+} in the FeCu alloy is magnetic.

These XMRS experiments have shown definitely that the FeCu alloy is magnetic and that the observed $T_{C,Alloy}$ is indeed a T_C (or a magnetic ordering temperature) as there was no measured coercivity in the Fe^{3+} and Cu^0/Cu^{2+} components above this temperature, where the alloy is paramagnetic.

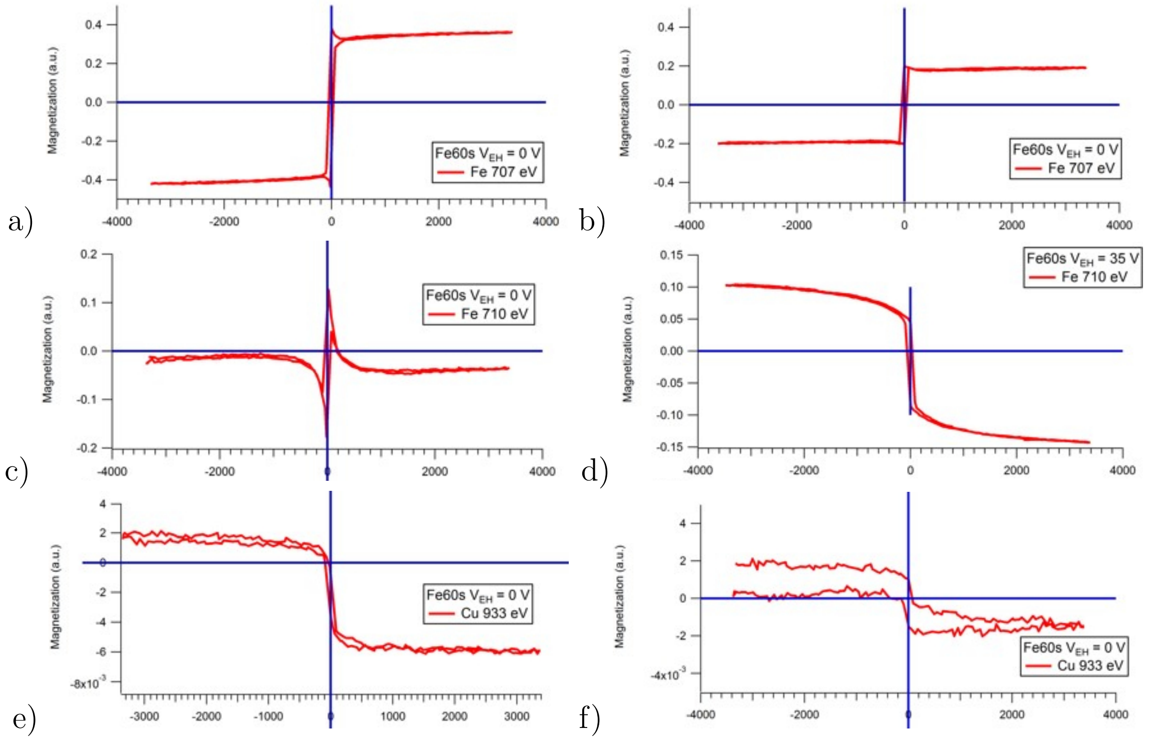

Figure 5.45: XMRS on the Fe60s $V_{EH} = 0$ V series of films at the energies of the metallic Fe peak (~707 eV), Fe in the FeCu alloy (~710 eV), and Cu in the FeCu alloy (~934 eV) a) Fe ~707 eV at 50 K, b) Fe ~707 eV at 250 K, c) Fe ~710 eV at 50 K, d) Fe ~710 eV at 250 K, e) Cu ~934 eV at 50 K, f) Cu ~934 eV at 250 K

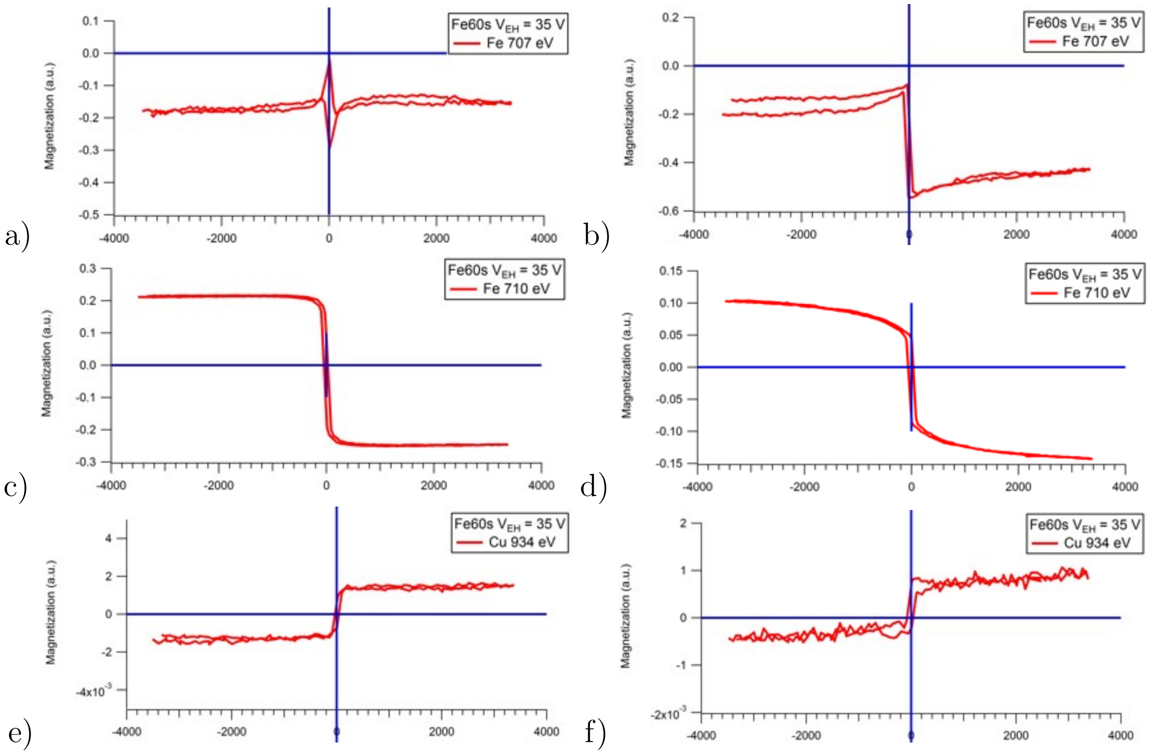

Figure 5.46: XMRS on the Fe60s V_{EH} = 35 V series of films at the energies of the metallic Fe peak (∼707 eV), Fe in the FeCu alloy (∼710 eV), and Cu in the FeCu alloy (∼934 eV) a) Fe ∼707 eV at 50 K, b) Fe ∼707 eV at 250 K, c) Fe ∼710 eV at 50 K, d) Fe ∼710 eV at 250 K, e) Cu ∼934 eV at 50 K, f) Cu ∼934 eV at 250 K

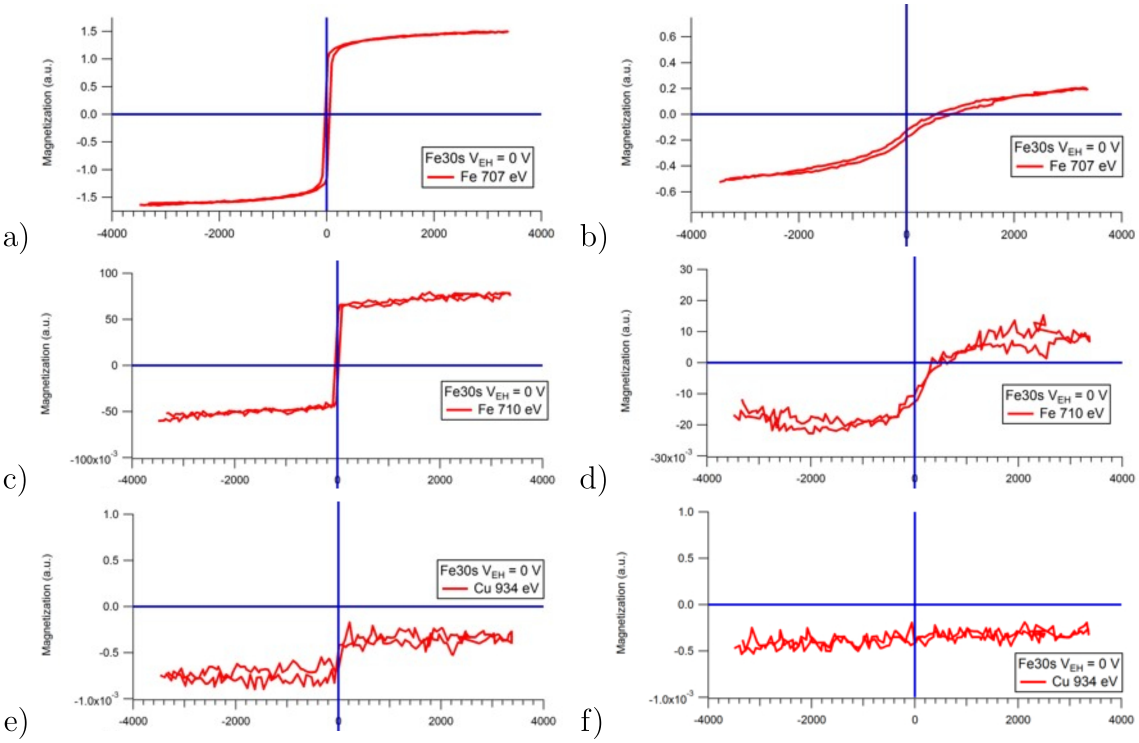

Figure 5.47: XMRS on the Fe30s V_{EH} = 0 V series of films at the energies of the metallic Fe peak (∼707 eV), Fe in the FeCu alloy (∼710 eV), and Cu in the FeCu alloy (∼934 eV) a) Fe ∼707 eV at 50 K, b) Fe ∼707 eV at 250 K, c) Fe ∼710 eV at 50 K, d) Fe ∼710 eV at 250 K, e) Cu ∼934 eV at 50 K, f) Cu ∼934 eV at 250 K

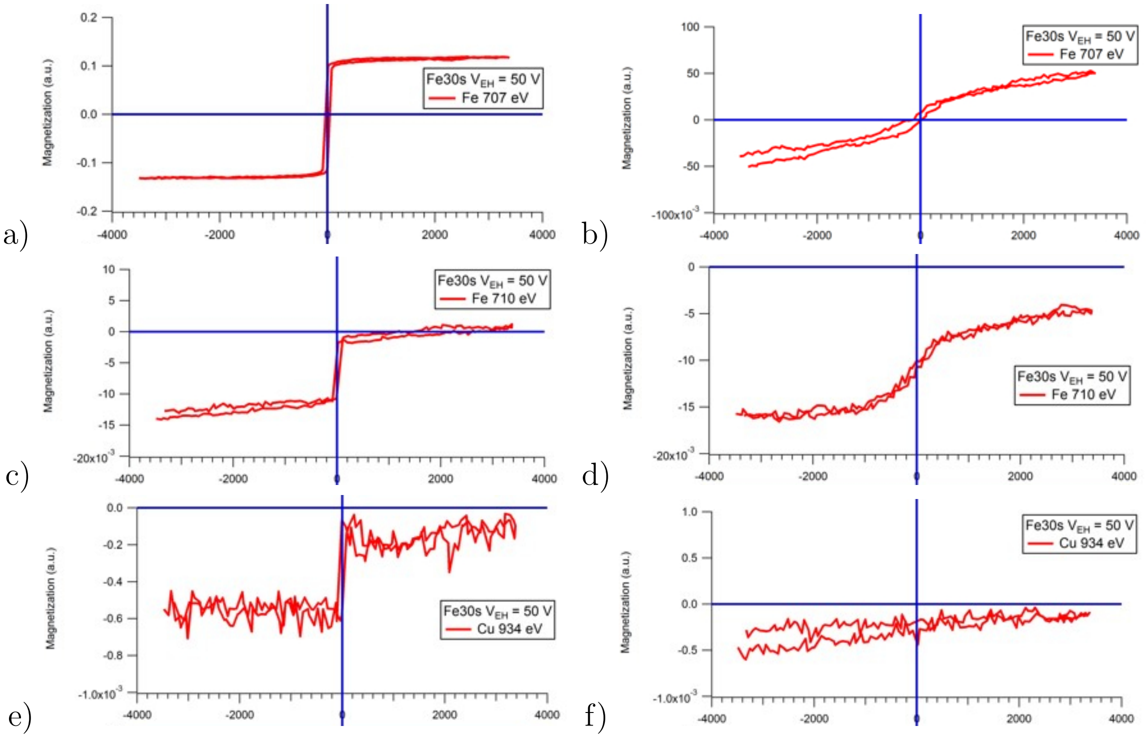

Figure 5.48: XMRS on the Fe30s V_{EH} = 50 V series of films at the energies of the metallic Fe peak (∼707 eV), Fe in the FeCu alloy (∼710 eV), and Cu in the FeCu alloy (∼934 eV) a) Fe ∼707 eV at 50 K, b) Fe ∼707 eV at 250 K, c) Fe ∼710 eV at 50 K, d) Fe ∼710 eV at 250 K, e) Cu ∼934 eV at 50 K, f) Cu ∼934 eV at 250 K

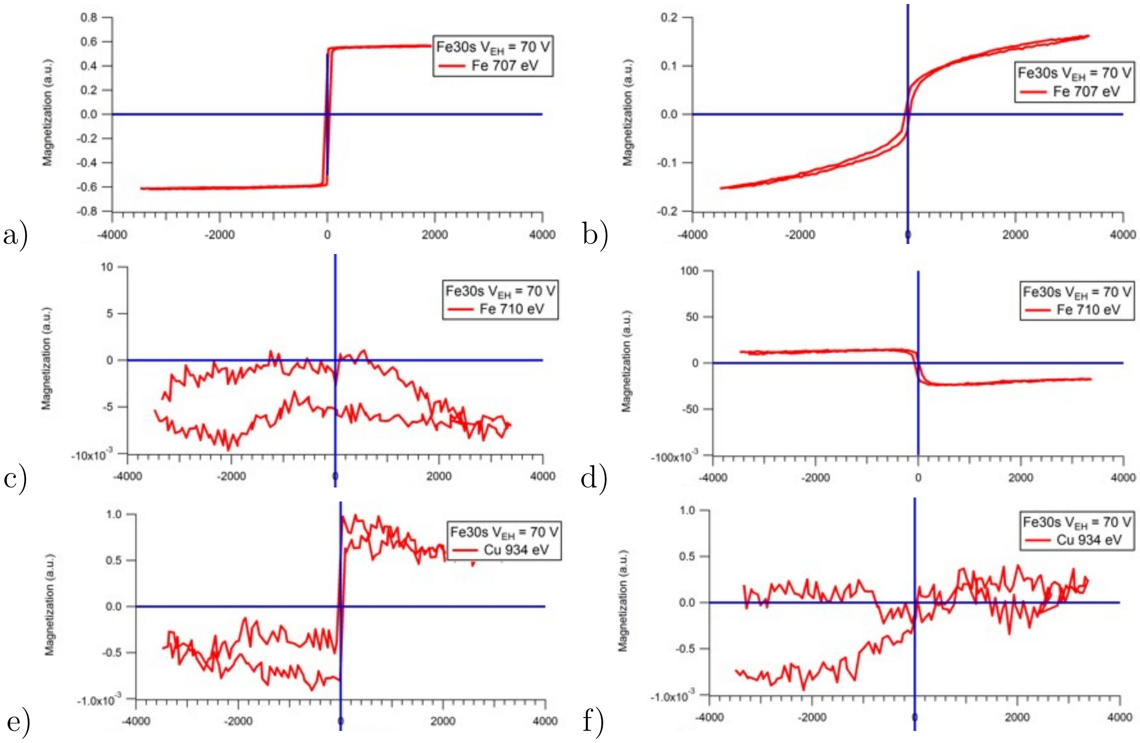

Figure 5.49: XMRS on the Fe30s V$_{EH}$ = 70 V series of films at the energies of the metallic Fe peak (∼707 eV), Fe in the FeCu alloy (∼710 eV), and Cu in the FeCu alloy (∼934 eV) a) Fe ∼707 eV at 50 K, b) Fe ∼707 eV at 250 K, c) Fe ∼710 eV at 50 K, d) Fe ∼710 eV at 250 K, e) Cu ∼934 eV at 100 K, f) Cu ∼934 eV at 250 K

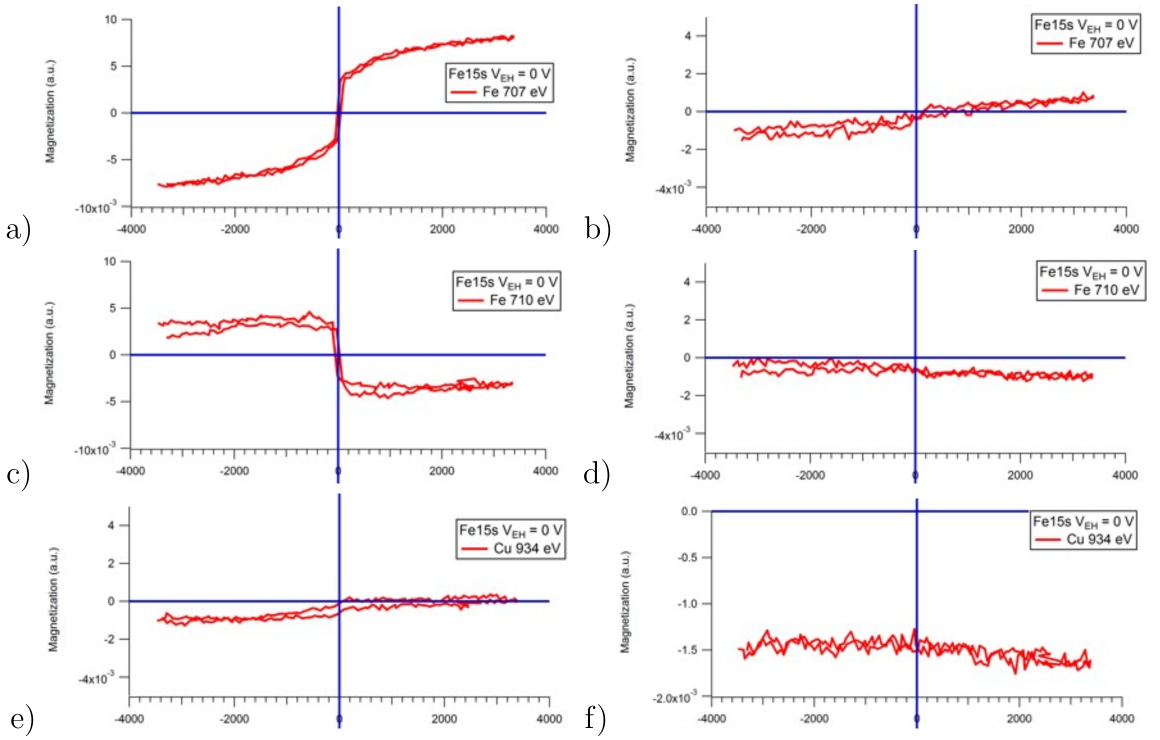

Figure 5.50: XMRS on the Fe15s V$_{EH}$ = 0 V series of films at the energies of the metallic Fe peak (∼707 eV), Fe in the FeCu alloy (∼710 eV), and Cu in the FeCu alloy (∼934 eV) a) Fe ∼707 eV at 50 K, b) Fe ∼707 eV at 250 K, c) Fe ∼710 eV at 50 K, d) Fe ∼710 eV at 250 K, e) Cu ∼934 eV at 50 K, f) Cu ∼934 eV at 250 K

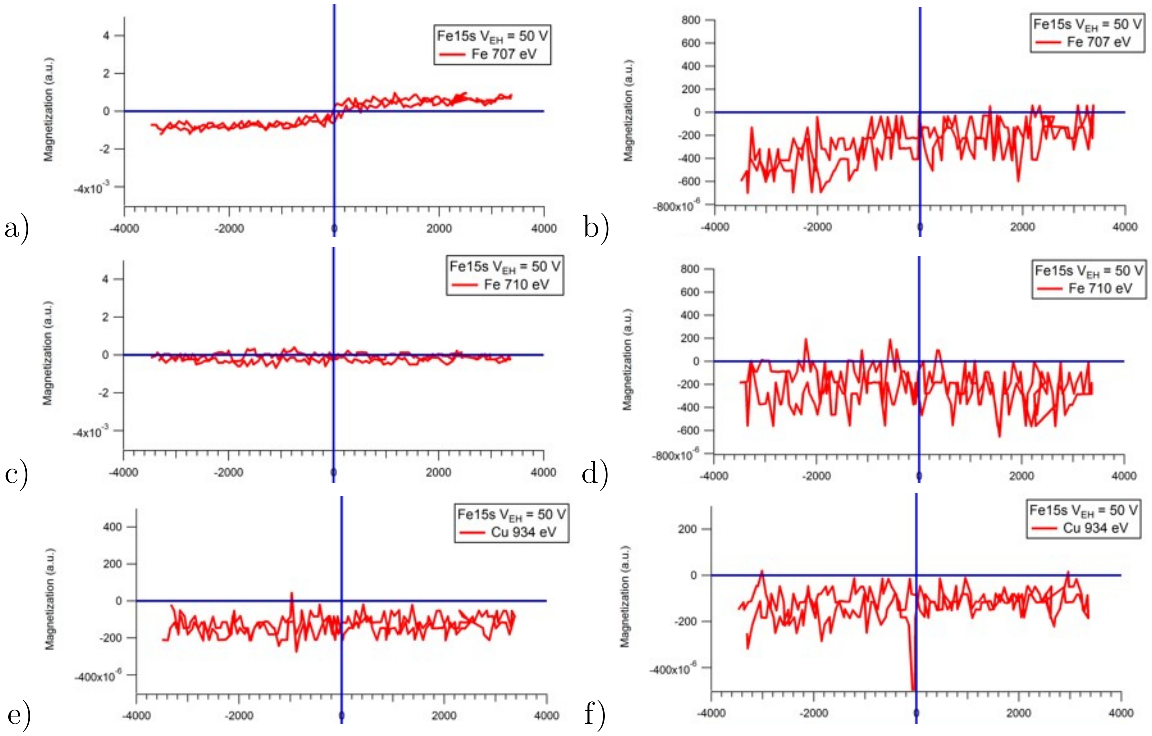

Figure 5.51: XMRS on the Fe15s V$_{EH}$ = 50 V series of films at the energies of the metallic Fe peak (∼707 eV), Fe in the FeCu alloy (∼710 eV), and Cu in the FeCu alloy (∼934 eV) a) Fe ∼707 eV at 50 K, b) Fe ∼707 eV at 250 K, c) Fe ∼710 eV at 50 K, d) Fe ∼710 eV at 250 K, e) Cu ∼934 eV at 50 K, f) Cu ∼934 eV at 250 K

5.5 Summary

To study the effects of inter- and intra-particle interactions on the magnetism, we have fabricated nanostructured thin films of iron and copper using a dual ion-beam deposition system. Experiments to determine the composition and morphology of these films indicated that they can be categorized into three distinct morphologies: multilayers, dispersions and a mixed phase. We have shown that an interfacial FeCu alloy has formed at the interface between the iron nanocrystallites and the copper matrix that surrounds them leading to significant intraparticle interaction effects on the magnetism of these films. We have observed that with increased intermixing, the distribution of nanocrystallite volumes was increased which altered the interparticle interactions between the iron nanocrystallites resulting in a larger distribution of blocking temperatures, or put another way, a larger distribution of the energy barrier altering the superparamagnetic behaviour of these films. These interparticle (or intercrystallite) effects result in a significant overlap between the dynamical freezing associated with the nanostructured thin films T_Bs, and the spin (moment) dynamics around $T_{C,Alloy}$. *ac* susceptibility experiments showed that by altering the amount of intermixing between the iron nanocrystallites and the copper matrix, a reduced frequency dependence of the in-phase and out-of-phase components occurs. This reduction in the susceptibility was likely the result of an altered iron nanocrystallite volume distribution and, speaking to the intraparticle interactions, the altered $T_{C,Alloy}$ was due to the amount of intermixing between Fe and Cu controlled by this iron nanocrystallite volume. The effects of the formation of interfacial FeCu alloy on the intraparticle magnetism were readily observed in the x-ray absorption and magnetic circular dichroism spectra. Here, we see evidence for both metallic iron (Fe^0) and Fe^{3+} in both octahedral- and tetrahedral-like environments. In addition, metallic Cu and Cu^{2+} were also observed. Due to the interactions between the iron nanocrystallites and the FeCu alloy, an induced magnetism on the Cu^0 and Cu^{2+} were observed. The temperature evolution of these effects were obtained from x-ray magnetic resonance scattering experiments which showed that below $T_{C,Alloy}$, Cu^0 (and Cu^{2+}, but only at 50 K) were magnetic. Clear evidence of this $T_{C,Alloy}$ can be observed here as only the copper in the FeCu alloy was magnetic, thus, above this temperature, where the FeCu alloy would be paramagnetic, there was no longer any measurable induced magnetism on the Cu^0 or Cu^{2+}.

Chapter 6

Discussion

In the previous chapters, the effects of inter- and intra-particle interactions on the magnetism of three different nanoscale systems were presented; i) Cu/γ-Fe_2O_3 nanoparticles (Chapter 3), ii) undoped and V-doped SiO_2/FeCo nanoparticles (Chapter 4), and iii) Fe/Cu nanostructured thin films (Chapter 5). The discussion of these experimental results centred around the individual systems themselves, whereas in this chapter these interaction effects in the context of all three systems will be presented. First, the identification of the interfacial phase and its affects on the microstructure and composition of the nanoparticles/nanocrystallites will be reviewed. Next, the effect of these interfacial phases on the overall magnetism (magnetometry and susceptometry) of the three systems will be examined. Finally, a comparison of the role of the interfacial phase on the element specific magnetism will be presented.

6.1 Identification of the Interfacial Phase

To begin, the role of atoms which lie near or on the surface of a nanoparticle/ nanocrystallite or at interfacial regions between nanoparticle core and shell become increasingly important as size decreases. The importance of the surface and interface electronic configuration on the magnetic properties becomes increasingly relevant as this surface-to-volume ratio increases[62; 113]. To explore these surface effects in detail, we have fabricated several nanoscale systems where we have altered the nature of the magnetic exchange interactions (e.g. superexchange or indirect exchange) at the nanoparticle surface. Nanostructured thin films of Fe crystallites embedded in a copper matrix experience indirect exchange (i.e. RKKY interactions). Here, the magnetic Fe nanocrystallites polarize the conduction electrons of the matrix which then interact with other magnetic Fe nanocrystallites. Cu/γ-Fe_2O_3 nanoparticles experience superexchange interactions. Unlike indirect exchange, superexchange interactions are described by the coupling of next-nearest magnetic ions through a non-magnetic cation. In this case, Fe ions in either the A- or B-sites of the maghemite spinel interact through the oxygen cations (e.g. J_{AA}, J_{BB}, or J_{AB}). The copper shell alters these interactions by introducing new exchange pathways (e.g. Fe-O-Cu). SiO_2/FeCo nanoparticles bridge the gap between indirect exchange (RKKY exchange interactions) and superexchange interactions providing a system where both types of exchange interactions are present. The FeCo core atoms experience indirect exchange while the effect of the SiO_2 shell on the FeCo surface atoms is to introduce superexchange (through the formation of Fe- and Co-silicates) interactions.

XAS experiments are an excellent tool for identifying interfacial phases as the transition energies (e.g. L-edge) are sensitive to the electronic environment of the element being studied. Spectra collected at the L-edges of Fe and Cu for the Cu/γ-Fe_2O_3 nanoparticles showed typical spectral features for an iron-oxide and metallic Cu. Also, spectral features for Cu^{2+} in an octahedral coordination environment (e.g. CuO or Cu-doped Fe_3O_4) were observed. The integrated area (proportional to the amount of material) of the metallic copper absorption features increased with increasing amounts of copper, suggesting that the Cu^{2+} observed was not the result of surface oxidation; evidence for the formation of an interfacial phase with Cu^{2+} character. Similar characterizations were made for the undoped and V-doped SiO_2/FeCo nanoparticles and the Fe/Cu thin films. For the silica coated FeCo nanoparticles we observed typical metallic Fe and Co spectral features. In addition, spectral features for octahedral Fe^{3+} and Co^{2+} were observed and confirmed with modeling of the spectra using CTM4XAS. These spectral features are the result of the change in the electronic environment around the Fe and Co surface atoms (similar results were observed with XPS), as there was no oxygen contamination, the formation of interfacial metal-silicate phases were the cause of these spectral features. The ratio of octahedral Fe^{3+} intensity to that of Co^{2+} indicated that Co-silicates formed preferentially (in agreement with XPS findings). Similar alterations of the local electronic environment of Fe and Cu were observed in the Fe/Cu thin films. Here, oxidation of the iron was not observed suggesting that these changes are the result of the formation of an interfacial FeCu alloy. With the reduction in Fe content, or an increased amount of intermixing (controlled through the End-Hall voltage of the secondary ion-beam,

V_{EH}), the spectral features become less metallic-like as the Fe^{3+} spectral component increased in intensity relative to the metallic Fe component. These changes were the result of the increased intermixing promoted by the larger V_{EH} during film growth which resulted in the increased formation of the interfacial FeCu alloy component. We have shown that in all three nanoscale systems studied here, the electronic environment of the nanoparticle/nanocrystallite has been altered by the formation of these interfacial phases.

Further evidence that supports the claim that interfacial phases are being formed at the interface between the maghemite nanoparticles and the copper shell can be observed from Mössbauer spectroscopy experiments. Fe ions on the surface of a γ-Fe_2O_3 nanoparticle have a very different chemical environment than those of the core. At the surface, vacancies are distributed randomly throughout the octahedral sites which results in an effective surface magnetocrystalline anisotropy that differs from the core anisotropy. These surface effects reduce the saturation magnetization and result in the random canting of the surface spins in a spin-glass like manner[114; 9; 115]. The effects of the Cu shell on the surface Fe ions are readily visible with Mössbauer spectroscopy. Mössbauer spectroscopy experiments of bare γ-Fe_2O_3 nanoparticles have shown that at 10 K a singlet component describing the fluctuating (faster than the measuring time of the Mössbauer effect) Fe surface spins is required to describe fully the spectra. With the addition of a Cu shell, we observed that the singlet component reduced in absorption, with increased Cu shell thickness, indicating that these once fluctuating Fe surface spins had been constrained on the timescale of the Mössbauer experiment ($\sim 10^{-6}$ s). These Fe surface spins had become part of a new magnetic sextet component between ± ∼4 mm s^{-1} that indicated slowly fluctuating Fe spins. For the 0.5 nm thick shell, B_{HF} was observed to be ∼22 T, and the B_{HF} increased further to 25 T with a shell of 1.0 nm thick, showing that the Fe surface spins had been altered directly by the intimate contact with the Cu shell. Additional evidence of the alteration of the Fe surface spins with the copper coating was provided by the variation of the ± ∼8 mm s^{-1} line intensities indicating that the recoil-free fraction of the ^{57}Fe at the octahedral and tetrahedral sites of the γ-Fe_2O_3 were altered from the increased number of surface moments with different Fe environments (i.e. Fe-O-Fe superexchange was being stiffened[116; 59]). Furthermore, the Cu/γ-Fe_2O_3 spectra did not present an electric quadrupole shift further indicating that the distorted coordination experienced by bare γ-Fe_2O_3 was no longer present. These effects on the Fe surface spins are the result of the altered environment due to the Cu coating.

Room temperature CEMS experiments on several of the Fe/Cu nanostructured thin films have been performed to further identify the nature of the interfacial alloy and definitively exclude the presence of an iron oxide phase. From the collected spectra, no evidence for a measurable sextet indicated that α-Fe was not present. Furthermore, the characteristic hyperfine field parameters (isomer shift and electric field quadrupole) of ferro- or ferri-magnetic iron oxides were absent, indicating that the films did not contain these oxides. To further characterize the role that this interfacial FeCu alloy plays on the atomic Fe magnetism, future temperature dependent CEMS experiments will be performed.

For the undoped and V-doped SiO_2/FeCo nanoparticles, temperature dependent Mössbauer spectroscopy experiments will be performed allowing us to identify uniquely the type of Fe-silicates being formed (e.g. $Si_2Fe_{2.5}O_{12}$[117]) and the origin of the intrinsic atomic magnetism resulting from these Fe-silicates. As will be discussed, the effects of these interfacial phases can be observed in element specific XMCD experiments.

6.2 Interfacial Phases' Effects on the Magnetism

At the size scales relevant for these three nanoscale systems (e.g. the single-domain limit), the nanoparticles/nanocrystallites become superparamagnetic. This means that there is a dynamical freezing of the single domain magnetizations at a temperature described by the barrier to rotation of the magnetization set by the nanoparticles volume, V, and anisotropy energy, K, $E_B = KV$, where $E_B = k_B T_B$. For an idealized single-domain nanoparticle all the moments behave as a single "super" moment. Above T_B, the system has enough thermal energy to overcome the energy barrier and spontaneous flipping of the magnetization occurs such that the time-averaged magnetization is zero. Below T_B, the system does not have enough thermal energy to overcome this barrier and the magnetization becomes trapped. For actual nanoparticles or crystallites (e.g. Cu/γ-Fe_2O_3, SiO_2/FeCo, or Fe nanocrystallites in a copper matrix), this simplistic model neglects the effects of surface spin disorder due to the very different chemical environment at the surface (e.g. broken coordination, reduced number of nearest neighbors, or intermixing) as well as both inter- and intra-particle interactions. A magnetically "dead layer" develops as these surface spins are frustrated resulting in a reduced magnetization. As the system is cooled, these surface spins begin to freeze and if the sample is cooled in an applied field, align with this field. The effect of this field-cooling process is observed as, for example, an exponential increase in the saturation magnetization. Therefore, these surface spins play a significant role on the overall magnetism of "single-domain" nanoparticles. As described above, the application of a surface coating in the form of a Cu or SiO_2 shell for the γ-Fe_2O_3 or FeCo nanoparticles, respectively, and depositing Fe nanocrystallites in a copper matrix, has resulted in the formation of an interfacial phase which has altered these surface spins allowing them to be recaptured by the core and once again contributing to the overall magnetism.

The T_B which describes, along with the anisotropy energy, the energy barrier to superparamagnetic spin flips, can be determined from susceptibility experiments (χ_{dc}(T) and χ_{ac}(T,ν)). After initially zero-field cooling (ZFC) the system, T_B can be determined from the maximum in the χ_{dc}^{ZFC}(T) curve for a non-interacting, single-domain nanoparticle or the frequency dependent maximum of χ'_{ac}(T,ν). For the non-interaction system, a description of the nanoparticles magnetocrystalline anisotropy can be determined from the Néel-Brown model. However, if interparticle interactions are present (i.e. dipole-dipole interactions or exchange interactions via a metallic matrix), a difference in the maximum of the χ_{dc}^{ZFC}(T) and χ_{dc}^{FC}(T) curves occurs which is representative of the temperature where these interaction energies are equivalent to that provided by the applied field to reorient the nanoparticles magnetization at that temperature. In addition, the frequency dependence of the T_B cannot be described using the Néel-Brown model. Here, the nanoparticles overall anisotropy can then be described using the Vogel-Fulcher law which still describes the dynamical freezing in terms of "glassiness" and provides an additional energy term, T_0, which describes the onset of correlations or interactions amongst particle magnetizations.[98]

For all three nanoscale systems an increase in T_B with increased shell thickness and intermixing was observed in addition to a broadening of the maxima, indicators of an increased magnetic anisotropy due to the interfacial phase which a larger anisotropy like a Cu-ferrite or Fe- and Co-silicates which likely altered the surface spin environment of the nanoparticle/nanocrystallite cores. A reduced surface spin disorder of the cores would result in an increased magnetic volume compared to their uncoated counterparts where the surface moments were disordered (e.g. bare γ-Fe_2O_3). A reduction in the surface spin disorder was observed in M_S(T) (see below). In addition, spin-glass-like behaviour of the χ_{dc}^{FC}(T) (e.g. the decreased χ_{dc}^{FC}(T) below T_B) was observed for the SiO_2/FeCo nanoparticles and is likely an indication of a combination of spin-glass like disorder resulting from the random nature of the nanoparticle orientations (magnetizations during ZFC) and interparticle interactions. T_B was also determined from the frequency dependent maximum in χ'_{ac}(T,ν). In both cases, we observe significant broadening of the susceptibilities maxima which suggests a change in the anisotropy of the nanoparticle/nanocrystallite core. The description of this anisotropy can be obtained from either the Néel-Arrhenius model for non-interacting systems or the Vogel-Fulcher model for systems where interparticle interactions are present. For the SiO_2 coated FeCo nanoparticles, significant interparticle interactions are present and the Vogel-Fulcher law must be applied to determine the nanoparticles overall anisotropy. The Vogel-Fulcher description provides a mechanism that allows for the description of the onset of the interactions between nanoparticles, T_0. The progression of T_0 to larger values with an increased SiO_2 shell thickness was to be expected as $T_0 \sim M_S^2$[98] and M_S was observed to increase (see Table 6.1) with SiO_2 shell thickness (described below). In addition, the overall anisotropy increased (see Table 6.1) with SiO_2 shell thickness, of which a component from the interfacial anisotropy (responsible for the high field paramagnetic susceptibility) increased, a clear indication that the metal silicate interfacial layer affects the overall magnetism of the undoped and V-doped FeCo nanoparticle core. A similar analysis of the Cu/γ-Fe_2O_3 nanoparticles was problematic due to the significant broadening in the maximum of the susceptibility with temperature making a unique determination of T_B difficult. These difficulties were also observed in the Fe/Cu thin films as significant overlap between the dynamical freezing associated with the nanostructured thin films T_Bs due to interparticle interactions, and the spin (moment) dynamics around $T_{C,Alloy}$.

A prominent feature of disordered surface spins on the magnetism can be seen in the exponential like decrease, with warming, of the saturation magnetization. Using a simple modified Bloch $T^{3/2}$ law that incorporates a term describing the freezing of the surface spins (T_F), the temperature dependence of M_S(T) of the Cu/γ-Fe_2O_3

Table 6.1: Fit parameters from Vogel-Fulcher analysis of χ'_{AC}(T) data

	K (10^5 J/m^3)	T_0 (K)
FeCo/SiO_2(3 nm)	3.2 ± 0.2	9 ± 1
FeCo/SiO_2(4 nm)	3.0 ± 0.2	8 ± 1
FeCo/SiO_2(6 nm)	4.5 ± 0.2	29 ± 1
FeCoV/SiO_2(5 nm)	2.6 ± 0.2	26.5 ± 0.5

and SiO_2/FeCo nanoparticles can be described. Above T_F ($T >\sim 25$ K) the M_S(T) was described by $M_S(T)/M_S(0) = \left(1 - BT^{3/2}\right)$, where B was the Bloch constant which is inversely proportional to the exchange constant J. Below T_F, the behaviour of M_S(T) required an extra $A \exp(T/T_F)$ with A a phenomenological constant that scaled with the relative amount of frozen surface moments compared with the ordered core moments.

Intraparticle interactions between the Cu or SiO_2 shell and the γ-Fe_2O_3 or FeCo core, respectively, altered the surface spins such that they were able to contribute to the overall magnetism of these nanoparticles. Initially, below T_F, M_S(T) decreased rapidly with warming for the bare γ-Fe_2O_3 nanoparticles. The copper coated nanoparticles exhibited a much weaker decrease in M_S(T) between 2 and ~15 K with warming due to fewer disordered surface spins. Similarly, for the SiO_2/FeCo nanoparticles we did not observe any evidence for disordered surface spins, however, in the V-doped FeCo nanoparticles, disordered surface spins were observed, suggesting that in the V-doped nanoparticles, the formation of a V-oxide at the interface hindered the recapturing of the disordered surface spins. The measured M_S(T) permitted an indirect measure of the trends from core/surface magnetism. We observed that with increasing Cu shell thickness, the term that describes exchange ($B \sim 1/J$) decreased suggesting a stronger Fe-O-Fe exchange of the surface spins (Fig. 6.1), perhaps resulting from Cu-O-Fe exchange. For the undoped and V-doped SiO_2/FeCo nanoparticles, we observed an increase in B suggesting that the exchange was weakened by the formation of the metal silicates. However, for the thickest of the SiO_2 shells, which also corresponds to the thickest metal silicate interfacial phase[117], a large decrease in the value of B

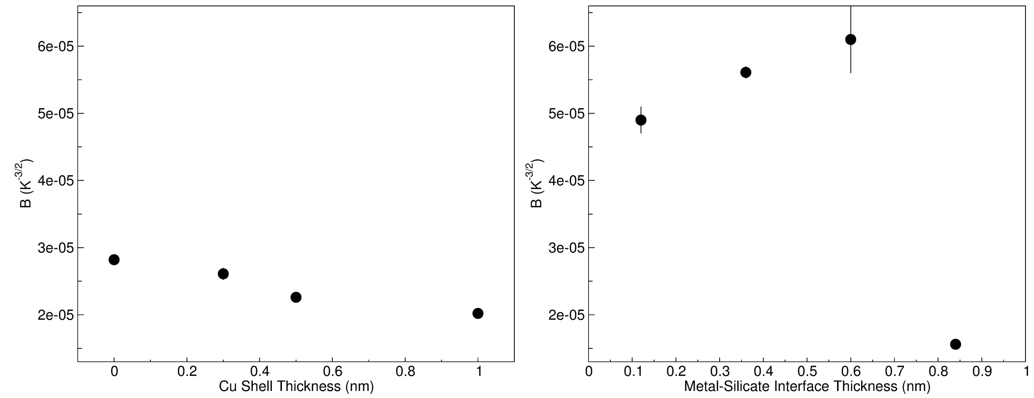

Figure 6.1: Plot of B as a function of: left) Cu shell thickness and right) Metal-silicate interface thickness for the undoped and V-doped SiO_2/FeCo nanoparticles.

was observed. This decreased B indicates that the exchange J had increased relative to the other SiO_2 encapsulated nanoparticles, likely due to the thicker metal-silicate interfacial phase. In addition, for the thickest of the undoped SiO_2/FeCo nanoparticles, with the increased interface shell thickness, M_S(T) increased as well, becoming comparable to bulk ferrites as the once "lost" surface spins are recaptured. These results suggest that the recapturing of the once disordered surface spins by the coating process is due to the increased exchange interactions promoted by this interfacial phase.

As B is inversely proportional to the exchange constant J, a comparison between samples, where the interfacial metal-silicate thickness was determined by mapping the SiO_2 shell thickness to the interfacial phase volume[117], provides a means to describe the strength of the exchange interactions resulting from the addition of a Cu or SiO_2 shell. For the Cu/γ-Fe_2O_3 nanoparticles, we observed a decrease in B and an increase in T_B as a function of shell thickness. From fits of the M_S(T) to the modified Bloch $T^{3/2}$ function described above, we observed that B decreased by $\sim$7% between the uncoated and the 0.3 nm coated nanoparticles, a further ∼15% reduction was observed for the 0.5 nm coated nanoparticles, and a further reduction of ∼11% for the 1.0 nm thick Cu shell nanoparticles. This decrease in the value of B indicates that the exchange interactions were strengthened by the addition of the Cu shell. This strengthening was likely the result of the formation of the interfacial Cu-ferrite. As we have postulated previously, as the Cu shell's thickness increased, the amount of Cu-ferrite at the interface increased and it is this additional interfacial phase that drives the stiffening of the exchange. Fits of the M_S(T) for the undoped and V-doped SiO_2/FeCo nanoparticles showed a different trend in the exchange interaction strength than that observed with the Cu/γ-Fe_2O_3 nanoparticles. With increased SiO_2 shell thickness we observed a gradual increase in B which indicates a reduced exchange interaction strength. However, for the SiO_2(6 nm)/FeCo nanoparticles, a significant decrease in B was observed indicating that the exchange interactions had been strengthened significantly. This change in exchange interaction strength may be the result of the increased amount of interfacial metal silicates. As we have discussed previously, with the V-doped SiO_2/FeCo nanoparticles, V-oxide has likely formed at the interface between the FeCo core and SiO_2 shell resulting in the decreased exchange interaction strength is likely the result of the increased metal silicates. With the SiO_2(6 nm)/FeCo nanoparticles, a significant increase in the anisotropy and T_0 were observed. Further evidence that the increased presence of metal silicates has altered the overall magnetism of these undoped SiO_2/FeCo nanoparticles. The variation in the calculated B's is much larger in the undoped and V-doped SiO_2/FeCo nanoparticles than that of the Cu/γ-Fe_2O_3 nanoparticles. For this system we have a much more complex interface phase consisting of Co-silicates and Fe-silicates and also V-oxide for the V-doped nanoparticles where the relative ratio of Co- to Fe-silicates is not 50/50, as observed by XPS. This altered composition and increased complexity likely contributes to the larger variation of B with SiO_2 shell thickness.

The static magnetic properties of the three nanoscale systems were determined by field-cooled hysteresis loops. For a superparamagnetic nanoparticle, $\mu_0 H_C(\mathrm{T}) = 0$ T at T_B. Good agreement with $\mu_0 H_C(\mathrm{T}) = 0$ T with the T_B's determined from susceptibility experiments for all three nanoscale systems (Figs. 3.9, 4.15, and 5.38) indicated that the uniaxial anisotropy description of the energy barrier of which a nanoparticle's magnetization must overcome to flip orientations (180° magnetization spin-flip) was appropriate for the static magnetizations; $\mu_0 H_C(T) = 2K/M_S\left(1 - \sqrt{T/T_B}\right)$. For the Cu/$\gamma$-$Fe_2O_3$ system, with increasing Cu shell thickness, better agreement with this description was observed. The parent γ-Fe_2O_3 nanoparticles showed the largest disagreement with this model as a result of the significant surface spin disorder. The better agreement with this description of $\mu_0 H_C(\mathrm{T})$ is further evidence for the alteration of K with Cu shell thickness. For the 1.0 nm thick Cu shell sample, good agreement with the above description was observed; pointing towards the core γ-Fe_2O_3 of the nanoparticle behaving like a simple single-domain nanoparticle. The calculated T_B was in agreement with the T_Bs determined from susceptibility data, and assuming γ-Fe_2O_3 nanoparticles regained their bulk M_S, the fit yielded a $K = 2.5 \pm 0.2 \times 10^4$ J m^{-3}, in good agreement with bulk values. This uniaxial description of $\mu_0 H_C(\mathrm{T})$ was able to describe the intermediate temperature $H_C(\mathrm{T})$ for the SiO_2/FeCo nanoparticles. In this temperature regime ($0.5 < T/T_B < 1.0$), the FeCo nanoparticles cores have recaptured their once disordered surface spins. At the lowest temperatures, this description is no longer satisfied as dynamical freezing from interparticle interactions alters the energy landscape which results in the larger observed coercivities for the thinner SiO_2 shell samples (3 and 4 nm) compared with the 6 nm shell nanoparticles. The V-doped SiO_2/FeCo nanoparticles had a considerably increased coercivity at all temperatures relative to the undoped SiO_2/FeCo nanoparticles due to the increased anisotropy and reduced saturation magnetization. Similar to these two nanoparticle systems, the Fe nanocrystallites embedded in a Cu matrix showed similar $\mu_0 H_C$(T) behaviour with $\mu_0 H_C(\mathrm{T}) = 0$ at T_B in agreement with susceptibility experiments. However, near $\mathrm{T}_{C,Alloy}$, a rapid increase in $\mu_0 H_C$(T) followed by a plateau up to 400 K was observed. This significant increase in $\mu_0 H_C$(T) is likely due to intraparticle exchange interactions between the soft FeCu alloy and the population of the smallest iron nanocrystallites that are magnetically ordered through exchange coupling. These exchange coupled Fe nanocrystallites were no longer being pinned by the alloy interactions and could once again contribute to $\mu_0 H_C$(T). Similar to the Cu/γ-Fe_2O_3 and SiO_2/FeCo nanoparticles, with increased intermixing (i.e. increased interfacial phase) the anisotropy was altered, in agreement with ac susceptibility measurements.

Evidence for multiple spin populations, core and surface, can be provided by any measurable exchange bias field shift from field-cooling before measuring the hysteresis loops. For γ-Fe_2O_3, the core of the Cu/γ-Fe_2O_3 nanoparticles, field cooling set a preferred orientation onto the disordered surface spins and exchange coupling between the core and surface spins occurs. This exchange coupling set the uniaxial anisotropy resulting in a small $\mu_0 H_{EX}$. The bare γ-Fe_2O_3 nanoparticles presented the largest $\mu_0 H_{EX}$, which decreased significantly after 5 K, in agreement with the T_Fs determined from M_S(T). $\mu_0 H_{EX}(T)$ continued to decrease with warming tracking $M_S(T)$ and $\mu_0 H_{EX}(T > T_B) = 0$ T in agreement with the T_Bs. These results provided evidence that with warming, the number of available surface spins decreased, therefore fewer were able to couple to the ordered core spins, decreasing $\mu_0 H_{EX}$; the Cu coated nanoparticles showed a reduced number of surface spins, decreasing $\mu_0 H_{EX}$. For the thickest Cu shell, an elimination of $\mu_0 H_{EX}$ altogether was observed, in agreement with the M_S(T). These trends indicated the presence of stiffer exchange and a reduced number of disordered surface spins with increasing Cu shell thickness, in agreement with the observed B's from fits of M_S(T) described above.

No measurable exchange bias loop shift for the Fe/Cu thin films that indicates that even a monolayer of an oxide had not formed around the Fe nanocrystallite cores[32]. Similarly, for the undoped SiO_2/FeCo nanoparticles there was no measurable exchange bias loop shift, which further supports the effects of the interfacial metal silicates on the surface spins, however, the V-doped SiO_2/FeCo nanoparticles presented an $\mu_0 H_{EX}$ at $T < 20$ K ($H_{EX}(T$=5 K$) = 141 \pm 1$ mT) which is due to the formation of an antiferromagnetic V-oxide, supported by the observed exponential-like M_S(T) below 20 K (see Fig. 4.13) and XAS results.

6.3 Interfacial Phases' Effects on the Elemental Magnetism

To elucidate the effects of these spontaneously formed interfaces (e.g. $CuFe_2O_4$, Fe-silicate, or FeCu alloy) on the magnetism of the three nanoscale systems presented in the previous chapters; i) Cu/γ-Fe_2O_3, ii) undoped and V-doped SiO_2/FeCo, and iii) Fe/Cu nanostructured thin films, temperature and field dependent elemental magnetic measurements were performed. The x-ray absorption and magnetic circular dichroism spectroscopy (XAS and XMCD) experiments were carried out over the $L_{3,2}$ transition edges of Fe, Co, Cu, and V using both the total electron yield (TEY) and the total fluorescence yield (TFY). The spectral features observed result from the spin-orbit interactions of the $2p$ core-shell with the intensity of these features being proportional to the number of empty $3d$ valence states. These spectra are generally broad for the transition metals (e.g. Fe^0, Co^0, and Cu^0) reflecting the width of the empty d-band, however, for the transition metal oxides (e.g. γ-Fe_2O_3), fine structure originating from multiplet and crystal field effects (multiplet structure) is observed. These multiplet effects result from spin-orbit interactions of the different valence holes in the ground state, as well as from the coupled states between the $3d$ valence holes and the $2p$ core. Therefore, spectra are characteristic of the coordination environment surrounding the atoms or ions with their intensity being proportional to the site specific magnetization. Recently, with sum-rule analysis[56], it has become possible to quantify the ratio of the spin and orbital magnetic moments from the integrated area of the magnetic circular dichroic spectra.

As stated above, the shape of the absorption spectra provides clear evidence of composition. In all cases, the observed iron spectra (700 - 740 eV) have characteristics similar to that found in iron oxides such as maghemite. For the Cu/γ-Fe_2O_3 nanoparticles, this was to be expected. However, for the undoped and V-doped SiO_2/FeCo nanoparticles as well as the Fe/Cu nanostructured thin films, where it has been shown that no oxygen contamination occurred, the iron oxide-like spectra show the formation of interfacial phases that have altered the electronic environment of the metallic Fe. The absorption spectra observed in the undoped and V-doped SiO_2/FeCo nanoparticles shows clearly that Fe-silicates formed at the interface between the FeCo core and the SiO_2 shell, in agreement with XPS and magnetometry experiments. The iron oxide-like behaviour observed in the Fe/Cu nanostructured thin films was more surprising. As no oxygen contamination had occurred, these iron oxide-like spectral features were the result of intermixing between the Fe nanocrystallites and the Cu matrix in the form of an FeCu alloy which altered significantly the Fe electronic environment such that its spectral features appear similar to octahedral Fe^{3+} in agreement with CEMS where the FeCu metallic features isomer shift described a change in the electron density around the Fe atoms. As the Fe XPS and XAS spectra for the SiO_2/FeCo nanoparticles and Fe/Cu nanostructured thin films was shown to be affected by their respective shell/matrix, we would expect to see similar effects in the Cu spectra for the Cu/γ-Fe_2O_3 nanoparticles and the Fe/Cu nanostructured thin films, and the Co spectra for the SiO_2/FeCo nanoparticles. Indeed, we do see oxide-like behaviour in both the Cu and Co $L_{3,2}$ transition edge spectra; further evidence for the formation of these interfacial phases.

From the absorption spectra, we have evidence that the electronic environment of the Fe, Co, and Cu have been altered by the formation of these interfacial phases (e.g. $CuFe_2O_4$, Fe-silicates, or FeCu alloy). It is reasonable to assume that if the electronic environments have been altered, then the elemental magnetism will also have been altered. From the difference of the left and right circularly polarized absorption spectra, the magnetic dichroism can be studied. As the intensity of the spectral features is proportional to the elemental magnetization, any observed dichroic signal that changes orientation with field suggests magnetic character. For both metallic Fe and Co, such behaviour was expected, and the observed dichroic spectra support this. However, metallic Cu is diamagnetic and copper oxides are antiferromagnetic, therefore, we would not expect magnetic circular dichroic spectra. For both Cu/γ-Fe_2O_3 nanoparticles and Fe/Cu nanostructured materials we observed induced magnetism in the Cu (a non-zero dichroic spectrum that reversed with a change in field polarity). The intensity of the spectral features in a magnetic circular dichroic spectra are proportional to the elemental magnetization, and a difference in the magnitude of the maximum at the transition edges (e.g. Fe L_3) with a change in field polarity (e.g. ± 5 T) describes pinning of the moments. For all three nanostructured systems studied, differences in the spectral intensity with field polarity suggest clearly that the surface moments were pinned, in agreement with magnetometry and susceptometry experiments. We observed for the Cu/γ-Fe_2O_3 nanoparticles that the amount of pinned Fe surface moments increased as the thickness of the Cu shell increased. For the 0.3 and 0.5 nm thick Cu shells, we observed a small changes (<5%) in the B-sites and a much larger change (<10%) in the A-site magnetization with a change in field polarity indicating that it was mostly the A-site Fe atoms that canted and only a small contribution from the B-site Fe atoms were affected. However, with the 1.0 nm thick Cu shell, we observed a much larger difference in the XMCD intensity of all three sites with respect to the 0.3 and 0.5 nm thick Cu shell samples (B1-site: ∼38%, B2-site: ∼34%, and A-site: ∼15%). This suggested that all the Fe surface atoms (A-

Table 6.2: Observed pinning in undoped and V-doped SiO_2/FeCo nanoparticles from XMCD spectra as measured by the percent difference in the L_3 transition edge intensity with a change in field polarity.

	Fe (%)	Co (%)
FeCo/SiO_2(3 nm)	6 ± 1	15± 1
FeCo/SiO_2(4 nm)	29± 1	36± 1
FeCo/SiO_2(6 nm)	23± 1	23± 1
FeCoV/SiO_2(5 nm)	17± 1	13± 1

and B-sites) were affected by the copper coating and the B-sites were affected more strongly than the A-site.

Similar trends were observed with the undoped and V-doped SiO_2/FeCo nanoparticles. Here the intensity ratio increased in general with SiO_2 (e.g. shell thickness) suggesting that more of the Fe and Co surface atoms were being pinned from the increased shell thickness (Table 6.2). This trend was observed only for the undoped SiO_2/FeCo nanoparticles. For the V-doped nanoparticles, we observed a reduced ratio comparable to that of the thinnest silica coated FeCo nanoparticles. This reduction is likely the result of much less Fe- and Co-silicate being formed at the interface due to the preferred formation of a V-oxide, an antiferromagnetic material (no observable V $L_{3,2}$ XMCD spectrum). Also, the differences observed between the field polarities were much larger at the Co L-edge than the Fe L-edge, likely the result of the preferred formation of Co-silicates over Fe-silicates, in agreement with XAS and XPS experiments.

To further describe the effects of the formation of these interfacial phases on the elemental magnetism for these three nanoscale systems, temperature and field dependent studies were performed. In the Cu/γ-Fe_2O_3 systems the observed Fe^{3+} spectral features were consistent with that of super-exchange based γ-Fe_2O_3 and the Cu spectral features showed evidence of induced magnetism in the observed Cu^{2+} component. The total Fe magnetization (sum of the absolute intensity at the A-site and the B-sites) for the 0.3 and 0.5 nm Cu shell nanoparticles decreased with warming by $\sim$50%[32]. Important to this discussion is the differences in the temperature dependencies of the A- and B-sites individually. For the three samples studied, the B-sites temperature dependencies were similar, that is, the B-site magnetizations decreased with warming at a rate independent of the thickness of the Cu shell. However, the A-site's temperature dependence varied (see below). This decreased magnetization was consistent with the observations of the surface and core magnetism behaviour of the atomic Fe magnetism from Mössbauer spectra, as well as the overall magnetism described by the magnetometry and susceptometry. In addition, these changes in the total Fe elemental magnetism for the 0.3 and 0.5 nm Cu/γ-Fe_2O_3 nanoparticles were mirrored by the reduction in the Cu^{2+} interfacial magnetization. With warming, the Cu elemental magnetization decreased more rapidly, relative to that of total Fe magnetization, becoming essentially zero by 200 K. Since the Cu magnetization was a small fraction of the total, these changes in the elemental magnetization would not be observable in clear fashion in the magnetometry (e.g. overall magnetism). The effect on the temperature dependence of the elemental magnetism for the 1.0 nm Cu/γ-Fe_2O_3 nanoparticle sample was readily observed. A significant increase of the total Fe magnetization ($\sim$40 % larger at 10 K) was observed and below 50 K, the total Fe magnetization remained constant. In addition, the Cu^{2+} interfacial magnetism was different than that of the thinner Cu coated samples. Here, the Cu^{2+} magnetization's temperature dependence was negative and varied little with warming. This change in polarity (compared with the 0.3 and 0.5 nm thick Cu coated samples) suggested that the Cu canting had changed (Fe-O-Cu interfacial exchange) and the weaker T dependence may result from an increased amount of interfacial Cu^{2+} from the increased copper coating thickness so that we observed a more typical antiferromagnetic behaviour. The antiferromagnetic-like reorientation observed here suggests an enhanced interfacial exchange coupling, in agreement with the observed temperature dependence of the saturation magnetization. For the three Cu/γ-Fe_2O_3 samples, the variation of the overall Fe^{3+} magnetization with temperature was mirrored equally by the B-sites. The A-site magnetization was opposite in polarity (coupled antiferromagnetically to the B-site) and showed a decrease in magnetization between 10 and 50 K (∼30%), then becoming essentially unchanged with further warming. However, relative to the B-sites magnetization, the A-site magnetization varied more in the 0.3 nm thick Cu shell sample (∼18% decrease), the variation of the A-site was similar to the B-sites in the 0.5 nm thick Cu shell sample, and the variation of the A-site relative to the B-sites was reduced in the 1.0 nm thick Cu shell sample (∼8% decrease). These differences in the A-site's temperature dependence relative to the B-site's suggests that the A-site was influenced more from the formation of the Cu^{2+} and that the observed differences in the total Fe magnetization were likely due to the differences in the A-site's magnetizations temperature dependence. The Cu^{2+} magnetization was aligned with the Fe B-site, likely due, in-part, to their larger numbers (∼1.6x) and they canted in the direction of the applied field, unlike the A-sites which remain collinear in γ-Fe_2O_3. The total Fe^{3+} magnetizations for the three Cu/γ-Fe_2O_3 nanoparticles showed a rapid increase in magnetization followed by a plateau as the Fe^{3+} magnetization became saturated with an applied field $\geq$ -1 T, in agreement with magnetometry experiments. For all three samples, we observe little change in the field dependence of the B1 site compared with the A site (B1/A), however, B2/A changes with field suggesting that the B2 magnetizations are canting into the direction of the A-site Fe. The Cu^{2+} magnetization for the Cu(0.3 nm)/γ-Fe_2O_3 sample saturated in a similar applied field. However, the Cu(0.5 nm)/γ-Fe_2O_3 nanoparticle sample showed a continuous increase in magnetization which effected directly the Fe^{3+} sites such that they saturated in a slightly larger applied field and had a larger magnetization compared with the Cu(0.3 nm)/γ-Fe_2O_3 nanoparticles. The Cu(1.0 nm)/γ-Fe_2O_3 sample showed a rapid decrease in magnetization up to an applied field of ∼0.5 T, followed by a much more gradual temperature dependence, indicating a reduction in canting of the Cu^{2+} moments and a return to antiferromagnetic behaviour.

The field dependence of the indirect exchange-based Fe and Co magnetizations in the undoped and V-doped SiO_2/FeCo nanoparticles were determined from the maximum of the Fe and Co L_3 transition edge. The observed Fe and Co magnetizations, a combination of the metallic Fe or Co and O_h Fe^{3+} or Co^{2+} components, showed a gradual increase with field (up to 5 T), in agreement with magnetometry experiments. The Co magnetizations were observed to increase more (∼70%) with field compared with the Fe magnetizations and likely the result of the preferred formation of the Co-silicates over the Fe-silicates as the amount of Fe and Co in the 4 nm nanoparticles is similar. Due to the nature of the elemental peak magnetization, decoupling the contribution from the metallic and metal-silicate components was not possible. As a result of this, identifying uniquely the component(s) responsible for the paramagnetic-like increase in magnetization with field was problematic. However, as we know that this effect is likely the result of an increased surface anisotropy[113], it is reasonable to suggest that the metal-silicate components (e.g. Fe^{3+} and Co^{2+}) are the cause.

To quantify the element specific magnetism of the interfacial intermixing in the nanoparticles and the nanostructured thin films, sum-rule analysis[54; 55] on the XMCD spectra was performed. We observed that with all three nanostructured samples an increase in the integrated XMCD intensity from an offset from zero in the XMCD signal at the highest energies (energies greater than those for the L_2 transition edge). Considering that *d*-orbitals are highly localized and should not contribute to an XMCD spectrum beyond the L_2 transition edge, the observed XMCD spectral intensity at these energies may be the result of excited and polarized *s*-electrons which do not contribute to the calculations of m_l/m_s[103; 104]. Therefore, in order to compare the ratio of orbit-to-spin magnetic moment between samples, the integral was terminated at the same point above the L_2 transition edge where the XMCD signals slope was smallest. Furthermore, the integrated area over the L_3 edge, p in the sum-rule analysis, was terminated at the same energies for all samples (e.g. 717 eV for Fe). Once p and q have been determined from the integrated area of the XAS normalized XMCD spectra, the element specific orbit-to-spin ratio of the magnetic moments were calculated[56]. The Cu/γ-Fe_2O_3 nanoparticle systems did not present *s*- and *p*-state intermixing with the *d*-state transitions.

A comparison of the average value of the XMCD intensity at energies well above the L_2 transition edge speaks to the relative amount of excited or polarized *s*-electrons (e.g. $3s$ or $4s$ core electrons, see Fig. 6.2). For the SiO_2/FeCo nanoparticles, the average value of the XMCD intensity at these energies for both Fe and Co was unchanged within error. This indicates that the observed differences in the calculated *p*s and *q*s (see below) were not influenced by changes in the amount of excited or polarized *s*-electrons. Furthermore, the observed XMCD intensity due to these core electrons is intrinsic to the undoped and V-doped SiO_2/FeCo nanoparticles themselves and not a function of the amount of silica present. To determine if these effects are the result of the silica coating or inherent to the FeCo nanoparticles themselves, future XMCD experiments on bare undoped and V-doped FeCo nanoparticles will be necessary. Unlike the SiO_2/FeCo (undoped and V-doped) nanoparticles, the XMCD intensity at energies above the L_2 edge for the Fe/Cu nanostructured thin films varied as a function of $T_{C,Alloy}$ (an intrinsic measure of the amount of intermixing - e.g. the amount of interfacial FeCu alloy). We observed that this average value of the XMCD intensity decreased with an increase in $T_{C,Alloy}$ for the Fe spectra. These results suggest that with more intermixing (decrease in $T_{C,Alloy}$), the *s*-electrons were affected more easily which points towards the FeCu interfacial alloy being the cause. A similar description of the *s*-electrons effect on the Cu spectra was not possible as the signal-to-noise was poor. Within spectral uncertainties, the average intensity were zero; no measurable excitation or polarization of the *s*-electrons. These results may be due to the relative magnitudes of the XMCD intensity found for the Fe and the Cu as the magnetism observed in the Cu was induced by the Fe and only observed for the FeCu interfacial

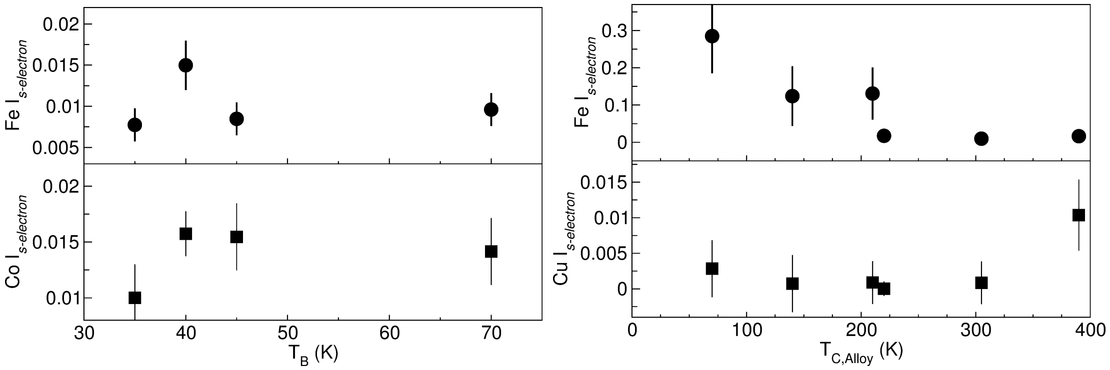

Figure 6.2: Average *s*-electron XMCD intensity well above the L_2 transition edge. Left) SiO_2/FeCo nanoparticles, Right) Fe/Cu nanostructured thin films

phase below $T_{C,Alloy}$. The observed differences between these two samples may be the result of the different exchange interactions at work. Consider, in the undoped and V-doped SiO_2/FeCo nanoparticles, superexchange interactions occur at the interface where the metal silicates have formed (e.g. Fe-O-Fe or Co-O-Co). However, in the Fe/Cu nanostructured thin films, we have indirect exchange interactions occurring, the magnetic impurities (Fe nanocrystallites) are polarizing the conduction electrons (RKKY exchange interactions). These polarized conduction electrons may more easily affect core electrons (*s*-electrons) resulting in the observed $T_{C,Alloy}$ dependence.

A comparison of the different *p*s and *q*s for the different nanoscale systems are presented in figure 6.3. For the undoped and V-doped SiO_2 nanoparticles, we observed that p_{Fe} increased slightly in magnitude with an increase in T_B suggesting that the contribution from the orbital magnetic moment of the Fe moment was altered, q_{Fe} did not appear to change with T_B suggesting that the spin contribution was constant across all four samples. Similarly, p_{Co} increased in magnitude with T_B and q_{Co} remained relatively independent of T_B. A similar analysis was attempted for the Fe/Cu nanostructured thin films. A plot of p_{Fe} and q_{Fe}s as a function of $T_{C,Alloy}$ is shown in figure 6.3 (p_{Cu} and q_{Cu} could not be determined as the signal-to-noise of the XMCD spectra was poor). We observe that both p_{Fe} and q_{Fe} depend on $T_{C,Alloy}$, with the magnitude of p_{Fe} decreasing with increasing $T_{C,Alloy}$. However, importantly, unlike the SiO_2/FeCo nanoparticles, it is not clear where the L_3 transition terminates and the L_2 transition begins. That is to say, there is significant mixing of the $2_p^{3/2}$ and $2_p^{1/2}$ character, also known as 2p3d hybridization (in agreement with with Mössbauer spectroscopy). The evolution of q_{Fe} with $T_{C,Alloy}$ is less apparent, however, with the largest $T_{C,Alloy}$ values, similar to p_{Fe}, the magnitude of q_{Fe} is small and relatively unchanged. The observed trends in the ps and qs speak to the altered orbital magnetic moments resulting from the altered electronic environments at the surface of the FeCo nanoparticles and Fe nanocrystallites.

The m_l/m_s calculated from the sum-rules[56] for the undoped and V-doped SiO_2/ FeCo nanoparticles and the Fe/Cu nanostructured thin films (Fig. 6.3). The m_l/m_s could not be calculated for the Cu/γ-Fe_2O_3 nanoparticles as spectra were only collected over the L_3 transition edge. For the undoped and V-doped SiO_2/FeCo nanoparticles we observed bulk-like Fe (from the octahedral Fe^{3+} of the interfacial Fe-silicate) orbit-to-spin, however, the Co (from the octahedral Co^{2+} of the interfacial Co-silicates) orbit-to-spin values were enhanced significantly compared to bulk fcc and hcp Co, in agreement with the observed XMCD temperature and field dependence. This enhanced spin-to-orbit ratio could be due to the preferred formation of Co-silicates over Fe-silicates. From the XMCD spectra, it would appear that the metallic Fe and a component from the Fe-silicates were coupled antiferromagnetically, whereas the metallic Co and the Co-silicates where coupled ferromagnetically. The metallic Fe

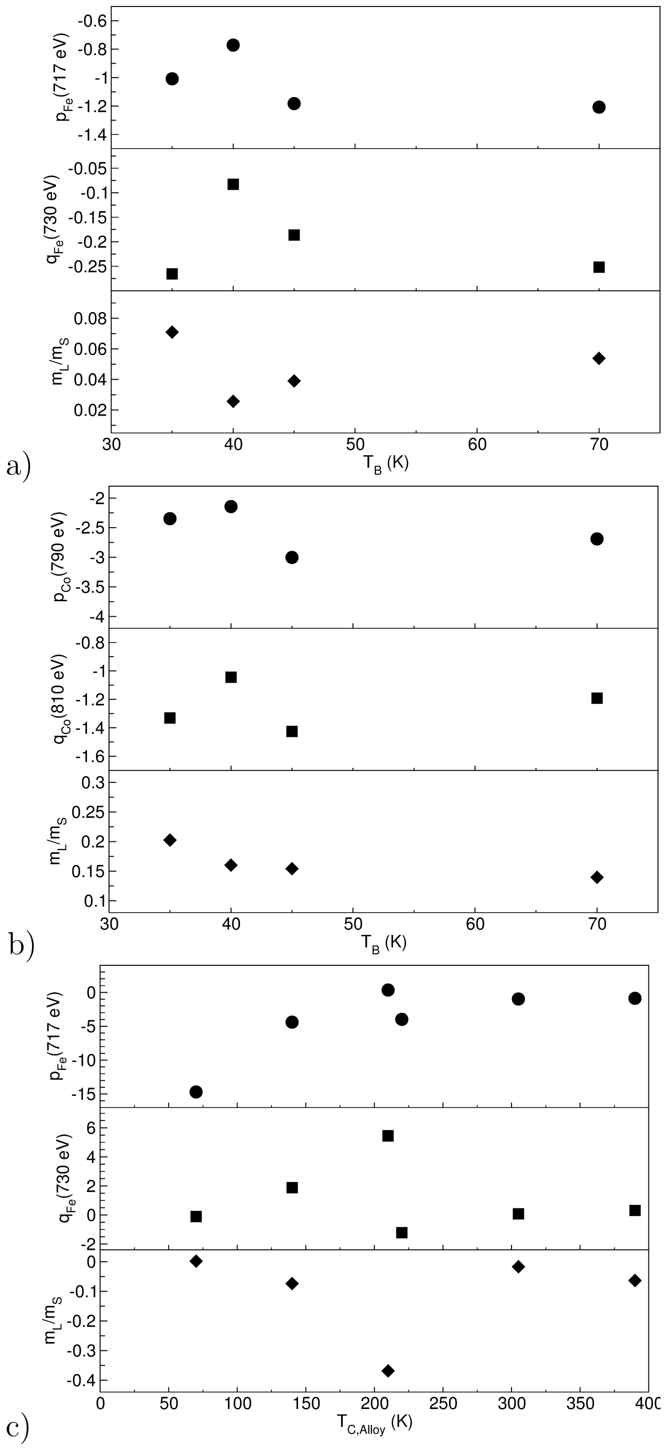

Figure 6.3: p and q values at Fe and Co energies calculated from the integrated XMCD intensity of the SiO_2/FeCo nanoparticles (a and b) and Fe/Cu nanostructured films c). m_l/m_s calculated by applying sum-rule analysis as described in the text. Error bars are smaller than the symbol size.

and Co magnetizations were coupled ferromagnetically, as would be expected for an FeCo alloy. For the Fe/Cu nanostructured thin films, owing to the $2p3d$ hybridization described above, the integrated area of the XMCD spectra varied greatly from sample to sample. As a result of this hybridization, application of the sum-rules [54; 55] is problematic as it is required that there is a clear separation between the L_3 and L_2 transition edges. Therefore, as this hybridization character appears to be similar in all the samples, only a comparison between the different Fe/Cu nanostructured thin films is valid. The calculated m_l/m_s for these Fe/Cu nanostructured thin films as a function of $T_{C,Alloy}$ is plotted in figure 6.3. The m_l/m_s values do not vary much with $T_{C,Alloy}$ unlike the p_{fe} and q_{Fe}, however, the sign of m_l/m_s changes due to the $2p3d$ hybridization described previously.

To better understand the origin of the unusual temperature dependence of the coercivity observed near $T_{C,Alloy}$ of the Fe/Cu nanostructured thin films, XMRS experiments were performed at temperatures below $\mathrm{T}_{C,Alloy}$, and above (where possible). Below T_C, the Fe in the nanocrystallites and the FeCu alloy would be ferromagnetic, however, above T_C, the interfacial FeCu alloy would be paramagnetic. We suggest, from the observed magnetometry, that above $T_{C,Alloy}$, the smallest of the Fe nanocrystallites which were pinned by the interfacial FeCu alloy and not able to contribute to the coercivity are no longer being pinned and are once again able to contribute to the coercivity. It is because of this pinning mechanism that above $T_{C,Alloy}$, we observed an increase in the coercivity. Element specific hysteresis loops were collected for metallic Fe, Fe^{3+}, and Cu^{2+} where the Fe^{3+} and Cu^{2+} behaviour is from the FeCu alloy. The 50 K elemental hysteresis loops for metallic Fe were similar to the overall loops obtained from magnetometry. The presence of a vertical loop shift indicates that pinning of the metallic Fe magnetization was present, in agreement with the XMCD spectra. Further evidence of pinning can be observed in the Fe^{3+} elemental hysteresis loops as the loops are mirrored along the field axis, relative to the metallic Fe loops, indicating that the difference between the circularly polarized photons electron yield has been altered. Furthermore, the measured elemental coercivity of the metallic Fe component persists at temperatures above where the elemental coercivity of the Fe^{3+} component is zero (above $T_{C,Alloy}$), strengthening our arguments about the origins of the temperature dependent coercivity and $\chi_{dc}(T)$. Similar results were observed for the Cu^{2+} elemental hysteresis loops. These experiments have shown definitely that the FeCu alloy is magnetic and that the observed $T_{C,Alloy}$ is a T_C (or magnetic ordering temperature) as there was no measured coercivity in the Fe^{3+} and Cu^{2+} components above this temperature, where the alloy is paramagnetic. These results further support the idea that above $T_{C,Alloy}$, the smallest of the Fe nanocrystallites are once again able to contribute to the overall magnetism.

The spontaneous formation of an interfacial phase at the core/shell or nanocrystallite/matrix interface has been shown to occur in all three of the nanoscale systems studied herein. These observations suggest that the interface is not a simple change from one phase to another (i.e. a sharp interface) but rather a new interfacial phase intermediate to the core/shell or nanocrystallite/matrix forms. As these interfacial phases are (super)exchange coupled directly with the surface ions of the nanoparticle/nanocrystallite core, the role they play on the elemental, atomic and overall magnetism is substantial and must be accounted for in order to describe fully the observed magnetism of these nanoscale systems.

Chapter 7

Summary and Conclusions

The formation of magnetically active interfacial phases has provided several key insights into the physics of the magnetism of the Cu/γ-Fe_2O_3, SiO_2/FeCo, and Fe/Cu nanoscale systems. These interfacial phases alter the electronic environment of the core's surface atoms through exchange interaction mechanisms (direct, indirect, and superexchange) allowing these once frustrated spins to align with the core moments, once again contributing to the overall magnetism of the system. The mechanism of the formation of these interfacial phases depends crucially on the nature of the nanoparticle core. We saw that for the Fe nanocrystallites embedded in a copper matrix, an interfacial alloy of FeCu formed and was influenced strongly by the amount of energy added to the system by the secondary End-Hall ion-beam. However, for the undoped and V-doped SiO_2/FeCo core/shell nanoparticles, we observed the effective oxidation of surface Fe and Co atoms from the oxygen in the SiO_2 shell forming metal silicates. These results were confirmed by the addition of a 2% at. wt. of V during the synthesis of the nanoparticle core. As V-oxides have a larger enthalpy of formation compared with Fe- and Co-oxides, we observed the preferential formation of V-oxide at the surface as the V was oxidized by the oxygen in the SiO_2 shell. This formation of V-oxide occurred at the expense of the formation of the Fe- and Co-silicates. For the Cu/γ-Fe_2O_3 core/shell nanoparticles, we observed octahedral Cu^{2+} in the elemental absorption spectra. This suggests, that at the surface of the γ-Fe_2O_3 nanoparticle core, Cu is occupying the B-site vacancies forming a thin (<0.2 Å) copper doped Fe-oxide (e.g. $CuFe_2O_4$). The formation of the interfacial phase was influenced by the types of nanoparticle/nanocrystallite cores. These differences also result in different exchange interactions that lead to the changes in the nanomagnetism.

In Chapter three, we discussed the magnetism observed in Cu/γ-Fe_2O_3 nanoparticles as a function of Cu shell thickness. The identification of the microstructure and composition of these nanoparticles using x-ray diffraction, electron diffraction, x-ray absorption spectroscopy, and Mössbauer spectroscopy led to the determination that a Cu doped Fe-oxide had formed at the interface between core and shell. In addition, for the thickest Cu shell, Cu^{2+} with antiferromagnetic CuO behaviour likely formed (as evidenced by the antiferromagnetic-like reorientation in the Cu XMCD). With the increase in the Cu shell thickness, more of this interfacial phase was able to form. The effects on the magnetism of this interfacial phase were readily observed in the temperature dependencies of the saturation magnetization, coercivity, and exchange bias field shift. The decreased temperature dependence of M_S was due to fewer disordered surface spins. In addition, fits of the $M_S(T)$ to the modified Bloch law showed an increase in the exchange integral with an increase in Cu shell thickness suggesting that the formation of this interfacial phase drives the strengthening of the exchange interactions. Similar changes in the $H_C(T)$ and $H_{EX}(T)$ were observed. The effects of the Cu^{2+} on the elemental magnetism was readily observed in the XMCD spectra at the L-edges of Fe and Cu. Induced octahedral Cu^{2+} magnetism was observed, with temperature and field dependence describing the effect of pinning, similar to the Fe^{3+} elemental magnetism. Considering that Cu filled some of the B-site vacancies in the γ-Fe_2O_3, would similar affects be observed in a core of Fe_3O_4 where there are no vacancies?

The undoped and V-doped SiO_2/FeCo nanoparticles provided further insight into the role of the interfacial phase on the magnetism. Unlike the Cu/γ-Fe_2O_3 nanoparticles, where the induced Cu magnetism resulted from the formation of a Cu-ferrite-like phase, here the formation of Fe- and Co-silicates through the oxidation of the surface Fe and Co by the oxygen in the SiO_2 shell occurred. These presence of these magnetically active metal silicates shows clearly that the SiO_2 shell is not inert and plays alters the magnetic properties of the nanoparticles significantly. Like the Cu/γ-Fe_2O_3 nanoparticles, we observed changes to the temperature dependencies of the $M_S(T)$ and $H_C(T)$. With an increased silica shell thickness, an increase in M_S was observed suggesting clearly that the magnetization becomes more bulk-like recovering any "lost" surface spins with Fe-O and Co-O coordination being reinforced. The $H_C(T)$ over the intermediate temperature ranges ($T > T_B$) showed an increase in coercivity with an increase in the silica shell. However, below T_B, we observed the opposite, as spin-glass-like behaviour from the interparticle interactions altered the energy landscape resulting in the larger H_C's with the thinner silica shell. To further understand the direct consequences of these interfacial metal-silicates, the identification of the Fe-silicates formed using Mössbauer spectroscopy should be explored. Ab initio simulations, using the VASP[118] package, of the collected x-ray photoelectron spectra should be performed in order to better understand the formation of the interfacial metal silicates and their electronic environment. In addition, understanding the mechanisms by which the vanadium dopant appears to be "sucked" out of the entire FeCo nanoparticle to reside on the surface during the SiO_2 coating process, by doping with other materials with larger enthalpy of formations than the metal-silicates should be attempted.

Nanostructured thin films of Fe nanocrystallites embedded in a Cu matrix were fabricated using a dual ion-beam deposition system. The addition of energy during the Fe deposition provided a mechanism for altering the amount of intermixing between the Fe nanocrystallites and the Cu matrix. This resulted in the formation of an interfacial FeCu alloy whose thickness depended on the amount of energy added. Microstructure and composition experiments identified that both the Fe and Cu were cubic and that there was a clear preferred orientation to the Cu. From the temperature dependent *dc* and *ac* susceptibilities, we observed both blocking behaviour as the Fe nanocrystallites became superparamagnetic and a magnetic transition as the FeCu alloy became paramagnetic. With increased intermixing, the temperatures at which these two processes occurred converged. Interestingly, it is this convergence of T_B and $T_{C,Alloy}$ that points to this material being a good magnetocaloric material. These magnetocaloric properties will be explored in the future. The identification that the observed ferromagnetic-to-paramagnetic transition was a T_C was accomplished from XMRS experiments that showed no elemental Cu magnetism above $T_{C,Alloy}$ and mag-

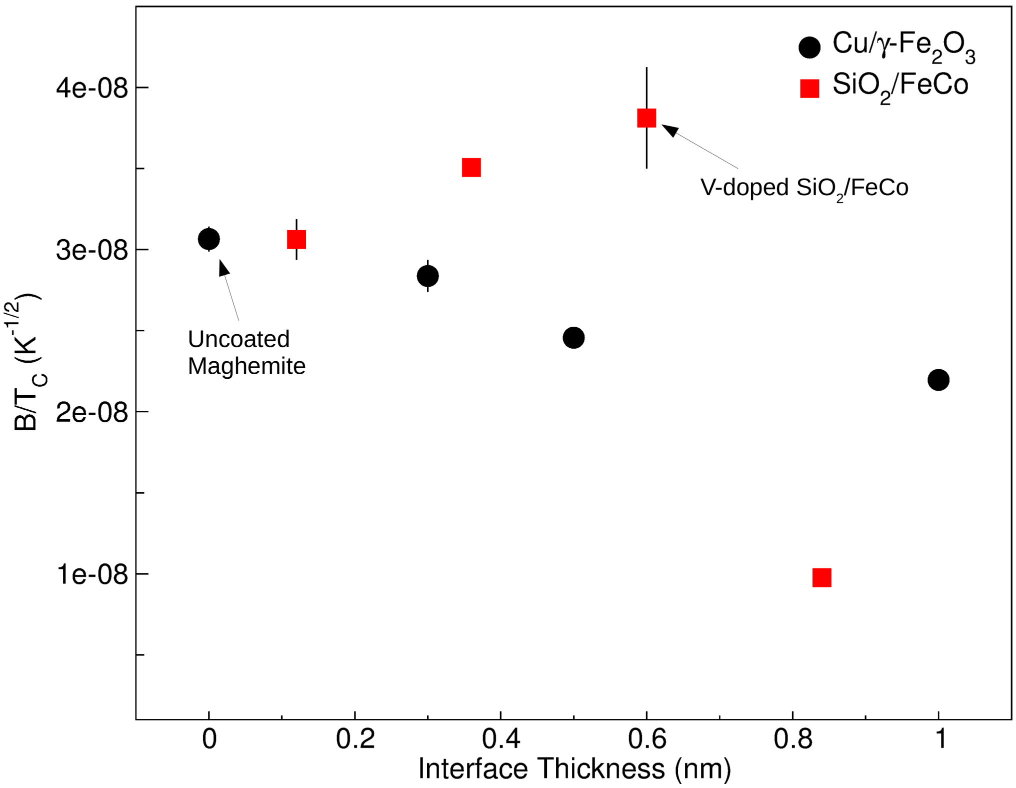

Figure 7.1: Plot of B normalized to the T_C of maghemite and FeCo as a function of interface thickness for the undoped and V-doped SiO_2/FeCo and Cu/γ-Fe_2O_3 nanoparticles.

netic Cu^{2+} behaviour below. In addition, it is this transition from ferromagnetic to paramagnetic that causes the sudden rapid increase in the measured $H_C(T)$ as the once pinned smaller Fe nanocrystallites are able to once again contribute to the coercivity.

In summary, we have shown that the formation of an interfacial phase occurs readily in the nanoscale systems studied. The nature of the interfacial phase depends crucially on the microstructure and composition of the nanoparticle/nanocrystallite core. There is a fundamental difference in the behaviour of the interfacial phase when the exchange interactions in the nanoscale system are solely superexchange based or a mixture of indirect exchange and superexchange as indicated by the interfacial thickness dependence of the normalized Bloch constant (Fig. 7.1). These results suggests clearly that the interaction between nanoparticle core and interface are of significant importance to the overall magnetization of these nanoscale system. Furthermore, these magnetically active interfacial phases allow the once frustrated surface spins to contribute to the overall magnetism, yielding bulk-like magnetizations.

7.1 Future work

Many questions have arisen during the course of these scientific investigations that would advance further our understanding of the fundamental magnetism of the systems studied and similar systems. Below is a short list of future work designed to address some of these questions:

A low temperature CEMS detector should be constructed. This detector will allow for the identification of the local nuclear environment around the Fe nuclei of thin films below their blocking temperatures. For example, identification of the hyperfine parameters and their temperature dependence of the γ-Fe nanocrystallites and the FeCu alloy formed in the Fe/Cu nanostructured thin films.

Determine uniquely the Fe-silicate(s) that have formed in the undoped and V-doped SiO_2/FeCo nanoparticles with transmission Mössbauer spectroscopy[117]. In addition, a detailed characterization of the composition, structure, and magnetism of uncoated FeCo and V-doped FeCo will address whether the observed properties of the coated FeCo and V-doped FeCo nanoparticles are inherent to the cores themselves or are the result of the SiO_2 shell.

The magnetocaloric effect depends crucially on the rate of change of the magnetization as a function of temperature. At T_B (and T_C) in the three systems studied, $M(T)$ varies rapidly. By examining isothermal magnetization curves near these temperatures, it would be interesting to understand the physics behind tuning the dynamical freezing (T_B) and spin fluctuations (T_C), maximizing the change in magnetic entropy over a selected, useful, range of temperatures.

The unique determination of the spin structure of core/shell nanoparticles is of considerable interest. Polarized small angle neutron scattering is ideally suited to explore the nature of the surface/interfacial spin orientation[119; 120; 121]. Currently, the analysis of these experiments remains model dependent, however, determination of the structure factor from small angle x-ray scattering experiments can simplify the choice of models. By combining both x-ray and neutron scattering experiments new insights into the role of an interfacial phase on the spin structure and magnetism of core/shell nanoparticles can be explored in detail.

Appendix A

Experimental Acknowledgments

Contributions to this thesis were made by several collaborators. In this chapter, tables are provided that list the name and affiliation of these collaborators and the work that they provided towards the study of the Cu/γ-Fe_2O_3 nanoparticles, undoped and V-doped FeCo and SiO_2/FeCo nanoparticles, and the Fe/Cu nanostructured thin films.

Table A.1: Experiments and data analysis performed by collaborators on the Cu/γ-Fe_2O_3 nanoparticle system.

System	**Experiment**	**Name**	**Role**
Cu/γ-Fe_2O_3	Synthesis	Elizabeth Skoropata, University of Manitoba	Mrs. Skoropata designed the synthesis procedure and helped with the synthesis.
	XRD	Neil Ball, University of Manitoba	Mr. Ball Helped set up diffractometer and I perforned all data collection and analysis.
	TEM	Prof. Hao Ouyang, National Tsing Hua University, Taiwan	Organized TEM/HRTEM image collection and HRTEM image analysis. I performed all TEM image analysis.
	Mössbauer Spectroscopy	Ryan Desautels	I collected the spectra and performed the requisite data analysis.
	Magnetometry	Ryan Desautels	I collected the data and performed the requisite analysis.
	XAS/XMCD	Dr. John Freeland, Argonne National Laboratory, USA	Dr. Freeland helped with sample mounting and beamline setup. I collected the spectra and performed all requisite data analysis.

Table A.2: Experiments and data analysis performed by collaborators on the undoped and V-doped FeCo and SiO_2/FeCo nanoparticle systems.

System	**Experiment**	**Name**	**Role**
FeCo, SiO_2/FeCo	Synthesis	Dr. Michael Rowe, Toyota Research Institute North America, USA	Dr. Rowe designed synthesis procedure and helped synthesize nanoparticles.
	XRD	Dr. Michael Rowe	Dr. Rowe helped set up diffraction pattern collection. I performed all data analysis.
	TEM	Dr. Taghi Daroudi, Electron Microscope Facility, Clemson Univeristy, USA	Dr. Daroudi collected the TEM images. I performed all TEM image analysis.
	XPS	Michael Jones, Toyota Research Institute North America, USA	Mr. Jones helped set up XPS system. I performed all data collection and analysis.
	Magnetometry	Ryan Desautels	I collected the data and performed the requisite analysis.
	XAS/XMCD	Dr. John Freeland,	Dr. Freeland helped with sample mounting and beamline setup. I collected the spectra and performed all requisite data analysis.

Table A.3: Experiments and data analysis performed by collaborators on the Fe/Cu nanostructured thin film systems.

System	**Experiment**	**Name**	**Role**
Fe/Cu Films	Fabrication	Dr. Ko-Wei Lin, National Chung Hsing University, Taiwan	Dr. Lin helped organize film fabrication. I fabricated all nanostructured films.
	TEM	Dr. Ko-Wei Lin	Dr. Lin's graduate students collected TEM images and I performed all image analysis.
	XRD, XRR, CEMS	Ryan Desautels	I collected patterns and performed requisite data analysis.
	Magnetometry	Ryan Desautels	I collected data and performed requisite data analysis.
	XAS/XMCD	Dr. John Freeland	Dr. Freeland helped with sample mounting and with beamline setup. I collected the spectra and performed all requisite data analysis

Bibliography

[1] J. L. Dormann, D. Firorani, and E. Tronc. Magnetic relaxation in fine particle systems. In I. Prigogine and Stuart A. Rice, editors, *Advances in Chemical Physics XCVIII*, page 283. John Wiley & Sons, Inc., New York, 1997.

[2] Quantum Design Periodic Table. http://www.qdusa.com/; Accessed: September 23rd, 2015.

[3] S. Sun, C. B. Murray, D. Weller, L. Folks, and A. Moser. *Science*, 287:1989–1992, 2000.

[4] W. H. De Jong and P. J. Borm. *Int. J. Nanomed.*, 3:133–149, 2008.

[5] W. H. Meiklejohn and C. P. Bean. *Phys. Rev.*, 105:904–913, 1957.

[6] R. M. Persoons, E. De Grave, P. M. A. de Bakker, and R. E. Vandenberghe. *Phys. Rev. B*, 47:5894, 1993.

[7] E. Skoropata, R. D. Desautels, C.-C. Chi, H. Ouyang, J. W. Freeland, and J. van Lierop. *Phys. Rev. B*, 89:024410, 2014.

[8] E. C. Stoner and E. P. Wohlfarth. *Philos. T. Roy. Soc. A*, 240:599, 1948.

[9] J. M. D. Coey. *Phys. Rev. Lett.*, 27:1140–1142, 1971.

[10] A. H. Morrish and K. Haneda. *J. Magn. Magn. Mater.*, 35:105, 1983.

[11] J. Nogués, J. Sort, V. Langlais, V. Skumryev andS. Suriñach, J. S. Muñoz, and D. Baró. *Phys. Rep.*, 422:65, 2005.

[12] S. Bose, A. R. Bhattacharyya, P. V. Kodgire, A. R. Kulkarni, and A. Misra. *J. Nanosci. Nanotechnol.*, 8:1867, 2008.

[13] Zureks. Bethe-slater curve. Source: Own work; Liscence: CC0 1.0; Accessed: September 23rd, 2015.

[14] M. A. Ruderman and C. Kitell. *Phys. Rev.*, 96:99, 1954.

[15] T. Kasuya. *Prog. Theor. Phys.*, 16:45, 1956.

[16] K. Yosida. *Phys. Rev.*, 106:893, 1957.

[17] P. Grünberg, R. Schreiber, Y. Pang, M. B. Brodsky, and C. H. Sowers. *Phys. Rev. Lett.*, 57:2442, 1986.

[18] C. Carbone and S. F. Alvarado. *Phys. Rev. B*, 36:2433, 1987.

[19] D. H. Mosca, F. Petroff, A. Fert, P. A. Schroeder, W. P. Pratt Jr., R. Loloee, and S. Lequien. *J. Magn.Magn. Mater.*, 94:L1, 1991.

[20] Melarn. MnO Superexchange Interaction. Source: Own work; Liscence: CC BY-SA 3.0; Accessed: September 23rd, 2015.

[21] J. B. Goodenough. *Phys. Rev.*, 100:564, 1955.

[22] H. A. Kramers. *Physica*, 1:182, 1934.

[23] M. Solzi. *Fundamental Properties of Nanoscale Materials.* World Scientific, River Edge, NJ, 1994.

[24] L. Néel. *Journal de Physics et la Radium*, 15:225, 1954.

[25] X. Battle and A. Labarta. *J. Phys. D: Appl. Phys.*, 35:R15, 2002.

[26] Alison Chaiken. Precession2. Source: Own work; Liscence: CC BY-SA 3.0; Accessed: December 23rd, 2015.

[27] A. H. Morrish. *The Physical Principles of Magnetism.* John Wiley & Sons, Inc., 1965.

[28] F. Bloch. *Z. Physik*, 61:206, 1930.

[29] E. Della Torre, L. H. Bennett, and R. E. Watson. *Phys. Rev. Lett.*, 94:147210, 2005.

[30] R. Aquino, J. Bepeyrot, M. H. Sousa, F. A. Tourinho, E. Dubois, and R. Perzynski. *Phys. Rev. B*, 72:184435, 2005.

[31] K. Mandal, Subarna Mitra, and P. Anil Kumar. *Europhys. Lett.*, 75:618, 2006.

[32] R. D. Desautels, E. Skoropata, Y.-Y. Chen, H. Ouyang, J. W. Freeland, and J. van Lierop. *J. Phys.: Condens. Matter*, 24:146001, 2012.

[33] V. K. Pecharsky and P. Y. Zavalij. *Fundamentals of Powder Diffraction and Structural Characterization of Materials.* Springer, 2nd edition, 2009.

[34] J. Rodriguez-Carvajal. *Physica B*, 192:55, 1993.

[35] W. A. Dollase. *J. Appl. Crystallogr.*, 19:267–272, 1986.

[36] P. Villars and K. Cenzual. Pearson's crystal data: Crystal structure database for inorganic compounds, Release 2014/15.

[37] H. M. Rietveld. *Acta. Cryst.*, 22:151–152, 1967.

[38] H. M. Rietveld. *J. Appl. Cryst.*, 2:65–71, 1969.

[39] E. Hecht. *Optics*. Addison-Wesley, Reading, MA, 2002.

[40] L. G. Parratt. *Phys. Rev.*, 95:359, 1954.

[41] A. Ulyanenkov. *Proc. SPIE.*, 5536:1–15, 2004.

[42] W. S. Rasband. Image processing and analysis in java, 2005.

[43] D. J. Smith. *Reports Prog. Phys.*, 41:1513–1580, 1997.

[44] P. R. Buseck, J. M. Cowley, and L. Eyring. *High Resolution Transmission Electron Microscopy and Associated Techniques*. Oxford University Press, New York, 1988.

[45] J. C. H. Spence. *Experimental High-Resolution Electron Microscopy*. Oxford University Press, 1981.

[46] NIST X-ray Photoelectron Spectroscopy Database. National Institute of Standards and Technology, Gaithersberg, 2012. http://srdata.nist.gov/xps/.

[47] *CasaXPS Manual*. Casa Software Ltd. http://www.casaxps.com/.

[48] Multipak. http://www.casaxps.com/.

[49] S. Doniach and M. Sunjic. *J. Phys.*, 4C31:285, 1970.

[50] D. A. Shirley. *Phys. Rev.*, 55:4709, 1972.

[51] L. Tröger, D. Arvanitis, K. Baberschke, H. Michaelis, U. Grimm, and E. Zschech. *Phys. Rev. B*, 46:3283, 1992.

[52] F. M. F. de Groot, J. C. Fuggle, B. T. Thole, and G. A. Sawatzky. *Phys. Rev. B*, 42:5459, 1990.

[53] E. Stavitski and F. M. F. de Groot. *Micron*, 41:687–694, 2010.

[54] B. T. Thole, P. Carra, F. Sette, and G. van der Laan. *Phys. Rev. Lett.*, 68:1943, 1992.

[55] P. Carra, B. T. Thole, M. Altarelli, and X. Wang. *Phys. Rev. Lett.*, 70:694, 1993.

[56] C. T. Chen, Y. U. Idzerda, H.-J. Lin, N. V. Smith, G. Meigs, E. Chaban, G. H. Ho, E. Pellegrin, and F. Sette. *Phys. Rev. Lett.*, 75:152, 1995.

[57] D. Cohen. *IEEE T. Magn.*, MAG-11:694, 1975.

[58] J. Clarke. *Sci. Am.*, 271:46, 1994.

[59] N. N. Greenwood and T. C. Gibb. *Mossbauer Spectroscopy.* Chapman and Hall Ltd, London, 1971.

[60] M. Darby Dyer, D. G. Agresti, M. W. Schaefer, C. A. Grant, and E. C. Sklute. *Annu. Rev. Earth Planet. Sci.*, 34:83–125, 2006.

[61] J. Rockenberger, E. C. Scher, and A. P. Alivisatos. *J. Am. Chem. Soc.*, 121:11595, 1999.

[62] T. N. Shendruk, R. D. Desautels, B. W. Southern, and J. van Lierop. *Nanotechnology*, 18:455704, 2007.

[63] R. D. Desautels, Y.-Y. Chen, H. Ouyang, S.-C. Lo, J. W. Freeland, and J. van Lierop. *J. Appl. Phys.*, 111:07B518, 2012.

[64] J. Park, K. An, Y. Hwang, J.-G. Park, H.-J. Noh, J.-Y. Kim, J.-H. Park, N.-M. Hwang, and T. Hyeon. *Nature Materials*, 3:891–895, 2004.

[65] R. D. Desautels, E. Skoropata, Y.-Y. Chen, H. Ouyang, J. W. Freeland, and J. van Lierop. *Appl. Phys. Lett.*, 99:262501, 2011.

[66] I. V. Golosovsky, M. Tovar, U. Hoffman, I. Mirebeau, F. Fauth, D. A. Kurdyukov, and Y. Kumzero. *JETP Lett.*, 83:298, 2006.

[67] S. Peng and S. Sun. *Angew. Chem. Int. Ed.*, 46:4155–4158, 2007.

[68] S. Brice-Profeta, M.-A. Arrio, E. Tronc, N. Menguy, I. Letard, C. Cartier dit Moulin, M. Nogues, C. Chaneac, J.-P. Jolivet, and Ph. Sainctavit. *J. Magn. Magn. Mater.*, 288:354, 2005.

[69] J. Ghijsen, L. H. Tjeng, J. van Elp, H. Eskes, J. Westerink, G. A. Sawatzky, and M. T. Czyzyk. *Phys. Rev. B*, 38:11322, 1988.

[70] R. C. O'Handley. *Modern Magnetic Materials, Principles and Applications.* Wiley, New York, 2000.

[71] R. H. Kodama. *J. Magn. Magn. Mater.*, 200:359, 1999.

[72] D. Jiles. *Introduction to Magnetism and Magnetic Materials.* Taylor and Francis, London, 1998.

[73] J. Restrepo, Y. Labay, and J. M. Greneche. *Physica B*, 384:221, 2006.

[74] K. Adebayo and B. W. Southern. e-print arXiv:cond-mat.stat.mech/1002.4648v2.

[75] J. Tucek, R. Jzoril, and D. Petridis. *J. Nanosci. Nanotehnol.*, 6:926, 2006.

[76] R. D. Desautels, E. Skoropata, and J. van Lierop. *J. Appl. Phys.*, 103:07D512, 2008.

[77] R. Nakajima, J. Stohr, and Y. U. Idzerda. *Phys. Rev. B*, 59:6421, 1999.

[78] K. Fauth. *Appl. Phys. Lett.*, 85:769, 2004.

[79] J. van Lierop, K.-W. Lin, J. Z.-Y. Guo, H. Ouyang, and B. W. Southern. *Phys. Rev. B*, 75:134409, 2007.

[80] R. J. Pollard. *J. Phys.: Condens. Matter*, 2:983, 1990.

[81] B. A. Parviz, D. Ryan, and G. M. Whitesides. *IEEE Trans. Adv. Packag.*, 26:233–241, 2003.

[82] M. T. Bohr. *IEEE. Trans. Nanotechnol.*, 1:56–62, 2002.

[83] G. M. Whitesides and B. Grzybowski. *Science*, 295:2418–2421, 2002.

[84] S. Tajima, T. Hattori, M. Kondoh, H. Kishimoto, M. Sugiyama, and T. Kikko. *IEEE Trans. Magn.*, 41:3280–3282, 2005.

[85] F. Hettstedt, H. Greve, U. Schurmann, A. Gerber, V. Zaporojtchenko, R. Knockel, F. Faupel, and E. Quandt. *Proceedings of the 37th European Microwave Conference*, page 207, 2007.

[86] H. Zeng, J. Li, J. P. Liu, Z. L. Wang, and S. Sun. *Nature*, 420:395–398, 2002.

[87] F. del Monte, M. P. Morales, D. Levy, A. Fernandez, M. Ocana, A. Roig, E. Molins, K. O'Grady, and C. J. Serna. *Langmuir*, 13:3627–3634, 1997.

[88] Y. K. Mishra, F. Singh, D. K. Avasthi, J. C. Pivin, D. Malinovska, and E. Pippel. *Appl. Phys. Lett.*, 91:063103, 2007.

[89] G. Rizza, Y. Ramjauny, T. Gacoin, L. Vielle, and S. Henry. *Phys. Rev. B*, 76:245414, 2007.

[90] S. Du, G. Zhou, X. Want, and L. Shang. *Adv. Mater. Res.*, 233-235:1188–1191, 2011.

[91] J. Lee, Y. Lee, J. K. Youn, H. B. Na, T. Yu, H. Kim, S.-M. Lee, Y.-M. Koo, J. H. Kwak, H. G. Park, H. N. Chang, M. Hwang, J.-G. Park, J. Kim, and T. Hyeon. *Small*, 4:143–152, 2008.

[92] C. Li, Z. Li, X. Du, and H. Guo. *Adv. Mater. Res.*, 178:291–295, 2011.

[93] M. P. Rowe, K. E. Plass, K. Kim, C. Kurdak, E. T. Zellers, and A. J. Matzger. *Chem. Mater.*, 16:3513–3517, 2004.

[94] D. J. Miller, M. C. Biesinger, and N. S. McIntyre. *Surf. Interface Anal.*, 33:299–305, 2002.

[95] P. M. A. Sherwood, D. Briggs, and M. P. Seah. *Practical Surface Analysis by Auger and X-ray Photoelectron Spectroscopy.* Wiley, Chichester, 1983.

[96] C. L. Chiena dn S. H. Liou, D. Kofalt, Wu Yu, T. Egami, and T. R. McGuire. *Phys. Rev.*, 33:3247–3250, 1986.

[97] V. Chakarian, Y. U. Idzerda, and C. T. Chen. *Phys. Rev. B*, 57:5312, 1998.

[98] R. W. Chantrell and E. P. Wohlfarth. *J. Magn. Magn. Mater.*, 40:1–11, 1983.

[99] J. A. Mydosh. *Spin glasses: an experimental introduction.* Taylor and Francis, London, 1993.

[100] R. H. Kodama, A. E. Berkowitzh, E. J. McNiff Jr., and S. F Foner. *Phys. Rev. Lett.*, 77:394, 1996.

[101] G. Xiao and C. Chien. *J. Appl. Phys.*, 61:3308, 1987.

[102] M. Respaud. *J. Appl. Phys.*, 86:556, 1999.

[103] K. Kuepper, M. Raeker, C. Taubitz, M. Uhlarz, C. Piamonteze, F. M. F. de-Groot, E. Arenholz, V. R. Galakhov, Y. M. Mukovskii, and M. Neumann. *J. Phys.: Condens. Matter*, 24:435602, 2012.

[104] W. L. O'Brein, B. P. Tonner, G. R. Harp, and S. S. P. Parkin. *J. Appl. Phys.*, 76:6462, 1994.

[105] J. T. Lau, A. Frölisch, M. Martins, R. Nietubyc, M. Reif, and W. Wurth. *New J. Phys.*, 4:98, 2002.

[106] P. Asselin, R. F. Evans, J. Barker, R. W. Chantrell, R. Yanes, O. Chubykalo-Fesenko, D. Hinzke, and U. Nowak. *Phys. Rev. B*, 82:054415, 2010.

[107] M. Manivel Raja, K. W. Lin, and R. J. Gambino. *J. Appl. Phys.*, 91:7439–7441, 2002.

[108] J.-J. Cuomo, S. M. Rossnagel, and H. R. Kaufman. *Handbook of ion beam processing technology: principles, deposition, film modification, and synthesis.* Noyes Publication, 1989.

[109] A. L. Patterson. *Phys. Rev.*, 56:978–982, 1939.

[110] K. Sumiyama, T. Yoskitake, and Y. Nakamura. *Trans. JIM*, 26:217–224, 1985.

[111] E. Lee, D. H. Kim, J. Hwang, K. Lee, S. Yoon, B. J. Suh, K. H. Kim, J.-Y. Kim, Z. H. Zhang, B. Kim, B. I. Min, and J.-S. Kang. *Appl. Phys. Lett.*, 102:133703, 2013.

[112] M. E. McHenry, M. A. Willard, and D. E. Laughlin. *Prog. Mater. Sci.*, 44:291, 1999.

[113] R. D. Desautels, M. P. Rowe, M. Jones, A. Whallen, and J. van Lierop. *Langmuir*, 31:2879–2884, 2015.

[114] B. Martinez, X. Obardors, L. Balcells, A. Rouanet, and C. Monty. *Phys. Rev. Lett.*, 80:181, 1998.

[115] A. E. Berkowitz, W. J. Schuele, and P. J. Flanders. *J. Appl. Phys.*, 39:1261, 1968.

[116] E. Skoropata, R. D. Desautels, and J. van Lierop. *J. Appl. Phys.*, 105:07B503, 2009.

[117] M. P. Rowe, S. Sullivan, R. D. Desautels, E. Skoropata, and J. van Lierop. *J. Mater. Chem. C*, page accepted, 2015.

[118] G. Kresse. Vienna Ab initio Simulation Package.

[119] T. Oku, T. Kikuchi, T. Shinohara, J. Suzuiki, Y. Ishii, M. Takeda, K. Kakurai, Y. Sasaki, M. Kishimoto, M. Yokoyama, and Y. Nishihara. *Physica B*, 404:2575, 2009.

[120] K. L. Krycka, J. A. Borchers, R. A. Booth, Y. Ijiri, K. Hasz, J. J. Rhyne, and S. A. Majetich. *Phys. Rev. Lett.*, 113:147203, 2014.

[121] S. Disch, E. Wetterskog, R. P. Hermann, A. Wiedenmann, U. Vainio, G. Salazar-alvarex, L. Bergström, and Th Brückel. *New. J. Phys.*, 14:013025, 2012.